

COMBUSTION ENGINEERING, INC.  
REPORT CENPD-153-NP, Rev. 1-NP

EVALUATION OF UNCERTAINTY IN THE  
NUCLEAR POWER PEAKING MEASURED BY THE  
SELF-POWERED, FIXED IN-CORE DETECTOR SYSTEM

A. Jonsson  
W. B. Terney  
M. W. Crump

May 1980

This report replaces the following two reports:  
CENPD-145, "INCA Method of Analyzing In-Core Detector Data in  
Power Reactors:  
CENPD-153, "Evaluation of Uncertainty in the Nuclear Form Factor  
Measured by Self-powered Fixed In-Core Detector Systems"

 **POWER  
SYSTEMS**  
COMBUSTION ENGINEERING, INC.

8007110248

LEGAL NOTICE

This report was prepared as an account of work sponsored by Combustion Engineering, Inc. Neither Combustion Engineering nor any person acting on its behalf:

a. Makes any warranty or representation, expressed or implied including the warranties of fitness for a particular purpose or merchantability, with respect to the accuracy, completeness, or usefulness of the information contained in this report, or that the use of any information, apparatus, method, or process disclosed in this report may not infringe privately owned rights; or

b. Assumes any liabilities with respect to the use of, or for damages resulting from the use of, any information, apparatus, method or process disclosed in this report.



#### ACKNOWLEDGEMENT

Many individuals have contributed to the contents and production of this report. The contributions of Dr. R. R. Lee, Mr. T. G. Ober, Dr. J. R. Rec, Dr. R. J. Krisst, Mrs. J. Santasiere, Mr. E. A. Williamson, Jr., Mr. R. P. Bandera, Dr. J. L. Biffer, and Mrs. D. Sopelak are gratefully acknowledged.

## FOREWORD

This revision to CENPD-153 combines two previous reports: CENPD-145, "INCA Method of Analyzing In-core Detector Data in Power Reactors," April 1975, and CENPD-153, "Evaluation of Uncertainty in the Nuclear Form Factor Measured by Self-Powered, Fixed In-Core Detector Systems," August 1974. The revision represents an extension of the data base for the uncertainty analysis to include several plants and later cycle cores.

## TABLE OF CONTENTS

### PART I - THE BASIC MEASUREMENT UNCERTAINTY

<u>Section</u>	<u>Title</u>	<u>Page</u>
I.0	INTRODUCTION	I.0.1
I.1	IN-CORE INSTRUMENT SYSTEM DESCRIPTION	I.1.1
1.0	INTRODUCTION	I.1.1
1.1	DESCRIPTION OF FIXED DETECTORS	I.1.1
1.1.1	Rhodium Detectors	I.1.1
1.1.2	Background Detectors	I.1.2
1.2	DESCRIPTION OF IN-CORE INSTRUMENT ASSEMBLIES	I.1.2
1.3	DETECTOR LAYOUT	I.1.3
1.4	INSTRUMENTATION AND READOUT	I.1.3
I.2	MEASUREMENT TECHNIQUES, CALIBRATION, REPRODUCIBILITY	I.2.1
2.0	GENERAL	I.2.1
2.1	FIXED IN-CORE DETECTORS	I.2.1
2.1.1	System Performance	I.2.1
2.1.2	Detector Calibration and Reproducibility	I.2.2
2.1.3	Detector Linearity	I.2.4
2.1.4	Detector Depletion	I.2.4
2.1.5	Background	I.2.5
2.2	REFERENCES	I.2.6
I.3	BASIC BOX POWER MEASUREMENT UNCERTAINTY FOR $F_q$ , $F_{xy}$ , and $F_r$	I.3.1
3.0	INTRODUCTION	I.3.1
3.0.1	Description of Method	I.3.1
3.0.2	Summary of Results	I.3.2
3.1	DESCRIPTION OF OPERATING DATA	I.3.2
3.1.1	Description of Measured Data	I.3.2
3.1.2	Operating Histories	I.3.3
3.1.2.1	Calvert Cliffs (CC) Unit 1	I.3.3
3.1.2.2	St. Lucie Unit 1	I.3.4
3.1.2.3	Millstone Unit 2	I.3.4
3.1.2.4	Calvert Cliffs (CC) Unit 2	I.3.4
3.1.2.5	Fort Calhoun Unit 1	I.3.5

TABLE OF CONTENTS Continued

PART I (Continued)

<u>Section</u>	<u>Title</u>	<u>Page No.</u>
3.2	DESCRIPTION OF CALCULATIONS	I.3.6
3.2.1	Description of Basic Core Follow Models	I.3.6
3.2.2	Correction of Calculation for Radial Shifts	I.3.7
3.3	STATISTICAL MODEL FOR CALCULATION OF ASSEMBLY POWER DISTRIBUTION UNCERTAINTIES	I.3.10
3.3.1	Definitions	I.3.10
3.3.2	The Sample Variance for the Difference Between Calculation and Measurement	I.3.12
3.3.2.1	$F_r$ Uncertainty: $S_{DFr}$	I.3.12
3.3.2.2	$F_q$ Uncertainty: $S_{DFq}$	I.3.12
3.3.2.3	$F_{xy}$ Uncertainty: $S_{DFxy}$	I.3.13
3.3.2.4	Summary	I.3.14
3.3.3	Procedure for Pooling Estimates	I.3.14
3.3.4	Procedure for Testing Poolability	I.3.16
3.3.5	Procedure for Computing One-sided Tolerance Limits	I.3.16
3.4	EVALUATION OF MEASUREMENT UNCERTAINTY	I.3.19
3.4.1	Random Component of Observed Differences Between Calculation and Measurement, $S_D$ , for the Various Reactors	I.3.19
3.4.1.1	Calvert Cliffs Unit 1	I.3.19
3.4.1.2	St. Lucie Unit 1	I.3.20
3.4.1.3	Millstone Unit 2	I.3.21
3.4.1.4	Calvert Cliffs Unit 2	I.3.21
3.4.1.5	Fort Calnoun Unit 1	I.3.22
3.4.2	Summary of Measurement Uncertainty	I.3.22
3.5	REFERENCES	I.3.26

TABLE OF CONTENTS (Continued)

PART II - SOFTWARE SYNTHESIS UNCERTAINTIES

<u>Section</u>	<u>Title</u>	<u>Page No.</u>
II.0	INTRODUCTION	II.0.1
II.1	INCA ANALYTICAL METHODS	II.1.1
1.0	GENERAL	II.1.1
1.1	DESCRIPTION OF CECOR METHODS	II.1.2
1.1.1	Definitions and System Description	II.1.2
1.1.2	Signal-to-Box Power Conversion	II.1.4
1.1.3	Planar Power Distributions	II.1.6
1.1.4	Axial Power Distribution	II.1.9
1.1.5	Total Power	II.1.11
1.1.6	Peak Pin Power Distributions	II.1.11
1.1.7	Detection of Azimuthal Flux Tilt	II.1.12
1.2	DESCRIPTION OF INCA/CECOR EDITS	II.1.15
1.3	REFERENCES	II.1.18
II.2	INCA LIBRARIES	II.2.1
2.0	INTRODUCTION	II.2.1
2.1	FORMALISM	II.2.2
2.1.1	Signal-to-Box Power Conversion Factors	II.2.2
2.1.2	Single Pin Power Peaking Factors	II.2.3
2.1.3	Coupling Coefficients	II.2.3
2.1.4	Azimuthal Tilt Functions	II.2.4
2.1.5	Axial Fitting Parameters	II.2.4
2.2	GENERATION AND QUALITY ASSURANCE OF INCA LIBRARIES	II.2.5
2.3	REFERENCES	II.2.6
II.3	SYNTHESIS UNCERTAINTIES	II.3.1
3.0	INTRODUCTION	II.3.1
3.0.1	Description of Methods	II.3.1
3.0.1.1	Box Power Uncertainty Analysis	II.3.1
3.0.1.2	Pin Peaking Uncertainty Analysis	II.3.2

TABLE OF CONTENTS (Continued)

PART II      inued)

<u>Section</u>	<u>Title</u>	<u>Page No.</u>
3.0.2	Summary of Results	II.3.4
3.1	BOX POWER SYNTHESIS UNCERTAINTIES	II.3.5
3.1.1	Description of Calculation Models	II.3.5
3.1.1.1	ROCS Reference Models	II.3.5
3.1.1.2	CECGR Synthesis Models	II.3.5
3.1.1.3	Summary of Calculation Models	II.3.6
3.1.2	Statistical Model for Calculation of Box Power Synthesis Uncertainties	II.3.7
3.1.2.1	Definitions	II.3.7
3.1.2.2	$F_r$ Uncertainty: $S_{SF_r}$	II.3.9
3.1.2.3	$F_q$ Uncertainty: $S_{SF_q}, \bar{D}_{SF_q}$	II.3.10
3.1.2.4	$F_{xy}$ Uncertainty: $S_{SF_{xy}}, \bar{D}_{SF_{xy}}$	II.3.11
3.1.2.5	Summary of Sample Variances and Biases	II.3.11
3.1.2.6	Procedure for Pooling Estimates for the Variance and Bias	II.3.12
3.1.2.7	Procedure for Computing One-Sided Tolerance Limits	II.3.14
3.1.3	Evaluation of Box Power Synthesis Uncertainties	II.3.17
3.1.3.1	Calvert Cliffs Unit 1 Cycle 1	II.3.17
3.1.3.2	Calvert Cliffs Unit 1 Cycle 2	II.3.18
3.1.3.3	Calvert Cliffs Unit 1 Cycle 3	II.3.19
3.1.3.4	Summary of Core Box Power Synthesis Errors	II.3.20
3.2	PIN PEAKING SYNTHESIS UNCERTAINTY	II.3.23
3.2.1	Description of Pin Peaking Models	II.3.23
3.2.2	Statistical Model for Calculation of Pin Peaking Synthesis Uncertainty	II.3.24
3.2.2.1	Definitions	II.3.24
3.2.2.2	$F_p$ Synthesis Uncertainty: $S_{SF_p}, \bar{D}_{SF_p}$	II.3.24

TABLE OF CONTENTS (Continued)

PART II (Continued)

<u>Section</u>	<u>Title</u>	<u>Page No.</u>
3.2.2.3	Procedure for Pooling Estimates for the Variance and Bias	II.3.25
3.2.2.4	Procedure for Computing One-Sided Tolerance Limit	II.3.25
3.2.3	Evaluation of Pin Peaking Synthesis Uncertainty	II.3.26
3.2.3.1	Calvert Cliffs Unit 2 Cycle 2	II.3.26
3.2.3.2	St. Lucie Unit 1 Cycle 2	II.3.26
3.2.3.3	Millstone Unit 2 Cycle 2	II.3.26
3.2.3.4	Calvert Cliffs Unit 1 Cycle 4	II.3.26
3.2.3.5	Summary of Pin Peaking Synthesis Errors	II.3.27
3.3	PIN PEAKING CALCULATIVE UNCERTAINTY	II.3.28
3.3.1	Description of Critical Experiments	II.3.28
3.3.1.1	Combustion Engineering Sponsored Critical Experiments (C-E Criticals)	II.3.28
3.3.1.2	KRITZ Experiments	II.3.31
3.3.1.3	BNWL Critical Experiments	II.3.36
3.3.2	Statistical Model for Calculation of $F_p$ Uncertainty	II.3.39
3.3.2.1	Definitions	II.3.39
3.3.2.2	The Sample Variance for the Difference Between Calculation and Measurement	II.3.41
3.3.2.3	The Measurement Uncertainty	II.3.43
3.3.2.4	An Estimate of $\sigma_{C_i}^2$	II.3.44
3.3.2.5	The Variance of $S_{C_i}^2$	II.3.45
3.3.2.6	The Number of Degrees of Freedom	II.3.46
3.3.2.7	Procedure for Pooling Estimates	II.3.46
3.3.3	Calculational Method	II.3.48
3.3.3.1	Design Method	II.3.48
3.3.3.2	Method of Incorporating Transport Results Into the Design Method	II.3.48

TABLE OF CONTENTS (Continued)

PART II (Continued)

<u>Section</u>	<u>Title</u>	<u>Page No.</u>
3.3.3.3	Pin/Box Factor and Pin Power Distribution Calculations for Comparison with Measurement	II.3.48
3.3.4	Statistical Error and Bias Evaluation	II.3.50
3.3.4.1	Geometry	II.3.50
3.3.4.2	The Bias, $\bar{D}$	II.3.51
3.3.4.3	The Random Component of Observed Differences Between Calculation and Measurement, $\sigma_D$	II.3.52
3.3.4.4	The Measurement Uncertainty, $\sigma_M$	II.3.55
3.3.4.5	The Calculational Uncertainty, $\sigma_C$	II.3.57
3.3.4.6	Summary	II.3.58
3.4	REFERENCES	II.3.60
APPENDIX 3.1	Transport Theory Adjustments in the Design PDQ Model	II.3.62

PART III - COMBINED UNCERTAINTIES

III.1	COMBINED MEASUREMENT AND SYNTHESIS UNCERTAINTIES	III.1.1
1.0	INTRODUCTION	III.1.1
1.1	STATISTICAL MODEL	III.1.1
1.1.1	Combination of the Pin/Box Synthesis and Calculative Uncertainties	III.1.2
1.1.2	Combination of Box Synthesis and Measurement Uncertainties	III.1.3
1.1.3	Combination of Box Peaking and Pin/Box Factor Uncertainties	III.1.4
1.1.4	Determination of a Tolerance Limit for Combined Uncertainty	III.1.6
1.2	NUMERICAL RESULTS FOR THE OVERALL INCA/CECOR MEASUREMENT UNCERTAINTY	III.1.8
1.3	REFERENCES	III.1.9



LIST OF TABLES

PART I

<u>TABLE</u>		<u>Page No.</u>
1. I	Properties of Self-Powered Detectors	I. 1. 4
2. I	Repeat Measurements of Reactor Calibration of Rhodium Detectors	I. 2. 7
2. II	Reproducibility Data for Rhodium Detectors	I. 2. 8
2. III	Depletion Properties of Rhodium-103 Detectors	I. 2. 9
3. I	Summary of Uncertainties for the Measurement of Peak Assembly Power	I. 3. 27
3. II	Calvert Cliffs Unit 1 Cycle 1 - Comparison Snapshot Operating Data	I. 3. 28
3. III	Calvert Cliffs Unit 1 Cycle 2 - Comparison Snapshot Operating Data	I. 3. 29
3. IV	Calvert Cliffs Unit 1 Cycle 3 - Comparison Snapshot Operating Data	I. 3. 30
3. V	St. Lucie Cycle 1 - Comparison Snapshot Operating Data	I. 3. 31
3. VI	St. Lucie Cycle 2 - Comparison Snapshot Operating Data	I. 3. 32
3. VII	Millstone II Cycle 1 - Comparison Snapshot Operating Data	I. 3. 33
3. VIII	Millstone II Cycle 2 - Comparison Snapshot Operating Data	I. 3. 34
3. IX	Clavert Cliffs Unit 2 Cycle 1 - Comparison Snapshot Operating Data	I. 3. 35
3. X	Calvert Cliffs Unit 2 Cycle 2 - Comparison Snapshot Operating Data	I. 3. 36
3. XI	Fort Calhoun Unit 1 Cycle 4 - Comparison Snapshot Operating Data	I. 3. 37
3. XII	Fort Calhoun Unit 1 Cycle 5 - Comparison Snapshot Operating Data	I. 3. 38
3. XIII	Calvert Cliffs Unit 1 Cycle 1 - ROCS Maneuver Structure	I. 3. 39
3. XIV	Calvert Cliffs Unit 1 Cycle 2 - ROCS Maneuver Structure	I. 3. 40

PART I (Continued)

<u>TABLES</u>		<u>PAGE NO.</u>
3.XV	Calvert Cliffs Unit 1 Cycle 3 - ROCS Maneuver Structure	I.3.41
3.XVI	St. Lucie Cycle 1 - ROCS Maneuver Structure	I.3.42
3.XVII	St. Lucie Cycle 2 - ROCS Maneuver Structure	I.3.43
3.XVIII	Millstone II Cycle 1 - ROCS Maneuver Structure	I.3.44
3.XIX	Millstone II Cycle 2 - ROCS Maneuver Structure	I.3.46
3.XX	Calvert Cliffs Unit 2 Cycle 1 - ROCS Maneuver Structure	I.3.47
3.XX1	Calvert Cliffs Unit 2 Cycle 2 - ROCS Maneuver Structure	I.3.49
3.XXII	Fort Calhoun Unit 1 Cycle 4 - ROCS Maneuver Structure	I.3.50
3.XXIII	Fort Calhoun Unit 1 Cycle 5 - ROCS Maneuver Structure	I.3.51
3.XXIVa	Calvert Cliffs Unit 1 Cycle 1 - Standard Deviation of Difference Between Calculation and Measurement and Results of Bartlett Tests for Data Pooling	I.3.52
3.XXIVb	Calvert Cliffs Unit 1 Cycle 1 - Results of Data Pooling and Bartlett Tests	I.3.53
3.XXVa	Calvert Cliffs Unit 1 Cycle 2 - Standard Deviation of Difference Between Calculation and Measurement and Results of Bartlett Tests for Data Pooling	I.3.54
3.XXVb	Calvert Cliffs Unit 1 Cycle 2 - Results of Data Pooling and Bartlett Tests	I.3.55
3.XXVIa	Calvert Cliffs Unit 1 Cycle 3 - Standard Deviation of Difference Between Calculation and Measurement and Results of Bartlett Tests for Data Pooling	I.3.56
3.XXVIb	Calvert Cliffs Unit 1 Cycle 3 - Results of Data Pooling and Bartlett Tests	I.3.57
3.XXVIIa	St. Lucie Unit 1 Cycle 1 - Standard Deviation of Difference Between Calculation and Measurement and Results of Bartlett Tests for Data Pooling	I.3.58
3.XXVIIb	St. Lucie Unit 1 Cycle 1 - Results of Data Pooling and Bartlett Tests	I.3.59
3.XXVIIIa	St. Lucie Unit 1 Cycle 2 - Standard Deviation of Difference Between Calculation and Measurement and Results of Bartlett Tests for Data Pooling	I.3.60
3.XXVIIIb	St. Lucie Unit 1 Cycle 2 - Results of Data Pooling and Bartlett Tests	I.3.61

## PART I (Continued)

<u>TABLE</u>		<u>PAGE NO.</u>
3.XXIXa	Millstone Unit 2 Cycle 1 - Standard Deviation of Difference Between Calculation and Measurement and Results of Bartlett Tests for Data Pooling	I.3.62
3.XXIXb	Millstone Unit 2 Cycle 1 - Results of Data Pooling and Bartlett Tests	I.3.63
3.XXXa	Millstone Unit 2 Cycle 2 - Standard Deviation of Difference Between Calculation and Measurement and Results of Bartlett Tests for Data Pooling	I.3.64
3.XXXb	Millstone Unit 2 Cycle 2 - Results of Data Pooling and Bartlett Tests	I.3.65
3.XXXIa	Calvert Cliffs Unit 2 Cycle 1 - Standard Deviation of Difference Between Calculation and Measurement and Results of Bartlett Tests for Data Pooling	I.3.66
3.XXXIb	Calvert Cliffs Unit 2 Cycle 1 - Results of Data Pooling and Bartlett Tests	I.3.67
3.XXXIIa	Calvert Cliffs Unit 2 Cycle 2 - Standard Deviation of Difference Between Calculation and Measurement and Results of Bartlett Tests for Data Pooling	I.3.68
3.XXXIIb	Calvert Cliffs Unit 2 Cycle 2 - Results of Data Pooling and Bartlett Tests	I.3.69
3.XXXIIIa	Fort Calhoun Unit 1 Cycle 4 - Standard Deviation of Difference Between Calculation and Measurement and Results of Bartlett Tests for Data Pooling	I.3.70
3.XXXIIIb	Fort Calhoun Unit 1 Cycle 4 - Results of Data Pooling and Bartlett Tests	I.3.71
3.XXXIVa	Fort Calhoun Unit 1 Cycle 5 - Standard Deviation of Difference Between Calculation and Measurement and Results of Bartlett Tests for Data Pooling	I.3.72
3.XXXIVb	Fort Calhoun Unit 1 Cycle 5 - Results of Data Pooling and Bartlett Tests	I.3.73
3.XXXV	Summary of Standard Deviations of Comparisons Between Calculations and Measurement	I.3.74
3.XXXVI	Results of Data Pooling and Bartlett Tests - All Cycles	I.3.75

PART I (Continued)

TABLE

PAGE NO.

3.XXXVII	Calvert Cliffs Unit 1 Cycle 3 - D' Normality Test on $F_q$	I.3.76
3.XXXVIII	Calvert Cliffs Unit 1 Cycle 3 - W Normality Test on $F_r$	I.3.77

PART II

<u>TABLE</u>		<u>PAGE NO.</u>
1. I	Error Analysis of the Axial Peak to Average Power Ratio for 1-D Axial Shapes	II.1.19
1. II	Error Analysis of the Axial Peak to Average Power Ratio for All Shapes	II.1.20
2. I	Summary of Computer Codes Used in Generation of INCA Libraries	II.2.7
3. I	Summary of Synthesis Uncertainties	II.3.64
3. II	Calvert Cliffs Unit 1 Cycle 1 - ROCS Maneuver Structure	II.3.65
3. III	Calvert Cliffs Unit 1 Cycle 2 - ROCS Maneuver Structure	II.3.66
3. IV	Calvert Cliffs Unit 1 Cycle 3 - ROCS Maneuver Structure	II.3.67
3. V	Calvert Cliffs Unit 1 Cycle 1 - CECOR Maneuver Structure and Failed Detectors	II.3.68
3. VI	Calvert Cliffs Unit 1 Cycle 3 - CECOR Maneuver Structure and Failed Detectors	II.3.69
3. VII	Calvert Cliffs Unit 1 Cycle 3 - CECOR Maneuver Structure and Failed Detectors	II.3.70
3. VIIIa	Calvert Cliffs Unit 1 Cycle 1 - Bias and Standard Deviation of Difference Between ROCS and CECOR Calculations	II.3.71
3. VIIIb	Calvert Cliffs Unit 1 Cycle 1 - Results of Box Power Data Pooling and Bartlett and Normal Deviate Tests	II.3.72
3. IXa	Calvert Cliffs Unit 1 Cycle 2 - Bias and Standard Deviation of Difference Between ROCS and CECOR Calculations	II.3.73
3. IXb	Calvert Cliffs Unit 1 Cycle 2 - Results of Box Power Data Pooling and Bartlett and Normal Deviate Tests	II.3.74
3. IXc	Calvert Cliffs Unit 1 Cycle 2 - Normality Test Results [ ]	II.3.75
3. IXd	Calvert Cliffs Unit 1 Cycle 2 - Normality Test Results [ ]	II.3.76
3. Xa	Calvert Cliffs Unit 1 Cycle 3 - Bias and Standard Deviation of Difference Between ROCS and CECOR Calculations	II.3.77
3. Xb	Calvert Cliffs Unit 1 Cycle 3 - Results of Box Power Data Pooling and Bartlett and Normal Deviate Tests	II.3.78

PART II (Continued)

<u>TABLE</u>		<u>PAGE NO.</u>
3.XI	Calvert Cliffs Unit 1 - Summary of Box Power Synthesis Error Bias and Standard Deviation Results for Cycles 1, 2, and 3	II.3.79
3.XII	Calvert Cliffs Unit 1 - Results of Pooling Synthesis Errors for Cycles 1, 2, 3	II.3.80
3.XIII	Bias and Standard Deviation of Difference for [ ] PDQ Calculations for Pin Peaking, and Results of Data Pooling	II.3.81
3.XIV	Normality Test Results for Pin-Peaking Synthesis Error Data	II.3.82
3.XV	C-E Criticals	II.3.31
3.XVI	Fuel Specification (KRITZ Experiments)	II.3.35
3.XVII	The Bias: Calculation - Measurement	II.3.51
3.XVIII	The Standard Deviation from Comparisons of Calculations and Measurement	II.3.53
3.XIX	$S_D^{HOT} / S_D^{COLD}$	II.3.55
3.XX	The Measurement Uncertainty in Critical Experiments	II.3.56

PART III

1.I	Summary of Measurement and Synthesis Uncertainty Components for INCA/CECOR Core Peaking Factors	III.1.10
-----	---	----------

LIST OF FIGURES

PART I

<u>FIGURE</u>		<u>PAGE NO.</u>
1-1	Typical Neutron Detector and Detector Assembly	I.1.5
1-2	Loading & Instrument Pattern - Standard 3410 First Cycle Core	I.1.6
1-3	Loading & Instrument Pattern - Standard System 80 First Cycle Core	I.1.7
1-4	Loading & Instrument Pattern - Arkansas Nuclear Unit 2 First Cycle Core	I.1.8
1-5	In-core Instrumentation Wiring Diagram	I.1.9
2-1	Relative Rhodium Total Sensitivity vs Integrated Detector Charge	I.2.10
3-1	Loading & Instrument Pattern - Calvert Cliffs Unit 1 Cycle 1	I.3.78
3-2	Loading & Instrument Pattern - Calvert Cliffs Unit 1 Cycle 2	I.3.79
3-3	Loading & Instrument Pattern - Calvert Cliffs Unit 1 Cycle 3	I.3.80
3-4	Loading & Instrument Pattern - St. Lucie Cycle 1	I.3.81
3-5	Loading & Instrument Pattern - St. Lucie Cycle 2	I.3.82
3-6	Loading & Instrument Pattern - Millstone II Cycle 1	I.3.83
3-7	Loading & Instrument Pattern - Millstone II Cycle 2	I.3.84
3-8	Loading & Instrument Pattern - Calvert Cliffs Unit 2 Cycle 1	I.3.85
3-9	Loading & Instrument Pattern - Calvert Cliffs Unit 2 Cycle 2	I.3.86
3-10	Loading & Instrument Pattern - Fort Calhoun Unit 1 Cycle 4	I.3.87
3-11	Loading & Instrument Pattern - Fort Calhoun Unit 1 Cycle 5	I.3.88
3-12	ROCS Axial Mesh Structure	I.3.89

PART I (Continued)

<u>FIGURE</u>		<u>PAGE NO.</u>
3-13 (a-e)	Comparisons of Measured and Calculated Powers - Calvert Cliffs Unit 1 Cycle 1 at 850 MWD/T	I.3.90
3-14 (a-e)	Comparison of Measured and Calculated Powers - Calvert Cliffs Unit 1 Cycle 2 at 989 MWD/T	I.3.95
3-15 (a-e)	Comparison of Measured and Calculated Powers - Calvert Cliffs Unit 1 Cycle 3 at 1202 MWD/T	I.3.100
3-16 (a-e)	Comparison of Measured and Calculated Powers - St. Lucie Cycle 1 at 888 MWD/T	I.3.105
3-17 (a-e)	Comparison of Measured and Calculated Powers - St. Lucie Cycle 2 at 1361 MWD/T	I.3.110
3-18 (a-e)	Comparison of Measured and Calculated Powers - Millstone II Cycle 1 at 1350 MWD/T	I.3.115
3-19 (a-e)	Comparison of Measured and Calculated Powers - Millstone II Cycle 2 at 500 MWD/T	I.3.120
3-20 (a-e)	Comparison of Measured and Calculated Powers - Calvert Cliffs Unit 2 Cycle 1 at 1440 MWD/T	I.3.125
3-21 (a-e)	Comparison of Measured and Calculated Powers - Calvert Cliffs Unit 2 Cycle 2 at 809 MWD/T	I.3.130
3-22 (a-e)	Comparison of Measured and Calculated Powers - Fort Calhoun Unit 1 Cycle 4 at 1000 MWD/T	I.3.135
3-23 (a-e)	Comparison of Measured and Calculated Powers - Fort Calhoun Unit 1 Cycle 5 at 300 MWD/T	I.3.140
3-24	Distribution of Deviations in $F_q$ Calvert Cliffs Unit 1 Cycle 3	I.3.145
3-25	Distribution of Deviations in $F_q$ St. Lucie Cycle 2	I.3.146
3-26	Distribution of Deviations in $F_r$ Calvert Cliffs Unit 1 Cycle 3	I.3.147

PART II

1-1	Axial Control Rod and Detector Arrangement for Four Detector System	II.1.21
1-2	Representative Axial Shapes from One-Dimensional Analyses	II.1.22



PART II (Continued)

<u>FIGURE</u>		<u>PAGE NO.</u>
1-3	Typical Axial Shapes - One- and Three-Dimensional Analyses	II.1.23
1-4	Typical Cycle 2 CECOR Axial Boundary Conditions	II.1.24
2-1	Power to Rhodium Signal Conversion Factors vs Assembly Average Burnup	II.2.8
2-2	Single Pin Peaking Factor Variation with Burnup	II.2.9
2-3	Typical Average Coupling Coefficient Behavior	II.2.10
2-4	Radial Tilt Function $g(r)$	II.2.11
2-5	Generation and Quality Assurance of INCA Libraries	II.2.12
3-1	Loading and Instrument Pattern - Calvert Cliffs Unit 1 Cycle 1	II.3.83
3-2	Loading and Instrument Pattern - Calvert Cliffs Unit 1 Cycle 2	II.3.84
3-3	Loading and Instrument Pattern - Calvert Cliffs Unit 1 Cycle 3	II.3.85
3-4	Calvert Cliffs Unit 1 - Axial Geometries for ROCS and CECOR Models	II.3.86
3-5a	Calvert Cliffs Unit 1 Cycle 1 - Comparison of ROCS (R) and CECOR (C) Box Power Fractions - 500 MWD/T	II.3.87
3-5b	Calvert Cliffs Unit 1 Cycle 1 - Comparison of ROCS (R) and CECOR (C) Box Peak to Core Average Power - 500 MWD/T	II.3.88
3-5c	Calvert Cliffs Unit 1 Cycle 1 - Comparison of ROCS (R) and CECOR (C) Box Power Fractions - 10,000 MWD/T	II.3.89
3-5d	Calvert Cliffs Unit 1 Cycle 1 - Comparison of ROCS (R) and CECOR (C) Box Peak to Core Average Power - 10,000 MWD/T	II.3.90
3-5e	Calvert Cliffs Unit 1 Cycle 1 - Comparison of ROCS (R) and CECOR (C) Box Power Fractions - 16,000 MWD/T (18% Rod Bank 5 Insertion)	II.3.91
3-5f	Calvert Cliffs Unit 1 Cycle 1 - Comparison of ROCS (R) and CECOR (C) Box Peak to Core Average Power - 16,000 MWD/T (18% Rod Bank 5 Insertion)	II.3.92
3-5 (g-i)	Calvert Cliffs Unit 1 Cycle 1 - Comparison of ROCS and CECOR Planar Peak to Plane Average Box Powers	II.3.93

PART II (Continued)

<u>FIGURE</u>		<u>PAGE NO.</u>
3-5 (j-1)	Calvert Cliffs Unit 1 Cycle 1 - Comparison of ROCS and CECOR Core Average Axial Shapes	II. 3.96
3-5m	Calvert Cliffs Unit 1 Cycle 1 - Comparison of ROCS (R) and CECOR (C) Assembly Burnup - 16,000 MWD/T	II. 3.99
3-6a	Calvert Cliffs Unit 1 Cycle 2 - Comparison of ROCS (R) and CECOR (C) Box Power Fractions - 325 MWD/T	II. 3.100
3-6b	Calvert Cliffs Unit 1 Cycle 2 - Comparison of ROCS (R) and CECOR (C) Box Peak to Core Average Power - 325 MWD/T	II. 3.101
3-6c	Calvert Cliffs Unit 1 Cycle 2 - Comparison of ROCS (R) and CECOR (C) Box Power Fractions - 4192 MWD/T	II. 3.102
3-6d	Calvert Cliffs Unit 1 Cycle 2 - Comparison of ROCS (R) and CECOR (C) Box Peak to Core Average Power - 4192 MWD/T	II. 3.103
3-6e	Calvert Cliffs Unit 1 Cycle 2 - Comparison of ROCS (R) and CECOR (C) Box Power Fractions - 1330 MWD/T	II. 3.104
3-6f	Calvert Cliffs Unit 1 Cycle 2 - Comparison of ROCS (R) and CECOR (C) Box Peak to Core Average Power - 8330 MWD/T	II. 3.105
3-6 (g-i)	Calvert Cliffs Unit 1 Cycle 2 - Comparison of ROCS and CECOR Planar Peak to Plane Average Box Powers	II. 3.106
3-6 (j-1)	Calvert Cliffs Unit 1 Cycle 2 - Comparison of ROCS and CECOR Core Average Axial Shapes	II. 3.109
3-6m	Calvert Cliffs Unit 1 Cycle 2 - Comparison of ROCS (R) and CECOR (C) Assembly Burnup - 8330 MWD/T	II. 3.112
3-7a	Calvert Cliffs Unit 1 Cycle 3 - Comparison of ROCS (R) and CECOR (C) Box Power Fractions - 495 MWD/T	II. 3.113
3-7b	Calvert Cliffs Unit 1 Cycle 3 - Comparison of ROCS (R) and CECOR (C) Box Peak to Core Average Power - 495 MWD/T	II. 3.114
3-7c	Calvert Cliffs Unit 1 Cycle 3 - Comparison of ROCS (R) and CECOR (C) Box Power Fractions - 801 MWD/T (50% ROD BANK 5 INSERTION)	II. 3.115
3-7d	Calvert Cliffs Unit 1 Cycle 3 - Comparison of ROCS (R) and CECOR (C) Box Peak to Core Average Power - 801 MWD/T (50% ROD BANK 5 INSERTION)	II. 3.116
3-7e	Calvert Cliffs Unit 1 Cycle 3 - Comparison of ROCS (R) and CECOR (C) Box Power Fractions - 5994 MWD/T	II. 3.117

PART II (Continued)

<u>FIGURE</u>		<u>PAGE NO.</u>
3-7f	Calvert Cliffs Unit 1 Cycle 3 - Comparison of ROCS (R) and CECOR (C) Box Peak to Core Average Power - 5994 MWD/T	II. 3. 118
3-7g	Calvert Cliffs Unit 1 Cycle 3 - Comparison of ROCS (R) and CECOR (C) Box Power Fractions - 8578 MWD/T	II. 3. 119
3-7h	Calvert Cliffs Unit 1 Cycle 3 - Comparison of ROCS (R) and CECOR (C) Box Peak to Core Average Power - 8578 MWD/T	II. 3. 120
3-7 (i-1)	Calvert Cliffs Unit 1 Cycle 3 - Comparison of ROCS and CECOR Planar Peak to Plane Average Box Powers	II. 3. 121
3-7 (m-p)	Calvert Cliffs Unit 1 Cycle 3 - Comparison of ROCS and CECOR Core Average Axial Shapes	II. 3. 125
3-7q	Calvert Cliffs Unit 1 Cycle 3 - Comparison of ROCS (R) and CECOR (C) Assembly Burnup - 8578 MWD/T	II. 3. 129
3-8	Distribution of Deviations in $F_q$ Box Synthesis - Calvert Cliffs Unit 1 Cycle 2	II. 3. 130
3-9	Distribution of Deviations in $F_r$ Box Synthesis - Calvert Cliffs Unit 1 Cycle 2	II. 3. 131
3-10	Distribution of Deviations in $F_{xy}$ Box Synthesis - Calvert Cliffs Unit 1 Cycle 2	II. 3. 132
3-11	Loading and Instrument Pattern - Calvert Cliffs Unit 2 Cycle 2	II. 3. 133
3-12	Loading and Instrument Pattern - St. Lucie Cycle 2	II. 3. 134
3-13	Loading and Instrument Pattern - Millstone II Cycle 2	II. 3. 135
3-14	Loading and Instrument Pattern - Calvert Cliffs Unit 1 Cycle 4	II. 3. 136
3-15	Calvert Cliffs Unit 2 Cycle 3 - Comparison of [ ] PDQ Peak Pin to Box Average Pin Power	II. 3. 137
3-16	St. Lucie Unit 1 Cycle 2 - Comparison of [ ] PDQ Peak Pin to Box Average Pin Power	II. 3. 138
3-17	Millstone Unit 2 Cycle 2 - Comparison of [ ] PDQ Peak Pin to Box Average Pin Power	II. 3. 139
3-18	Calvert Cliffs Unit 1 Cycle 4 - Comparison of [ ] PDQ Peak Pin to Box Average Pin Power	II. 3. 140
3-19	Distribution of Deviations in $F_p$ Synthesis	II. 3. 141

PART II (Continued)

<u>FIGURE</u>		<u>PAGE NO.</u>
3-20	Block Diagram of Semi-automatic Fuel Rod Scanner for C-E Criticals	II.3.142
3-21	Numbering System for Power Scan and Buckling Measurements - C-E No. 12	II.3.143
3-22	Numbering System for Power Scan and Buckling Measurements - C-E No. 43	II.3.144
3-23	Numbering System for Power Scan and Buckling Measurements - C-E No. 32, 53, 56	II.3.145
3-24	Arrangement for the Gamma Scanning KRITZ Experiments	II.3.146
3-25	KRITZ U-WH2 Core Layout	II.3.147
3-26	KRITZ Lattice Pu-WH2	II.3.148
3-27	BNWL Fuel Description	II.3.149
3-28	Dual Channel Gamma Scanning System - BNWL Experiments	II.3.150
3-29	UO <sub>2</sub> - 2.35% <sup>235</sup> U Core w/water Holes - BNWL GPL-88	II.3.151
3-30	UO <sub>2</sub> - 2.34% <sup>235</sup> U Core w/water Holes and KG-33 Glass Shims - BNWL GPL-92	II.3.152
3-31	DIT (K=1) vs Measured Pin Powers - C-E No. 12	II.3.153
3-32	DIT (K=1) vs Measured Pin Powers - C-E No. 32	II.3.154
3-33	DIT (K=1) vs Measured Pin Powers - C-E No. 43	II.3.155
3-34	DIT (K=1) vs Measured Pin Powers - C-E No. 53 Core	II.3.156
3-35	DIT (K=1) vs Measured Pin Powers - C-E No. 56 Core	II.3.157
3-36	DIT (K=1) vs Measured Pin Powers - KRITZ U-WH2 Core	II.3.158
3-37	DIT (K=1) vs Measured Pin Powers - KRITZ Pu-WH2 Core (Cold)	II.3.159
3-38	DIT (K=1) vs Measured Pin Powers - KRITZ Pu-WH2 (Hot)	II.3.160
3-39	Comparison of Measured/DIT Bias as a Function of Hydrogen/ Uranium Atom Ratio	II.3.161
3-40	Summary of Runs 12, 32, 43, 53, 56 - Distribution of $\epsilon_{ij}$	II.3.162

EVALUATION OF UNCERTAINTY  
IN THE NUCLEAR POWER PEAKING  
MEASURED BY THE SELF-POWERED, FIXED IN-CORE  
DETECTOR SYSTEM

PART I

THE BASIC MEASUREMENT UNCERTAINTY

Applicability, Purpose and Organization of the Report

The principal in-core instrumentation in Mark V fuel assembly reactors is provided by strings of four or five short rhodium, self-powered detectors arranged axially in the central water holes of about 20% of all fuel assemblies. Moveable detectors have been installed in some plants but have not been used in power distribution monitoring. This report is applicable to fixed rhodium detector systems when the signals are processed through the INCA/CECOR system of codes.

The purpose of the report is to quantify the numerical uncertainties associated with the use of the fixed in-core detector system in inferring the core power peaking factors:

- $F_q$ , the local peak pin power to core average power ratio.
- $F_{xy}$ , the planar peak pin power to planar average power ratio.
- $F_r$ , the axially integrated peak pin power to core average power ratio.

The measurement uncertainties determined for these peaking factors are in the form of 95%/95% probability/confidence one-sided tolerance limits and will be used in conjunction with Technical Specification limits on these quantities to establish appropriate LCO (Limiting Conditions of Operation) and LSSS (Limiting Safety System Settings) limits for plant operation and safety analysis.

This report is in three parts. Part I contains the determination of the uncertainty associated with the measurement of assembly average power in instrumented locations: the Basic Measurement Uncertainty. It includes uncertainties in all components of the assembly power, viz., in the raw signal, in the background correction factors, in the initial calibrated sensitivity, in the sensitivity depletion, and in the signal-to-power

conversion. The basic measurement uncertainty in assembly power is determined directly, without determining the uncertainty of the individual components, by comparing measured and calculated values as described in I.3.

Part II determines the software dependent uncertainty, called the synthesis uncertainty. This includes components due to the radial coupling from instrumented to uninstrumented assemblies, due to the axial expansion of the power profile and due to the translation of assembly power to pin power via the pin-to-box factors.

Part III contains the statistical model for the combination of the basic measurement uncertainty with the synthesis uncertainty and the final numerical results.

#### Continued Applicability

The analysis of this report is based on operational data from a limited but large sample of fuel cycles and reactors using 14x14 fuel and 4-detector arrangements for determination of the basic measurement uncertainty. Since this component is determined mainly by the hardware properties of the instrumentation (calibration and sensitivity depletion), it is expected to be insensitive to differences (size, fuel assembly geometry) in core design and detector arrangement. The numerical results of Chapter I.3 show that the variations observed between reactors and cycles, although statistically significant because of the large data base, are in fact small compared to the overall uncertainties. The synthesis uncertainty is principally dependent upon the number of axial detectors per string. As shown in Part II, 5-detector arrangements are expected to be conservatively bounded by the analysis made for 4-detector strings. Throughout this analysis, for both the basic measurement uncertainty and for the synthesis uncertainty, whenever statistical tests show that pooling of data from all reactors, all cycles or all time-points, etc., is not justified, the most unfavorable data have consistently been chosen as representative of the data base. For reload cycles analyzed subsequent to the completion of the analyses included in

the data base of this report, no departures of the uncertainties from that data base have been observed. For all of the above reasons it is therefore concluded that the data base for the uncertainties will remain applicable to all future reactors and cycles employing rhodium, self-powered, fixed in-core detectors in Mark V fuel.

### Summary

The results of the analyses show that:

- $F_q$  can be measured with an accuracy of 6.2%.
- $F_{xy}$  can be measured with an accuracy of 5.3%.
- $F_r$  can be measured with an accuracy of 6.0%.

Thus the overall measurement uncertainty is such that there is a 95 percent probability that at least 95 percent of the true  $F_q$ ,  $F_{xy}$ , and  $F_r$  values will be less than the value inferred from the INCA/CECOR measurement plus 6.2, 5.3 and 6.0%, respectively.



## I.1 IN-CORE INSTRUMENT SYSTEM DESCRIPTION

### 1.0 INTRODUCTION

The in-core instrumentation supplied in C-E reactor plants is primarily based on self-powered rhodium detectors. In reactors using the Mark V fuel assembly, the instruments are placed in the center water hole of selected assemblies. In addition to these fixed detectors, the 3410 MWth and System 80 reactors are equipped with movable self-powered rhodium detectors which can provide a continuous record of the axial flux distribution in each instrumented assembly. In a few of the early plants (Maine Yankee and St. Lucie) selected locations can be accessed by movable miniature fission chambers. In addition, background cables have been provided in a number of locations in all reactor cores. This topical report addresses the measurement accuracy of fixed in-core rhodium detectors.

### 1.1 DESCRIPTION OF FIXED DETECTORS

#### 1.1.1 Rhodium Detectors

The primary mechanism by which the neutron radiation incident on the rhodium detector is converted to a signal is through neutron capture in the emitter producing a capture product which decays through beta emission. Some of the beta particles are energetic enough to escape from the emitter, resulting in a positive charge on the emitter. Rhodium-103 has a 150-barn 2200 m/sec capture cross section and its capture product (Rhodium-104) emits beta particles possessing an end-point energy of 2.4 Mev with a 42-second half-life.<sup>†</sup> The rhodium detectors are 40 cm long, and four or five of these segments are located at selected axial positions in each string. See Figure 1-1. Table 1.1 lists properties of the rhodium detectors for the neutron spectrum in the Pool Test Reactor at Chalk River. The rhodium detectors are 40 cm long with a diameter of approximately 18 mils and an initial sensitivity, as determined by calibration in the Pool Test Reactor at Chalk River, of typically  $3.5 \times 10^{-20}$  amp/nv.

<sup>†</sup> An isomeric state,  $\text{Rh}^{104m}$ , is also produced approximately 7.3% of the time with a 4.41-min. half-life.

### 1.1.2 Background Detectors

The background detectors measure the signal generated in the detector signal cable due to, for example, Compton and photoelectrons as a result of gamma interaction with the cable materials as well as neutron activation of the cable insulator. The electrons which could cause current flow in addition to that of the emitter material are the results of the imbalance between those leaving the center wire and those absorbed by the center wire. In order to be representative of the background signal experienced by the rhodium detectors, the background detector is manufactured identical to the lead wire on the rhodium detector. It consists of an Inconel 600 lead wire and outer sheath with  $Al_2O_3$  insulator. The physical dimensions are identical to the detector lead wire, i.e., 0.040 inches O.D. with 0.006 inch diameter center lead. The background detector is full core length, thus representing the worst case signal contribution to the axially spaced rhodium detectors.

The background detector is read across a dropping resistor as are the rhodium signals. The measured values are utilized to verify that the required background correction is small.

### 1.2 DESCRIPTION OF IN-CORE INSTRUMENT ASSEMBLIES

The fixed instrument assemblies for the Palisades, Maine Yankee, Fort Calhoun, Millstone, Calvert Cliffs and St. Lucie plants consist of chromel-alumel thermocouples, four rhodium self-powered neutron detectors, and a background cable in selected locations terminated at either the top or bottom of the detector assembly. The four detectors are axially centered at 20, 40, 60 and 80% of the core height. The newer C-E designs, including Arkansas Nuclear One Unit 2, System 80 and the 3410 MWth plants, have five rhodium self-powered detectors in a string, axially centered at 10, 30, 50, 70 and 90% of the core height.

### 1.3 DETECTOR LAYOUT

Detailed detector location maps for the operating, 14x14 fuel, plants are included in Chapter I.3 (see Figures 3-1 to 3-11). For the 3410-class, System 80 and Arkansas plants, standard layouts are shown in Figures 1-2 through 1-4, respectively.

### 1.4 INSTRUMENTATION AND READOUT

The instrumentation associated with the fixed in-core detectors is relatively simple, as shown in Figure 1-5. In essence, it consists of a load resistor for each detector, multiplexing system, amplifier, and A-D converter to digitize the signals. The output of the self-powered detectors is a low level current, which on flowing through a load resistor produces a measurable voltage. This voltage is amplified and then digitized by the A-D converter. The resulting digitized signal is fed to either a data-logger or to the plant computer. A complete scan of the in-core detectors can be accomplished in about 20 seconds.

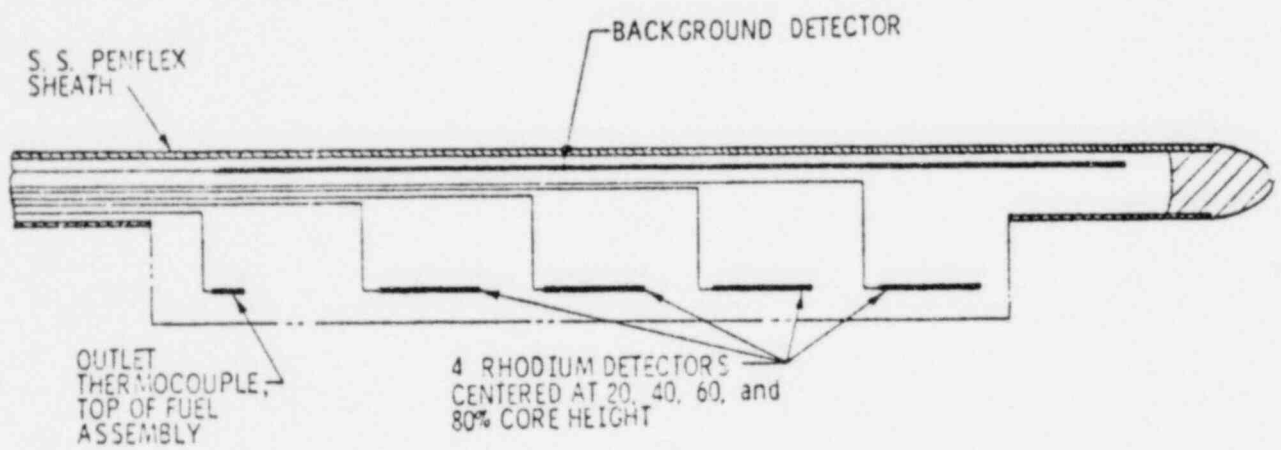
To ensure that essentially all of the detector current flows through the  $10^5$  ohm load resistor, the leakage resistance of the cable (effectively in parallel with the load resistor) is maintained at a value greater than  $10^8$  ohms. This is checked periodically by placing an additional  $10^5$  ohm resistor in parallel and calculating the leakage resistance. This ensures that no more than 0.1% of the current flows through the leakage resistance.

TABLE 1.I

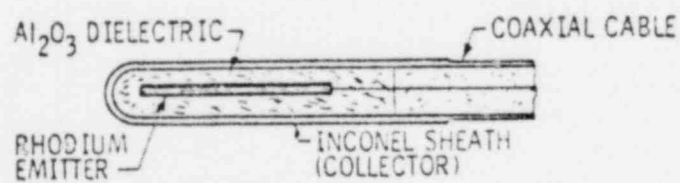
Properties of Self-Powered Detectors

<u>Property</u>	<u>Rhodium Detector</u>
Length	40 cm
Diameter	18 mils
Sensitivity in the PTR Spectrum	$3.5 \times 10^{-20}$ amp/nv

Figure 1-1  
 TYPICAL NEUTRON DETECTOR AND DETECTOR ASSEMBLY



TYPICAL INSTRUMENT ASSEMBLY



TYPICAL RHODIUM DETECTOR

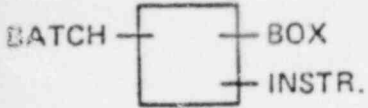
Figure 1-2  
LOADING & INSTRUMENT PATTERN  
STANDARD 410 FIRST CYCLE CORE

BATCH ——— BOX  
          ———— INSTR.

		C 1		C 2		C 3		C 4								
		C 5	C 6	C+ 7	C+ 8	B 9	C+ 10	C+ 11	C 12	C 13						
		1		2		3		4		5						
		C 14	C 15	B 16	A 17	B 18	A 19	B 20	A 21	B 22	C 23	C 24				
		C 25	C 26	B 27	A 28	B 29	A 30	B 31	A 32	B 33	A 34	B 35	C 36	C 37		
		6		7		8		9		10		11		12		
C 38	C 39	B 40	A 41	B 42	A 43	B 44	A 45	B 46	A 47	B 48	A 49	B 50	C 51	C 52		
C 53	B 54	A 55	B 56	A 57	B 58	A 59	B 60	A 61	B 62	A 63	B 64	A 65	B 66	C 67		
		13		14		15		16		17		18		19		
C+ 68	A 69	B 70	A 71	B 72	A 73	B 74	A 75	B 76	A 77	B 78	A 79	B 80	A 81	C+ 82		
C 83														C 84		
20	C+ 85	B 86	A 87	B 88	A 89	B 90	A 91	B 92	A 93	B 94	A 95	B 96	A 97	B 98	C+ 99	21
C 100														C 101		
	22		23		24		25		26		27		28			C 102
C 103	B 102	A 103	B 104	A 105	B 106	A 107	B 108	A 109	B 110	A 111	B 112	A 113	B 114	A 115	B 116	
C 117														C 118		
C+ 119	B 120	A 121	B 122	A 123	B 124	A 125	B 126	A 127	B 128	A 129	B 130	A 131	B 132	C+ 133		C 134
36	29		30		31		32		33		34		35			37
C+ 136	A 137	B 138	A 139	B 140	A 141	B 142	A 143	B 144	A 145	B 146	A 147	B 148	A 149	C+ 150		C 135
C 151	B 152	A 153	B 154	A 155	B 156	A 157	B 158	A 159	B 160	A 161	B 162	A 163	B 164	C 165		
38		39		40		41		42		43		44				
C 166	C 167	B 168	A 169	B 170	A 171	B 172	A 173	B 174	A 175	B 176	A 177	B 178	C 179	C 180		
C 181	C 182	B 183	A 184	B 185	A 186	B 187	A 188	B 189	A 190	B 191	C 192	C 193				
45		46		47		48		49		50		51				
C 194	C 195	B 196	A 197	B 198	A 199	B 200	A 201	B 202	C 203	C 204						
C 205	C 206	C+ 207	C+ 208	B 209	C+ 210	C+ 211	C 212	C 213								
52		53		54		55		56								
		C 214	C 215	C 216	C 217											



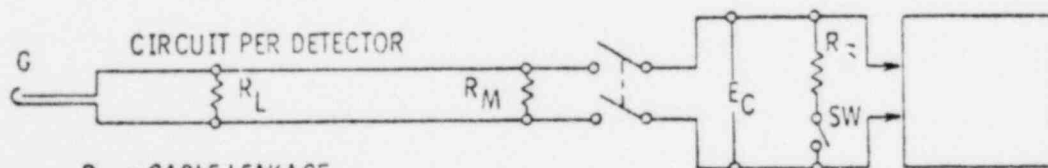
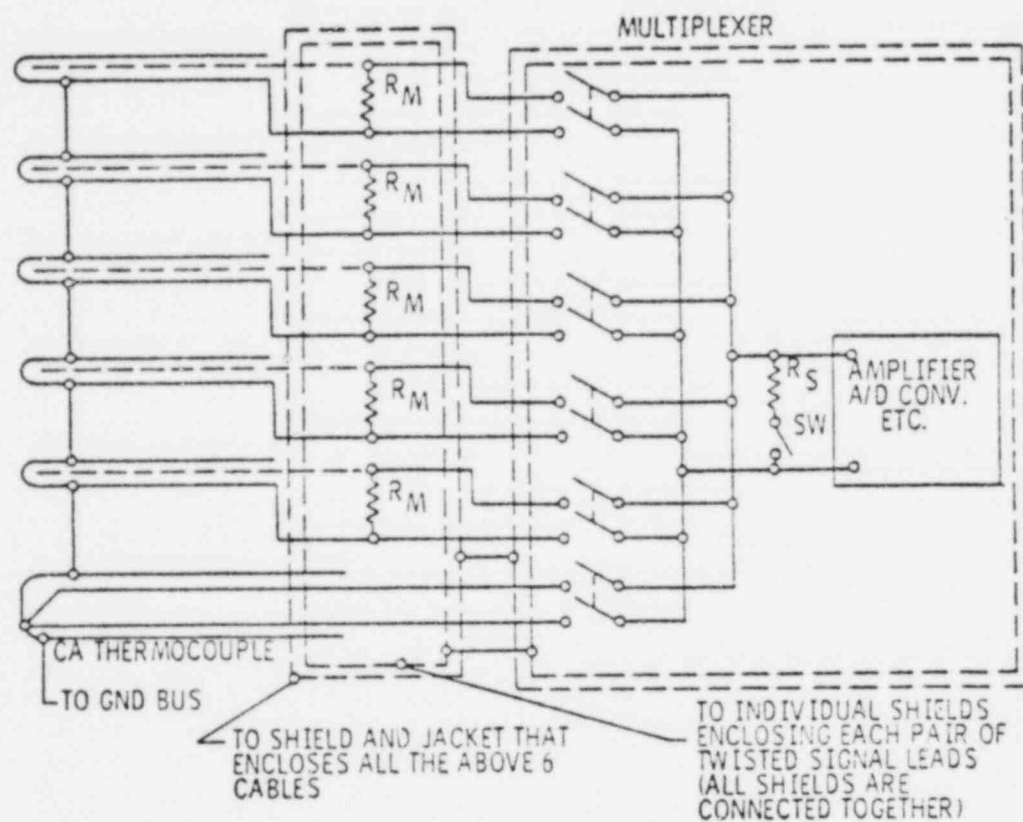
Figure 1-4  
LOADING & INSTRUMENT PATTERN  
ARKANSAS NUCLEAR UNIT 2 FIRST CYCLE CORE



		C4 1		C3 2		C3 3		C3 4		C4 5																					
		C4 6		C2 7		C1 8		B+ 9		A 10		B+ 11		C1 12		C2 13		C4 14													
		1		2		3		4																							
		C5 15		C2 16		A 17		B+ 18		A 19		B+ 20		A 21		B+ 22		A 23		C2 24		C5 25									
		C4 26		C2 27		A 28		B+ 29		A 30		B+ 31		A 32		B+ 33		A 34		B+ 35		A 36		C2 37		C4 38					
		5		6		7		8		9		10																			
		C2 39		A 40		B+ 41		A 42		B+ 43		A 44		B+ 45		A 46		B+ 47		A 48		B+ 49		A 50		C2 51					
		C4 52		C1 53		B+ 54		A 55		B+ 56		A 57		B+ 58		A 59		B+ 60		A 61		B+ 62		A 63		B+ 64		C1 65		C4 66	
		11		12		13		14		15		16		17																	
		C3 67		B+ 68		A 69		B+ 70		A 71		B+ 72		A 73		B+ 74		A 75		B+ 76		A 77		B+ 78		A 79		B+ 80		C3 81	
		18		19																											
		C3 82		A 83		B+ 84		A 85		B+ 86		A 87		B+ 88		A 89		B+ 90		A 91		B+ 92		A 93		B+ 94		A 95		C3 96	
		20		21		22		23		24		25																			
		C3 97		B+ 98		A 99		B+ 100		A 101		B+ 102		A 103		B+ 104		A 105		B+ 106		A 107		B+ 108		A 109		B+ 110		C3 111	
		26		27																											
		C4 112		C1 113		B+ 114		A 115		B+ 116		A 117		B+ 118		A 119		B+ 120		A 121		B+ 122		A 123		B+ 124		C1 125		C4 126	
		28		29		30		31		32		33		34																	
		C2 127		A 128		B+ 129		A 130		B+ 131		A 132		B+ 133		A 134		B+ 135		A 136		B+ 137		A 138		C2 139					
		C4 140		C2 141		A 142		B+ 143		A 144		B+ 145		A 146		B+ 147		A 148		B+ 149		A 150		C2 151		C4 152					
		35		36		37		38		39		40																			
		C5 153		C2 154		A 155		B+ 156		A 157		B+ 158		A 159		B+ 160		A 161		C2 162		C5 163									
		C4 164		C2 165		C1 166		B+ 167		A 168		B+ 169		C1 170		C2 171		C4 172													
		41		42		43		44																							
		C4 173		C3 174		C3 175		C3 176		C4 177																					



Figure 1-5  
IN-CORE INSTRUMENTATION WIRING DIAGRAM



- $R_L$  • CABLE LEAKAGE
- $R_M$  • DETECTOR MEASURING RESISTANCE (e.g.  $50 \times 10^3 \Omega$ )
- $R_S$  • SPECIAL RESISTOR (e.g.  $20 \times 10^3 \Omega$ )

## I.2 MEASUREMENT TECHNIQUES, CALIBRATION, REPRODUCIBILITY

### 2.0 GENERAL

During normal operating conditions, signals proportional to the rhodium activation rates are obtained from the various detectors. These signals are related to local power by use of calculated signal-to-power conversion factors for the appropriate core conditions (see Chapter II.1). The measured signals are corrected for background, calibration, and depletion.

These effects (background, calibration, and depletion) individually contribute to the overall uncertainty associated with use of the in-core instruments for measurement of power peaking. The approach employed for determination of this uncertainty does not provide for a separate determination of these components. Instead, a comparison of measured and predicted powers (Chapter I.3) gives the combined uncertainty due to background, calibration, depletion and signal-to-power conversion. The purpose of the following discussion is, therefore, only to show that the individual effects are sufficiently well understood, and that the uncertainty component due to calibration as determined in separate measurements is small and consistent with the overall result determined from the power reactor comparisons.

### 2.1 FIXED IN-CORE DETECTORS

#### 2.1.1 System Performance

The fixed in-core detector systems in C-E operating reactors have been found, over the past several years, to operate effectively and dependably with 100% availability. There have been brief periods of time during which they could not be automatically scanned due to unavailability of the plant computer. However, it was still possible to read the detector signals during these periods manually.

In all reactors, there have been some detectors which were damaged during installation and others which failed during operation. Early failures at Palisades, where the highest detector signal loss occurred, were attributed to fracture of the detector cable adjacent to the braze at the detector. Modification of the design for later application has substantially improved operational reliability.

The impact of failed detectors on the determination of core power distributions has not been a serious problem because of the ample initial supply of detector channels.

### 2.1.2 Detector Calibration and Reproducibility

Detector calibration is carried out by the vendor, Reuter-Stokes Canada, Ltd., using the Pool Test Reactor (PTR) and the ZED-2 reactor at Chalk River Nuclear Laboratories. All detectors are calibrated relative to standard detectors. This relative calibration is performed in the PTR where the detectors are loaded into a calibration fixture. The fixture is a lucite rod about 3 cm in diameter with ten locations, one of which is reserved for the standard detector.

The major uncertainty in the relative calibration is due to the slightly different flux levels in the calibration locations. They are measured at approximately yearly intervals. The calibration uncertainty has been determined by repeating the calibration letting the detector occupy different positions in the calibration fixtures. Deviations between pairs of such measurements indicate the accuracy. Table 2.I shows results from a set of such reproducibility experiments. Analysis of the data in the table yields a sample standard deviation for the difference between two measurements of 0.43% for a sample size of  $n=18$  (the standards remain in the same location). The sample standard deviation associated with an individual measurement is therefore  $0.43/\sqrt{2} = 0.31\%$ . This estimate of the relative calibration uncertainty may be compared with the overall, basic measurement uncertainty as determined in Chapter I.3 (see Table 3.I) which is in the range of 1.66-1.93%

for the standard deviation. Thus, the calibration uncertainty represents only a fraction of the total uncertainty.

All rhodium detectors are calibrated using this method. While the calibration environment in the PTR is different than in an operating PWR (PTR is a pool reactor with a highly thermalized neutron spectrum, different gamma spectra and lower water temperature), the procedure is adequate because a relative, not absolute, calibration is needed. Any changes resulting from the PWR environment are reflected directly in the uncertainty component evaluated in Chapter I.3.

Absolute calibration of the detectors is carried out using cobalt wires attached to the outside of selected detectors for exposure in standard conditions. The wires are absolutely counted and their activations interpreted to give the absolute flux at the detector location. The uncertainty in the measured absolute flux is  $\pm 4-6\%$  which, in turn, is reflected as a similar uncertainty in the absolute sensitivity of the detectors. Absolute calibration of the detectors, although useful, is by no means as important as their relative inter-calibration since the reactor power level is determined by calorimetric measurements and calculations.

An additional measure of the reproducibility of the detector signals under operating conditions has been obtained by accumulating a large number of readings during power operation at Palisades. During several periods of steady state operation, repeated measurements were obtained from all 180 rhodium in-core detectors. After known bad detectors and those affected by slight control rod movements had been eliminated, about 4800 duplicate measurements of detector signals were compared. The results of this evaluation are shown in Table 2.II. By comparing sequential pairs of measurements, the standard deviation between pairs of readings was found to be 0.35%, averaged over the total data set. The sample standard deviation of a single measurement is found to be 0.25% which is consistent with the estimate obtained from the PTR measurements.

The above two sets of measurements, the initial calibration and the repeat measurements during operation, have evaluated the same physical characteristic, namely the ability of the detector to yield the same signal when irradiated in the same flux.

### 2.1.3 Detector Linearity

At normal power reactor flux levels, rhodium self-powered detectors respond linearly to the incident flux because in all cases their signal is directly proportional to their reaction rates. Calibration measurements carried out in PTR and repeated in ZED-2 give calibration factors in close agreement despite the fact that the reactors differ in flux level by a ratio of 4.5.

Work carried out by Böck, et al. (2.1) also shows a linear response to neutron flux for self-powered detectors.

### 2.1.4 Detector Depletion

In order to interpret the signals accurately from fixed in-core detectors, it is necessary to properly represent the effects of detector depletion. Rhodium detectors have a significant depletion rate because of the magnitude of the cross sections. They deplete about 1.4% per full power month of operation, resulting in roughly 25% depletion over one cycle. The depletion properties of detectors are summarized in Table 2.III.

The rhodium detector sensitivity is related to the total charge accumulated. As shown by Laaksonen and Saastamoinen (2.2) the relative sensitivity  $\left(\frac{S}{S_0}\right)$ , at any time (t) is related to the fraction  $\frac{Q}{Q_\infty}$ , of total available charge collected to that time as follows:

$$\frac{S(t)}{S_0} = \left(1 - \frac{Q(t)}{Q_\infty}\right)^n \quad (2.1)$$

$Q_{\infty}$  is a property of the detector and is essentially independent of the spectrum in which the detector is used. It is determined from measurements in controlled conditions and is provided to C-E by the detector vendor. Theoretical considerations indicate that the actual depletion behavior is bounded by a linear curve ( $n = 1.0$ ) for a spatially flat absorption rate in the detector wire, and by a depletion that varies by the square root ( $n=0.5$ ) of the relative depletion for a fictitious case where the absorption lies entirely on the surface of the emitter. Realistic absorption distributions within the wire are intermediate between the two extremes as shown in Figure 2-1. For a neutron spectrum similar to that expected in C-E reactors, Saastamoinen predicts an  $n$  close to .75. Small variations about this value are insignificant for cores with detectors of approximately the same age, since the detectors are normalized among themselves and then related to the calorimetric power determination for purposes of inferring absolute quantities. In practice, the value of the exponent is determined from operating data for detectors of varying age and located in symmetric locations. The value of  $n$  thus derived accounts for any errors in the depletion dependence of the signal-to-power conversion factor. Errors due to the choice of constants in Equation (2.1) are automatically included in the basic box power measurement uncertainty because of the method used to estimate it. See Chapter I.3.

#### 2.1.5 Background

The term "background" is used for the sum of all currents generated in the detector and cable which are not the result of neutron interaction with the detector emitter itself. The main contributors to the background signal are cable "self" signal, detector cable cross talk, and gamma induced background.

The cable "self" signal is due to ( $\gamma, e$ ) reactions in the sheath and lead wire, neutron activation of the aluminum in the insulation, and pickup of externally generated electrons such as from neutron activation of the manganese in the stainless steel Penflex sheathing.

Detector and cable cross talk effects are due to decay electrons from the emitter impinging on adjacent detectors and cables.

An additional contribution to the background is due to the gamma sensitivity of the detector. The gamma field impinging on the detector causes photo and Compton electrons to be ejected from the emitter and collector. This signal is proportional to the local neutron flux since the gamma field is neutron induced.

These effects result in a background which is of the order of 1% of the detector signal. The background is compensated by means of calculated factors that depend on axial position, i.e., length of lead cable in active core region. A 1% correction is assumed for the detector with the longest lead cable and other detectors in each string are adjusted according to lead cable length. The correction factors are verified by comparison with measured background.

## 2.2 REFERENCES

- 2.1 H. Böck, P Gebureck, D. Stegemann, "Transient Response of Self-Powered Neutron Detectors," Nucl. Inst. and Meth., 123 (117), 1975.
- 2.2 T. Laaksonen and J. Saastamoinen, "Calculational Studies of Sensitivity Characteristics and Their Burnup Behavior for Rhodium Self-Powered Neutron Detectors," Paper presented at IAEE Specialists Meeting on In-Core Instrumentation and Failed Fuel Detection and Location, Toronto, Ontario, Canada, 1974.

TABLE 2.I

Repeat Measurements of Reactor Calibration  
of Rhodium Detectors

Detector #	Position 1	$S_1^{1)}$	Position 2	$S_2^{1)}$	$\Delta S = S_2 - S_1$
Standard	1	1.0000	1	1.0000	0 %
2RH4-1R1	2	1.0095	7	1.0001	-.94
2	3	1.0083	8	1.0116	.33
4	4	1.0001	9	1.0065	.64
5	5	1.0031	10	1.0037	.06
6R2	6	1.0050	2	1.0098	.48
7	7	1.0066	3	1.0029	-.37
8	8	1.0009	4	.9964	-.45
9	9	1.0127	5	1.0091	-.36
10R1	10	1.0118	6	1.0086	-.32
Standard	1	1.0000	1	1.0000	0
2RH4-48	2	1.0123	6	1.0101	-.23
49	3	1.0194	7	1.0170	-.16
50	4	1.0162	8	1.0126	-.36
51	5	1.0176	9	1.0117	-.59
52	6	1.0211	10	1.0165	-.46
53	7	1.0170	2	1.0099	-.71
54	8	1.0109	3	1.0151	.42
55R1	9	1.0187	4	1.0140	-.47
56	10	1.0163	5	1.0136	-.27

---

1) Relative sensitivity



TABLE 2.II

## Reproducibility Data for Rhodium Detectors

<u>Date</u>	<u>Reactor Power</u>	<u>Number of Comparisons</u>	<u>Standard Deviation</u>
10/22/74	433 Mw	3143	0.39%
5/4/73	720 Mw	141	0.35%
6/25/73	712 Mw	1521	0.24%
		4805	$S_D = 0.35\%$

For A Single Measurement

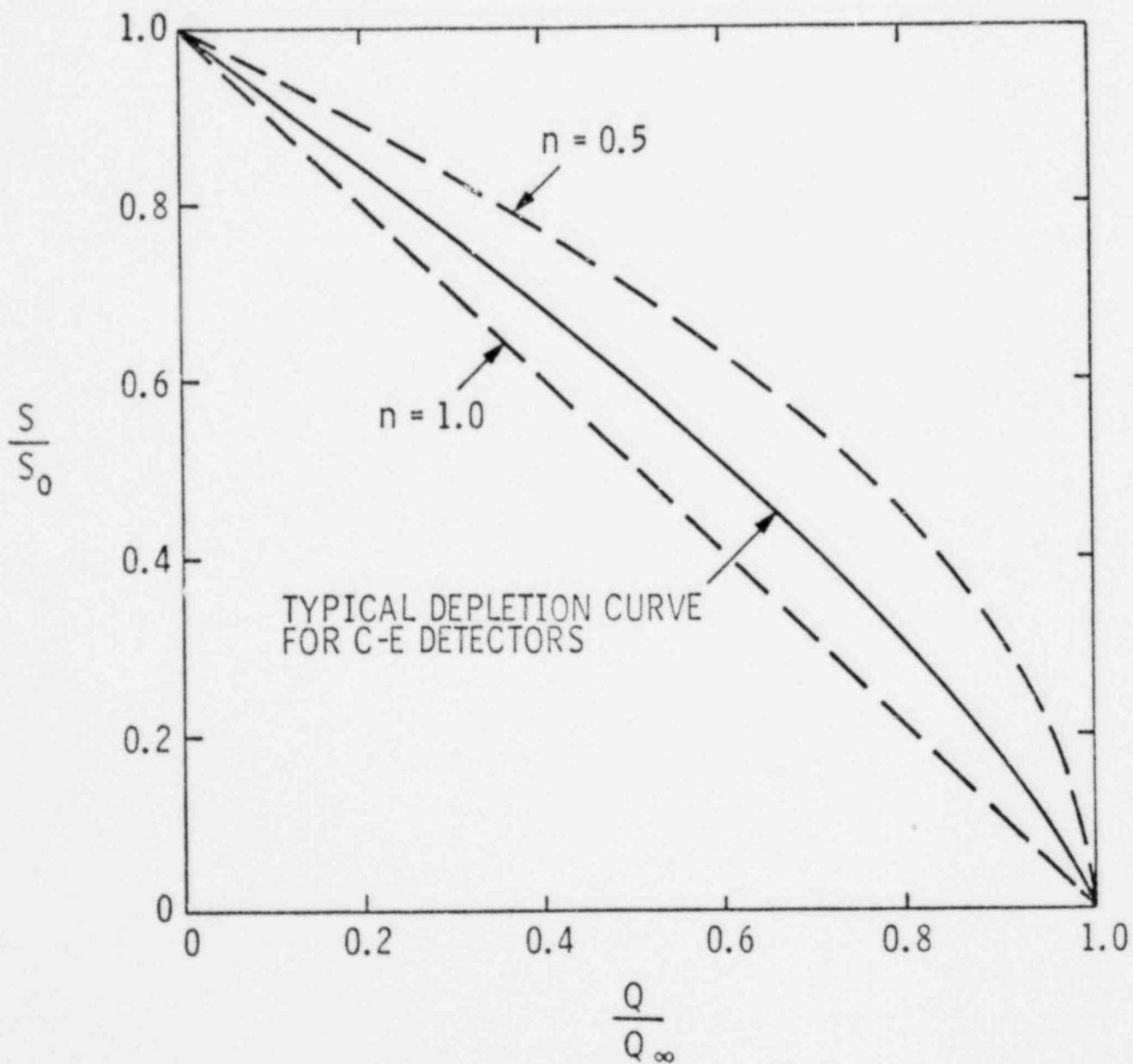
$$s = \frac{S_D}{\sqrt{2}} = 0.25\%$$

TABLE 2.III

Depletion Properties  
of Rhodium-103 Detectors

<u>Property</u>	<u>Value</u>
$\sigma_{a1}$ (PWR Spectrum)	9 b
$\sigma_{a2}$ (PWR Spectrum)	75 b
Depletion Rate in $10^{13}$ nv flux (Maxwellian)	0.23% per month
Monthly Depletion Rate in PWR Spectrum	1.4% per month

Figure 2-1  
RELATIVE RHODIUM TOTAL SENSITIVITY  
vs INTEGRATED DETECTOR CHARGE



### I.3 BASIC BOX POWER MEASUREMENT UNCERTAINTY FOR $F_q$ , $F_{xy}$ AND $F_r$

#### 3.0 INTRODUCTION

##### 3.0.1 Description of Method

The uncertainty to be attributed to the fuel assembly power distribution can be obtained by comparing detailed calculations of the fuel assembly box powers with those inferred from in-core measurements with the INCA system using fixed, in-core rhodium detectors<sup>(3.1)</sup>. The resulting deviation is a reflection of both measurement and calculational uncertainties and errors. In particular, it is often affected adversely by approximations in various features of the calculational model, such as inaccurate representations of the core geometry produced by simplifications in the spatial mesh, by inadequate theory for the core shroud, reflector and core barrel, or by cross section reactivity biases. As the theoretical model of the core is improved in areas of known weakness, the deviations are observed to decrease and will eventually reach a level which is typical of detector uncertainties alone. By eliminating systematic radial and axial shifts from the calculation, improved calculational results can be achieved which approach truth and lead to deviations which approach the measurement uncertainty from a conservative direction.

Such comparisons of measured and calculated box powers have been made for several C-E reactors through several cycles. These include the first three cycles of Calvert Cliffs Unit 1, the first two cycles of Calvert Cliffs Unit 2, Millstone Unit 2, and St. Lucie Unit 1, for the 217 assembly cores, and the fourth and fifth cycles of the 133 assembly Fort Calhoun core. Overall, comparisons have been made at some 170 time points with on the order of 30-40 instrumented assemblies at each time. The operating data are described in Section 3.1.

Estimates have been made of 1) the uncertainty of radial power sharing ( $\sigma_{F_r}$ ) by comparing axially summed measured and calculated box powers for all levels in all instrumented boxes with intact detector strings; 2) the overall peak power uncertainty ( $\sigma_{F_q}$ ) by comparing all the box powers for all instrumented assemblies with intact detectors at all detector levels; and 3) the planar peak power uncertainty ( $\sigma_{F_{xy}}$ ) by comparing the box powers at all locations with intact detectors at each detector level. The calculational and statistical models are described in Sections 3.2 and 3.3.

### 3.0.2 Summary of Results

The estimates of uncertainty for the pooled data, as well as the number of degrees of freedom, are summarized in Table 3.I for all these quantities. The results are described in Section 3.4.

## 3.1 DESCRIPTION OF OPERATING DATA

### 3.1.1 Description of Measured Data

The measured data consist of the powers in assemblies with fixed in-core rhodium detectors. The conversion of detector signals to box powers by the in-core analysis system is described in detail in Part II. It is achieved through the use of signal to power conversion factors (W') calculated as a function of assembly burnup from fine-mesh 2-D PDQ calculations which account for the rhodium detectors, and through the use of depletion dependent sensitivity factors including initial calibration and background corrections. Calculational errors in these factors are therefore included when comparing the measured assembly power with the true power distribution.

The measured data are examined in three ways to provide estimates of the uncertainties on  $F_r$ ,  $F_q$  and  $F_{xy}$ . For  $F_r$ , the sum of the powers from each level in the instrumented boxes with fully intact strings is used. For  $F_{xy}$  at each detector level, the powers in the instrumented boxes over the length of the valid detectors are used. The powers over the length of each intact detector for all instrumented boxes at all levels are used for the  $F_q$  uncertainty analysis.

### 3.1.2 Operating Histories

Except for initial startup and escalation to power at beginning of cycle (BOC) and coastdowns at end of cycle (EOC), all plants operated at essentially full power with all rods out (ARO) or with only small rod bite. INCA measurements, called CECOR snapshots, were taken periodically throughout each cycle. The overall operating histories, core descriptions and instrument locations for all reactors are given below, together with the actual snapshots and the failed detectors at each time point.

#### 3.1.2.1 Calvert Cliffs (CC) Unit 1

CC Unit 1 has operated through 3 cycles. The loading pattern and instrument locations for the first cycle are shown in Figure 3-1. After power escalation, the core operated with ARO 100% power from 850 to 15,500 MWD/T. This was followed by coastdown with the lead rod bank (Bank 5) inserted less than 18% until EOC at 16.7 GWD/T.<sup>†</sup> Table 3.II lists the CECOR snapshots with the pertinent data including failed detectors used for the comparisons to determine measurement uncertainties.

The second cycle of Unit 1 operated with ARO at 100% power until 5000 MWD/T. From then until 7500 MWD/T it operated at a stretch power of 102%, followed by 90% power operation until EOC at a cycle burnup of 8325 MWD/T, all ARO except at EOC. The loading and instrument patterns are shown on Figure 3-2. The snapshot operating data are given in Table 3.III.

The loading map and instrument pattern for Cycle 3 are shown in Figure 3-3. The core operated at 95-100% power from 1600 MWD/T until EOC at 9440 MWD/T, with occasional lead bank insertions of 5-10%. Table 3.IV summarizes the operating data for the snapshots.

---

<sup>†</sup>The lead bank rods for all 217 assembly cores are in assemblies 19, 26, 36, 103, 109, 115, 182, 192 and 199.

### 3.1.2.2 St. Lucie Unit 1

St. Lucie Unit 1 has operated through three complete cycles. The loading and instrument pattern for Cycle 1A are shown in Figure 3-4. The core operated at 100% power from about 2000 MWD/T until EOC at 12.4 GWD/T. There were small lead bank insertions (5-10%) from 10 GWD/T until EOC with a 3% bite on the other rods from 11 GWD/T to EOC. The operating data for the snapshots are given in Table 3.V.

The second cycle operated essentially at 100% power from 300 MWD/T to EOC in a mostly ARO condition with occasional 5-10% insertion of the lead bank. Figure 3-5 shows the loading and instrument patterns and Table 3.VI gives the operating data.

### 3.1.2.3 Millstone Unit 2

Millstone Unit 2 has operated through two complete cycles. The loading pattern and instrument map are shown in Figure 3-6. During the first cycle, the core did not reach ARO full power operation until 1400 MWD/T. After that, it operated at full power until EOC at 15.1 GWD/T with a 5-10% lead bank insertion from 9 GWD/T on. The snapshot operating data are shown in Table 3.VII.

The second cycle loading map and instrument pattern are given in Figure 3-7. It operated at 100% power from 200 MWD/T until very near EOC at 9.2 GWD/T, with about a 10% lead bank insertion during most of the cycle. Table 3.VIII gives the comparison snapshots operating data.

### 3.1.2.4 Calvert Cliffs (CC) Unit 2

CC Unit 2 has operated through one complete cycle. The loading map and instrument pattern for the first cycle are given in Figure 3-8. It operated ARO at 100% power from 400 MWD/T until 8250 MWD/T. It then went to stretch power until 12 GWD/T followed by 70% operation from 12 to 14 GWD/T, and 90%

power operation until EOC at 16.2 GWD/T. During the latter period the lead bank was inserted less than 10% with a 3% bite insertion for the rest of the rods. Table 3.X gives the operating conditions at the snapshot points.

The loading map and instrument pattern for the second cycle are given in Figure 3-9. The core has operated at 95-100% power from 300 MWD/T until 4000 MWD/T with frequent lead bank rod insertions of less than 5-10%. Table 3.X summarizes the available snapshot operating data.

#### 3.1.2.5 Fort Calhoun Unit 1

Fort Calhoun Unit 1 has operated through five complete cycles. The loading map and instrument pattern for the fourth cycle are given in Fig. 3-10. It essentially operated ARO at full power throughout the cycle. The snapshot operating data are given in Table 3.XI.

The fifth cycle loading map and instrument pattern are given in Figure 3-11. The core has again operated ARO at full power. Table 3.XII gives the comparison snapshot operating data.



## 3.2 DESCRIPTION OF CALCULATIONS

### 3.2.1 Description of Basic Core Follow Models

The 3-D spatial calculations performed to generate the information for this chapter were done with the coarse mesh, higher order difference diffusion theory ROCS code (References 3.2, 3.3, 3.4) in two neutron energy groups. Each fuel assembly was represented by 4 nodes in the x-y direction. A quarter core configuration was used with zero current boundary conditions along the axes. The core was thus assumed to be quadrant symmetric in a reflected sense. Any asymmetries actually occurring were included in the full core power comparisons of instrumented boxes. The external boundary conditions were represented as albedos calculated from 2-D, 4 group fine-mesh PDQ<sup>(3.5)</sup> representations of the core, in which the reflector and snroud cross sections were generated in such a way that the material albedos matched those from a multigroup  $S_8$  transport solution. The cross sections for the basic fuel cells were generated by the CEPAC code<sup>(3.6)</sup>, accounting for the correct leakage and soluble boron concentration in the spectrum calculation.

Axially, the 136.7 inch high 217 assembly cores were represented by 24 nodes. The 128 inch high Ft. Calhoun core was represented by 21 nodes. The mesh spacings for both core types are shown in Figure 3-12. Each detector level for either core type is represented by 2 axial meshes. The axial albedo boundary conditions are obtained from fine-mesh PDQ calculations.

The 3-D model for each reactor and cycle was depeleted in a core follow mode, which simulated the actual core operation from BOC to EOC. The actual ROCS depletion step structures for all of the cores and cycles are shown in Tables 3.XIII through 3.XXIII. The cases which were used for comparisons with the measurements are denoted by asterisks.

### 3.2.2 Correction of Calculation for Radial Shifts

Comparisons of calculated and measured radial signal distributions for core instruments have revealed the presence of systematic errors, corresponding to radial shifts in the calculated distributions. These are attributable to theoretical modeling inaccuracies, which include spatial mesh effects, inadequate reflector treatments, and cross section reactivity biases. Since these systematic errors in the calculations are related only to the gross radial power shape, they should not be included in the assessment of incore detector measurement error.

The corrected calculated distribution  $C$  is then used as the basis for comparisons to determine the measurement uncertainties. For the  $F_r$  uncertainties, the

radial shift is used on the radial distribution of the axially summed powers in the instrumented boxes. For  $F_{xy}$  and  $F_q$ , the radial shift is calculated at each level, [

]

3.3 STATISTICAL MODEL FOR CALCULATION OF ASSEMBLY POWER DISTRIBUTION  
UNCERTAINTIES

3.3.1 Definitions

- $C_i(L)$  Calculated corrected value of the assembly power in instrument location  $i$  at instrument level  $L$ .
- $M_i(L)$  Measured value of the assembly power in instrument location  $i$  at instrument level  $L$ .
- $D_i(L)$  Difference between calculated and measured value of the assembly power in instrument location  $i$  at instrument level  $L$ .
- $C_i$  Calculated value of the axially summed assembly power from each level of intact instrument string location  $i$ ;  
$$\sum_{L=1}^{N_{LEV}} C_i(L).$$
- $M_i$  Measured value of the axially summed assembly power from each level in intact instrument string location  $i$ ;  
$$\sum_{L=1}^{N_{LEV}} M_i(L).$$
- $D_i$  Difference between calculated and measured value of the axially integrated assembly power in intact instrument location  $i$ .
- $N(L)$  Number of intact instruments at detector level  $L$  ( $L=1, \dots, N_{LEV}$ ).
- $N_S$  Number of intact instrument strings in the core.  
 $N_{LEV}$  Number of detector levels; = 4.

$N_{DET}$	Number of intact instruments in core.
$N_{DEG}$	Total number of degrees freedom.
$N_{TOT}$	Total number of data points.
$\sigma_D$	The standard deviation of the differences between measurement and calculation
$\sigma_M$	The measurement standard deviation relative to the true power.
$\sigma_C$	The calculation standard deviation relative to the true power.

The basic relationship for  $\sigma_M$  is:

$$\sigma_M^2 = \sigma_D^2 - \sigma_C^2 \quad (3.5)$$

Because the calculations have been corrected to represent a close approximation of truth, it is expected that  $\sigma_C^2$  will be small. Equation (3.5) shows that:

$$\sigma_M^2 \leq \sigma_D^2 \quad (3.6)$$

Therefore, the unbiased sample variance,  $S_D^2$ , corresponding to  $\sigma_D^2$ , will be used to construct an upper bound for  $\sigma_M^2$ . Similarly, it can be shown that the one-sided tolerance limits satisfy

$$k_M S_M < k_D S_D \quad (3.7)$$

where  $S_M$  denotes the sample variance corresponding to  $\sigma_M$ , and  $k_M$  and  $k_D$  are probability/confidence factors.

### 3.3.2 The Sample Variance for the Difference Between Calculation and Measurement

#### 3.3.2.1 F<sub>r</sub> Uncertainty: S<sub>D<sub>Fr</sub></sub>

For the F<sub>r</sub> measurement uncertainty the axially summed measured and calculated assembly powers in all the intact detector string locations (N<sub>S</sub>) are compared. The normalization is:

$$\sum_{i=1}^{N_S} C_i = \sum_{i=1}^{N_S} M_i = N_S \quad (3.8)$$

The differences are given as:

$$D_i = C_i - M_i, \quad i=1, \dots, N_S \quad (3.9)$$

$$\bar{D} = \frac{1}{N_S} \sum_{i=1}^{N_S} D_i \quad (3.10)$$

The bias  $\bar{D}$  is identically zero because of the normalization. The sample variance of the difference is then:

$$S_{D_{Fr}}^2 = \frac{1}{N_S - 1} \sum_{i=1}^{N_S} (D_i - \bar{D})^2 = \frac{1}{N_S - 1} \sum_{i=1}^{N_S} D_i^2 \quad (3.11)$$

#### 3.3.2.2 F<sub>q</sub> Uncertainty: S<sub>D<sub>Fq</sub></sub>

For the F<sub>q</sub> measurement uncertainty the measured and calculated assembly powers for all intact detector locations at all levels in the core (N<sub>DET</sub>) are compared. The overall normalization is:

$$\sum_{L=1}^{N_{LEV}} \sum_{i=1}^{N(L)} C_i(L) = \sum_{L=1}^{N_{LEV}} \sum_{i=1}^{N(L)} M_i(L) = N_{DET} \quad (3.12)$$

[

] where the total number of intact detectors  $N_{DET}$  is given by

$$N_{DET} = \sum_{L=1}^{N_{LEV}} N(L) \quad (3.13)$$

The differences are given as:

$$D_i(L) = C_i(L) - M_i(L), \quad i=1, \dots, N(L), \\ L=1, \dots, N_{LEV} \quad (3.14)$$

$$\bar{D} = \frac{1}{N_{DET}} \sum_{L=1}^{N_{LEV}} \sum_{i=1}^{N(L)} D_i(L) \quad (3.15)$$

The bias is again identically zero because of the normalization. The sample variance of the difference is then:

$$S_{D_{Fq}}^2 = \frac{1}{N_{DET} - 4} \sum_{L=1}^{N_{LEV}} \sum_{i=1}^{N(L)} D_i^2(L) \quad (3.16)$$

### 3.3.2.3 $F_{xy}$ Uncertainty: $S_{D_{Fxy}}$

For the  $F_{xy}$  measurement uncertainty the measured and calculated assembly powers are compared at each level  $L$  for all intact detector locations,  $N(L)$ . The normalization is:



$$\sum_{i=1}^{N(L)} C_i(L) = \sum_{i=1}^{N(L)} M_i(L) = N(L) \quad (3.17)$$

The differences are given as:

$$D_i(L) = C_i(L) - M_i(L), \quad i=1, \dots, N(L) \quad (3.18)$$

with a bias

$$\bar{D} = \frac{1}{N(L)} \sum_{i=1}^{N(L)} D_i(L) \quad (3.19)$$

equal to zero because of the normalization.

The sample variance of the difference at level L is then:

$$S_{D_{F_{xy}}}^2(L) = \frac{1}{N(L)-1} \sum_{i=1}^{N(L)} D_i^2(L) \quad (3.20)$$

#### 3.3.2.4 Summary

The sample variances based on Equations 3.11, 3.16 and 3.20 are unbiased estimates of the true variances for  $F_r$ ,  $F_q$  and  $F_{xy}$ .

#### 3.3.3 Procedure for Pooling Estimates

The estimates for the variances discussed above are applicable to individual comparisons. Pooling for the whole data set is achieved by calculating the variance over the entire set of comparison cases,  $\ell=1, \dots, K$ , i.e.,

$$S_{D_K}^2 = \sum_{\ell=1}^K \sum_{j=1}^{M_\ell} (D_{j\ell} - \bar{D})^2 / \sum_{\ell=1}^K (N_\ell) \quad (3.21)$$

where  $M_\ell$  is the number of data points and  $N_\ell$  is the number of degrees of freedom in each comparison case  $\ell$ . Since the overall bias remains identically zero,

$$S_{D_K}^2 = \sum_{\ell=1}^K \sum_{j=1}^{M_\ell} (D_{j\ell})^2 / \sum_{\ell=1}^K (N_\ell) \quad (3.22)$$

Using the sample variances, this is equivalent to:

$$S_{D_K}^2 = \frac{\sum_{\ell=1}^K (M_\ell - 1) S_{D\ell}^2}{\sum_{\ell=1}^K (N_\ell)} \quad (3.23)$$

with the total number of degrees of freedom equal to

$$N_{DEG} = \sum_{\ell=1}^K (N_\ell) \quad (3.24)$$

and the total number of data points

$$N_{TOT} = \sum_{\ell=1}^K (M_\ell) \quad (3.25)$$

The total number of data points and degrees of freedom can then be used to determine the  $k$  value to obtain the one-sided tolerance limit at the 95%/95% probability/confidence level.

3.3.4 Procedure for Testing Poolability



3.3.5 Procedure for Computing One-sided Tolerance Limits



GENERAL PROCEDURE FOR JUSTIFYING AND CONFIRMING POOLABILITY

[

]

### 3.4 EVALUATION OF MEASUREMENT UNCERTAINTY

#### 3.4.1 Random Component of Observed Differences Between Calculation and Measurement, $S_D$ , for the Various Reactors

The method of estimating  $\sigma_D$  (and  $\sigma_M$ ) was described in detail in 3.3. The data for the quantities of interest are summarized below for each reactor.

##### 3.4.1.1 Calvert Cliffs Unit 1

Table 3.XXIVa gives the comparison results for the first cycle operation. Figures 3-13a through 3-13e show typical maps near BOC at 850 MW/D/T after escalation to full power for the 4 levels and for the axially summed comparisons. The results of level pooling for  $F_{xy}$  and time point pooling for all three quantities as well as the Bartlett test results are summarized in Table 3.XXIVb.

For  $F_{xy}$ , pooling the levels satisfies the Bartlett test except at three time points with the value at 10 GWD/T only marginally failing, as shown. When the level values are pooled over timepoints, this leads to results which do not satisfy the Bartlett test, as shown in Table 3.XXIVb. Therefore, as a conservative measure of the  $F_{xy}$  uncertainty for this cycle, the pooled level value at the worst time point is taken. This is the value given at the bottom of Table 3.XXIVa.

Table 3.XXIVb also shows that pooling the values for the  $F_r$  and  $F_q$  uncertainty for all times does not satisfy the Bartlett test. Again, as a conservative estimate of the cycle uncertainties, the worst values are used and are given in Table 3.XXIVa. In general, the pooled  $F_{xy}$  level and  $F_q$  values are very close because the average axial power shapes across the detector levels are relatively flat, with maximum variations on the order of 10-15%. When the axial shapes across the detectors become flatter, as with depletion, the values become essentially identical, as seen in Tables 3.XXIVa and b.

Table 3.XXVa gives the comparison results for the second cycle together with the overall pooled second cycle uncertainty estimates. Figure 3-14 shows typical BOC maps after power escalation at 989 MWD/T. The results of the Bartlett tests for pooling are given in Table 6.XXVb. These show that the levels pool and the values for all time points pool. The relatively low values of  $F_{calc}$  in the Bartlett tests for time point pooling, especially for  $F_r$ , are an indication that the data at the various time points are very similar. The level pooling does not display such a behavior, indicating that it is a time point pooling effect. Power distributions show less than a 1-2% variation throughout the cycle so that essentially the same situation is repeated and presented to the ROCS calculation and the CECOR measurement at each time point. A systematic, but unknown, error in the calculation or in the measurement will therefore be able to dominate the sample variance and provide such a correlation effect. The pooled values are the overall values given in Table 3.XXVa.

Table 3.XXVIa gives the data for cycle 3, while Figure 3-15 shows typical BOC3 maps during power escalation at 1200 MWD/T and 91% power. Table 3.XXVIb gives the pooling and Bartlett test results confirming that all levels and time points pool. The overall pooled values are given in Table 3.XXVIa.

#### 3.4.1.2 St. Lucie Unit 1

Table 3.XXVIIa gives the first cycle results for St. Lucie while Figure 3-16 shows a cycle 1 map during power escalation at 880 MWD/T and 50% power. The pooling and Bartlett test results are given in Table 3.XXVIIb. The  $F_{xy}$  level values pool at all time points, but the  $F_{xy}$  and  $F_q$  values do not pool over time points. The  $F_r$  values do. As a consequence, the estimates for the cycle given in Table 3.XXVIIa are the pooled  $F_r$  values and the worst time point values for  $F_{xy}$  and  $F_q$ .

Table 3.XXVIIIa gives the comparison results for the second cycle of St. Lucie. Figure 3-17 shows the BOC maps at 1360 MWD/T after escalation to full power. All levels and time points pool to give the overall values in Table 3.XXVIIIa. The results of the pooling and Bartlett tests are given in Table 3.XXVIIIb. The low values of  $F_{calc}$  for the Bartlett test are again associated with power distributions varying only slightly (~2%) throughout life.

#### 3.4.1.3 Millstone Unit 2

Table 3.XXIXa presents the cycle 1 comparison results and Figure 3-18 gives the BOC power comparisons at 1350 MWD/T after power escalation to full power. The levels pool at all time points except at 13,000 MWD/T where the Bartlett test is failed, but the values do not pool over time points as shown in Table 3.XXIXb. As a consequence, the estimates for the cycle uncertainties given in Table 3.XXIXa are taken as the worst values occurring during the cycle.

The second cycle results are given in Table 3.XXXa and maps at 500 MWD/T after escalation to full power are given in Figure 3-19. Table 3.XXXb shows that the four levels fail to pool at each time point with level 4 being consistently high throughout the cycle. As a consequence, the values for the worst level (level 4) are used for the time point pooling of  $F_{xy}$ . The values for  $F_{xy}$  as well as  $F_r$  and  $F_q$  pool over time points. The low values of  $F_{calc}$  for the time point pooling, particularly for  $F_{xy}$  at level 4, reveal that the actual measured power distributions change very little throughout life. These overall values are summarized in Table 3.XXXa.

#### 3.4.1.4 Calvert Cliffs Unit 2

The comparison results for Cycle 1 of Calvert Cliffs Unit 2 are given in Table 3.XXXIa with BOC maps at 1400 MWD/T after power escalation given in Figure 3-20. The pooling and Bartlett test results are given in Table 3.XXXIb. For  $F_{xy}$ , the levels pool except at four time points, with the



Bartlett test only being marginally failed at the second time point. However, all the quantities fail the test for pooling over the time points. As a consequence, the values at the worst time points are taken as conservative estimates of the uncertainties for the entire cycle and are the values in Table 3.XXXIa.

The comparison results for the second cycle are given in Table 3.XXXIIa. The maps at 810 MWD/T after power escalation are given in Figure 3-21. All levels and time points pool to give the overall values in Table 3.XXXIIa. The results of the pooling and Bartlett tests are given in Table 3.XXXIIb.

#### 3.4.1.5 Fort Calhoun Unit 1

Table 3.XXXIIIa presents the cycle 4 comparison results and Figure 3-22 gives the power comparisons at 1000 MWD/T. All the levels and time points pool to give the overall results in the table. The results of the pooling and Bartlett tests are given in Table 3.XXXIIIb. The low values of  $F_{calc}$  in the Bartlett test are again the result of the very small variation of the power distributions throughout life.

The comparison results for the fifth cycle are given in Table XXXIVa and the maps at 300 MWD/T are given in Figure 3-23. The results of the pooling studies are given in Table 3.XXXIVb and again show the similarity of the data and that both levels and time points pool. The overall pooled measurement uncertainties are given in Table 3.XXXIVa.

#### 3.4.2 Summary of Measurement Uncertainty

The standard deviation of the differences assigned for each reactor cycle is summarized in Table 3.XXXV. These represent the pooled values for later cycles and the worst values for the first cycles, except for the St. Lucie

$F_r$  value which is pooled over time.

The results of pooling the data over all cycles and over only either the first or later cycles are given in Table 3.XXXVI together with results of the Bartlett tests. This shows that pooling is not justified even though the spread between the minimum and maximum uncertainties is relatively small. Hence the basic measurement uncertainty is cycle and plant dependent. Therefore, as a conservative measure of the overall uncertainties the worst values, coming from Calvert Cliffs (CC) Unit 1 Cycle 3, will be used, data for which are in Table 3.XXVIa. Examination of the data for  $F_q$ ,  $F_{xy}$ , and  $F_r$  in this table shows a small variation of the sample variances with time in the cycle. This is expected on physical grounds because the power distribution remains relatively constant throughout the cycle. Hence, pooling is justified. Confirmation of this justification is provided by statistical tests as described in the following paragraph.

Normality tests (3.7) on the  $F_q/F_{xy}$  distribution of differences indicate that the hypothesis of normality is not unreasonable at each individual time point. This is shown in Table 3.XXXVII. For the set of time point pooled data, the D-prime test indicates that the distribution may not be normal. The sample distribution is given and compared to a normal distribution in Figure 3-24. Non-normality is associated with the double-peaked nature exhibited by the sample. The upper end of the distribution, which is important for the one-sided tolerance limit, is close to the normal shape however. Since the distribution may be non-normal, poolability (combining time points) is tested according to Reference 3.9; i.e., the time points represent successive sequences of observations and the observed differences in each sequence are classified according to the quartiles of the entire pooled set. The  $\chi^2$ -test is then applied to test the homogeneity of the data. Because the power distribution remains nearly the same throughout the cycle, it is expected that the measurement error will remain virtually the same throughout the cycle. This is reflected in the non-normality which indicates that the differences observed have systematic, but unknown components. The  $\chi^2$ -test further confirms this. The test result  $\chi^2$  (with

66 degrees of freedom)  $\approx 25.0$  indicates considerable homogeneity. The data is in fact more homogeneous than may be expected on the basis of random errors only. The physical reason for this is that some of the calculative error, conservatively, remains in the observed differences. Since the calculative error that remains is dominated by systematic, but unknown effects, the results is a relatively large contribution to the sample variance which remains fairly constant with burnup because the power distribution itself does not change much with burnup. Pooling of the data is therefore justified.

Determination of a one-sided tolerance limit for Calvert Cliffs Unit 1 Cycle 3 at the 95/95 probability/confidence level is done according to Reference 3.11. [

]

Figure 3-25 provides similar information for the  $F_q$  data of St. Lucie Unit 1 Cycle 2. This indicates a nearly similar distribution for the cycle that exhibits the uncertainties closest to the worst cycle. Figure 3-25 is included for illustrative purposes only. The data is not pooled with that of Calvert Cliffs Unit 1 Cycle 3.

When the  $F_r$  distribution of differences for CC Unit 1 Cycle 3 are tested for normality, they pass the W test at all time points and pass the D-prime test for the whole cycle at the 54% level. This is shown in Table 3.XXXVIII. The overall CC Unit 1 Cycle 3 distribution for  $F_r$  uncertainties is given in Figure 3-26. This shows that only [ ] of the points lie above the 95/95 one-sided tolerance limit.

The overall uncertainty to be applied to all cycles and plants is taken from the worst case of Table 3.XXXV as discussed above. Since this table

gives the sample standard deviations as absolute values, referred to an average power of unity, a conversion is necessary to obtain the final sample standard deviation in percent of peak power. Table 3.I quotes the measurement uncertainty in percent of peak power. These were obtained from the absolute values in Table 3.XXXV by dividing by the minimum peak box assembly power occurring during the cycle. Table 3.I also gives the associated number of degrees of freedom for use when combining the basic measurement uncertainty with other uncertainties in order to obtain the overall uncertainty. Further, the 95/95 probability/confidence limits on the basic measurement uncertainties for assembly powers are listed in Table 3.I.

3.5      REFERENCES

- 3.1      T. G. Ober, W. B. Terney, G. H. Marks, "INCA Method of Analysis In-Core Detector Data in Power Reactors," CENPD-145, April, 1975.
- 3.2      T. G. Ober, J. C. Stork, I. C. Rickard, J. K. Gasper, "Theory, Capabilities and Use of the Three Dimensional Reactor Operation and Control Simulator (ROCS)," Nucl. Sci. and Eng., 64 (605) 1977.
- 3.3      T. G. Ober, J. C. Stork, R. P. Bandera, W. B. Terney, "Extension of the ROCS Coarse-Mesh Physics Simulator to Two Energy Groups," Trans. Am. Nucl. Soc., 28, (763) 1978.
- 3.4      W. B. Terney, R. P. Bandera, T. G. Ober, "Qualification of C-E's 3-D Spatial Neutronics Codes for PWR Analyses," Trans. Am. Nucl. Soc., 30, (226) 1978.
- 3.5      W. R. Cadwell, "PDQ-7 Reference Manual," WAPD-TM-678, January, 1967.
- 3.6      Combustion Engineering Standard Safety Analysis Report (CESSAR), Chapter 4.3.
- 3.7      "Assessment of the Assumption of Normality (Employing Individual Observed Values)," ANSI N15.15-1974.
- 3.8      A. Hald, "Statistical Theory with Engineering Applications," P. 291, J. Wiley and Sons, Inc., 1955.
- 3.9      W. J. Conover, "Practical Non-parametric Statistics," P. 150, J. Wiley and Sons, Inc., 1971.
- 3.10     D. B. Owen, "Factors for One-sided Tolerance Limits and for Variables Sampling Plans," SCR-607, 1963.
- 3.11     W. J. Conover, Ibid., P. 117.

TABLE 3.1

Summary of Uncertainties<sup>†</sup>  
For the Measurement of Peak Assembly Power

Quantity	S	Number of Degrees of Freedom	$k_{95/95}$	kS
$F_r$	[ ]	681	1.725	[ ]
$F_{xy}$		185	1.801	
$F_q$		185	1.801	

---

<sup>†</sup>Quoted in percent of peak assembly value

TABLE 3.II  
 Calvert Cliffs Unit 1 Cycle 1  
 Comparison Snapshot Operating Data

Failed Detectors

Burnup	Power Level	Rod Insertion	Level 1	Level 2	Level 3	Level 4
850	100%	0%	None	None	23	None
3000	"	"	20	"	"	"
4000	"	"	"	"	"	"
5000	"	"	"	"	"	"
6000	"	"	"	"	"	"
7000	"	"	"	"	"	"
8000	"	"	"	"	"	"
9000	"	"	"	"	"	"
10000	"	"	"	"	"	35
11000	"	"	"	"	"	"
12000	"	"	"	"	"	"
13000	"	"	"	"	"	"
14000	"	"	20,26	"	"	35,8
15000	"	"	"	"	"	"
16000	95%	"	"	35	"	"

1.3.28

TABLE 3.III

Calvert Cliffs Unit 1 Cycle 2  
Comparison Snapshot Operating Data

Burnup	Power Level	Rod* Insertion	Failed Detectors			
			Level 1	Level 2	Level 3	Level 4
234	90%	0%	3,14,15,25,44,1,7	3,14,15,18,25,31,	3,14,15,25,44,1,7	3,14,15,25,44,1,7
332	100%	"	"	1,7,44	"	"
989	"	"	"	"	"	"
1436	"	"	"	"	"	"
1747	"	"	"	"	"	"
2087	"	"	"	"	"	"
2717	"	"	"	"	"	3,14,15,25,30,44,1,7
3338	"	"	"	3,14,15,18,25,31,43,		3,14,15,25,30,33,
3969	"	"	"	44,1,7	"	44,1,7
4184	"	"	"	3,14,15,18,24,25,31,	"	"
5057	102%	"	"	43,44,1,7	"	"
6006	"	"	"	"	"	2,3,14,15,25,30,
6446	104%	"	"	"	"	33,44,1,7
6924	103%	"	"	"	"	"
7334	104%	"	"	3,14,15,18,24,25,31,	3,14,15,25,29,44,	"
7555	102%	"	"	42,43,1,7,44	1,7	"
8258	97%	3%	"	"	"	"

\*Lead Bank

1.3.29



TABLE 3.IV  
 Calvert Cliffs Unit 1 Cycle 3  
 Comparison Snapshot Operating Data

Failed Detectors

I.3.30

Burnup	Power Level	Rod* Insertion	Level 1	Level 2	Level 3	Level 4
495	85%	0%	4,5,6,16,19,22,23,33	4,6,23,33,35,42	3,4,5,6,16,19,23,33	4,5,6,23,33
1202	91%	"	"	"	"	"
1611	93%	"	"	"	"	"
2021	99%	"	"	4,6,23,33,34,35,42	"	4,5,6,23,33,34
3011	94%	"	"	"	"	"
3811	95%	"	4,5,6,16,19,21,22,23,33	"	3,4,5,6,16,19,23,33,34	"
4626	"	"	"	"	"	4,5,6,23,33,34,45
5434	94%	"	"	"	"	"
5849	97%	7%	"	"	"	"
5994	96%	0%	"	"	"	"
6442	94%	"	4,5,6,16,19,21,22,23,33,34	"	"	"
6658	"	"	"	"	"	4,5,6,20,23,33,34,45
6658	95%	"	"	"	"	"
6869	"	"	"	"	3,4,5,6,8,16,19,23,33,34	"
7147	"	"	"	"	"	"
7327	87%	7%	"	"	"	"
7554	96%	"	"	"	3,4,5,6,8,16,19,21,23,33,34	"
7738	96%	"	"	"	"	"
7964	100%	"	"	"	"	"
8149	96%	"	"	"	"	"
8578	98%	8%	"	"	"	"
8822	100%	2%	"	"	"	"
9042	"	"	"	"	"	"
9440	"	0%	"	"	"	"

\*Lead Bank

TABLE 3.V  
St. Lucie Cycle 1  
Comparison Snapshot Operating Data

Burnup	Power Level	Rod* Insertion	Failed Detectors			
			Level 1	Level 2	Level 3	Level 4
888	51%	0	43	None	32	4,17
2139	100%	"	"	"	"	"
2982	"	"	"	"	"	"
3420	95%	"	"	"	"	"
4903	100%	"	"	"	"	"
5513	"	"	"	"	"	"
6029	"	"	"	"	"	"
6489	"	"	"	"	"	"
7093	"	"	"	"	"	"
8976	"	"	"	"	None	"
9910	"	"	41,43	15	"	"
11359	"	"	34,41,43	"	"	"
12414	"	6.2	"	"	"	"

1.3.31

\*Lead Bank

TABLE 3.VI  
St. Lucie Cycle 2  
Comparison Snapshot Operating Data

Failed Detectors

Burnup	Power Level	Rod* Insertion	Level 1	Level 2	Level 3	Level 4
189	90%	5%	6,29,43	29	11,29	23,29
317	98%	7%	"	"	29	"
560	98%	1%	"	"	"	"
1054	100%	9%	"	"	"	"
1361	"	1%	"	"	"	"
1726	"	"	"	"	"	"
2234	"	"	"	"	"	"
2724	"	"	"	"	29,32	9,23,29
3132	"	3%	"	"	"	"
3649	"	1%	"	"	"	"
4078	"	"	"	"	"	"
4200	"	"	"	"	"	"
4643	"	"	"	"	"	"
5087	"	16%	"	"	"	"
5424	"	1%	"	"	"	"
5948	"	"	"	"	"	"
6368	"	"	"	"	"	"
7030	"	"	"	"	29	9,18,23,29
7382	"	"	"	"	"	"
7885	"	"	"	"	"	"
8370	"	"	"	"	"	"

\*Lead Bank

1.3.32

TABLE 3.VII  
 Millstone II Cycle 1  
 Comparison Snapshot Operating Data

Burnup	Power Level	Rod* Insertion	Failed Detectors			
			Level 1	Level 2	Level 3	Level 4
1350	100%	0	8,27	16	None	None
2100	"	"	"	16,27	"	"
3350	"	"	"	"	"	"
4000	"	"	"	"	35	"
5100	"	"	"	"	"	"
6200	"	"	"	"	"	"
7500	"	"	8,10,27	"	"	"
9000	"	8%	"	"	"	"
10200	"	4%	8,10,17,18,27	16,17,27	"	"
11300	"	7%	"	"	"	"
12000	"	"	"	"	"	"
13100	93%	9%	"	"	"	"
14700	100%	"	"	"	"	"
15094	"	"	"	"	"	"

I.3.33

\*Lead Bank

TABLE 3.VIII  
 Millstone II Cycle 2  
 Comparison Snapshot Operating Data

Burnup	Power Level	Rod* Insertion	Failed Detectors			
			Level 1	Level 2	Level 3	Level 4
200	100%	12%	2,8,18,21,27,35	18,27,28,29	4,6,7,9,18,19,39,43	None
500	"	8%	"	"	4,6,7,9,18,19,28,39,43	"
1000	"	5%	"	"	"	25
1500	"	7%	"	"	"	"
2000	"	"	"	"	4,5,6,7,9,18,19,28,39,43	"
2400	"	8%	"	"	"	"
2800	"	"	2,8,18,21,27	16,18,27,28,29	4,5,6,7,9,18,19,28,43	"
3300	"	9%	"	"	"	"
3800	"	8%	"	"	"	"
4300	"	"	"	"	"	"
4800	"	"	"	"	"	"
5200	96%	7%	"	"	"	"
5300	100%	"	2,8,10,18,21,27	"	"	"
5800	"	"	"	"	"	"
6300	"	"	"	"	"	"
6800	"	6%	"	"	"	9,25
7300	"	"	"	"	1 4,5,6,7,9,18,19,28,43	"
7800	"	4%	"	"	"	"
8300	"	5%	"	"	"	"
8700	99%	6%	"	"	"	"
9100	96%	7%	"	"	"	"
9232	94%	"	"	"	"	"

\*Lead Bank

1.3.34

TABLE 3. IX  
 Calvert Cliffs Unit 2 Cycle 1  
 Comparison Snapshot Operating Data

Burnup	Power Level	Rod* Insertion	Failed Detectors			
			Level 1	Level 2	Level 3	Level 4
1440	100%	0%	None	32	18	None
3330	"	"	42	"	29	"
5630	"	"	"	31,32,35	26,29,41	22,29
6230	"	"	"	"	"	"
6880	"	"	"	"	"	"
7435	"	"	"	"	"	"
8750	105%	"	"	"	"	"
9980	103%	5%	"	"	18,26,29,41	"
10200	"	3%	"	"	"	18,22,29
10675	"	"	"	"	"	"
11980	"	"	"	"	"	22,23,28,29
12840	72%	"	"	14,31,32,35	"	"
13810	"	"	"	14,29,31,32,35	"	22,23,28,29,38

\*Lead Bank

1.3.35

TABLE 3.X  
 Calvert Cliffs Unit 2 Cycle 2  
 Comparison Snapshot Operating Data

Failed Detectors

Burnup	Power Level	Rod* Insertion	Level 1	Level 2	Level 3	Level 4
200	80%	0%	4,26,42	4,26,32,42	4,8,26,42	4,26,39,42
280	87%	9%	"	"	"	4,26,39,42,37
389	89%	8%	"	"	4,26,42	4,26,39,42
495	84%	"	4,15,26,42	"	1,4,26,42	4,13,26,39,42
809	"	0%	"	"	"	"
1273	"	23%	"	"	"	"
1438	98%	0%	"	"	"	"
1698	"	8%	"	"	1,4,8,26,42	"
3519	99%	0%	"	"	"	"
3943	"	"	"	"	"	"

\*Lead Bank

I.3.36

TABLE 3.XI  
Fort Calhoun Unit 1 Cycle 4  
Comparison Snapshot Operating Data

Burnup	Power Level	Rod* Insertion	Failed Detectors			
			Level 1	Level 2	Level 3	Level 4
200	100%	0%	10,11,23,25,28	11,16,23,25,28	1,10,11,16,28	1,11,16,21,22,28
1000	100%	0%	1,10,11,12,17,23,25	1,4,11,16,23,25	1,3,11,16,18	1,11,13,16,17,21,22,27
2000	100%	0%	10,11,12,17,23,25	1,5,6,11,16,17,23,25	1,3,6,11,18,23	1,13,14,16,17,21,22
3000	100%	0%	"	1,5,6,11,16,17,23,25	1,3,11,18	1,13,14,16,17,21,22,27,28
4000	100%	0%	"	5,6,11,17,23,25	1,3,6,18,23,24	1,6,13,14,17,21,22,23,24
5000	100%	0%	"	5,6,11,16,23,25	1,3,6,23,24,26	"
6000	100%	0%	"	5,6,11,17,23,25	"	"
7000	100%	0%	"	5,6,11,17,23,25	"	"
8200	100%	0%	10,12,17,23,24,25	5,6,11,17,21,25	1,3,6,16,23,24,26	6,13,14,17,21,22,23,24

\*All rods out



TABLE 3.XII  
 Fort Calhoun Unit 1 Cycle 5  
 Comparison Snapshot Operating Data

Failed Detectors

Burnup	Power Level	Rod* Insertion	Level 1	Level 2	Level 3	Level 4
300	100%	0%	1,9,10,12,16,24	1,9,16,23,24	1,6,9,16,23,24	1,9,13,14,16,22,23,24
1000	100%	0%	1,9,10,16,24	"	"	"
2000	100%	0%	1,9,10,16,24	"	"	"
3000	100%	0%	1,9,10,12,16,24	"	"	"
4000	100%	0%	1,9,10,16,23,24	"	"	"
5000	100%	0%	1,9,10,16,24	"	"	"
6000	100%	0%	1,9,10,16,24	"	"	"

\*All rods out

I.3.38

TABLE 3.XIII  
Calvert Cliffs Unit 1 Cycle 1

ROCS Maneuver Structure

Man #	Bu	Power	Rods <sup>†</sup>	Comparisons
00	0	20%	0%	
01	100	50%	"	
02	500	80%	"	
03	850	100%	"	*
04	1000	"	"	
05	2000	"	"	
06	3000	"	"	*
07	4000	"	"	*
08	5000	"	"	*
09	6000	"	"	*
10	7000	"	"	*
11	8000	"	"	*
12	9000	"	"	*
13	10000	"	"	*
14	11000	"	"	*
15	12000	"	"	*
16	13000	"	"	*
17	14000	"	"	*
18	15000	"	"	*
19	15500	"	"	
20	16000	95%	"	*
21	16500	68%	18%	
22	16670	57%	"	

---

<sup>†</sup> Lead Bank

TABLE 3.XIV  
 Calvert Cliffs Unit 1 Cycle 2  
 ROCS Maneuver Structure

Man #	Bu	Power	Rods <sup>†</sup>	Comparisons
00	0	49%	0%	
01	75	70%	"	
02	150	80%	"	
03	200	90%	"	*
04	325	100%	"	*
05	990	"	"	*
06	1436	"	"	*
07	1746	"	"	*
08	2087	"	"	*
09	2722	"	"	*
10	3341	"	"	*
11	3970	"	"	*
12	4192	"	"	*
13	5056	102%	"	*
14	6000	101%	"	*
15	6446	103%	"	*
16	7000	"	"	*
17	7360	"	"	*
18	7600	90%	"	*
19	8280	"	3.2%	*
20	8325	"	"	

<sup>†</sup>Lead Bank

TABLE 3.XV  
 Calvert Cliffs Unit 1 Cycle 3  
 ROCS Maneuver Structure

Man #	Bu	Power	Rods <sup>†</sup>	Comparisons
00	0	27%	50%	
01	177	84%	0%	
02	495	82%	"	*
03	801	57%	50%	
04	1202	91%	0%	*
05	1611	93%	"	*
06	2021	99%	"	*
07	2238	"	15.8%	
08	2582	93%	0%	
09	3011	94%	"	*
10	3811	95%	"	*
11	4626	"	"	*
12	5434	94%	"	*
13	5849	97%	7.2%	*
14	5994	96%	0%	
15	6442	94%		*
16	6658	"	"	*
17	6658	"	"	*
18	6869	0%	"	
19	6869	95%	"	*
20	7147	"	"	*
21	7327	87%	6.7%	*
22	7554	96%	"	*
23	7738	"	"	*
24	7964	100%	"	*
25	8149	95%	"	*
26	8578	98%	8.2%	*
27	8969	100%	0%	*
28	9440	"	"	

<sup>†</sup> Lead Bank

TABLE 3.XVI  
St. Lucie Cycle 1  
ROCS Maneuver Structure

Man #	Bu	Power	Rods <sup>†</sup>	Comparisons
Core Reconstituted - Cycle 1A				
03	780	0%	0%	
04	780	30%	"	
05	875	51%	"	*
06	1320	81%	"	
07	1750	90%	"	
08	2190	100%	"	*
09	3000	"	"	*
10	3440	95%	"	*
11	4410	100%	"	
12	4900	"	"	*
13	5500	"	"	*
14	6000	"	"	*
15	6490	"	"	*
16	7000	"	"	*
17	7500	"	"	
18	8000	"	"	
19	8975	"	"	*
20	9500	"	"	
21	9910	"	3%	*
22	10305	"	17% 3.4% <sup>††</sup>	
23	11360	"	5% "	*
24	12376	"	5% "	*

† Lead Bank

†† Other Rods

TABLE 3.XVII  
 St. Lucie Cycle 2  
 ROCS Maneuver Structure

Man #	Bu	Power	Rods <sup>†</sup>	Comparisons
00	0	50%	0%	
01	0	30%	5%	
02	189	90%	"	*
03	317	98%	7%	*
04	560	98%	9%	*
05	560	"	"	
06	1054	100%	"	*
07	1361	"	1%	*
08	1726	"	"	*
09	2234	"	"	*
10	2356	85%	3%	*
11	2724	100%	1%	*
12	3132	"	3%	*
13	3649	"	1%	*
14	4078	"	"	*
15	4200	"	"	
16	4200	"	"	*
17	4643	"	"	*
18	4643	"	"	
19	5087	"	16%	*
20	5087	"	"	
21	5424		1%	*
22	5948	"	"	*
23	6368	"	"	*
24	6458	"	"	
25	6458	"	"	*
26	7030	"	"	*
27	7382	"	"	*
28	7885	"	"	*
29	8382	"	"	*

<sup>†</sup> Lead Bank

TABLE 3.XVIII  
 Millstone II Cycle 1  
 ROCS Maneuver Structure

Man #	Bu	Power	Rods <sup>†</sup>	Comparisons
00	0	20%	0%	
01	100	50%	"	
02	300	"	"	
03	600	51%	47%	
04	650	"	0%	
05	850	81%	"	
06	985	"	27%	
07	1150	"	47%	
08	1275	88%	0%	
09	1350	100%	"	*
10	1700	94%	26%	
11	2100	100%	0%	*
12	2800	"	"	
13	3350	"	"	*
14	4000	"	"	*
15	4300	75%	"	
16	4700	100%	"	
17	5100	"	"	*
18	5700	"	"	
19	6200	"	"	*
20	6900	"	"	
21	7500	"	"	*
22	7900	"	"	
23	8500	"	6%	
24	9000	"	8%	*
25	9400	"	"	
26	10200		4%	*

<sup>†</sup> Lead Bank

TABLE 3. XVIII  
 Millstone II Cycle 1 (Continued)  
 ROCS Maneuver Structure

Man #	Bu	Power	Rods <sup>†</sup>	Comparisons
27	11000	97%	19%	
28	11300	100%	7%	*
29	12000	"	"	*
30	12600	"	"	
31	13100	93%	9%	*
32	13700	100%	"	
33	14200	"	"	
34	14700	"	"	*
35	15094	"	"	*

<sup>†</sup>Lead Bank



TABLE 3.XIX  
 Millstone II Cycle 2  
 ROCS Maneuver Structure

Man #	Bu	Power	Rods <sup>†</sup>	Comparisons
00	0	50%	10.4%	
01	70	96%	23.5%	
02	200	100%	12.9%	*
03	500	"	7.7%	*
04	1000	"	5.0%	*
05	1500	"	7.1%	*
06	2000	"	"	*
07	2400	"	8.2%	*
08	2800	"	"	*
09	3300	"	8.8%	*
10	3800	"	7.7%	*
11	4300	"	"	*
12	4800	"	"	*
13	5200	96%	7.1%	*
14	5300	100%	"	*
15	5800	"	"	*
16	6300	"	"	*
17	6800	"	6.4%	*
18	7300	"	6.0%	*
19	7800	"	4.3%	*
20	8300	"	5.3%	*
21	8700	99%	5.5%	*
22	9100	96%	6.6%	*
23	9232.3	94%	"	*

<sup>†</sup> Lead Bank

TABLE 3.XX  
Calvert Cliffs Unit 2 Cycle 1  
ROCS Maneuver Structure

Man #	Bu	Power	Rods <sup>†</sup>	Comparisons
00	0	50%	0%	
01	200	80%	"	
02	325	"	"	
03	400	100%	"	
04	650	"	25%	
05	1000	"	0%	
06	1440	"	"	*
07	2473	"	"	
08	3331	0%	"	
09	3331	100%	"	*
10	4088	"	"	
11	4400	"	"	
12	5000	"	"	
13	5631	"	"	*
14	6230	"	"	*
15	6880	"	"	*
16	7435	"	"	*
17	8261	106%		
18	8751	105%	2.5%	*
19	9169	95%	10%	
20	9983	103%	5%	*
21	10205	"	"	*
22	10675	"	"	*
23	11116	97%	"	
24	11979	103%	"	*
25	12369	78%	"	
26	12837	72%	"	*

<sup>†</sup>Lead Bank

TABLE 3.XX  
 Calvert Cliffs Unit 2 Cycle 1 (Continued)  
 ROCS Maneuver Structure

Man #	Bu	Power	Rods <sup>†</sup>	Comparisons
27	12959	105%	5%	
28	12959	72%	"	
29	13283	"	"	
30	13811	"	"	*
31	13811	74%	3.4%	
32	14313	66%	"	
33	15185	90%	"	
34	15525	91%	"	
35	16182	"	"	

<sup>†</sup>Lead Bank

TABLE 3.XXI  
 Calvert Cliffs Unit 2 Cycle 2  
 ROCS Maneuver Structure

Man #	Bu	Power	Rods <sup>†</sup>	Comparisons
00	0	49%	2%	
01	22	"	"	
02	33	80%	0%	
03	200	"	"	
04	200	94%	"	
05	280	"	10%	*
06	280	88%	9%	
07	389	90%	"	*
08	389	89%	8%	
09	495	84%	"	
10	558	97%	9%	*
11	809	"	0%	*
12	809	"	"	
13	1273	"	23%	*
14	1438	98%	0%	*
15	1698	"	8.4%	*
16	1914	"	0%	
17	2095	92%	6.7%	
18	2267	93%	9%	
19	2518	98%	0%	
20	2950	"	"	
21	3141	"	"	
22	3397	92%	13.4%	
23	3519	99%	"	*
24	3943	100%	"	*

<sup>†</sup> Lead Bank

TABLE 3.XXII  
 Fort Calhoun Unit 1 Cycle 4  
 ROCS Maneuver Structure

Man #	Bu	Power	Rods <sup>†</sup>	Comparisons
00	0	100%	0%	
01	200	"	"	*
02	500	"	"	
03	1000	"	"	*
04	2000	"	"	*
05	3000	"	"	*
06	4000	"	"	*
07	5000	"	"	*
08	6000	"	"	*
09	7000	"	"	*
10	8000	"	"	
11	8200	100%	0%	*

<sup>†</sup>All rods out.

TABLE 3.XXIII  
 Fort Calhoun Unit 1 Cycle 5  
 ROCS Maneuver Structure

Man #	Bu	Power	Rods <sup>+</sup>	Comparisons
00	0	100%	0%	
01	300	"	"	*
02	1000	"	"	*
03	2000	"	"	*
04	3000	"	"	*
05	4000	"	"	*
06	5000	"	"	*
07	6000	"	"	*
08	7000	"	"	
09	8000	"	"	
10	9000	"	"	
11	10000	100%	0%	

+All rods out

TABLE 3.XXIVa  
 Calvert Cliffs Unit 1 Cycle 1  
 Standard Deviation of Difference Between Calculation and Measurement  
 And Results of Bartlett Tests for Data Pooling

Burnup	$S_{F_{xy}} (N(L))$								$S_{F_q}$	$N_{DET}$	$S_{F_r}$	$N_S$
	Level 1	N(1)	Level 2	N(2)	Level 3	N(3)	Level 4	N(4)				
850	[ ]	45	[ ]	45	[ ]	44	[ ]	45	[ ]	179	[ ]	44
3K		44		"		"		"		178		43
4K		"		"		"		"		178		"
5K		"		"		"		"		178		"
6K		"		"		"		"		178		"
7K		"		"		"		"		178		"
8K		"		"		"		"		178		"
9K		"		"		"		"		178		"
10K		"		"		"		"		177		42
11K		"		"		"		"		177		"
12K		"		"		"		"		177		"
13K		"		"		"		"		177		"
14K		"		"		"		"		175		40
15K		43		"		"		"		175		"
16K		"		44		"		"		174		"

1.3.52

Overall

	$S_D$	$N_{DFG}$
$F_{xy}$	[ ]	2597
$F_q$		2597
$F_r$		618

+Worst Value

TABLE 3. XXIVb  
 Calvert Cliffs Unit 1 Cycle 1  
 Results of Data Pooling and Bartlett Tests

<u>F<sub>xy</sub> Pooled Level Results*</u>				<u>Pooled Time Point Results**</u>			
Burnup	S <sub>Fxy</sub>	F(3,∞) Calc	N <sub>DEG</sub>		S <sub>D</sub>	F(14,∞) Calc	N <sub>DEG</sub>
850	[		175	F <sub>xy</sub> ††	[		2597
3000			174	F <sub>q</sub> ††			2597
4000			174	F <sub>r</sub> ††			618
5000			174				
6000			174				
7000			174				
8000			174				
9000			174				
10000†			173				
11000			173				
12000			173				
13000			173				
14000			172				
15000†			171				
16000†			170				

\* For level pooling, F(3,∞) < 2.60 in order to pass at the 5% significance level.

† Levels fail to pool

\*\* For time point pooling, F(14,∞) < 1.69 in order to pass at the 5% significance level.

†† Time points fail to pool.

+ Worst Value

1.3.53



TABLE 3.XXVa  
 Calvert Cliffs Unit 1 Cycle 2  
 Standard Deviation of Difference Between Calculation and Measurement  
 And Results of Bartlett Tests for Data Pooling

Burnup	$S_{Fxy} (N(L))$								$S_{Fq}$	$N_{DET}$	$S_{Fr}$	$N_S$						
	Level 1	N(1)	Level 2	N(2)	Level 3	N(3)	Level 4	N(4)										
234	[ ]	38	[ ]	36	[ ]	38	[ ]	38	[ ]	150	[ ]	36						
332		"		"		"		"		"		"	"	"	150	"		
989		"		"		"		"		"		"	"	"	150	"		
1436		"		"		"		"		"		"	"	"	150	"		
1747		"		"		"		"		"		"	"	"	150	"		
2087		"		"		"		"		"		"	"	"	150	"		
2717		"		"		"		"		"		"	37	"	149	35		
3338		"		"		35		"		"		"	36	"	147	33		
3969		"		"		34		"		"		"	"	"	146	32		
4184		"		"		"		"		"		"	"	"	146	"		
5057		"		"		"		"		"		"	"	"	146	"		
6006		"		"		"		"		"		"	35	"	145	31		
6446		"		"		"		"		"		"	"	"	145	"		
6924		"		"		"		"		"		"	"	"	145	"		
7334		"		"		33		"		37		"	"	"	143	29		
7555		"		"		"		"		"		"	"	"	143	"		
8258		"		"		"		"		"		"	"	"	143	"		
										Overall								
						$S_D$				$N_{DEG}$								
$F_{xy}$			[ ]		2431													
$F_q$					2431													
$F_r$					543													

TABLE 3. XXVb  
 Calvert Cliffs Unit 1 Cycle 2  
 Results of Data Pooling and Bartlett Tests

F<sub>xy</sub> Pooled Level Results\*

Burnup	S <sub>Fxy</sub>	F(3,∞) Calc	N <sub>DEG</sub>
234	[		146
332			146
989			146
1436			146
1747			146
2087			146
2717			145
3338			143
3969			142
4184			142
5057			142
6006			141
6446			141
6924			141
7334			139
7555			139
8258	139		

Pooled Time Point Results\*\*

	S <sub>D</sub>	F(16,∞) Calc	N <sub>DEG</sub>
F <sub>xy</sub>	[		2431
F <sub>q</sub>			2431
F <sub>r</sub>			543

\* For level pooling, F(3,∞) < 2.60 in order to pass at the 5% significance level.

\*\* For time point pooling, F(16,∞) < 1.62 in order to pass at the 5% significance level.

1.3.55

TABLE 3.XXVIa

Calvert Cliffs Unit 1 Cycle 3

Standard Deviation of Difference Between Calculation and Measurement  
And Results of Bartlett Tests for Data Pooling

Burnup	$S_{Fxy} (N(L))$								$S_{Fq}$	$N_{DET}$	$S_{Fr}$	$N_S$
	Level 1	N(1)	Level 2	N(2)	Level 3	N(3)	Level 4	N(4)				
495		37		39		37		40		153		34
1202		"		"		"		"		153		"
1611		"		"		"		"		153		"
2021		"		38		"		39		151		33
3011		"		"		"		"		151		"
3811		36		"		36		"		149		32
4626		"		"		"		38		148		31
5434		"		"		"		"		148		"
5849		"		"		"		"		148		"
6442		35		"		"		"		147		"
6658		"		"		"		37		146		30
6658		"		"		"		"		146		"
6869		"		"		35		"		145		29
7147		"		"		"		"		145		"
7327		"		"		"		"		145		"
7554		"		"		34		"		144		"
7738		"		"		"		"		144		"
7964		"		"		"		"		144		"
8149		"		"		"		"		144		"
8578		"		"		"		"		144		"
8822		"		"		"		"		144		"
9042		"		"		"		"		144		"
9440		"		"		"		"		144		"

Overall

$F_{xy}$	$S_D$	$N_{DEG}$	
$F_{q}$			3288
$F_r$			3288
		681	

I.3.56

TABLE 3.XXVIb  
 Calvert Cliffs Unit 1 Cycle 3  
 Results of Data Pooling and Bartlett Tests

<u>F<sub>xy</sub> Pooled Level Results*</u>				<u>Pooled Time Point Results**</u>			
Burnup	S <sub>Fxy</sub>	F(3,∞) Calc	N <sub>DEG</sub>		S <sub>D</sub>	F(22,∞) Calc	N <sub>DEG</sub>
495	[	]	149	F <sub>xy</sub>	[	]	3288
1202			149	F <sub>q</sub>			3288
1611			149	F <sub>r</sub>			687
2021			147				
3011			147				
3811			145				
4626			144				
5434			144				
5849			144				
6442			143				
6658			142				
6658			142				
6869			141				
7147			141				
7327			141				
7554			140				
7738			140				
7964			140				
8149			140				
8578			140				
8822	140						
9042	140						
9440	140						

\* For level pooling, F(3,∞) < 2.60 in order to pass at the 5% significance level.

\*\* For time point pooling, F(22,∞) < 1.53 in order to pass at the 5% significance level.

1.3.57

TABLE 3.XXVIIa

St. Lucie Unit 1 Cycle 1

Standard Deviation of Difference Between Calculation and Measurement  
and Results of Bartlett Tests for Data Pooling

Burnup	$S_{Fxy} (N(L))$								$S_{Fq}$	$N_{DET}$	$S_{Fr}$	$N_S$			
	Level 1	N(1)	Level 2	N(2)	Level 3	N(3)	Level 4	N(4)							
888	[ ]	44	[ ]	45	[ ]	44	[ ]	43	[ ]	176	[ ]	41			
2139		"		"		"		"		"		"	"	176	"
2982		"		"		"		"		"		"	"	176	"
3420		"		"		"		"		"		"	"	176	"
4903		"		"		"		"		"		"	"	176	"
5513		"		"		"		"		"		"	"	176	"
6029		"		"		"		"		"		"	"	176	"
6489		"		"		"		"		"		"	"	176	"
7093		"		"		"		"		"		"	"	176	"
8976		"		"		"		"		45		"	"	177	42
9910		"		43		"		44		"		"	"	175	40
11359		"		42		"		"		"		"	"	174	39
12414		"		"		"		"		"		"	"	174	"

1.3.58

Overall

	$S_D$	$N_{DEG}$
$F_{xy}$	[ ]	2232
$F_{q}$		2232
$F_r$		516

+Worst value

TABLE 3.XXVIIb  
 St. Lucie Unit 1 Cycle 1  
 Results of Data Pooling and Bartlett Tests

<u>F<sub>xy</sub> Pooled Level Results*</u>				<u>Pooled Time Point Results**</u>			
Burnup	S <sub>Fxy</sub>	F(3,∞) Calc	N <sub>DEG</sub>		S <sub>D</sub>	F(12,∞) Calc	N <sub>DEG</sub>
888	[	]	172	F <sub>xy</sub> ††	[	]	2232
2139			172	F <sub>q</sub> ††			2232
2982			172	F <sub>r</sub>			516
3420			172				
4903			172				
5513			172				
6029			172				
6489			172				
7093			172				
8976			173				
9910			171				
11359			170				
12414			170				

\* For level pooling, F(3,∞) < 2.60 in order to pass at the 5% significance level.

\*\* For time point pooling, F(12,∞) < 1.75 in order to pass at the 5% significance level.

†† Time points fail to pool.

+ Worst Value

TABLE 3.XXVIIIa

St. Lucie Unit 1 Cycle 2

Standard Deviation of Difference Between Calculation and Measurement  
and Results of Bartlett Tests for Data Pooling

$S_{F_{xy}} (N(L))$

1.3.60

Burnup	Level 1	N(1)	Level 2	N(2)	Level 3	N(3)	Level 4	N(4)	$S_{F_q}$	$N_{DET}$	$S_{F_r}$	$N_S$					
189	[ ]	42	[ ]	44	[ ]	43	[ ]	43	[ ]	172	[ ]	40					
317		"		"		"		"		"		"	"	"	173	"	41
560		"		"		"		"		"		"	"	"	173	"	"
1054		"		"		"		"		"		"	"	"	173	"	"
1361		"		"		"		"		"		"	"	"	173	"	"
1726		"		"		"		"		"		"	"	"	173	"	"
2234		"		"		"		"		"		"	"	"	173	"	"
2724		"		"		"		"		"		43	"	42	171	"	39
3132		"		"		"		"		"		"	"	"	171	"	"
3649		"		"		"		"		"		"	"	"	171	"	"
4078		"		"		"		"		"		"	"	"	171	"	"
4200		"		"		"		"		"		"	"	"	171	"	"
4643		"		"		"		"		"		"	"	"	171	"	"
5087		"		"		"		"		"		"	"	"	171	"	"
5424		"		"		"		"		"		"	"	"	171	"	"
5948		"		"		"		"		"		"	"	"	171	"	"
6368		"		"		"		"		"		"	"	"	171	"	"
7030		"		"		"		"		"		44	"	41	171	"	"
7382	"	"	"	"	"	"	"	"	171	"	"						
7885	"	"	"	"	"	"	"	"	171	"	"						
8370	"	"	"	"	"	"	"	"	171	"	"						

Overall

	$S_D$	$N_{DEG}$
$F_{xy}$	[ ]	3520
$F_q$		3520
$F_r$		811

TABLE 3. XXVIIIb  
 St. Lucie Unit 1 Cycle 2  
 Results of Data Pooling and Bartlett Tests

<u>F<sub>-xy</sub> Pooled Level Results*</u>				<u>Pooled Time Point Results**</u>				
Burnup	S <sub>Fxy</sub>	F(3,∞) Calc	N <sub>DEG</sub>		S <sub>D</sub>	F(20,∞) Calc	N <sub>DEG</sub>	
189	[		168	F <sub>xy</sub>	[		3520	
317			169					F <sub>q</sub>
560			169					
1054			169					
1361			169					
1726			169					
2234			169					
2724			167					
3132			167					
3649			167					
4078			167					
4200			167					
4643			167					
5087			167					
5424			167					
5948			167					
6368			167					
7030			167					
7382			167					
7885			167					
8370	167							

1.3.61

\* For level pooling, F(3,∞) < 2.60 in order to pass at the 5% significance level.

\*\* For time point pooling, F(20,∞) < 1.57 in order to pass at the 5% significance level.



TABLE 3. XXIXa  
 Millstone Unit 2 Cycle 1  
 Standard Deviation of Difference Between Calculation and Measurement  
 and Results of Bartlett Tests for Data Pooling

Burnup	$S_{F_{xy}} (N(L))$								$S_{F_q}$	$N_{DET}$	$S_{F_r}$	$N_S$
	Level 1	N(1)	Level 2	N(2)	Level 3	N(3)	Level 4	N(4)				
1350	[ ]	43	[ ]	44	[ ]	45	[ ]	45	[ ]	177	[ ]	42
2100		"		43		"		"		176		"
3350		"		"		"		"		176		"
4000		"		"		"		44		175		41
5100		"		"		"		"		175		"
6200		"		"		"		"		175		"
7500		42		"		"		"		174		40
9000		"		"		"		"		174		"
10200		40		42		"		"		171		38
11300		"		"		"		"		171		"
12000		"		"		"		"		171		"
13100		"		"		"		"		171		"
14700		"		"		"		"		171		"
15094		"		"		"		"		171		"

Overall

	$S_D$	$N_{DEG}$
$F_{xy}$	[ ]	2372
$F_q$		2372
$F_r$		543
+Worst Value		

1.3.62

TABLE 3. XXIXb  
 Millstone Unit 2 Cycle 1  
 Results of Data Pooling and Bartlett Tests

<u>F<sub>xy</sub> Pooled Level Results*</u>				<u>Pooled Time Point Results**</u>				
Burnup	S <sub>Fxy</sub>	F(3,∞) Calc	N <sub>DEG</sub>		S <sub>D</sub>	F(13,∞) Calc	N <sub>DEG</sub>	
1350	[		173	F <sub>xy</sub> ††	[		2372	
2100			171	F <sub>q</sub> ††				2372
3350			171	F <sub>r</sub> ††				
4000			171					
5100			171					
6200			171					
7500			170					
9000			170					
10200			167					
11300			167					
12000			167					
13100†			167					
14700			167					
15094	167							

\* For level pooling, F(3,∞) < 2.60 in order to pass at the 5% significance level.

† Levels fail to pool

\*\* For time point pooling, F(13,∞) < 1.70 in order to pass at the 5% significance level.

†† Time points fail to pool.

+ Worst Value

1.3.63

TABLE 3.XXXa

Millstone Unit 2 Cycle 2

Standard Deviation of Difference Between Calculation and Measurement  
And Results of Bartlett Tests for Data Pooling

$S_{Fxy} (N(L))$

Burnup	Level 1	N(1)	Level 2	N(2)	Level 3	N(3)	Level 4	N(4)	$S_{Fq}$	$N_{DET}$	$S_{Fr}$	$N_S$	
200	[ ]	39	[ ]	41	[ ]	37	[ ]	45	[ ]	162	[ ]	30	
500		"		"		36		"		161		"	
1000		"		"		"		"		44		"	29
1500		"		"		"		"		"		"	"
2000		"		"		"		"		35		"	28
2400		"		"		"		"		"		"	"
2800		40		40		36		"		160		"	29
3300		"		"		"		"		160		"	"
3800		"		"		"		"		160		"	"
4300		"		"		"		"		160		"	"
4800		"		"		"		"		160		"	"
5300		39		"		"		"		159		"	28
5800		"		"		"		"		159		"	"
6300		"		"		"		"		159		"	"
6800		"		"		"		"		43		158	"
7300		"		"		"		35		"		157	27
7800		"		"		"		"		"		157	"
8300		"		"		"		"		"		157	"
8700		"		"		"		"		"		157	"
9100		"		"		"		"		"		157	"
9232	"	"	"	"	"	157	"						

Overall

	$S_D$	$N_{DEG}$
$F_{xy}$	[ ]	898
$F_q$		3254
$F_r$		571

I.3.64

TABLE 3. XXXb  
 Millstone Unit 2 Cycle 2  
 Results of Data Pooling and Bartlett Tests

<u>F<sub>xy</sub> Pooled Level Results*†</u>				<u>Pooled Time Point Results**</u>							
Burnup	S <sub>Fxy</sub>	F(3,∞) Calc	N <sub>DEG</sub>		S <sub>D</sub>	F(20,∞) Calc	N <sub>DEG</sub>				
200	[	]	158	]	[	]	]				
500			157					F All values Level 4 values only	]	]	]
1000			156								
1500			156					F <sub>r</sub>	]	]	]
2000			155								
2400			155					]	]	]	]
2800			156								
3300			156					]	]	]	]
3800			156								
4300			156					]	]	]	]
4800			156								
5300			155					]	]	]	]
5800			155								
6300			153					]	]	]	]
6800			153								
7300			153					]	]	]	]
7800			153								
8300			153					]	]	]	]
8700			153								
9100			153					]	]	]	]
9232	153										

\* For level pooling, F(3,∞) < 2.60 in order to pass at the 5% significance level.

† Levels fail to pool at all time points

\*\* For time point pooling, F(20,∞) < 1.57 in order to pass at the 5% significance level.

+ Worst value

TABLE 3.XXXIa

Calvert Cliffs Unit 2 Cycle 1

Standard Deviation of Difference Between Calculation and Measurement  
and Results of Bartlett Tests for Data Pooling

Burnup	$S_{F_{xy}} (N(L))$								$S_{F_q}$	$N_{DET}$	$S_{F_r}$	$N_S$
	Level 1	N(1)	Level 2	N(2)	Level 3	N(3)	Level 4	N(4)				
1440	[ ]	45	[ ]	44	[ ]	44	[ ]	45	[ ]	178	[ ]	43
3330	[ ]	44	[ ]	"	[ ]	"	[ ]	"	[ ]	177	[ ]	42
5630	[ ]	"	[ ]	42	[ ]	42	[ ]	43	[ ]	171	[ ]	37
6230	[ ]	"	[ ]	"	[ ]	"	[ ]	"	[ ]	171	[ ]	"
6880	[ ]	"	[ ]	"	[ ]	"	[ ]	"	[ ]	171	[ ]	"
7435	[ ]	"	[ ]	"	[ ]	"	[ ]	"	[ ]	171	[ ]	"
8750	[ ]	"	[ ]	"	[ ]	"	[ ]	"	[ ]	171	[ ]	"
9980	[ ]	"	[ ]	"	[ ]	41	[ ]	"	[ ]	170	[ ]	36
10675	[ ]	"	[ ]	"	[ ]	"	[ ]	42	[ ]	169	[ ]	"
11980	[ ]	"	[ ]	"	[ ]	"	[ ]	41	[ ]	168	[ ]	34
12840	[ ]	"	[ ]	41	[ ]	"	[ ]	"	[ ]	167	[ ]	33
13810	[ ]	"	[ ]	40	[ ]	"	[ ]	40	[ ]	165	[ ]	32

Overall

	$S_D$	$N_{DEG}$
$F_{xy}$	[ ]	2001
$F_q$	[ ]	2001
$F_r$	[ ]	429

+Worst value

TABLE 3.XXXIb  
 Calvert Cliffs Unit 2 Cycle 1  
 Results of Data Pooling and Bartlett Tests

Burnup	<u>F<sub>xy</sub> Pooled Level Results*</u>			<u>Pooled Time Point Results**</u>					
	S <sub>Fxy</sub>	F(3,∞) Calc	N <sub>DEG</sub>	S <sub>D</sub>	F(11,∞) Calc	N <sub>DEG</sub>			
1440	[		174	[		2001			
3330†			173				F <sub>xy</sub> ††		
5630			167					F <sub>q</sub> ††	
6230			167						F <sub>r</sub> ††
6880			167						
7435			167						
8750			167						
9980			166						
10675†			165						
11980†			164						
12840			163						
13810†			161						

\* For level pooling, F(3,∞) < 2.60 in order to pass at the 5% significance level.

† Levels fail to pool

\*\* For time point pooling, F(11,∞) < 1.79 in order to pass at the 5% significance level.

†† Time points fail to pool.

I.3.67

TABLE 3. XXXIIa

Calvert Cliffs Unit 2 Cycle 2

Standard Deviation of Difference Between Calculation and Measurement  
and Results of Bartlett Tests for Data Pooling

$S_{F_{xy}} (N(L))$

Burnup	Level 1	N(1)	Level 2	N(2)	Level 3	N(3)	Level 4	N(4)	$S_{F_q}$	$N_{DET}$	$S_{F_r}$	$N_S$				
200	[ ]	42	[ ]	41	[ ]	41	[ ]	41	[ ]	165	[ ]	39				
280		"		"		41		"				40	"	38		
389		"		"		"		"				42	"	40		
495		"		41		"		"				41	"	40	163	37
909		"		"		"		"				"	"	"	163	"
1275		"		"		"		"				"	"	"	163	"
1438		"		"		"		"				"	"	"	163	"
1698		"		"		"		"				40	"	"	162	36
1914		"		"		"		"				"	"	"	162	"
2095		"		"		"		"				"	"	"	162	"
2518		"		"		"		"				"	"	"	162	"
3141		"		"		"		"				"	"	"	162	"
3519		"		"		"		"				"	"	"	162	"
3943	"	"	"	"	"	"	"	162	"							

Overall

	$S_D$	$N_{DEG}$
$F_{xy}$	[ ]	2225
$F_q$		2225
$F_r$		503

TABLE 3.XXXIIb  
 Calvert Cliffs Unit 2 Cycle 2  
 Results of Data Pooling and Bartlett Tests

Burnup	<u>Pooled Level Results*</u>			<u>Pooled Time Point Results**</u>				
	$S_{F_{xy}}$	$F(3, \infty)$ Calc	$N_{DEG}$		$S_D$	$F(13, \infty)$ Calc	$N_{DEG}$	
200	[	]	161	$F_{xy}$	[	]	2225	
280			160				$F_q$	2225
389			160					$F_r$
495			159					
809			159					
1273			159					
1438			159					
1698			158					
1914			158					
2095			158					
2518			158					
3141			158					
3519			158					
3943	158							

\* For level pooling,  $F(3, \infty) < 2.60$  in order to pass at the 5% significance level.

\*\* For time point pooling,  $F(13, \infty) < 1.70$  in order to pass at the 5% significance level.

I.3.69



TABLE 3.XXXIIIa

Fort Calhoun Unit 1 Cycle 4

Standard Deviation of Difference between Calculation and Measurement  
and Results of Bartlett Tests for Data Pooling

Burnup	$S_{F_{xy}} (N(L))$								$S_{F_q}$	$N_{DET}$	$S_{F_r}$	$N_S$
	Level 1	N(1)	Level 2	N(2)	Level 3	N(3)	Level 4	N(4)				
200	[ ]	23	[ ]	23	[ ]	23	[ ]	22	[ ]	91	[ ]	19
1000	[ ]	21	[ ]	22	[ ]	23	[ ]	20	[ ]	86	[ ]	13
2000	[ ]	22	[ ]	20	[ ]	22	[ ]	21	[ ]	85	[ ]	12
3000	[ ]	22	[ ]	20	[ ]	24	[ ]	19	[ ]	85	[ ]	10
4000	[ ]	22	[ ]	22	[ ]	22	[ ]	19	[ ]	85	[ ]	12
5000	[ ]	22	[ ]	22	[ ]	22	[ ]	19	[ ]	85	[ ]	11
6000	[ ]	22	[ ]	22	[ ]	22	[ ]	19	[ ]	85	[ ]	12
7000	[ ]	22	[ ]	22	[ ]	22	[ ]	19	[ ]	85	[ ]	12
8200	[ ]	22	[ ]	22	[ ]	21	[ ]	20	[ ]	85	[ ]	11

Overall

	$S_D$	$N_{DEG}$
$F_{xy}$	[ ]	736
$F_q$	[ ]	736
$F_r$	[ ]	103

1.3.70

TABLE 3.XXXIIIb  
Fort Calhoun Unit 1 Cycle 4  
Results of Data Pooling and Bartlett Tests

Burnup	<u>Pooled Level Results*</u>			<u>Pooled Time Point Results**</u>		
	$S_{F_{xy}}$	$F_{calc}(3, \infty)$	$N_{DEG}$	$S_D$	$F_{calc}(8, \infty)$	$N_{DEG}$
200	[	]	87	[	]	736
1000			82			736
2000			81			103
3000			81			
4000			81			
5000			81			
6000			81			
7000			81			
8200			81			

\* For level pooling,  $F(3, \infty) < 2.60$  in order to pass at the 5% significance level.

\*\* For time point pooling,  $F(8, \infty) < 1.94$  in order to pass at the 5% significance level.

TABLE 3.XXXIVa

Fort Calhoun Unit 1 Cycle 5

Standard Deviation of Difference Between Calculation and Measurement  
and Results of Bartlett Tests for Data Pooling

$S_{Fxy} (N(L))$

Burnup	Level 1	N(1)	Level 2	N(2)	Level 3	N(3)	Level 4	N(4)	$S_{Fq}$	$N_{DET}$	$S_{Fr}$	$N_S$
300	[ ]	22	[ ]	23	[ ]	22	[ ]	20	[ ]	87	[ ]	17
1000	[ ]	23	[ ]	23	[ ]	22	[ ]	20	[ ]	88	[ ]	18
2000	[ ]	23	[ ]	23	[ ]	22	[ ]	20	[ ]	88	[ ]	18
3000	[ ]	22	[ ]	23	[ ]	22	[ ]	20	[ ]	87	[ ]	17
4000	[ ]	22	[ ]	23	[ ]	22	[ ]	20	[ ]	87	[ ]	18
5000	[ ]	23	[ ]	23	[ ]	22	[ ]	20	[ ]	88	[ ]	18
6000	[ ]	23	[ ]	23	[ ]	22	[ ]	20	[ ]	88	[ ]	18

Overall

	$S_D$	$N_{DEG}$
$F_{xy}$	[ ]	585
$F_q$	[ ]	585
$F_r$	[ ]	117

TABLE 3.XXXIVb  
 Fort Calhoun Unit 1 Cycle 5  
 Results of Data Pooling and Bartlett Tests

Burnup	<u>F<sub>xy</sub> Pooled Level Results*</u>			<u>Pooled Time Point Results**</u>		
	S <sub>Fxy</sub>	F <sub>calc</sub> (3,∞)	N <sub>DEG</sub>	S <sub>D</sub>	F <sub>calc</sub> (6,∞)	N <sub>DEG</sub>
300	[	]	83	F <sub>xy</sub> [	]	585
1000			84			585
2000			84			117
3000			83			
4000			83			
5000			84			
6000			84			

\* For level pooling, F(3,∞) < 2.60 in order to pass at the 5% significance level.

\*\* For time point pooling, F(6,∞) < 2.10 in order to pass at the 5% significance level.

TABLE 3. XXXV

Summary of Standard Deviations of  
Comparisons Between Calculations and Measurement

Reactor	$S_{Fxy}$	$N_{DEG}$	$S_{Fq}$	$N_{DEG}$	$S_{Fr}$	$N_{DEG}$
Calvert Cliffs Unit 1 Cycle 1	[	2597	[	2597	[	618
Calvert Cliffs Unit 1 Cycle 2		2431		2431		543
Calvert Cliffs Unit 1 Cycle 3		3288		3288		681
St. Lucie Unit 1 Cycle 1		2232		2232		516
St. Lucie Unit 1 Cycle 2		3520		3520		811
Millstone Unit 2 Cycle 1		2372		2372		543
Millstone Unit 2 Cycle 2		898		3254		571
Calvert Cliffs Unit 2 Cycle 1		2001		2001		429
Calvert Cliffs Unit 2 Cycle 2		2225		2225		503
Fort Calhoun Unit 1 Cycle 4		736		736		103
Fort Calhoun Unit 1 Cycle 5		585		585		117

+Worst Value

TABLE 3.XXXVI  
Results of Data Pooling and Bartlett Tests

All Cycles†				
	$S_D$	$F(10, \infty)$ calc	$F(10, \infty)$ Theoretical, $\alpha=5\%$	$N_{DEG}$
$F_{xy}$	[	]	1.8	22,885†
$F_q$			1.8	25,241†
$F_r$			1.8	5,435†
First Cycles†				
	$S_D$	$F(3, \infty)$ calc	$F(3, \infty)$ Theoretical, $\alpha=5\%$	$N_{DEG}$
$F_{xy}$	[	]	2.6	9202†
$F_q$			2.6	9292†
$F_r$			2.6	9106†
Later Cycles†				
	$S_D$	$F(6, \infty)$ calc	$F(6, \infty)$ Theoretical, $\alpha=5\%$	$N_{DEG}$
$F_{xy}$	[	]	2.1	13,683†
$F_q$			2.1	16,039†
$F_r$			2.1	3,329†

† Fail to pool

TABLE 3.XXXVII

Calvert Cliffs Unit 1 Cycle 3

D' Normality Test on  $F_q$

Burriup	$N_{DET}$	$S_{F_q}$	D'	$\alpha(\%)$
495	153			
1202	153			
1611	153			
2021	151			
3011	151			
3811	149			
4626	148			
5434	148			
5849	148			
6442	147			
6656	146			
6658	146			
6869	145			
7147	145			
7327	145			
7554	144			
7738	144			
7964	144			
8149	144			
8578	144			
8822	144			
9042	144			
9440	144			

Total Sample Size = 3380

TABLE 3.XXXVIII

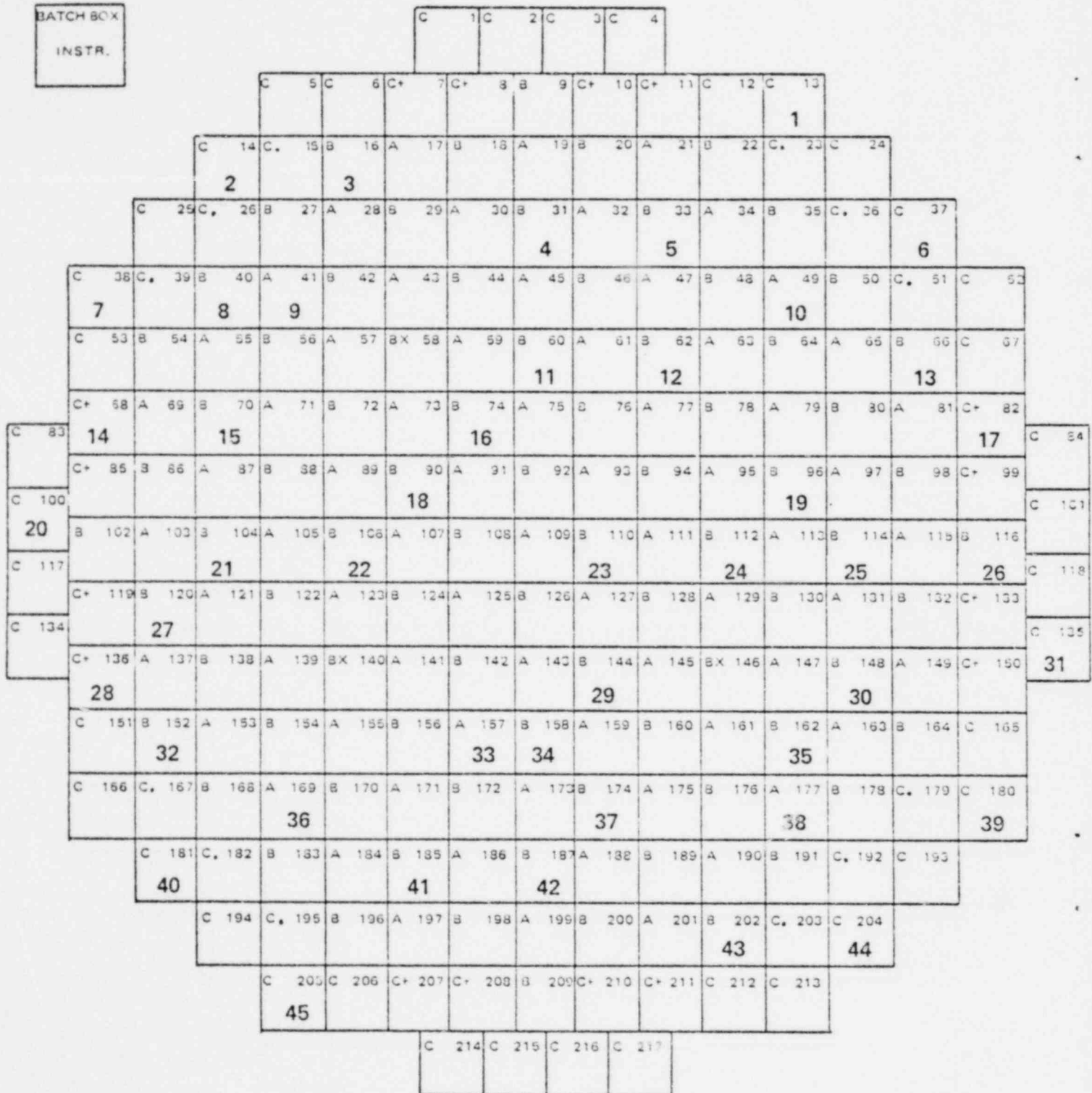
Calvert Cliffs Unit 1 Cycle 3

W Normality Test on  $F_r$

Burnup	$N_S$	$S_{Fr}$	W	P(%)
495	34			
1202	34			
1611	34			
2021	33			
3011	33			
3811	32			
4626	31			
5434	31			
5849	31			
6442	31			
6658	30			
6658	30			
6869	29			
7147	29			
7327	29			
7554	29			
7738	29			
7964	29			
8149	29			
8578	29			
8822	29			
9042	29			
9440	29			

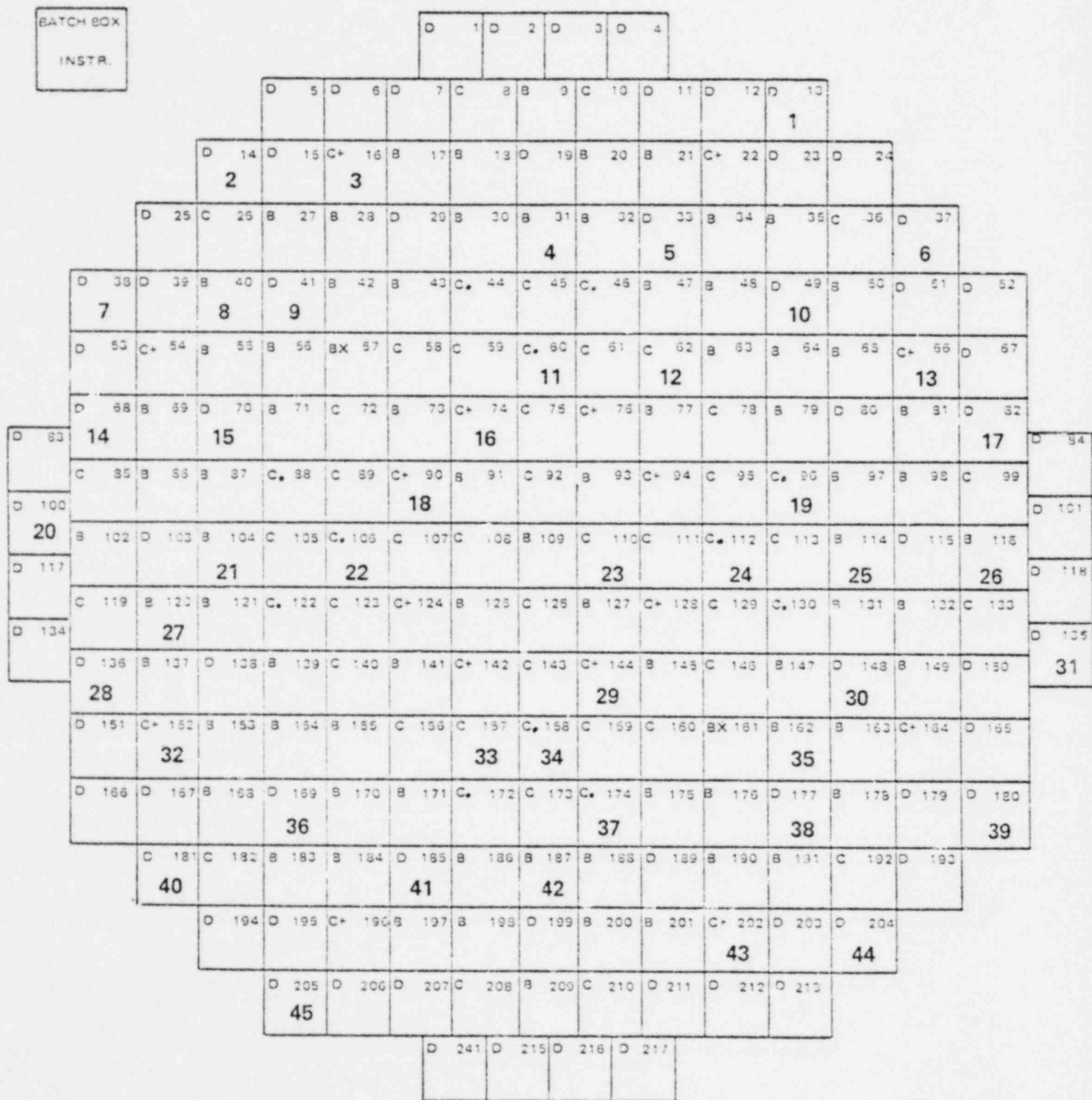


**FIGURE 3-1  
LOADING & INSTRUMENT PATTERN  
CALVERT CLIFFS UNIT I CYCLE 1**



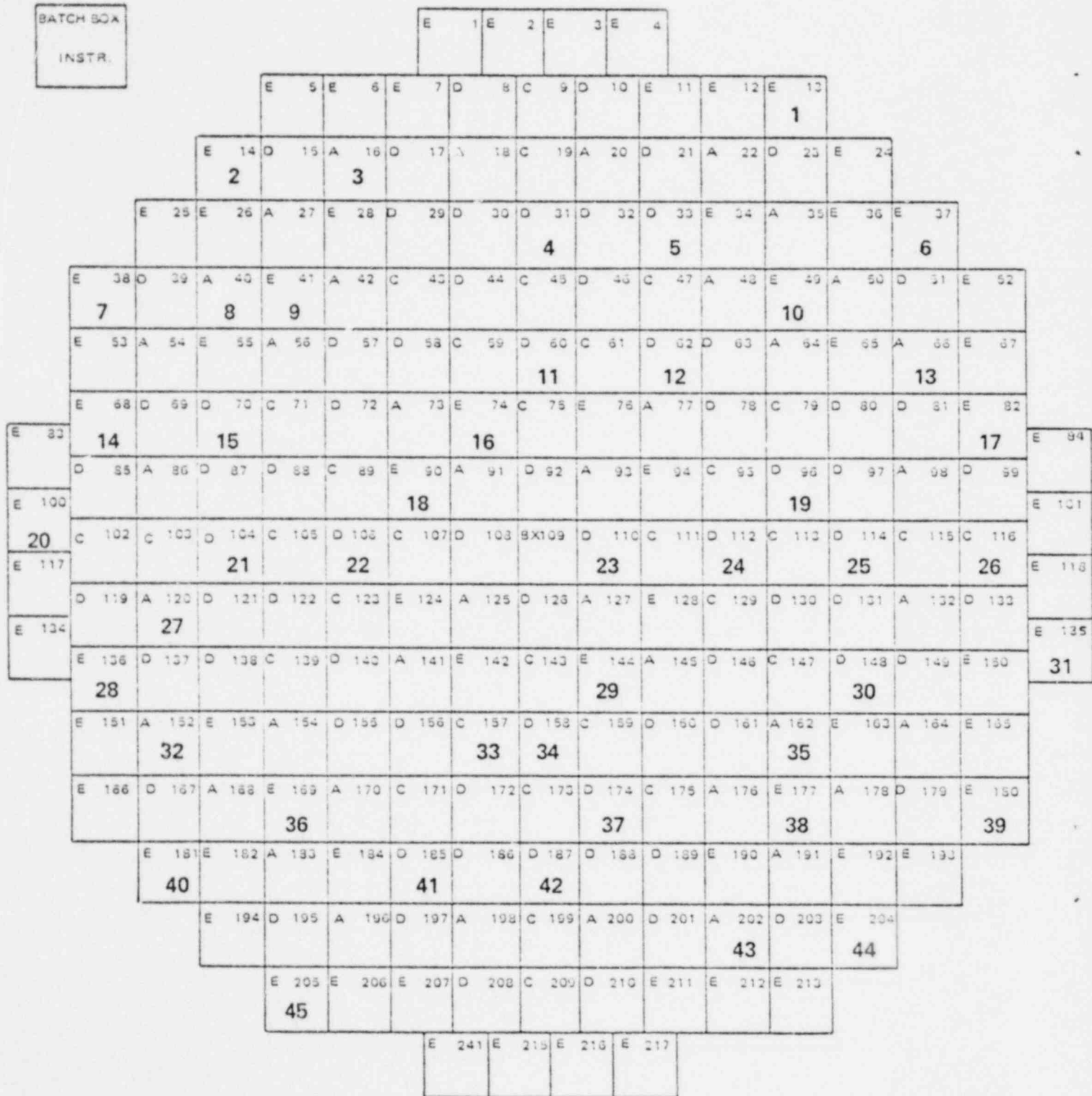
\* BX INDICATES TEST ASSEMBLY

FIGURE 3-2  
LOADING & INSTRUMENT PATTERN  
CALVERT CLIFFS UNIT I CYCLE 2



\* BX INDICATES TEST ASSEMBLY

**FIGURE 3-3  
LOADING & INSTRUMENT PATTERN  
CALVERT CLIFFS UNIT 1 CYCLE 3**



• BX INDICATES TEST ASSEMBLY

**FIGURE 3-4  
LOADING & INSTRUMENT PATTERN  
ST. LUCIE CYCLE 1**

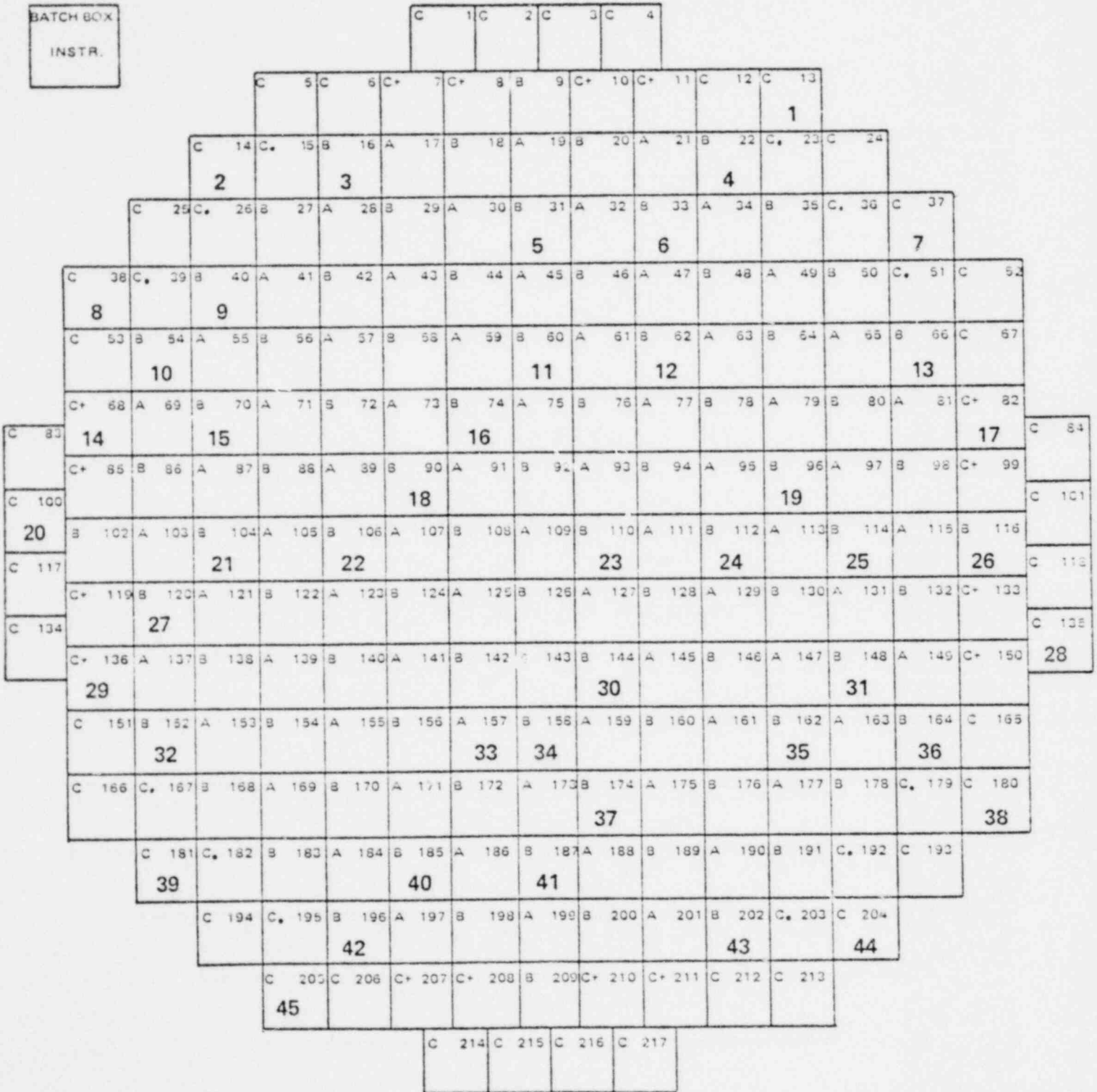


**FIGURE 3-5  
LOADING & INSTRUMENT PATTERN  
ST. LUCIE CYCLE 2**

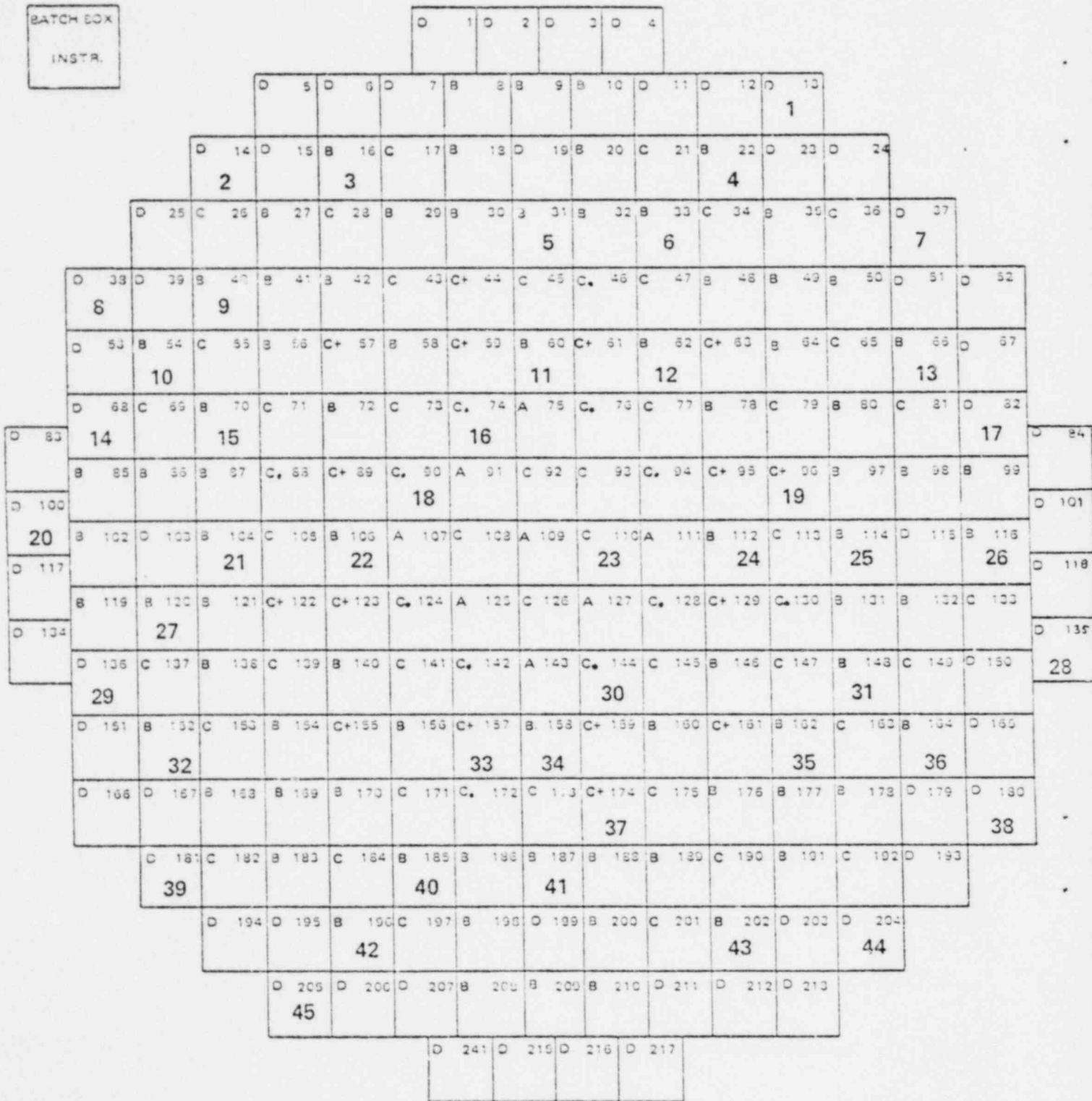
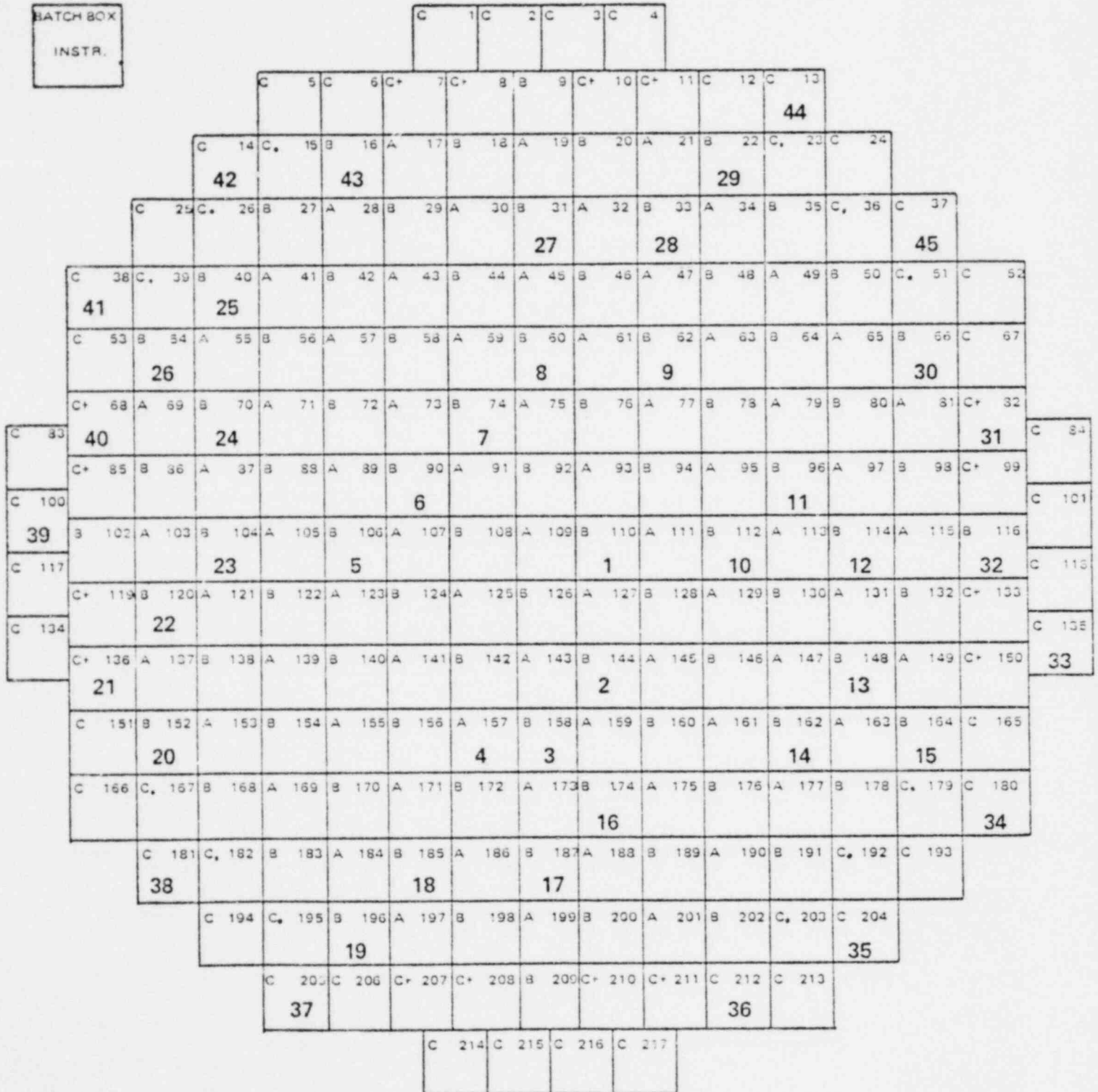


FIGURE 3-6  
LOADING & INSTRUMENT PATTERN  
MILLSTONE II CYCLE 1





**FIGURE 3-7**  
**LOADING & INSTRUMENT PATTERN**  
**MILLSTONE II CYCLE 2**

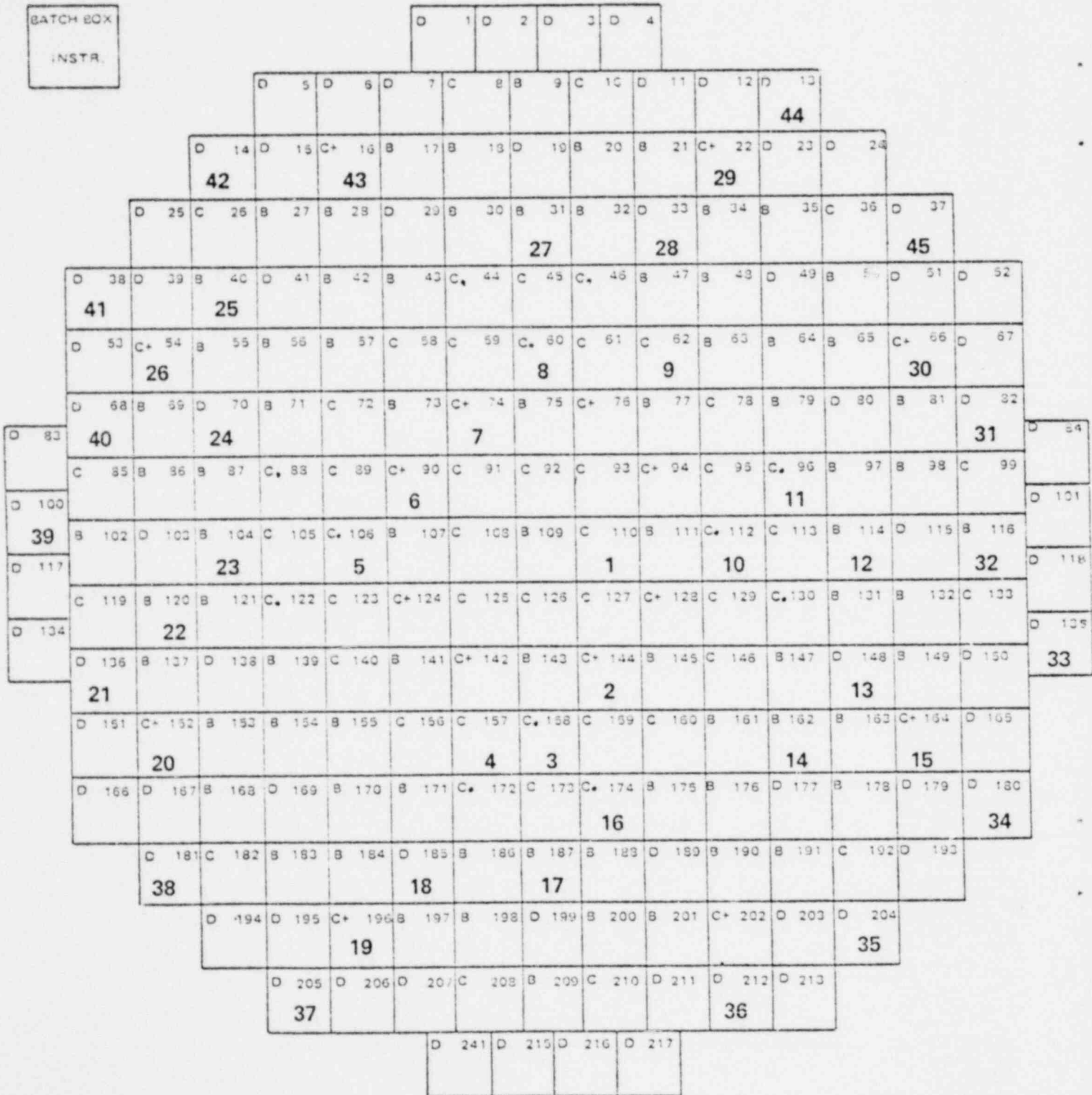


FIGURE 3-8  
LOADING & INSTRUMENT PATTERN  
CALVERT CLIFFS UNIT 2 CYCLE 1

TCH BOX  
INSTA.

C	1 C	2 C	3 C	4														
C	5 C	6 C+	7 C+	8 B	9 C+	10 C+	11 C	12 C	13									
C	14 C.	15 B	16 A	17 B	18 A	19 B	20 A	21 B	22 C.	23 C	24	1						
2		3								6								
C	25 C.	26 B	27 A	28 B	29 A	30 B	31 A	32 B	33 A	34 B	35 C.	36 C	37	5				
				4						6								
C	38 C.	39 B	40 A	41 B	42 A	43 B	44 A	45 B	46 A	47 B	48 A	49 B	50 C.	51 C	52	10		
7		8		9							10		13					
C	53 B	54 A	55 B	56 A	57 B	58 A	59 B	60 A	61 B	62 A	63 B	64 A	65 B	66 C	67	11		
							11						12		13			
C+	68 A	69 B	70 A	71 B	72 A	73 B	74 A	75 B	76 A	77 B	78 A	79 B	80 A	81 C+	82	14		
14		15			16									17				
C+	85 B	86 A	87 B	88 A	89 B	90 A	91 B	92 A	93 B	94 A	95 B	96 A	97 B	98 C+	99	18		
				18									19					
B	102 A	103 B	104 A	105 B	106 A	107 B	108 A	109 B	110 A	111 B	112 A	113 B	114 A	115 C	116	20		
				21							23		24		25		26	
C+	119 B	120 A	121 B	122 A	123 B	124 A	125 B	126 A	127 B	128 A	129 B	130 A	131 B	132 C+	133	117		
		27									29		30				31	
C+	136 A	137 B	138 A	139 B	140 A	141 B	142 A	143 B	144 A	145 B	146 A	147 B	148 A	149 C+	150	134		
28							33		34		35							
C	151 B	152 A	153 B	154 A	155 B	156 A	157 B	158 A	159 B	160 A	161 B	162 A	163 B	164 C	165			
32							33		34		35							
C	166 C.	167 B	168 A	169 B	170 A	171 B	172 A	173 B	174 A	175 B	176 A	177 B	178 C.	179 C	180			
		36									37		38				39	
C	181 C.	182 B	183 A	184 B	185 A	186 B	187 A	188 B	189 A	190 B	191 C.	192 C	193					
40		41					42											
C	194 C.	195 B	196 A	197 B	198 A	199 B	200 A	201 B	202 C.	203 C	204							
		43			44													
C	205 C	206 C+	207 B	208 C+	209 B	209	C+ 210	C+ 211	C 212	C 213								
45																		
				C 214				C 215		C 216		C 217						



**FIGURE 3-9  
LOADING & INSTRUMENT PATTERN  
CALVERT CLIFFS UNIT 2 CYCLE 2**

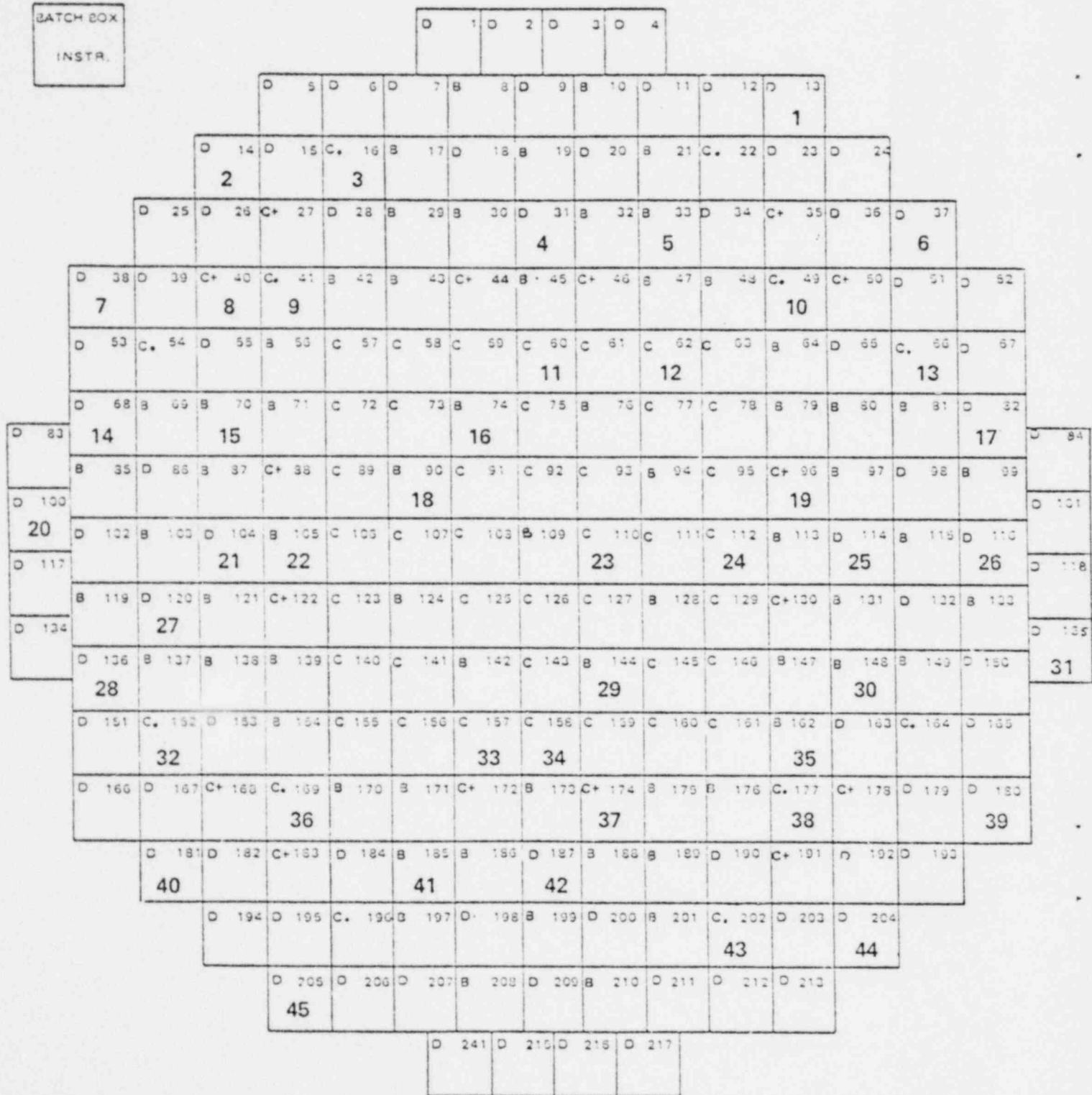


Figure 3-10  
LOADING & INSTRUMENT PATTERN  
FORT CALHOUN UNIT 1 CYCLE 4

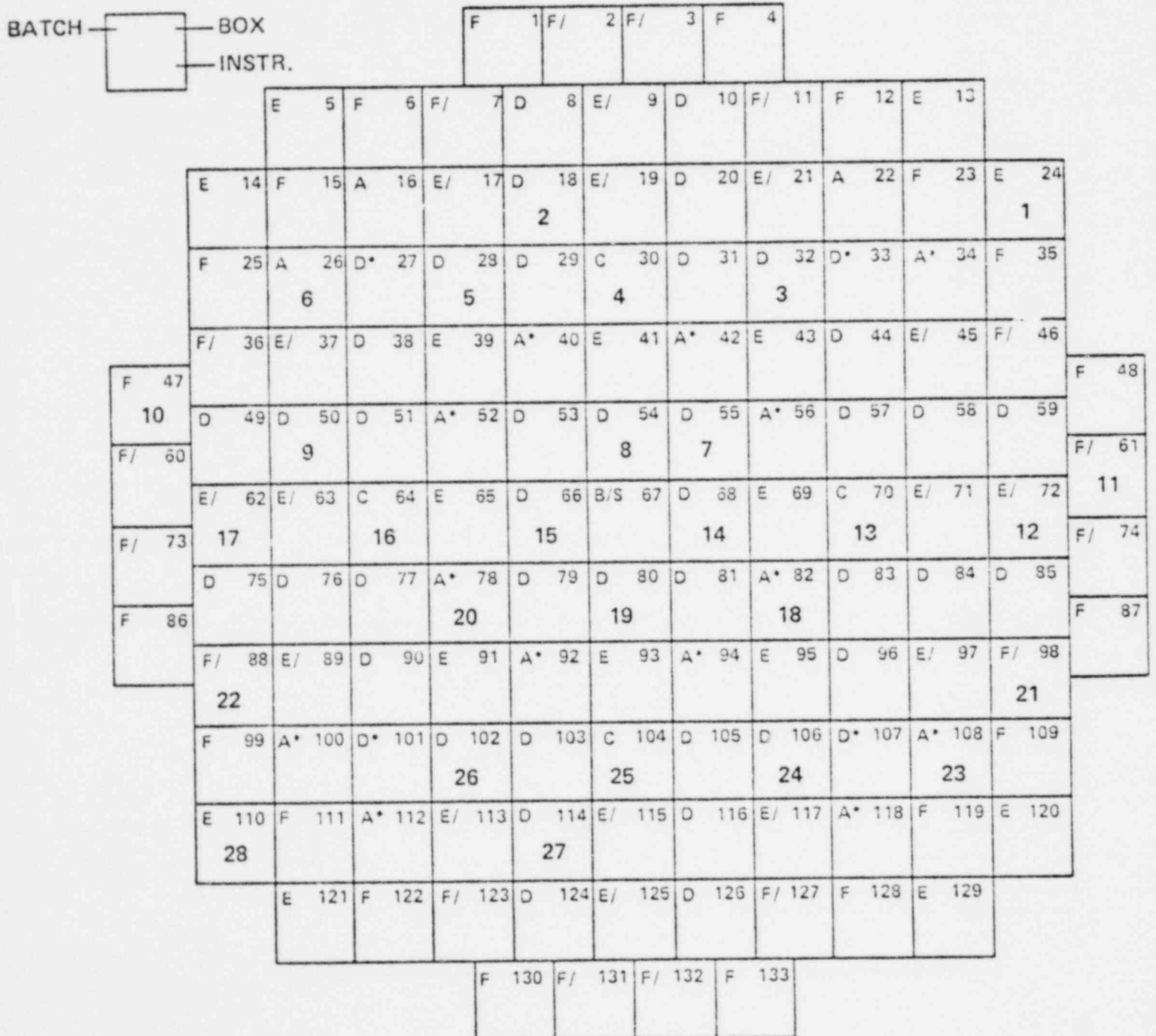


Figure 3-11  
LOADING & INSTRUMENT PATTERN  
FORT CALHOUN UNIT 1 CYCLE 5

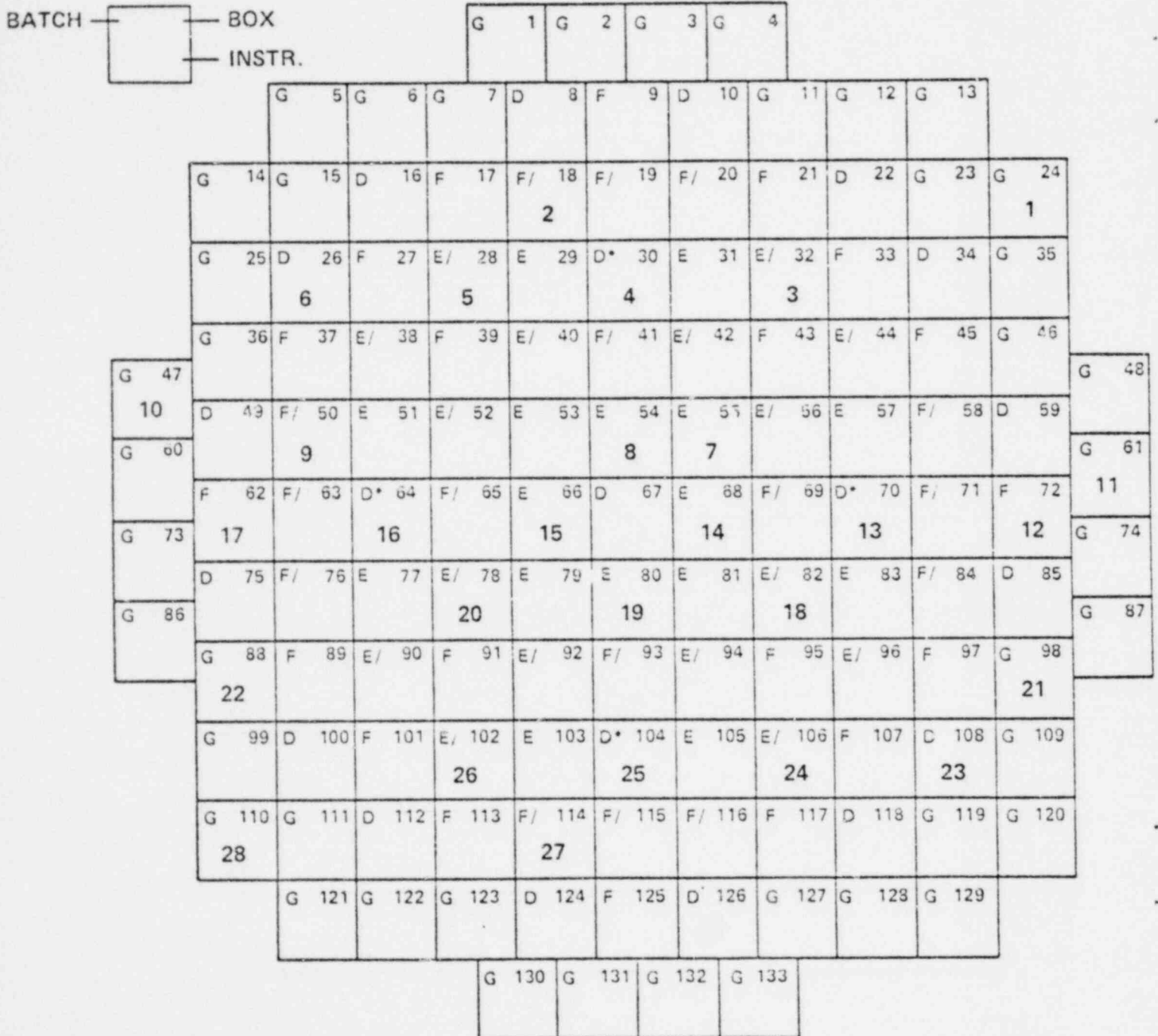
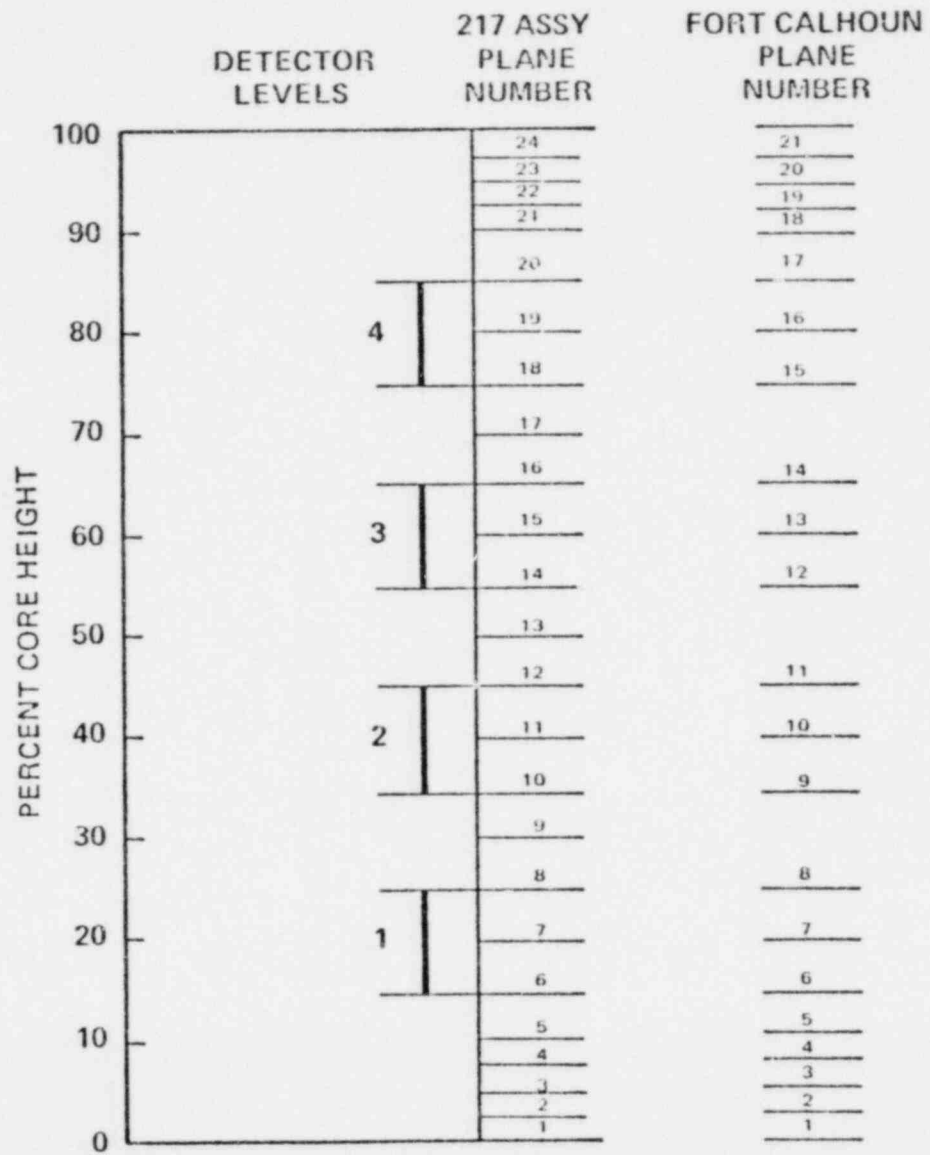


Figure 3-12  
ROCS AXIAL MESH STRUCTURE



1.3.89

FIGURE 3-13a

COMPARISONS OF MEASURED AND CALCULATED POWERS  
CALVERT CLIFFS UNIT 1 CYCLE 1 AT 850 MWD/T  
LEVEL 1

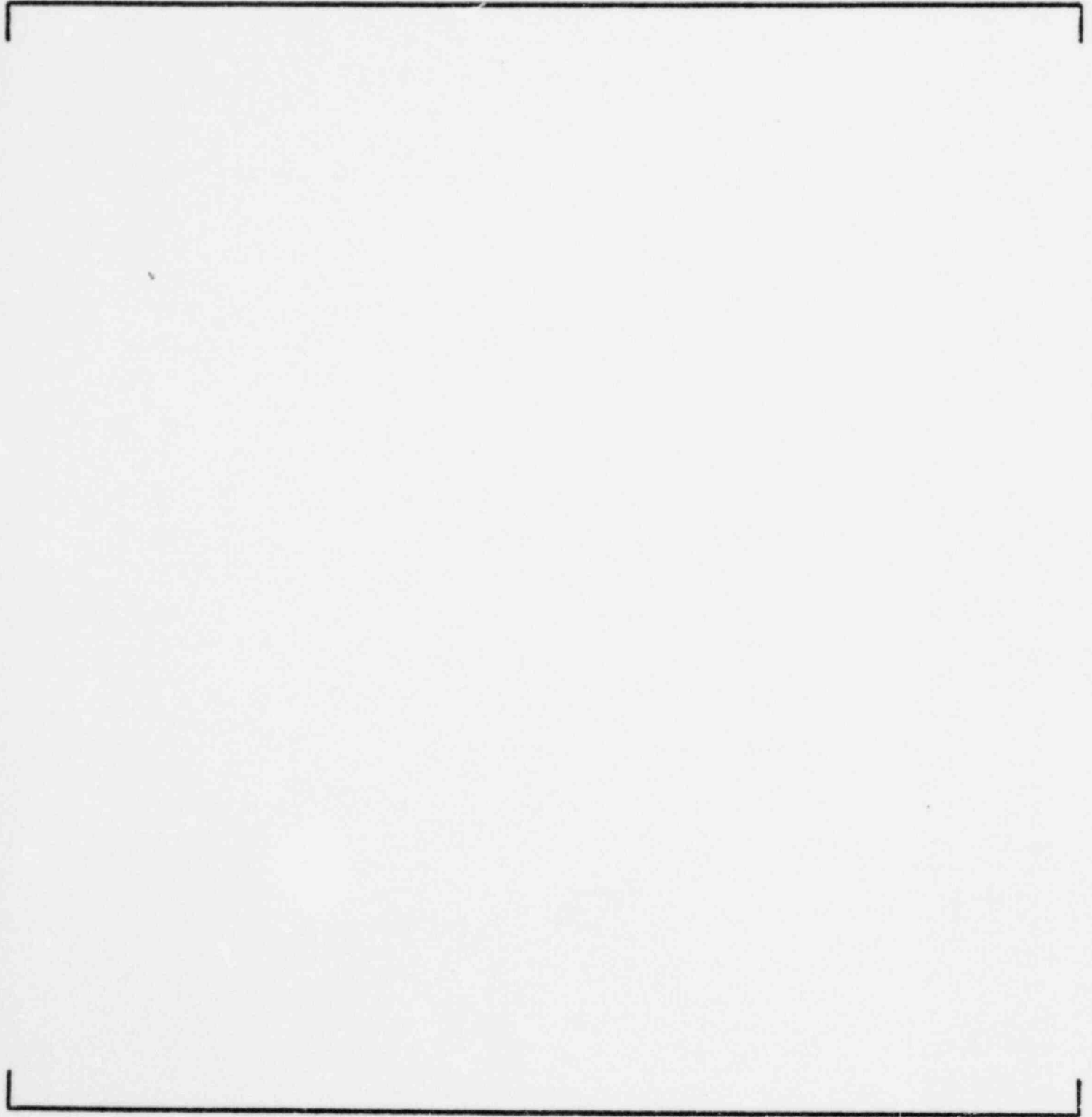


FIGURE 3-13b

COMPARISON OF MEASURED AND CALCULATED POWERS  
CALVERT CLIFFS UNIT 1 CYCLE 1 AT 850 MWD/T  
LEVEL 2

FIGURE 3-13c

COMPARISON OF MEASURED AND CALCULATED POWERS  
CALVERT CLIFFS UNIT 1 CYCLE 1 AT 850 MWD/T  
LEVEL 3

FIGURE 3-13d

COMPARISON OF MEASURED AND CALCULATED POWERS  
CALVERT CLIFFS UNIT 1 CYCLE 1 AT 850 MWD/T  
LEVEL 4



FIGURE 3-13e

COMPARISON OF MEASURED AND CALCULATED POWERS  
CALVERT CLIFFS UNIT 1 CYCLE 1 AT 850 MWD/T  
SUMMED LEVELS

FIGURE 3-14a

COMPARISON OF MEASURED AND CALCULATED POWERS  
CALVERT CLIFFS UNIT 1 CYCLE 2 AT 989 MWD/T  
LEVEL 1

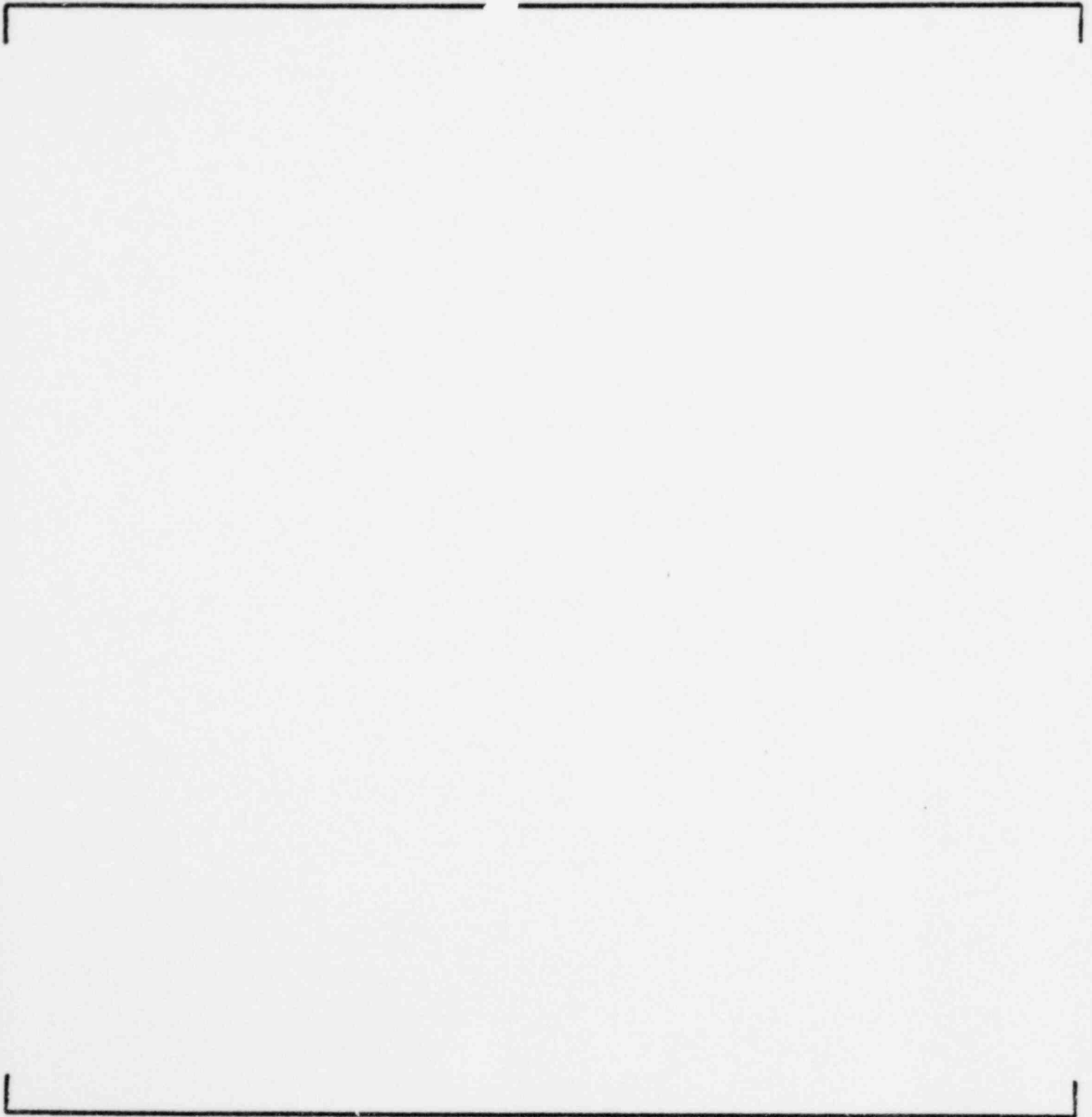


FIGURE 3-14b

COMPARISON OF MEASURED AND CALCULATED POWERS  
CALVERT CLIFFS UNIT 1 CYCLE 2 AT 989 MWD/T  
LEVEL 2

FIGURE 3-14c

COMPARISON OF MEASURED AND CALCULATED POWERS  
CALVERT CLIFFS UNIT 1 CYCLE 2 AT 989 MWD/T  
LEVEL 3

FIGURE 3-14d

COMPARISON OF MEASURED AND CALCULATED POWERS  
CALVERT CLIFFS UNIT 1 CYCLE 2 AT 989 MWD/T  
LEVEL 4

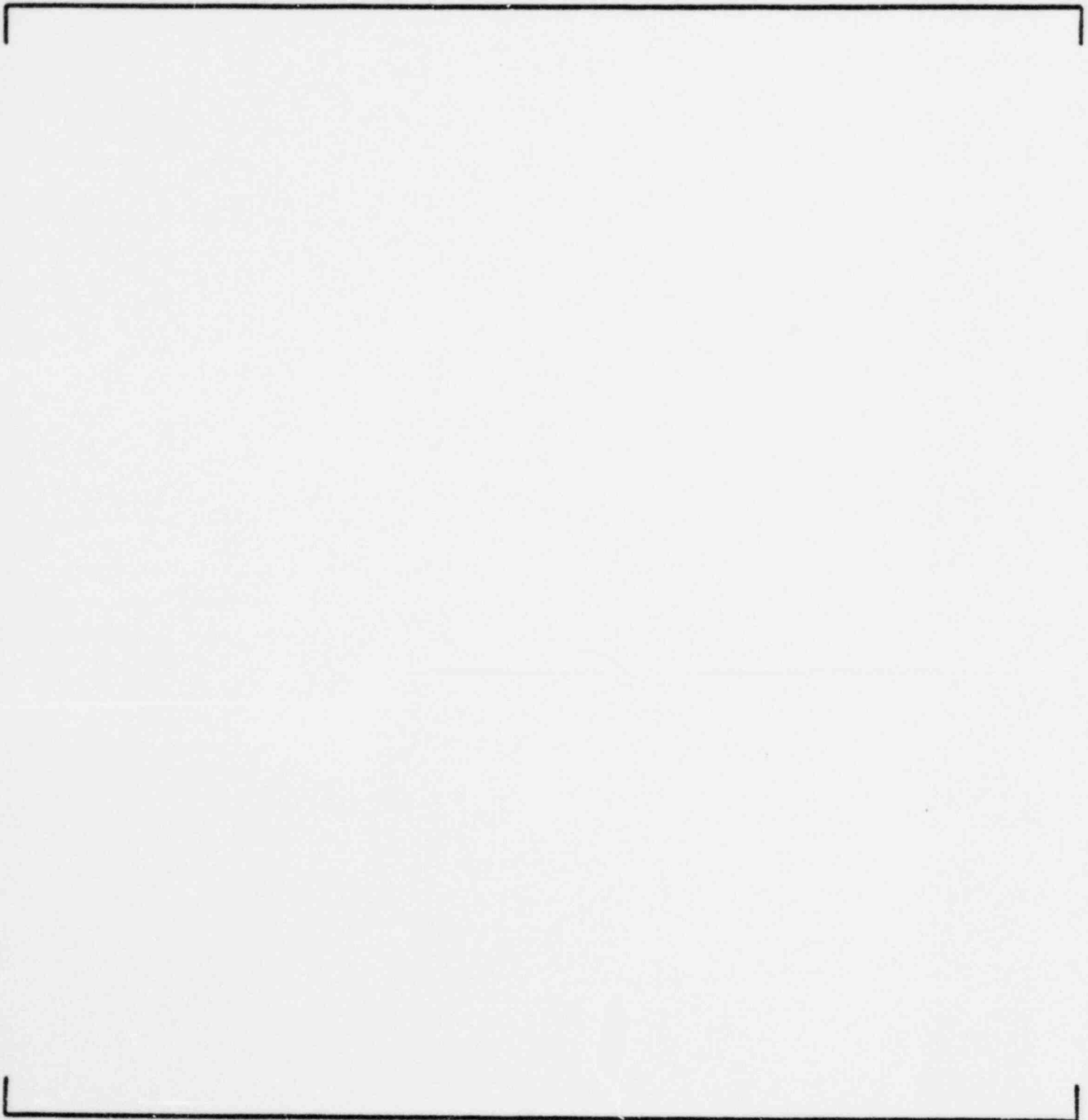


FIGURE 3-14e

COMPARISON OF MEASURED AND CALCULATED POWERS  
CALVERT CLIFFS UNIT 1 CYCLE 2 AT 989 MWD/T  
SUMMED LEVELS

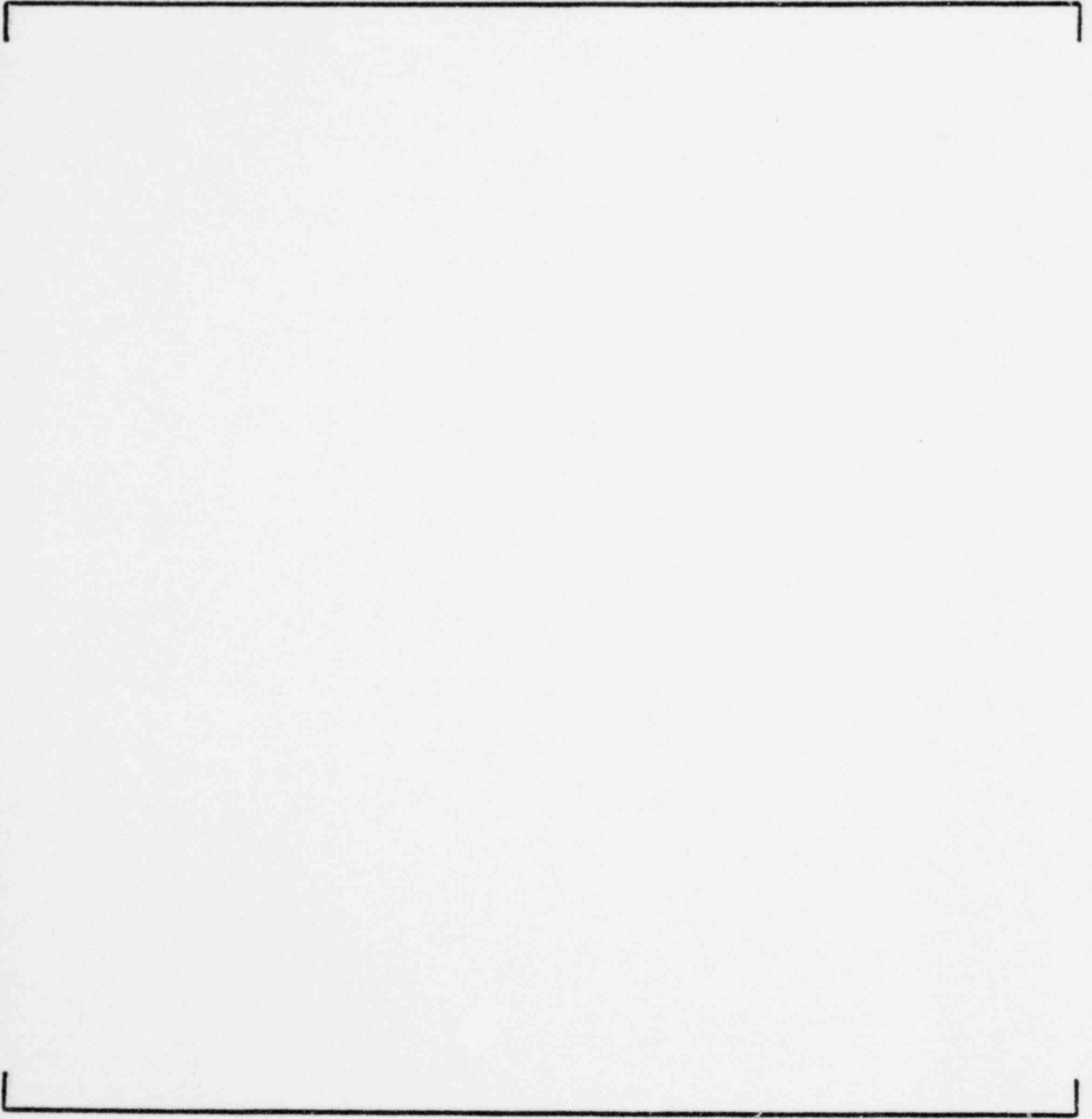


FIGURE 3-15a

COMPARISON OF MEASURED AND CALCULATED POWERS  
CALVERT CLIFFS UNIT 1 CYCLE 3 at 1202 MWD/T  
LEVEL: 1

FIGURE 3-15b

COMPARISON OF MEASURED AND CALCULATED POWERS  
CALVERT CLIFFS UNIT 1 CYCLE 3 at 1202 MWD/T  
LEVEL 2



FIGURE 3-15c

COMPARISON OF MEASURED AND CALCULATED POWERS  
CALVERT CLIFFS UNIT 1 CYCLE 3 AT 1202 MWD/T

LEVEL 3

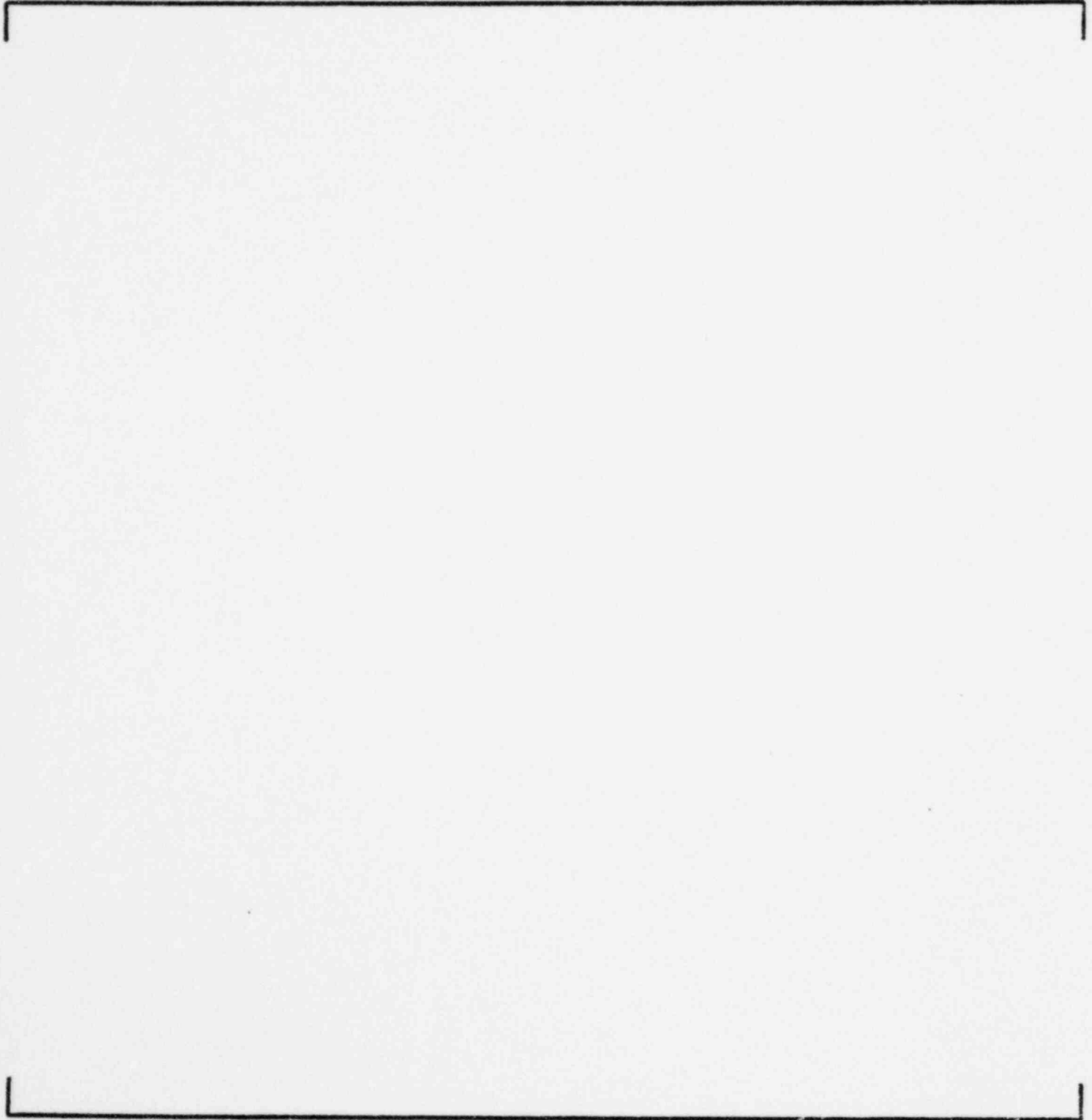


FIGURE 3-15d

COMPARISON OF MEASURED AND CALCULATED POWERS  
CALVERT CLIFFS UNIT 1 CYCLE 3 AT 1202 MWD/T

LEVEL 4

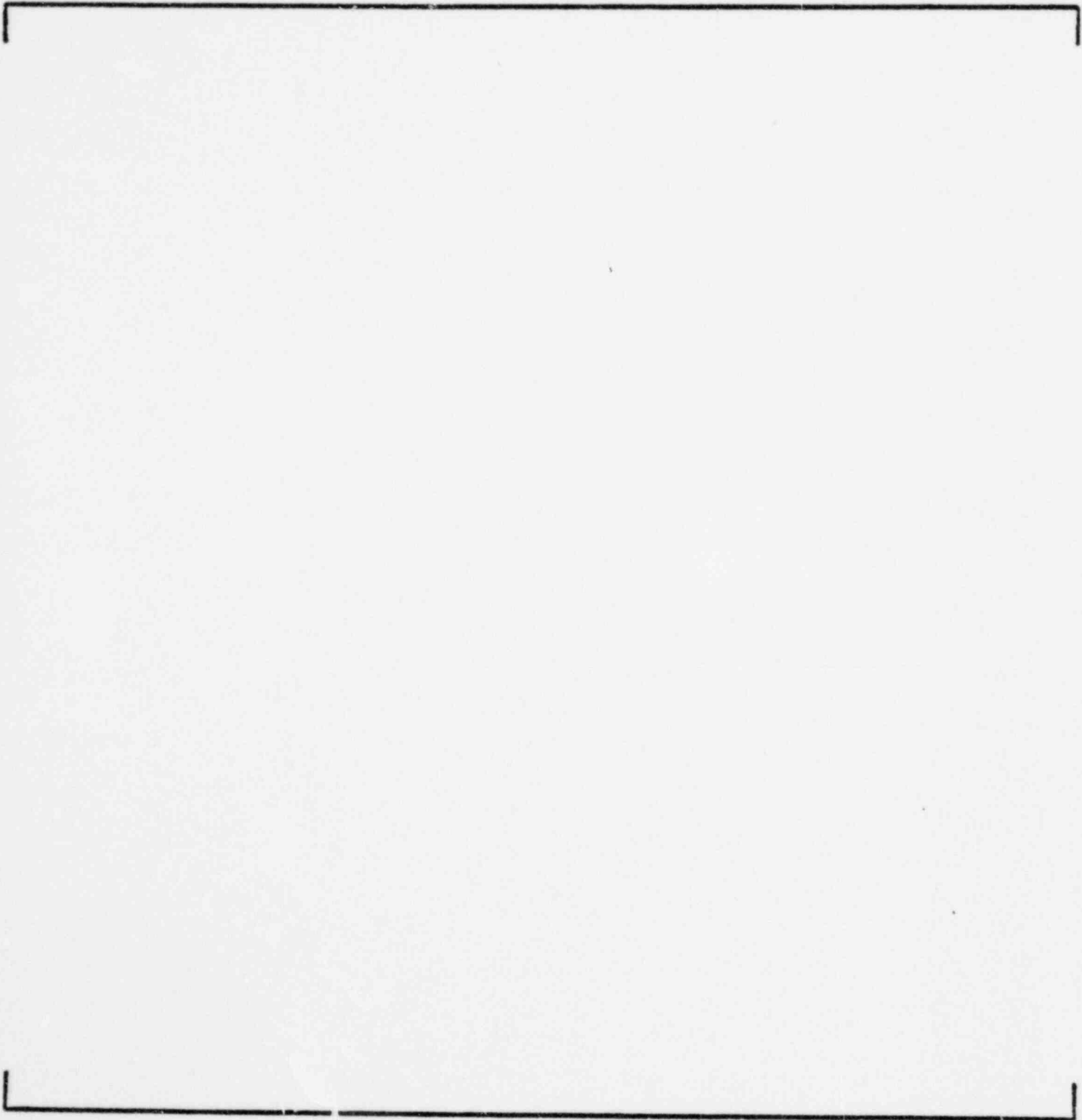


FIGURE 3-15e

COMPARISON OF MEASURED AND CALCULATED POWERS  
CALVERT CLIFFS UNIT 1 CYCLE 3 AT 1202 MWD/T  
SUMMED LEVELS

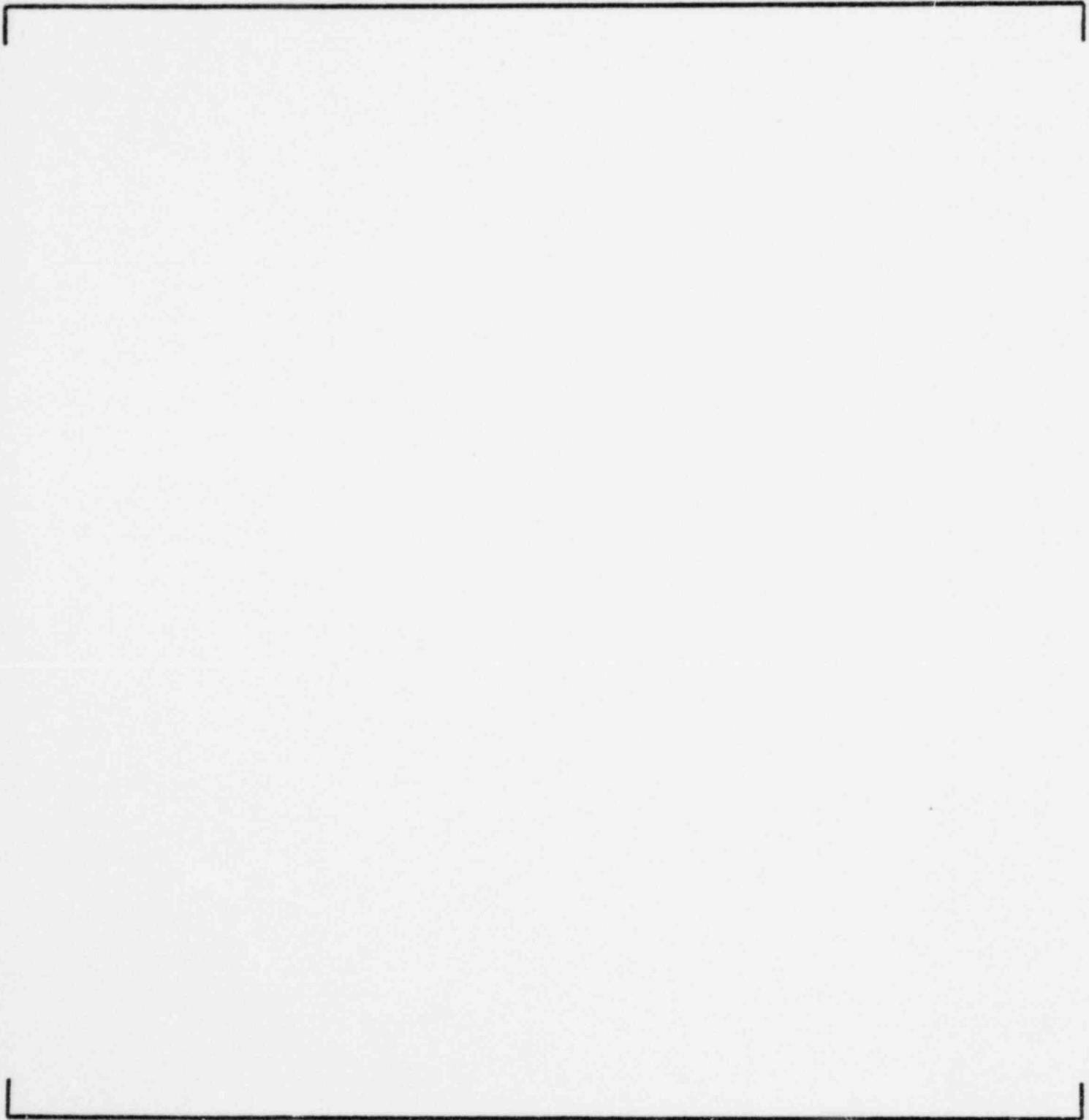


FIGURE 3-16a

COMPARISON OF MEASURED AND CALCULATED POWERS  
ST. LUCIE CYCLE 1 AT 888 MWD/T  
LEVEL 1

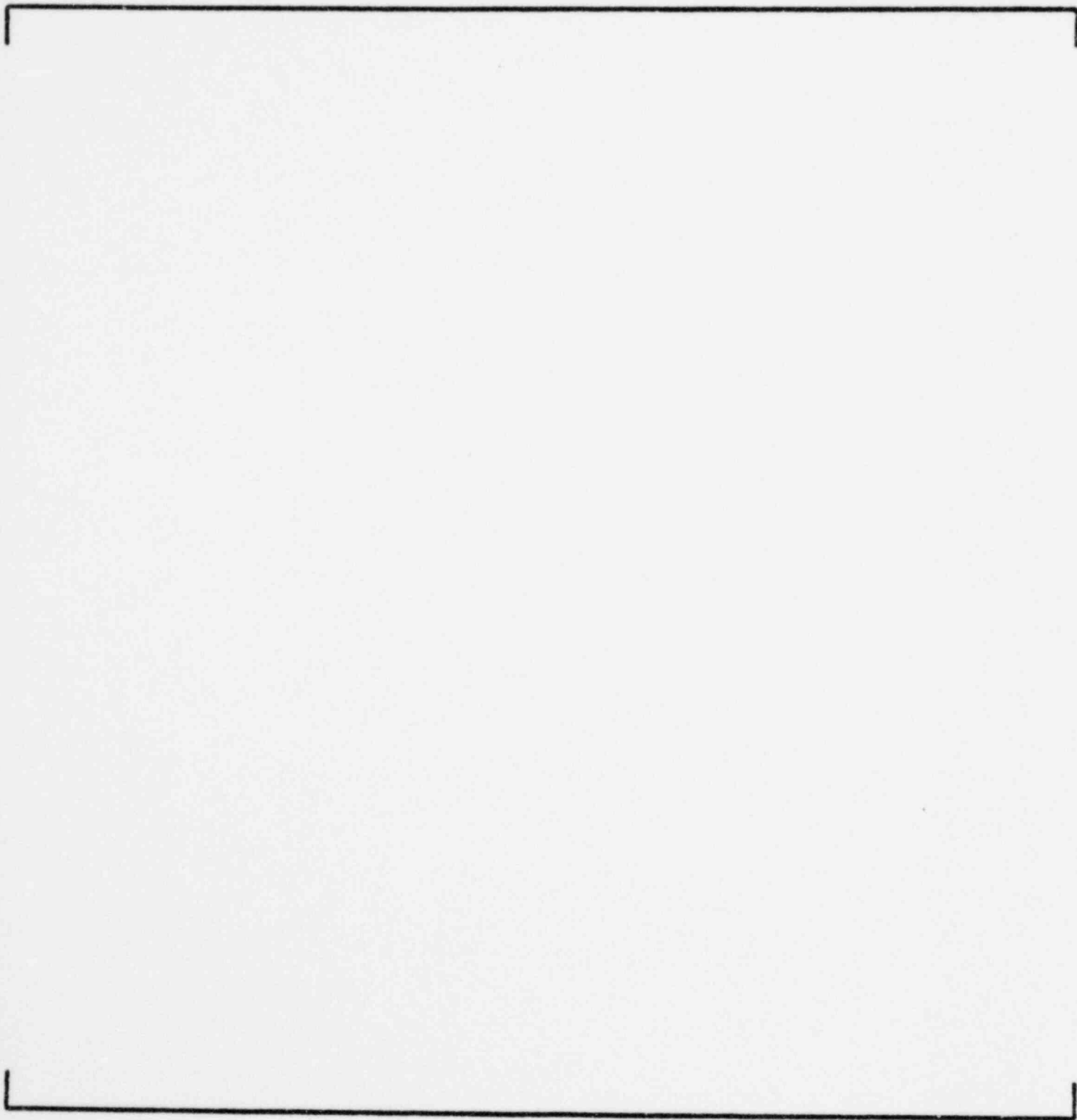


FIGURE 3-16b

COMPARISON OF MEASURED AND CALCULATED POWERS  
ST. LUCIE CYCLE 1 AT 888 MWD/T  
LEVEL 2

FIGURE 3-16c

COMPARISON OF MEASURED AND CALCULATED POWERS  
ST. LUCIE CYCLE 1 AT 888 MWD/T  
LEVEL 3

FIGURE 3-16d

COMPARISON OF MEASURED AND CALCULATED POWERS  
ST. LUCIE CYCLE 1 AT 888 MWD/T  
LEVEL 4

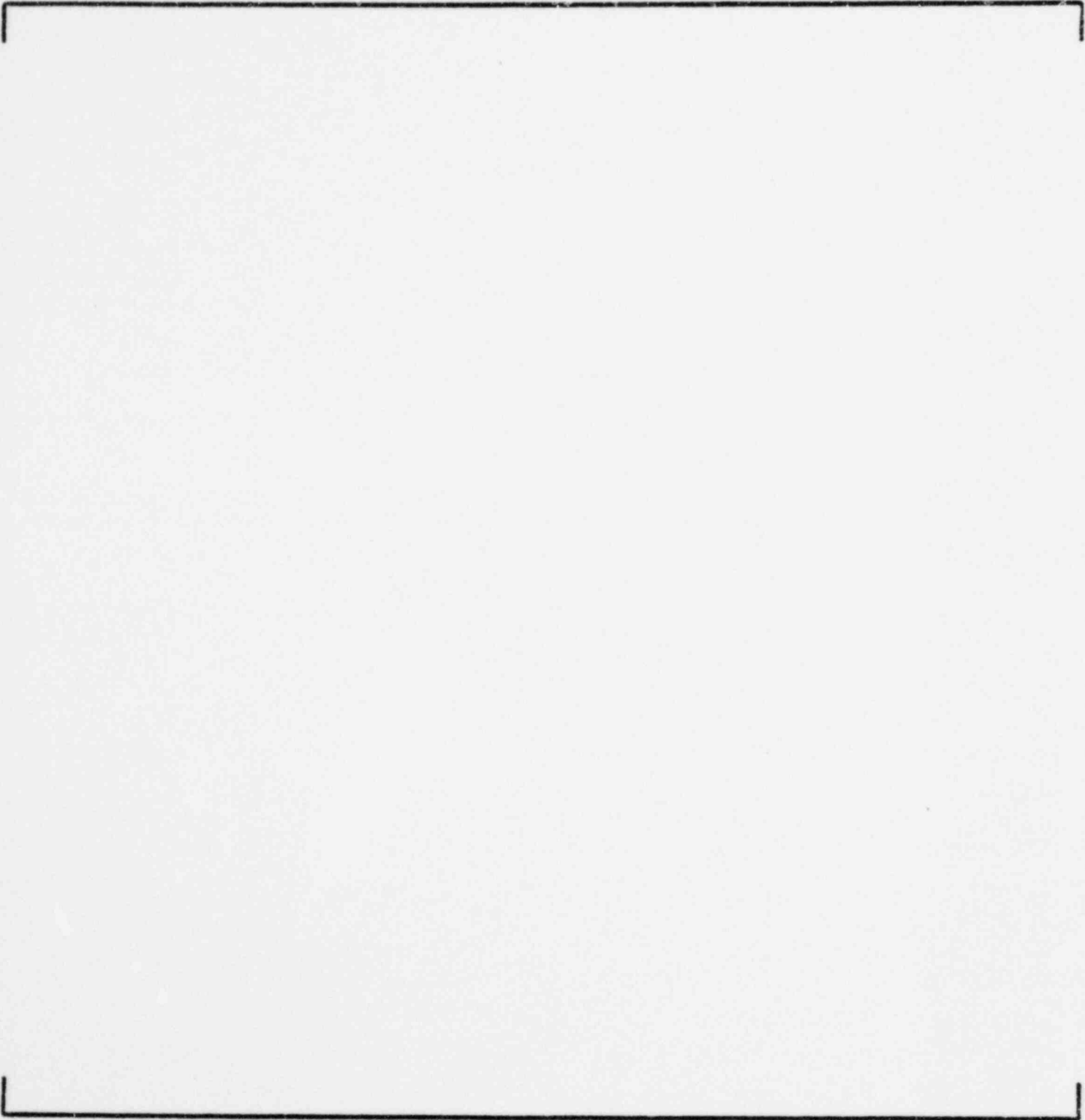


FIGURE 3-16e

COMPARISON OF MEASURED AND CALCULATED POWERS  
ST. LUCIE CYCLE 1 AT 888 MWD/T  
SUMMED LEVELS

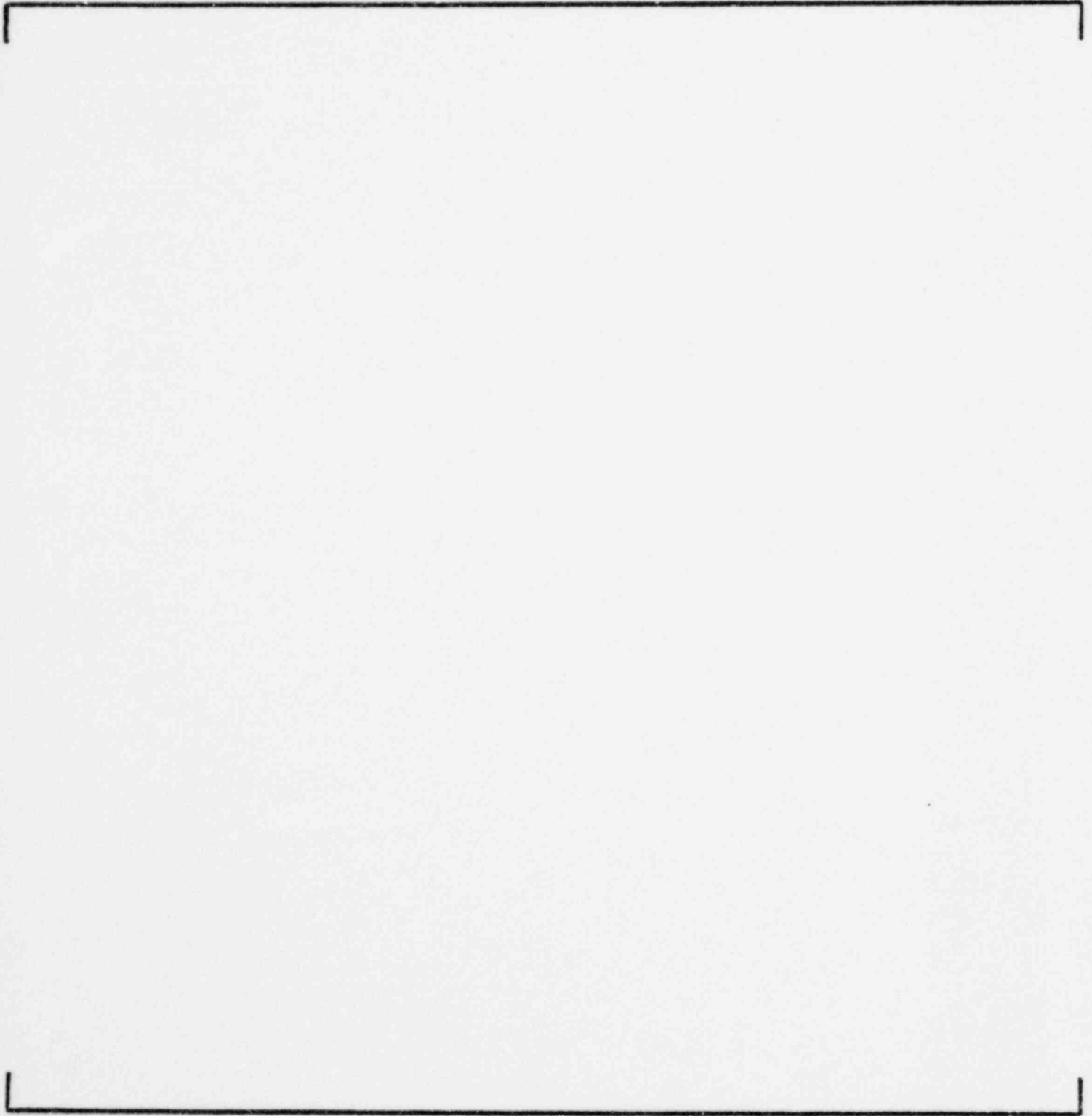




FIGURE 3-17a

COMPARISON OF MEASURED AND CALCULATED POWERS  
ST. LUCIE CYCLE 2 AT 1361 MWD/T  
LEVEL 1

FIGURE 3-17b

COMPARISON OF MEASURED AND CALCULATED POWERS  
ST. LUCIE CYCLE 2 AT 1361 MWD/T  
LEVEL 2

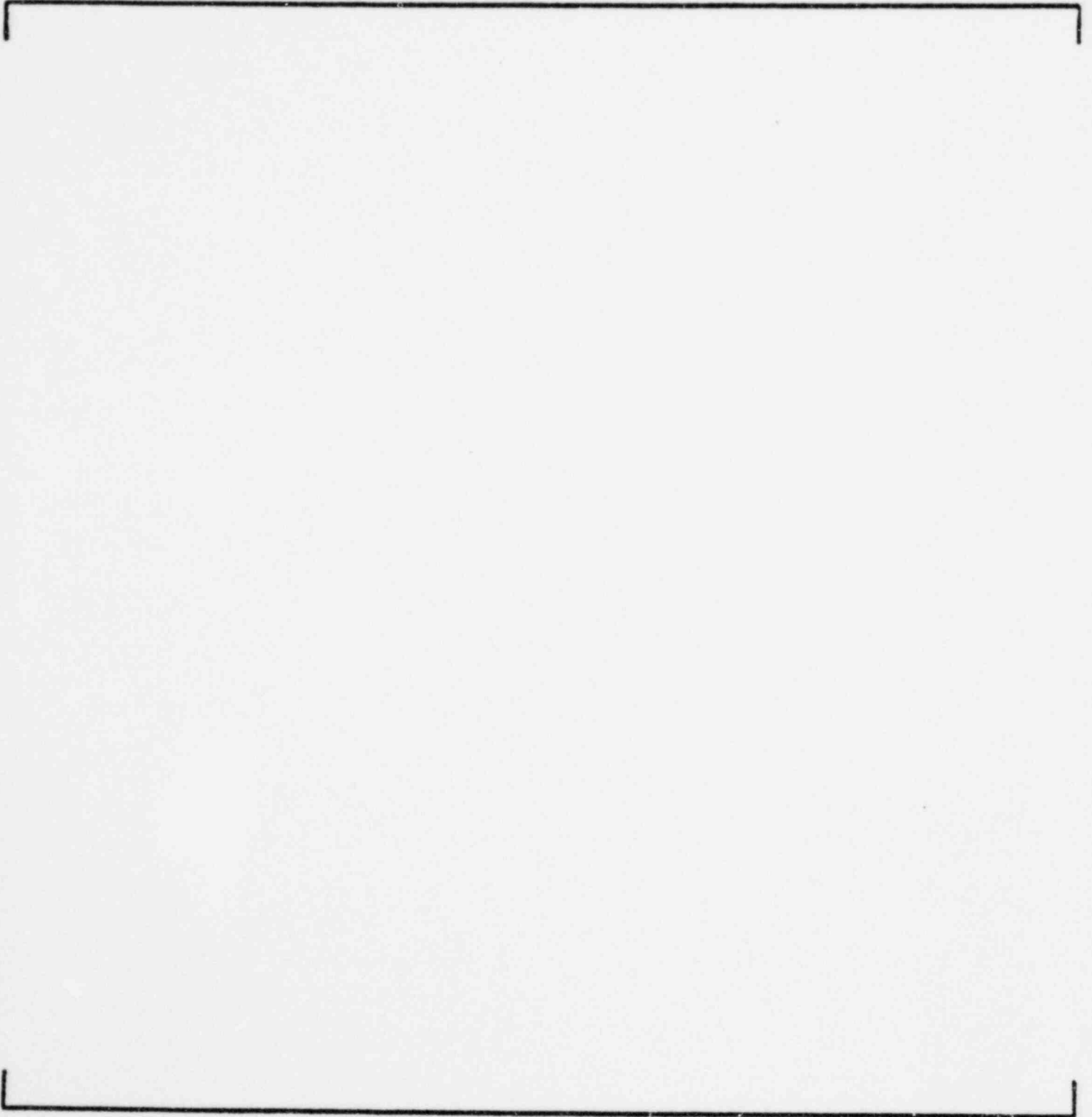


FIGURE 3-17c

COMPARISON OF MEASURED AND CALCULATED POWERS  
ST. LUCIE CYCLE 2 AT 1361 MWD/T  
LEVEL 3

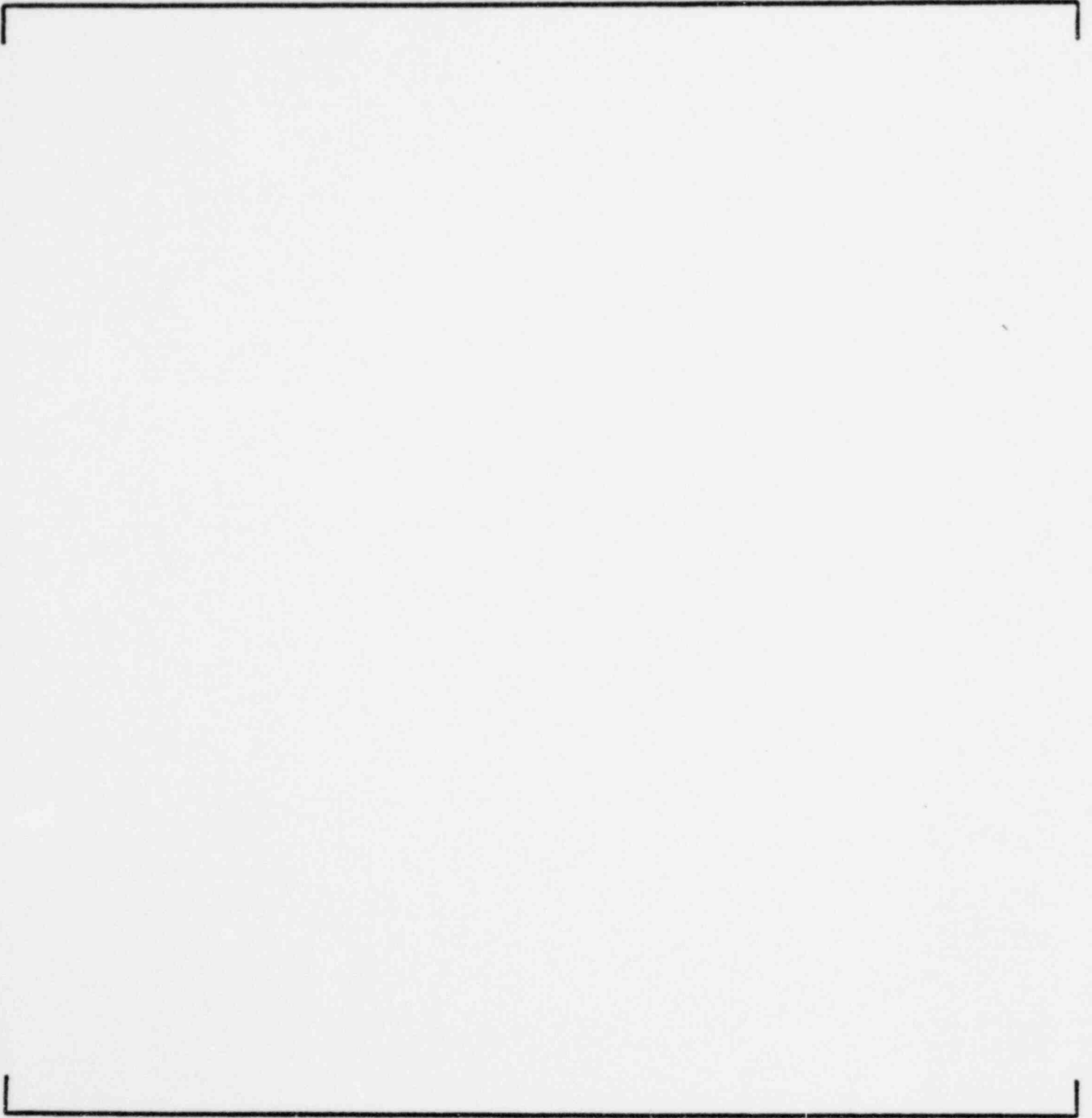


FIGURE 3-17d

COMPARISON OF MEASURED AND CALCULATED POWERS  
ST. LUCIE CYCLE 2 AT 1361 MWD/T  
LEVEL 4

FIGURE 3-17e

COMPARISON OF MEASURED AND CALCULATED POWERS  
ST. LUCIE CYCLE 2 AT 1361 MWD/T  
SUMMED LEVELS

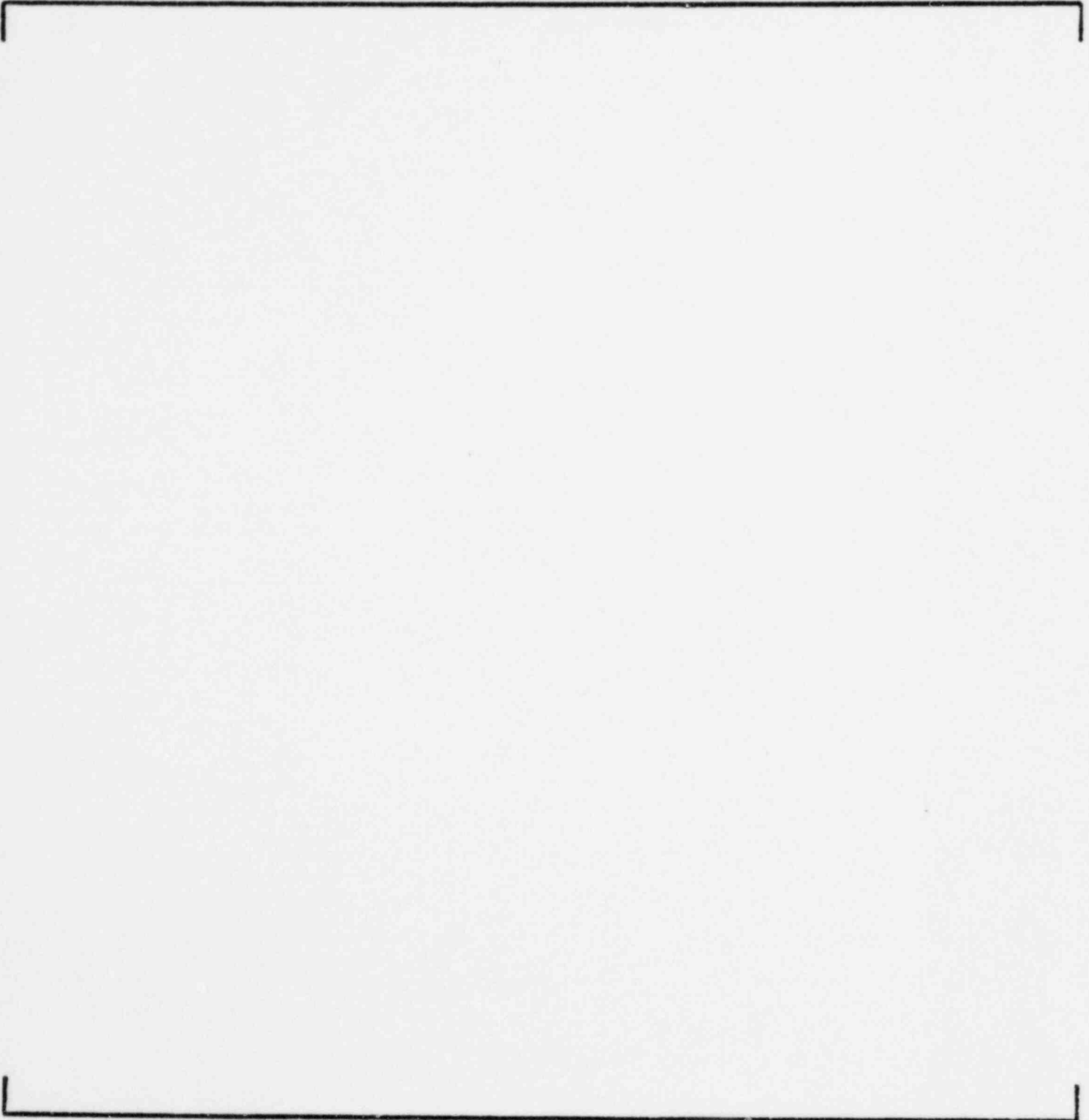


FIGURE 3-18a

COMPARISON OF MEASURED AND CALCULATED POWERS  
MILLSTONE II CYCLE 1 AT 1350 MWD/T  
LEVEL 1

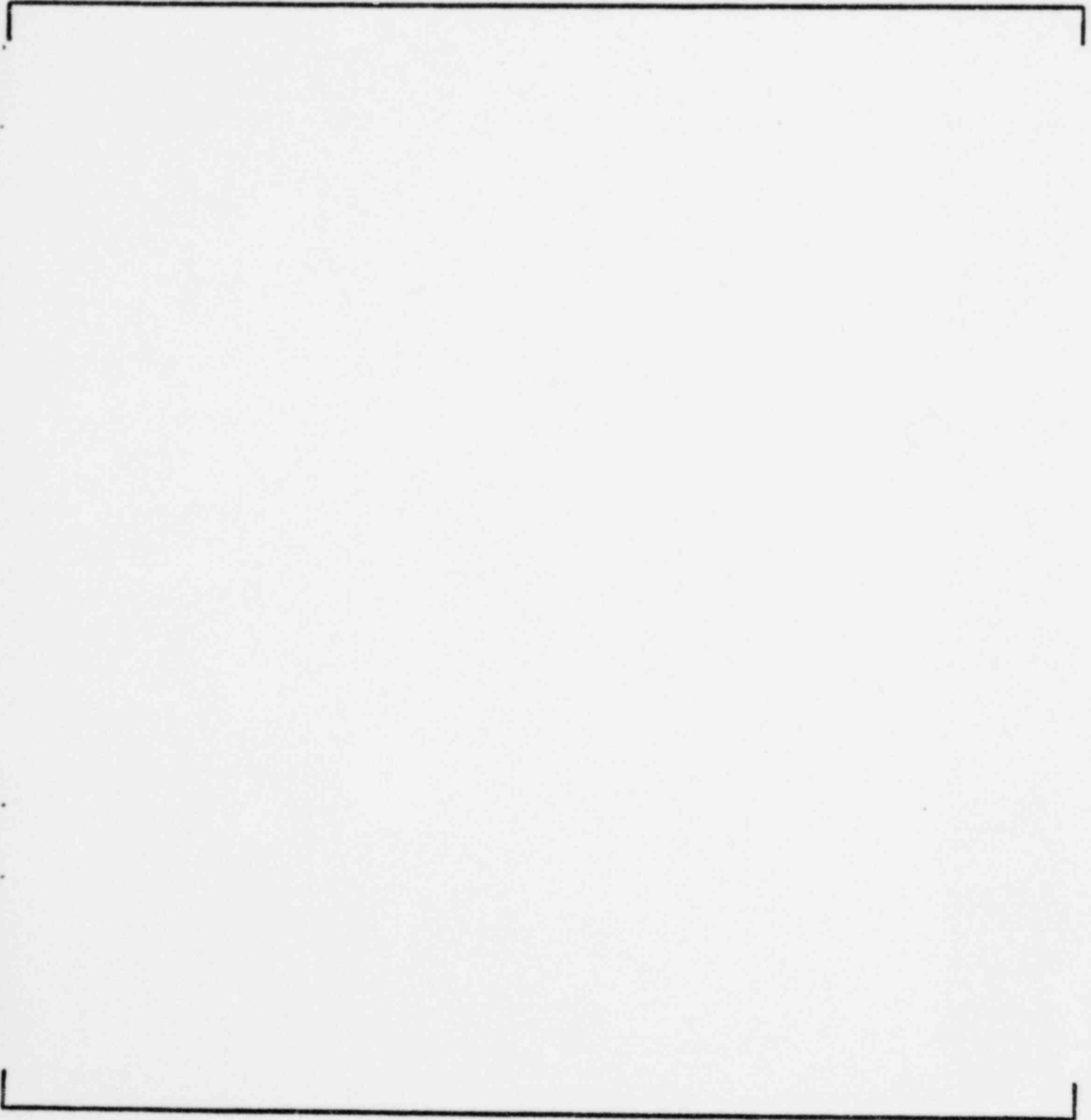


FIGURE 3-18b

COMPARISON OF MEASURED AND CALCULATED POWERS  
MILLSTONE II CYCLE 1 AT 1350 MWD/T  
LEVEL 2

FIGURE 3-18c

COMPARISON OF MEASURED AND CALCULATED POWERS  
MILLSTONE II CYCLE 1 AT 1350 MWD/T  
LEVEL 3

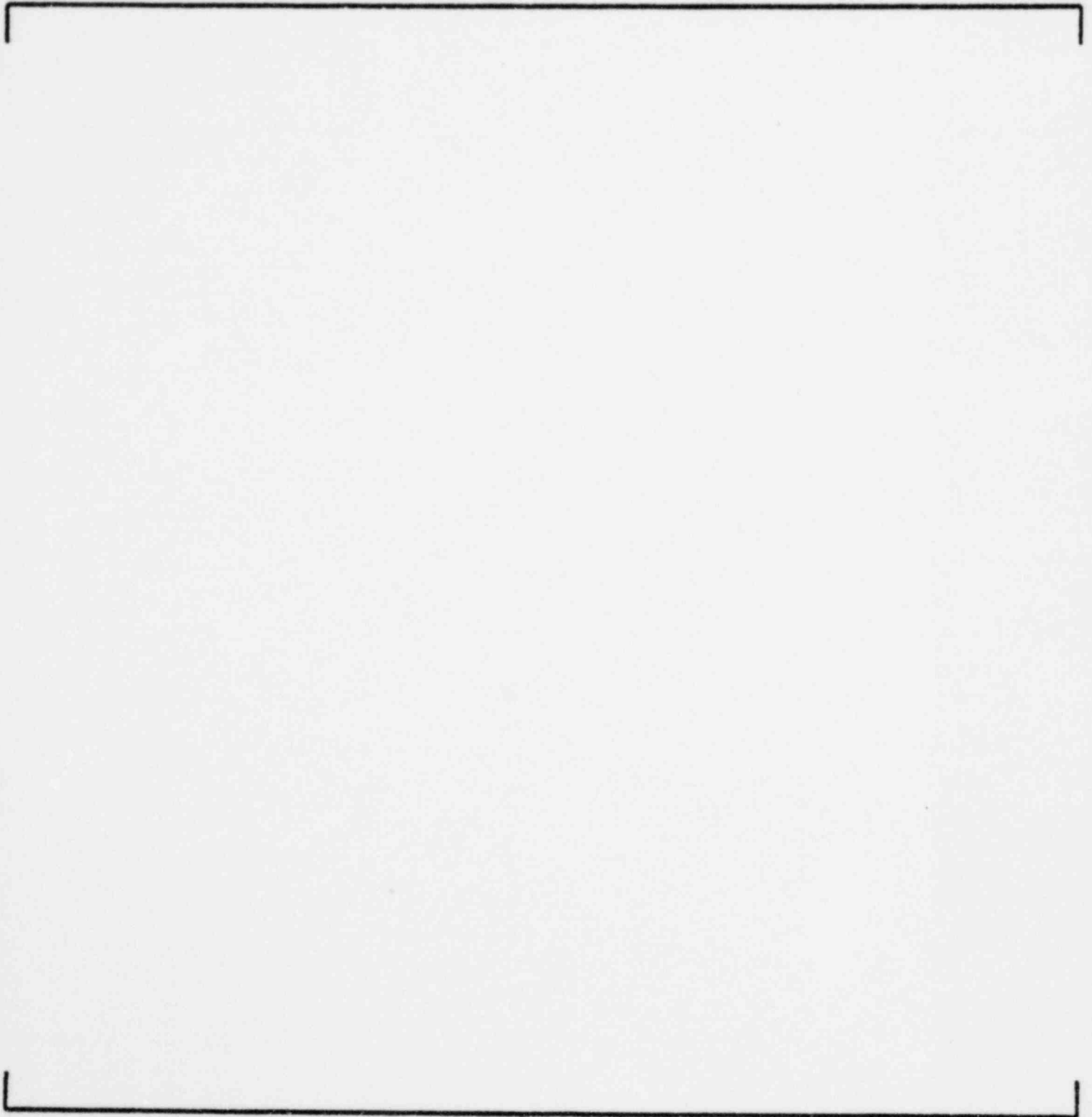




FIGURE 3-18d

COMPARISON OF MEASURED AND CALCULATED POWERS  
MILLSTONE II CYCLE 1 AT 1350 MWD/T  
LEVEL 4

FIGURE 3-18e

COMPARISON OF MEASURED AND CALCULATED POWERS  
MILLSTONE II CYCLE 1 AT 1350 MWD/T  
SUMMED LEVELS

FIGURE 3-19a

COMPARISON OF MEASURED AND CALCULATED POWERS  
MILLSTONE II CYCLE 2 AT 500 MWD/T  
LEVEL 1

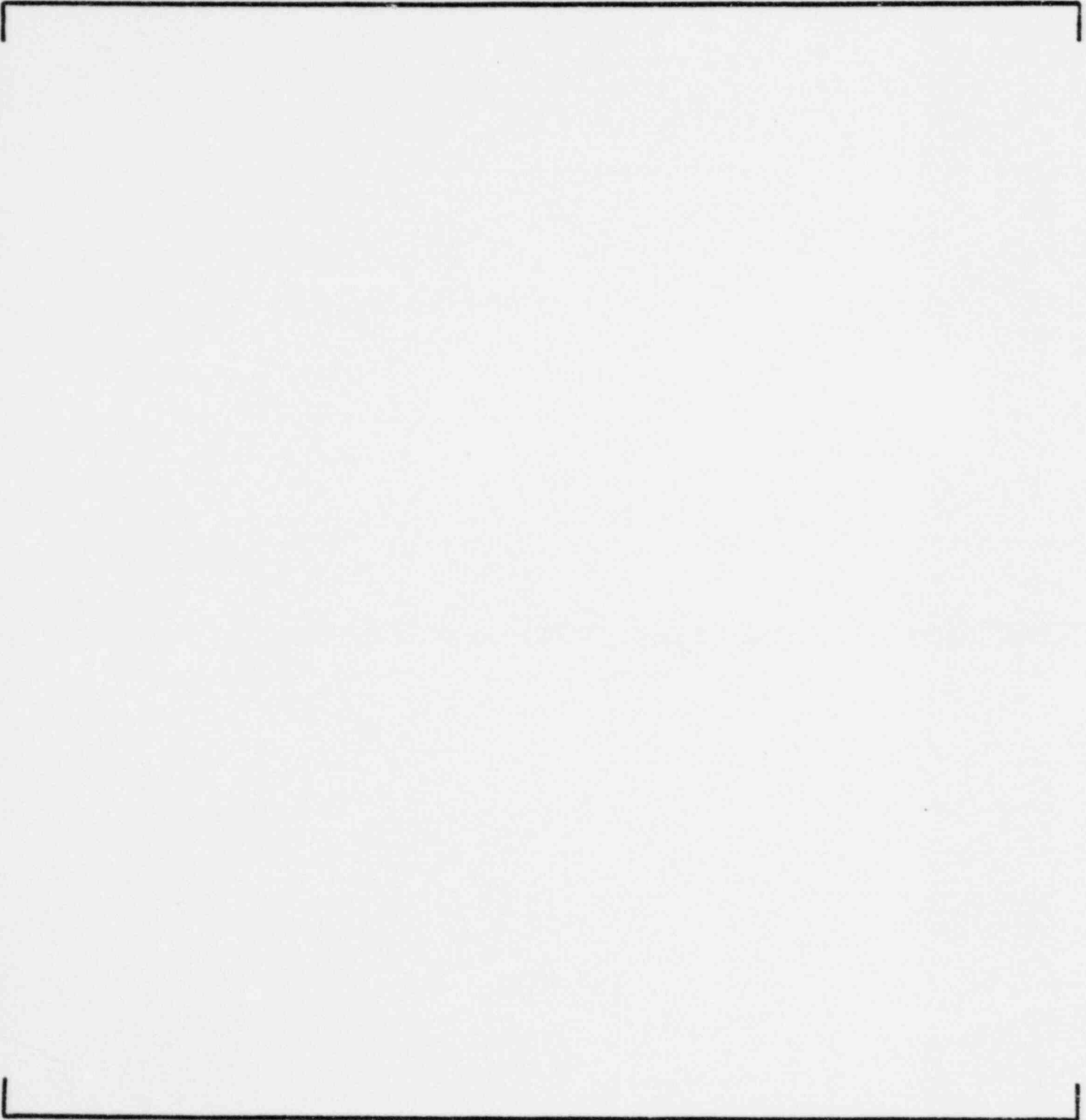


FIGURE 3-19b

COMPARISON OF MEASURED AND CALCULATED POWERS  
MILLSTONE II CYCLE 2 AT 500 MWD/T  
LEVEL 2

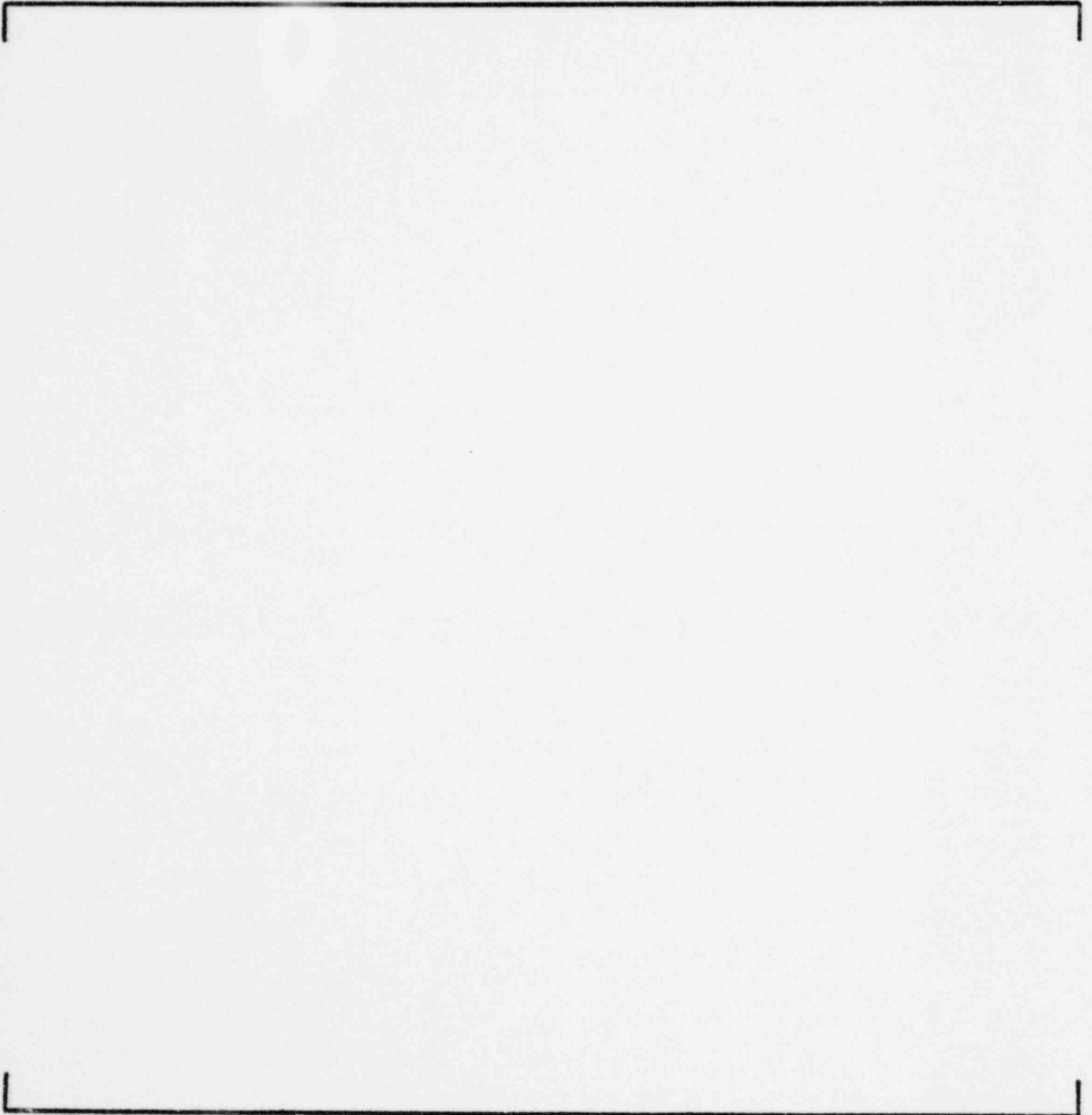


FIGURE 3-19c

COMPARISON OF MEASURED AND CALCULATED POWERS  
MILLSTONE II CYCLE 2 AT 500 MWD/T  
LEVEL 3

FIGURE 3-19d

COMPARISON OF MEASURED AND CALCULATED POWERS

MILLSTONE II CYCLE 2 AT 500 MWD/T

LEVEL 4

FIGURE 3-19e

COMPARISON OF MEASURED AND CALCULATED POWERS  
MILLSTONE II CYCLE 2 AT 500 MWD/T  
SUMMED LEVELS

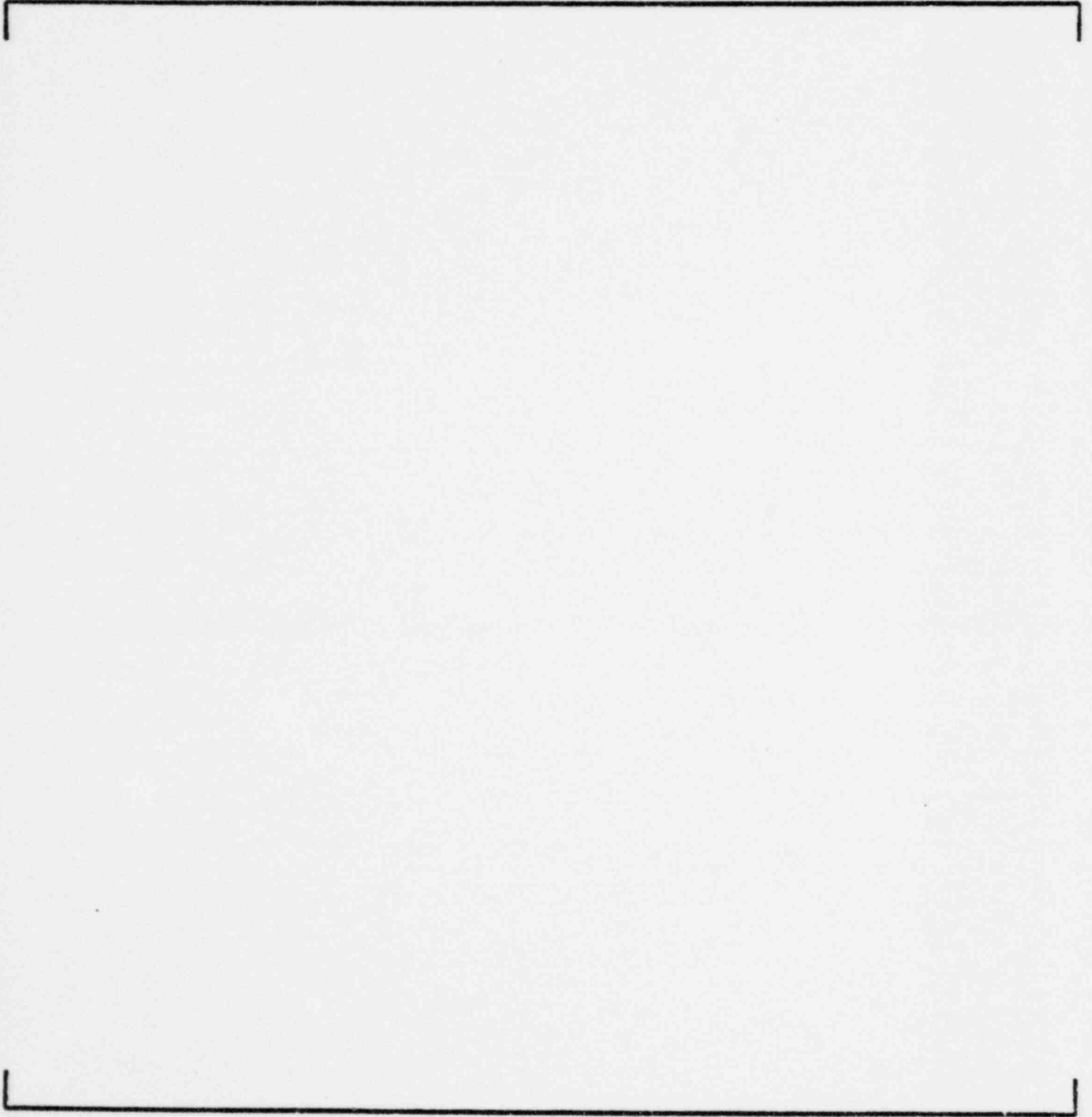


FIGURE 3-20a

COMPARISON OF MEASURED AND CALCULATED POWERS  
CALVERT CLIFFS UNIT 2 CYCLE 1 AT 1440 MWD/T  
LEVEL 1

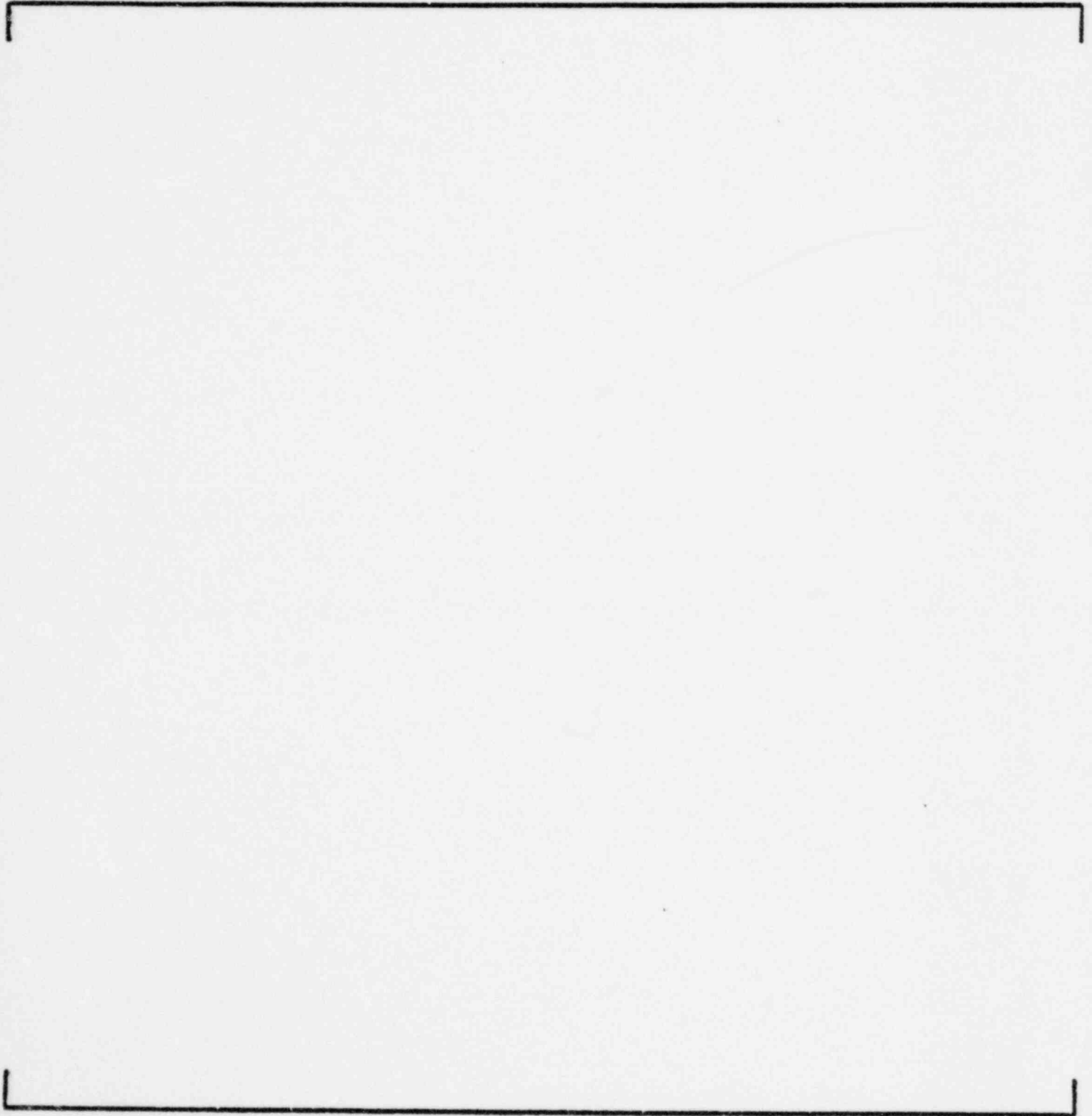




FIGURE 3-20b

COMPARISON OF MEASURED AND CALCULATED POWERS  
CALVERT CLIFFS UNIT 2 CYCLE 1 at 1440 MWG/T  
LEVEL 2

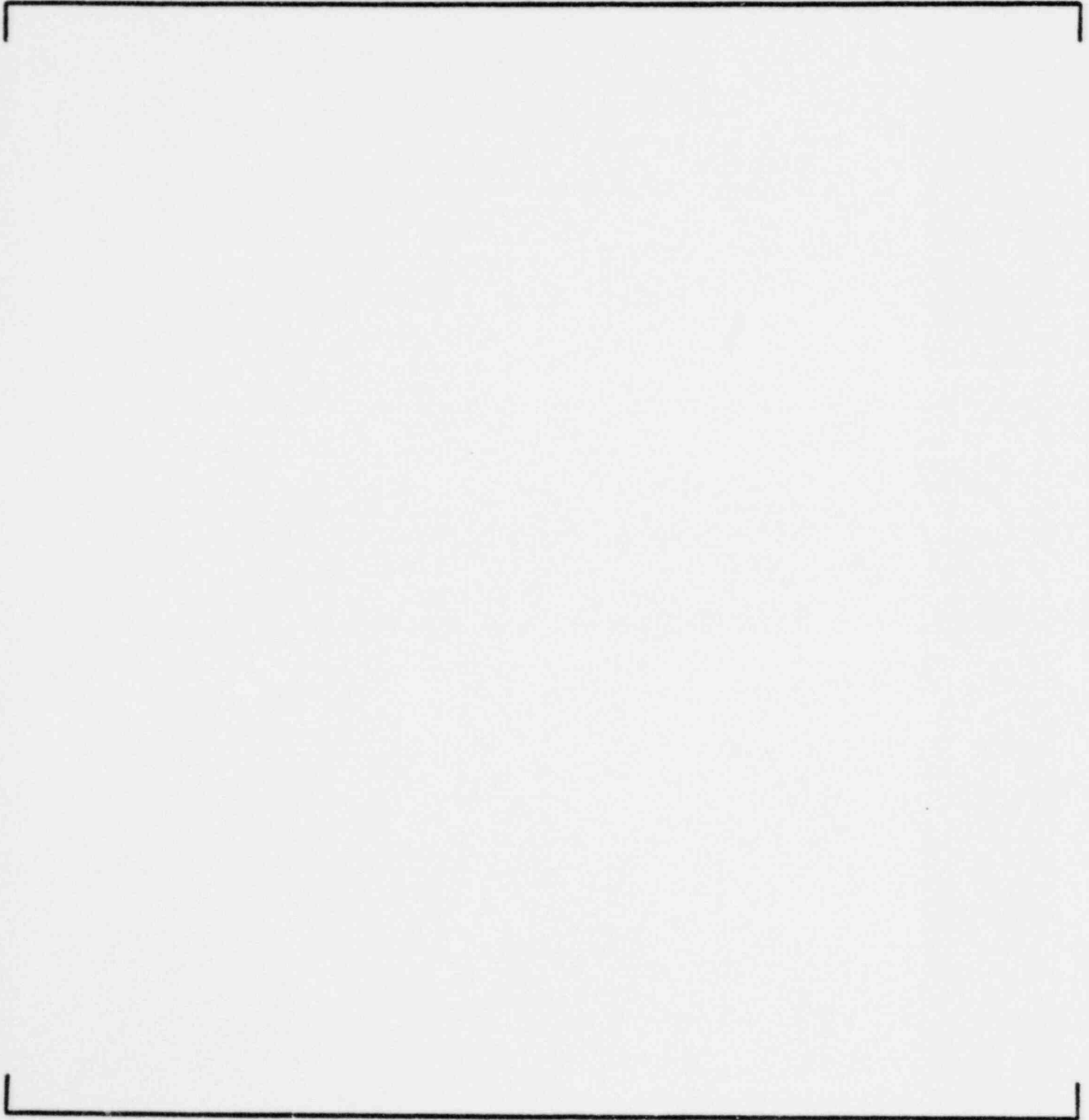


FIGURE 3-20c

COMPARISON OF MEASURED AND CALCULATED POWERS  
CALVERT CLIFFS UNIT 2 CYCLE 1 AT 1440 MWD/T  
LEVEL 3

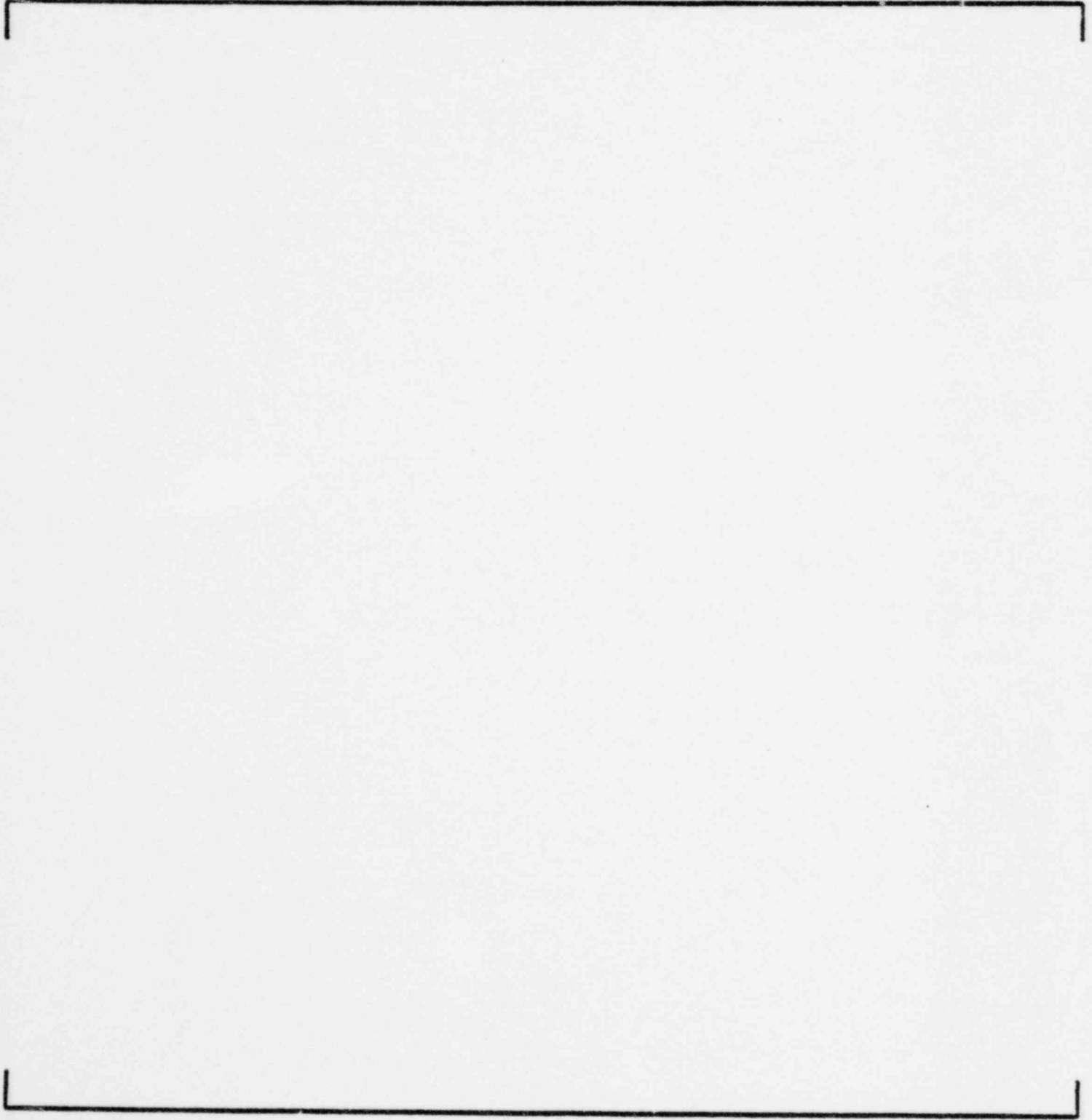


FIGURE 3-20d

COMPARISON OF MEASURED AND CALCULATED POWERS  
CALVERT CLIFFS UNIT 2 CYCLE 1 AT 1440 MWD/T  
LEVEL 4

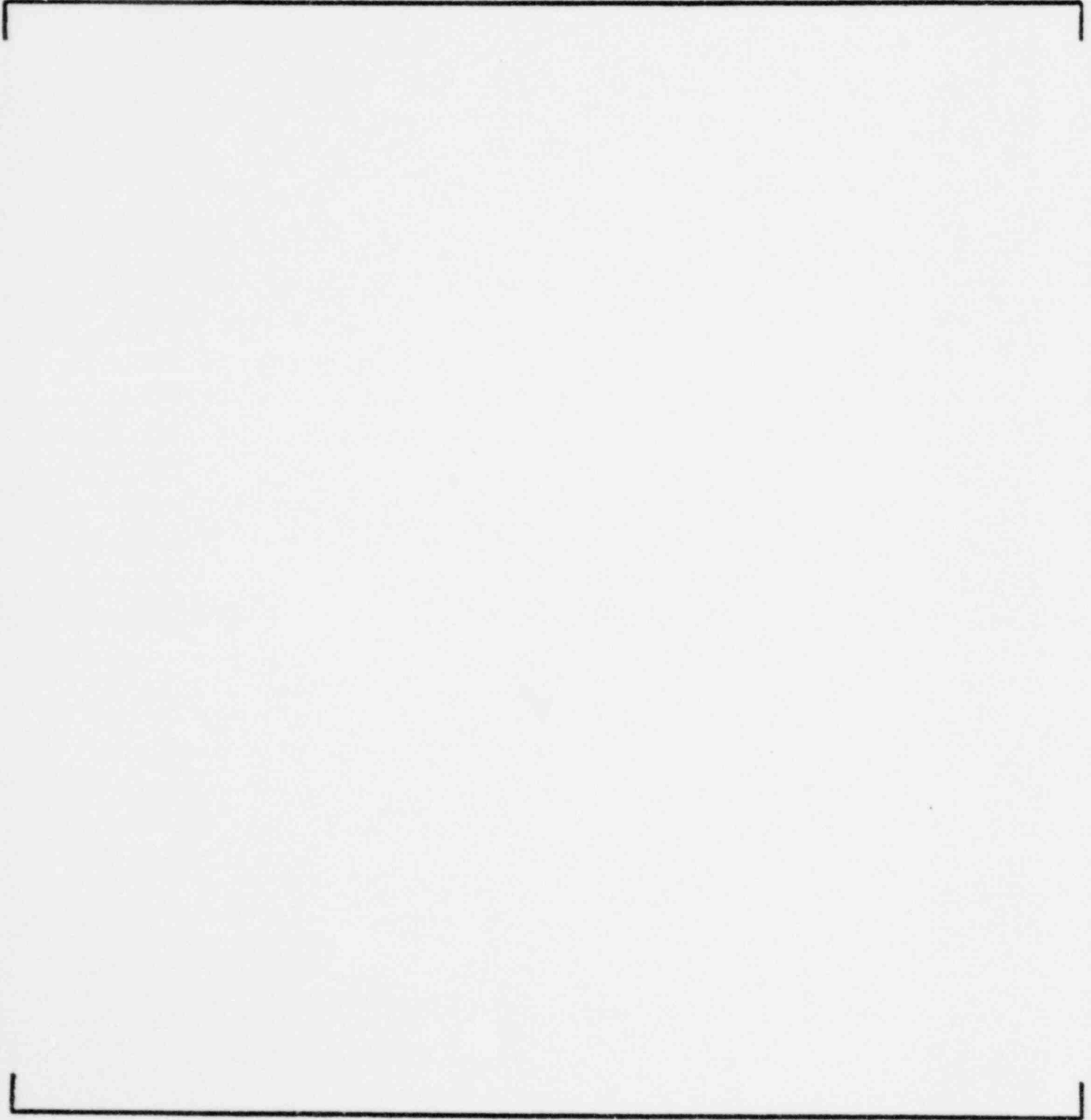


FIGURE 3-20e

COMPARISON OF MEASURED AND CALCULATED POWERS  
CALVERT CLIFFS UNIT 2 CYCLE 1 AT 1440 MWD/T  
SUMMED LEVELS

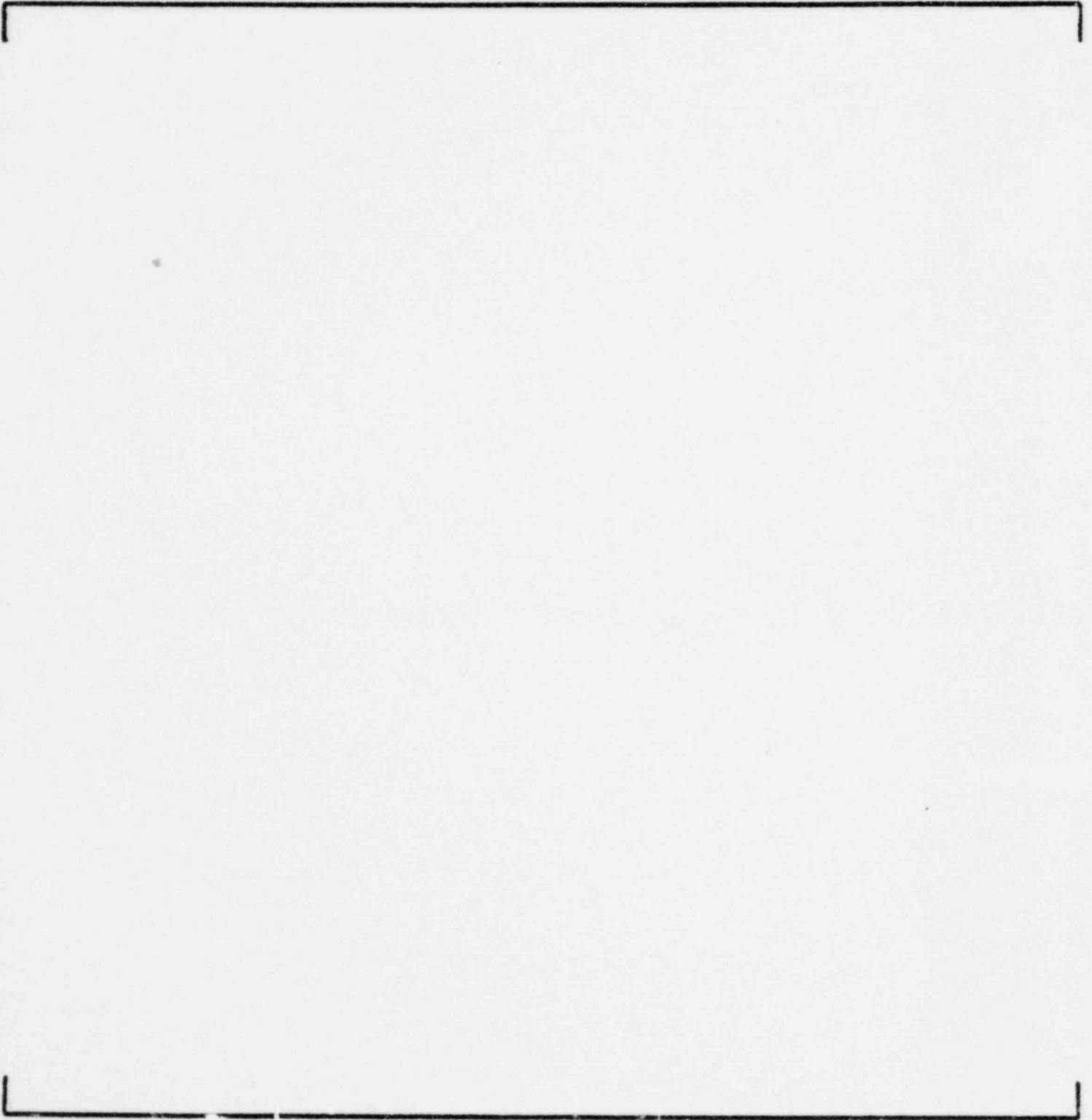


FIGURE 3-21a

COMPARISON OF MEASURED AND CALCULATED POWERS  
CALVERT CLIFFS UNIT 2 CYCLE 2 AT 809 MWD/T  
LEVEL 1

FIGURE 3-21b

COMPARISON OF MEASURED AND CALCULATED POWERS  
CALVERT CLIFFS UNIT 2 CYCLE 2 AT 809 MWD/T  
LEVEL 2

FIGURE 3-21c

COMPARISON OF MEASURED AND CALCULATED POWERS  
CALVERT CLIFFS UNIT 2 CYCLE 2 AT 809 MWD/T  
LEVEL 3

FIGURE 3-21d

COMPARISON OF MEASURED AND CALCULATED POWERS  
CALVERT CLIFFS UNIT 2 CYCLE 2 AT 809 MWD/T  
LEVEL 4

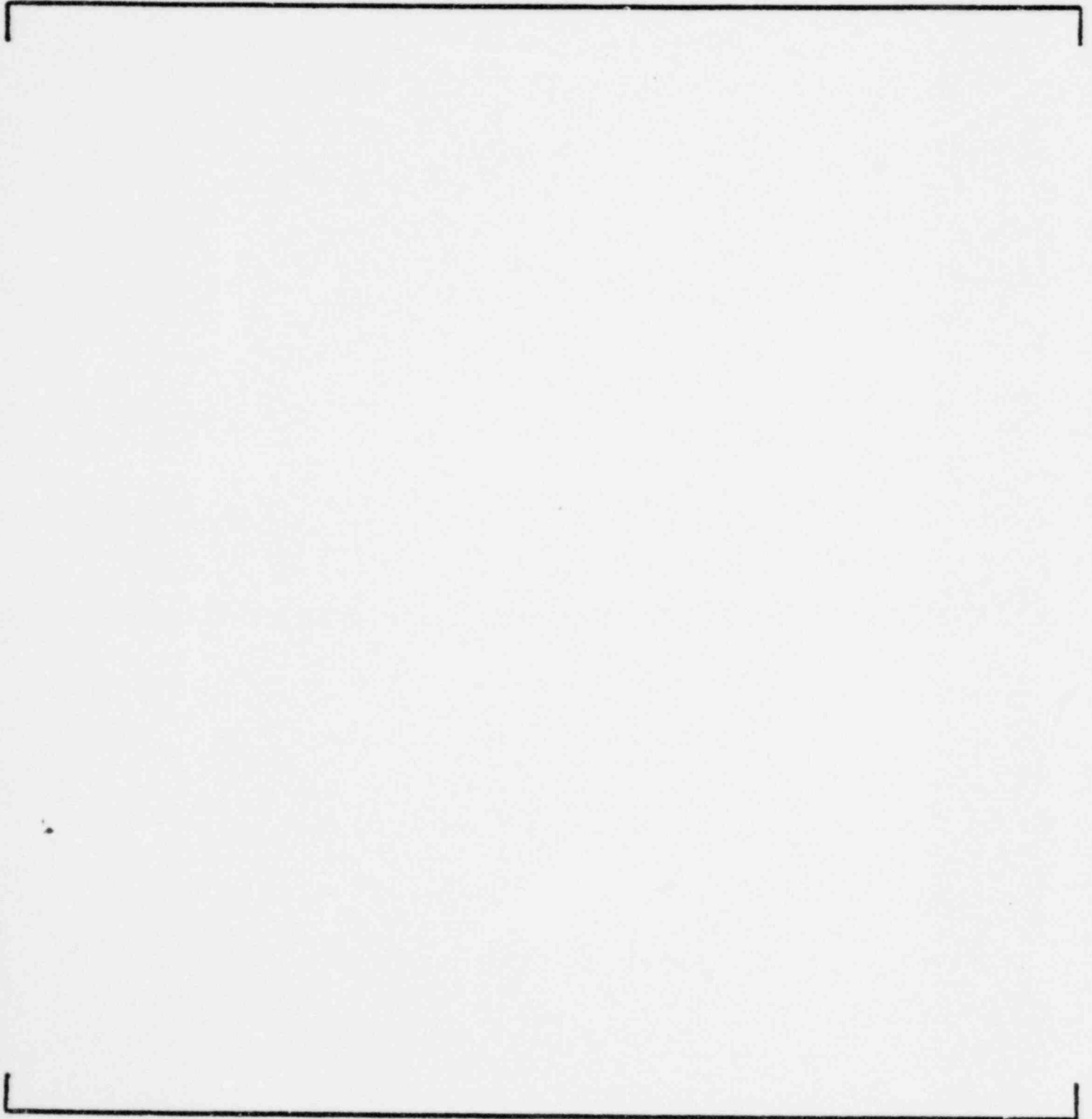




FIGURE 3-21e

COMPARISON OF MEASURED AND CALCULATED POWERS  
CALVERT CLIFFS UNIT 2 CYCLE 2 AT 809 MWD/T  
SUMMED LEVELS

Figure 3-22a  
COMPARISON OF MEASURED AND CALCULATED POWERS  
FORT CALHOUN UNIT 1 CYCLE 4 AT 1000 MWD/T  
LEVEL 1

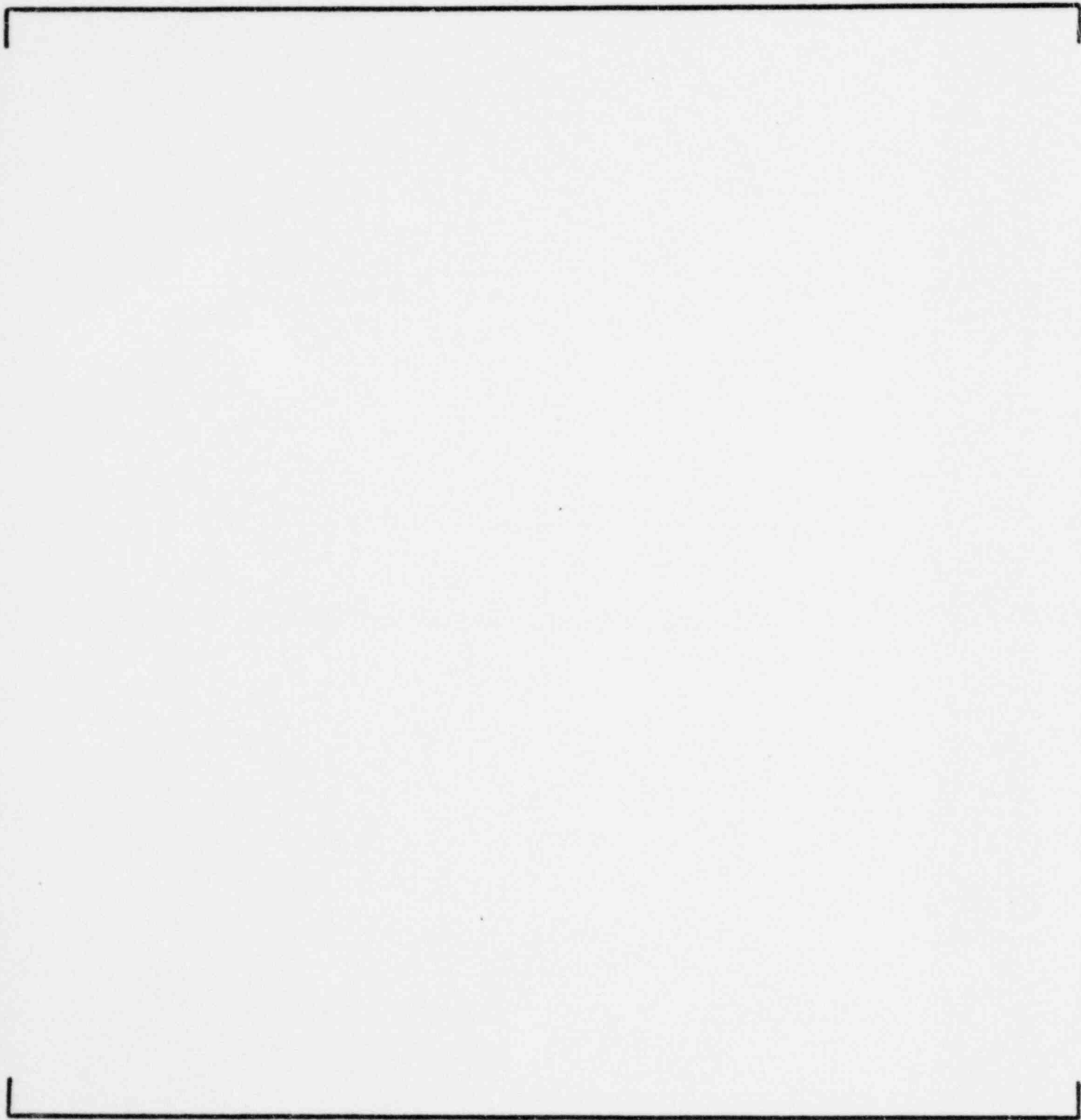


Figure 3-22b  
COMPARISON OF MEASURED AND CALCULATED POWERS  
FORT CALHOUN UNIT 1 CYCLE 4 AT 1000 MWD/T  
LEVEL 2

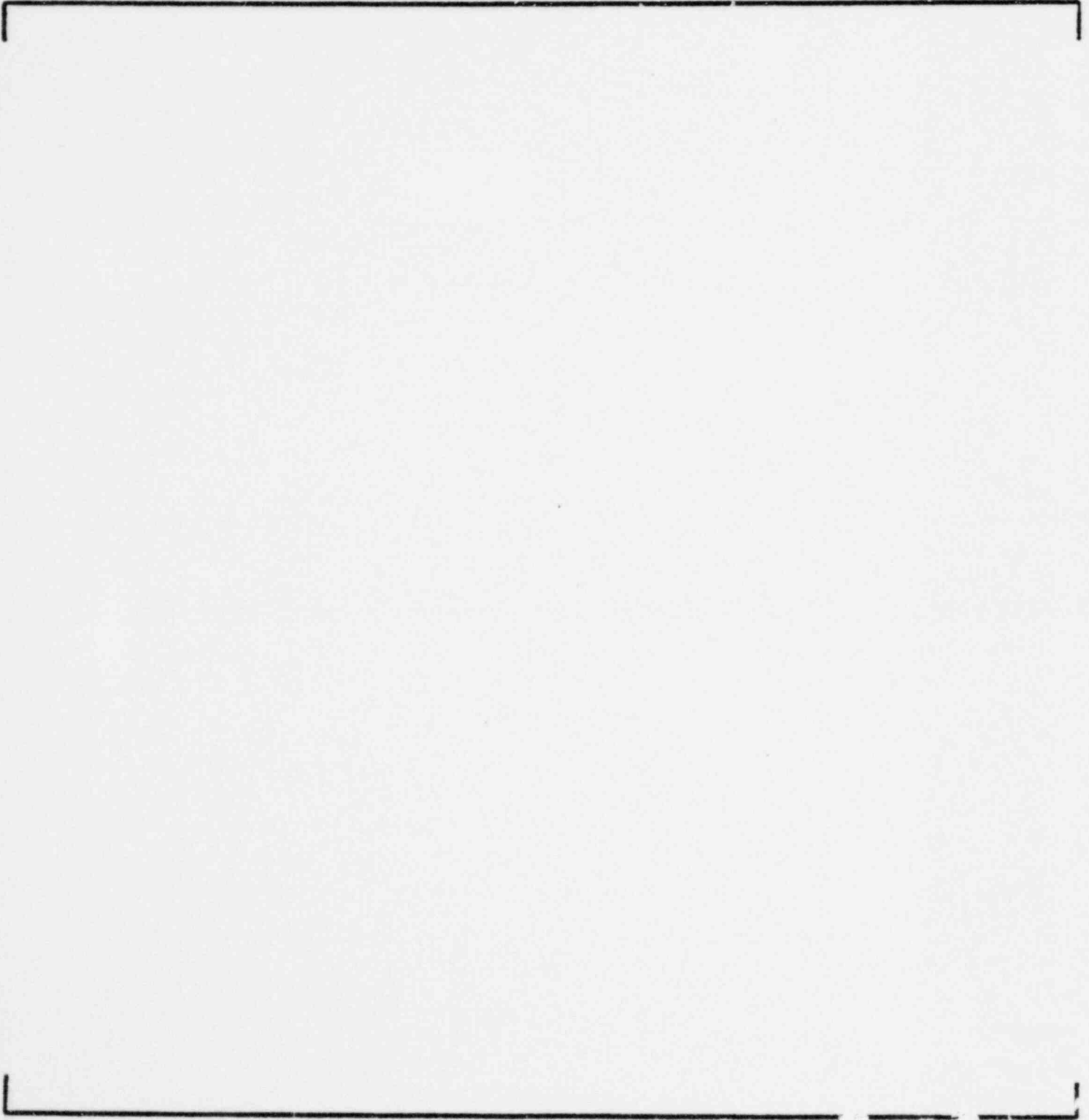


Figure 3-22c  
COMPARISON OF MEASURED AND CALCULATED POWERS  
FORT CALHOUN UNIT 1 CYCLE 4 AT 1000 MWD/T  
LEVEL 3

Figure 3-22d  
COMPARISON OF MEASURED AND CALCULATED POWERS  
FORT CALHOUN UNIT 1 CYCLE 4 AT 1000 MWD/T  
LEVEL 4

Figure 3-22e  
COMPARISON OF MEASURED AND CALCULATED POWERS  
FORT CALHOUN UNIT 1 CYCLE 4 AT 1000 MWD/T  
SUMMED LEVELS

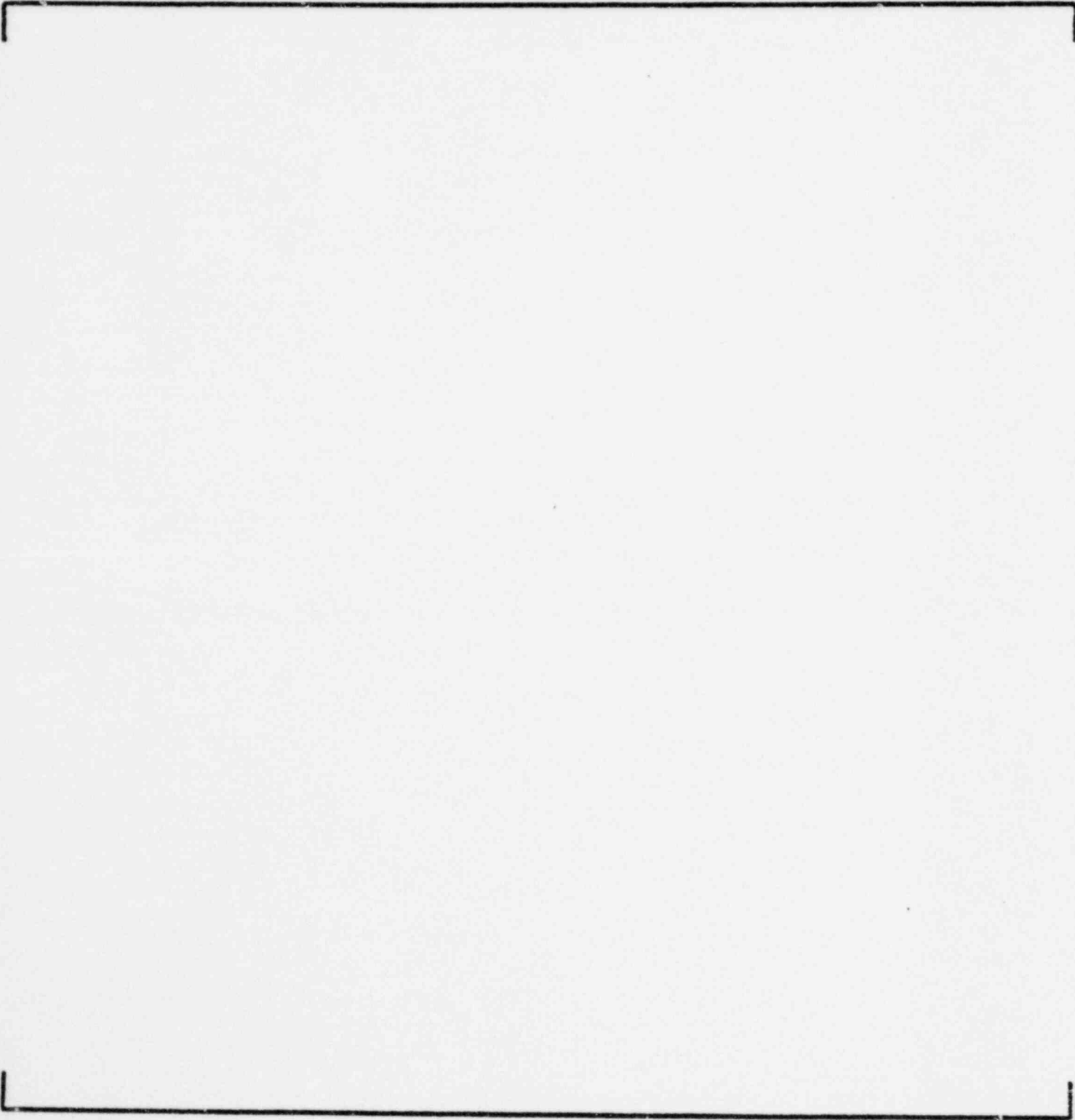


Figure 3-23a  
COMPARISON OF MEASURED AND CALCULATED POWERS  
FORT CALHOUN UNIT 1 CYCLE 5 AT 300 MWD/T  
LEVEL 1

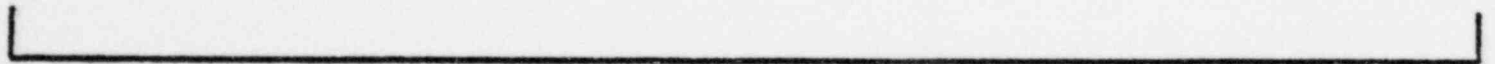
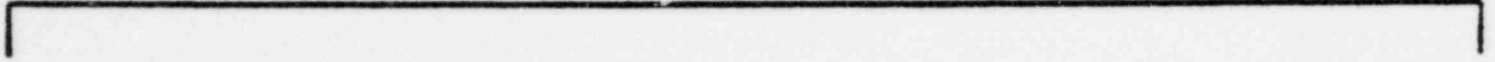


Figure 3-23b  
COMPARISON OF MEASURED AND CALCULATED POWERS  
FORT CALHOUN UNIT 1 CYCLE 5 AT 300 MWD/T  
LEVEL 2

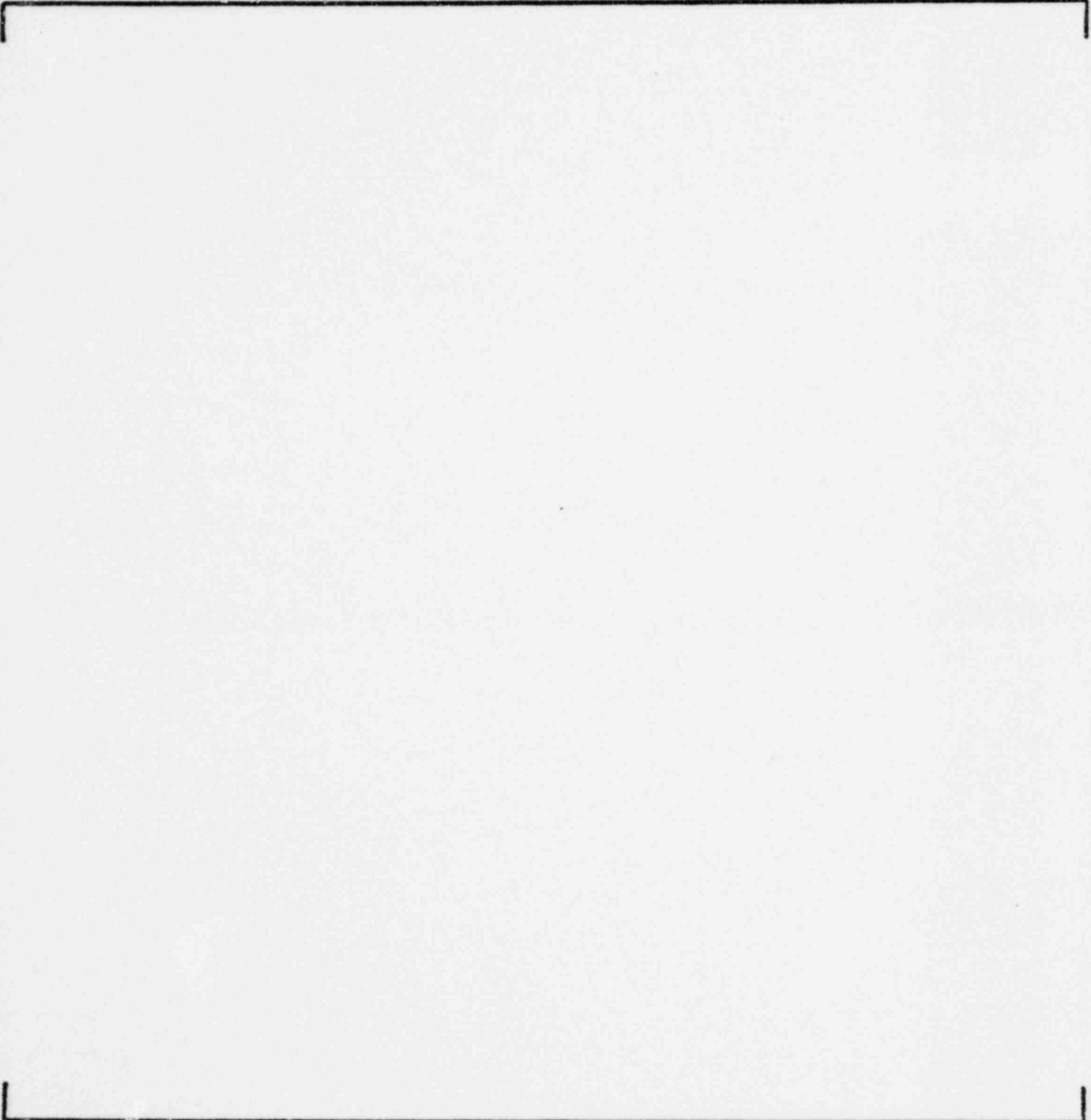




Figure 3-23c  
COMPARISON OF MEASURED AND CALCULATED POWERS  
FORT CALHOUN UNIT 1 CYCLE 5 AT 300 MWD/T  
LEVEL 3

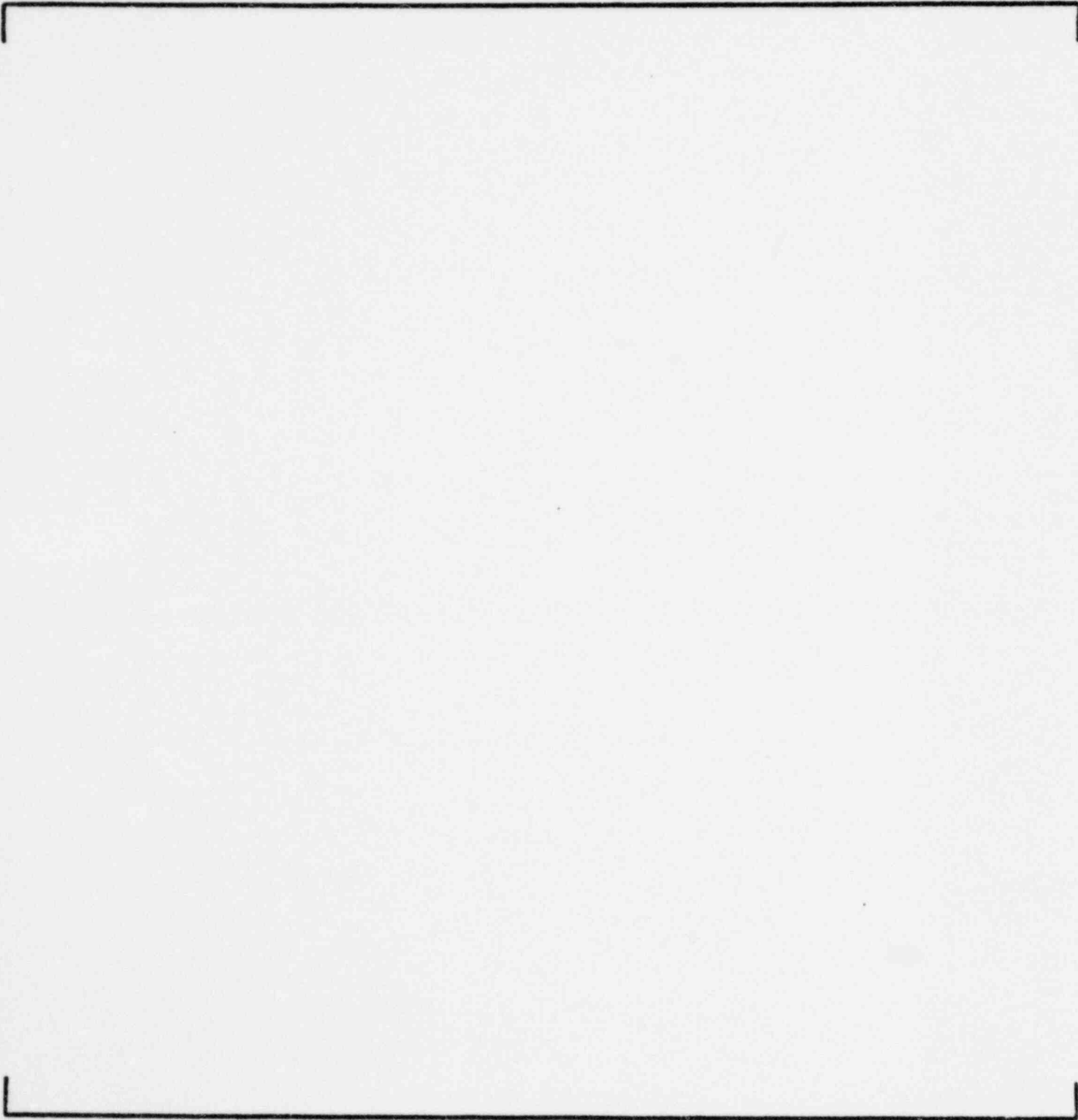


Figure 3-23d  
COMPARISON OF MEASURED AND CALCULATED POWERS  
FORT CALHOUN UNIT 1 CYCLE 5 AT 300 MWD/T  
LEVEL 4

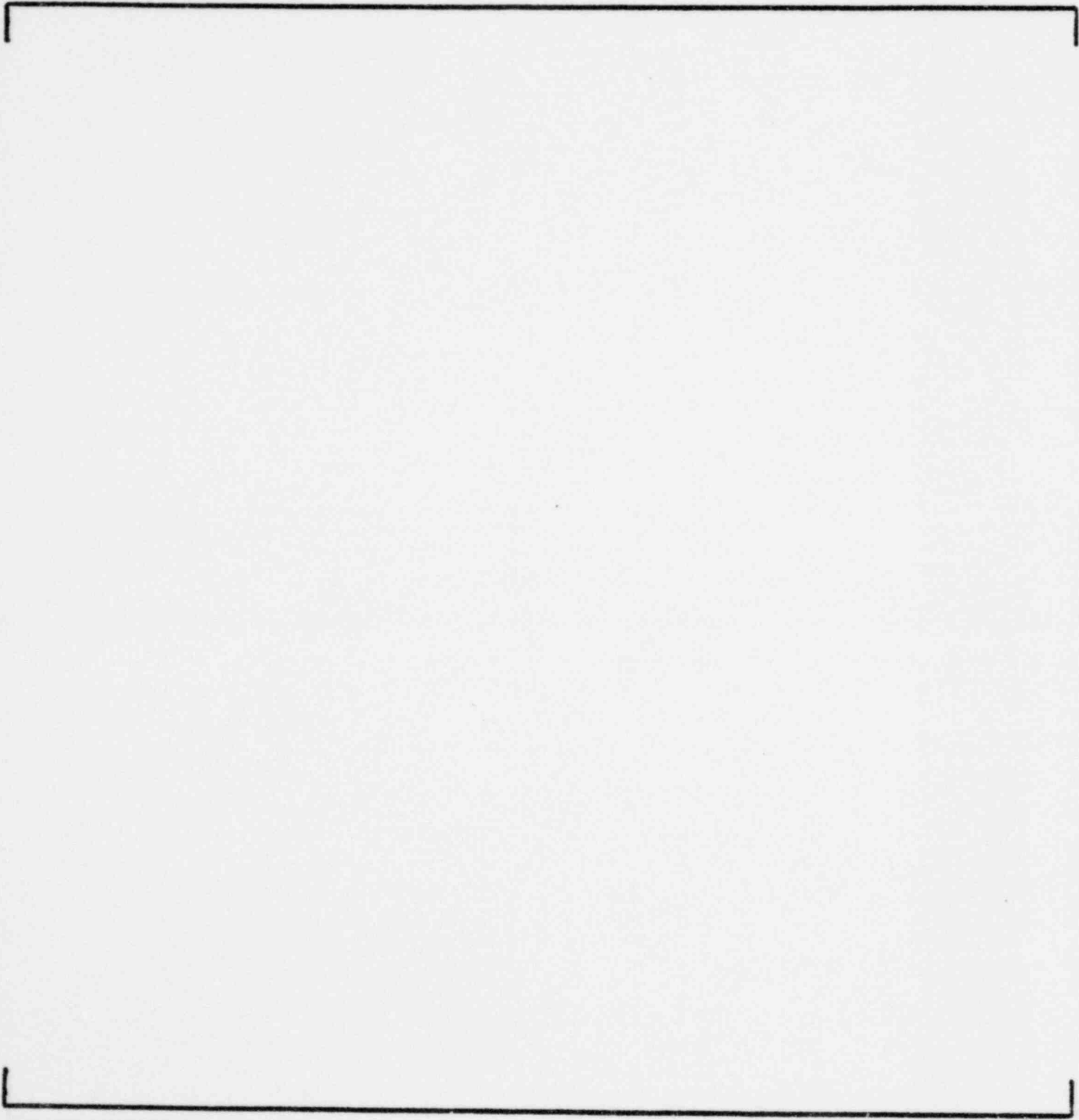


Figure 3-23e  
COMPARISON OF MEASURED AND CALCULATED POWERS  
FORT CALHOUN UNIT 1 CYCLE 5 AT 300 MWD/T  
SUMMED LEVELS

Figure 3-24

DISTRIBUTION OF DEVIATIONS IN  $F_q$   
CALVERT CLIFFS UNIT 1 CYCLE 3

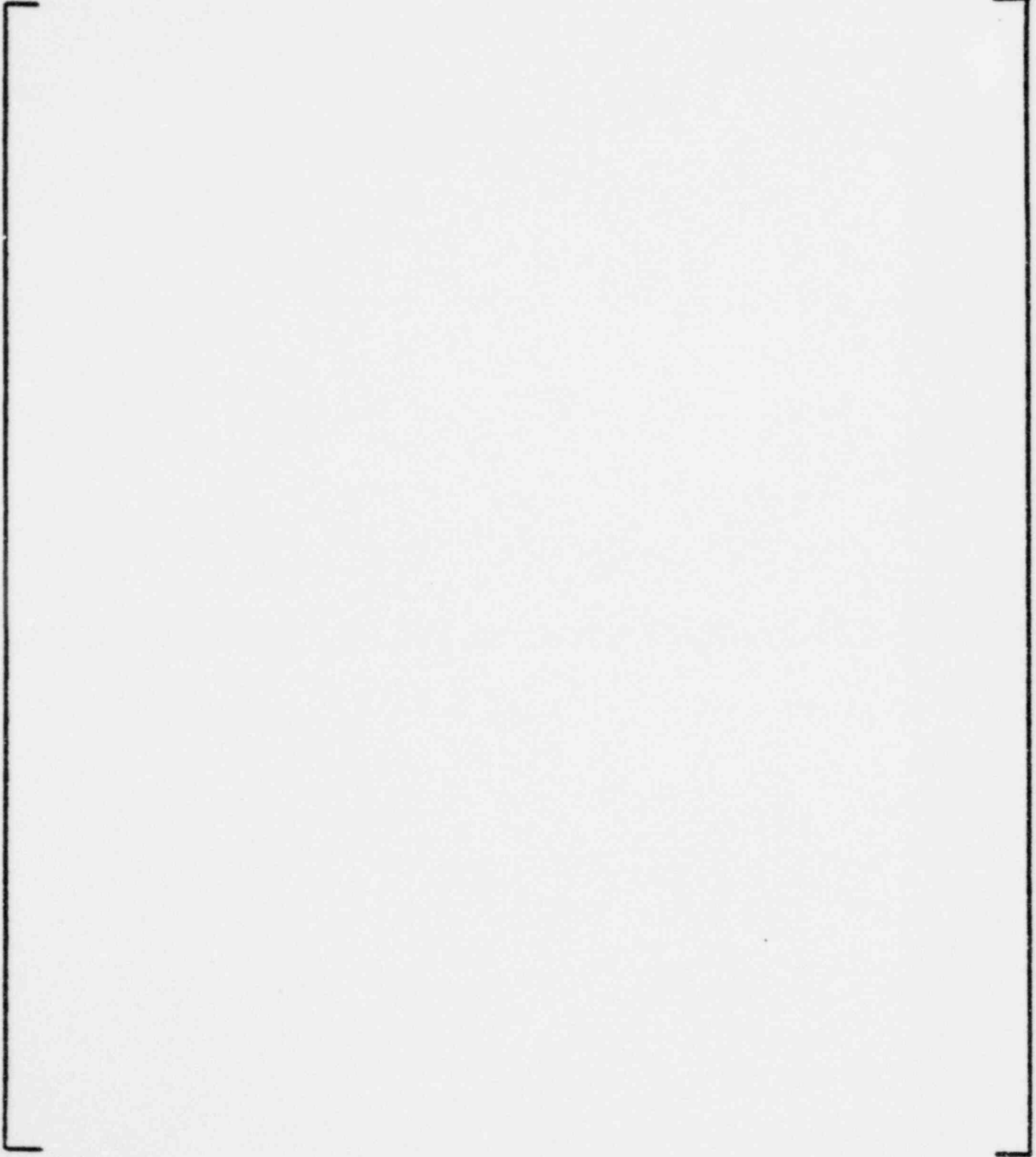


Figure 3-25

DISTRIBUTION OF DEVIATIONS IN  $F_q$   
ST. LUCIE CYCLE 2

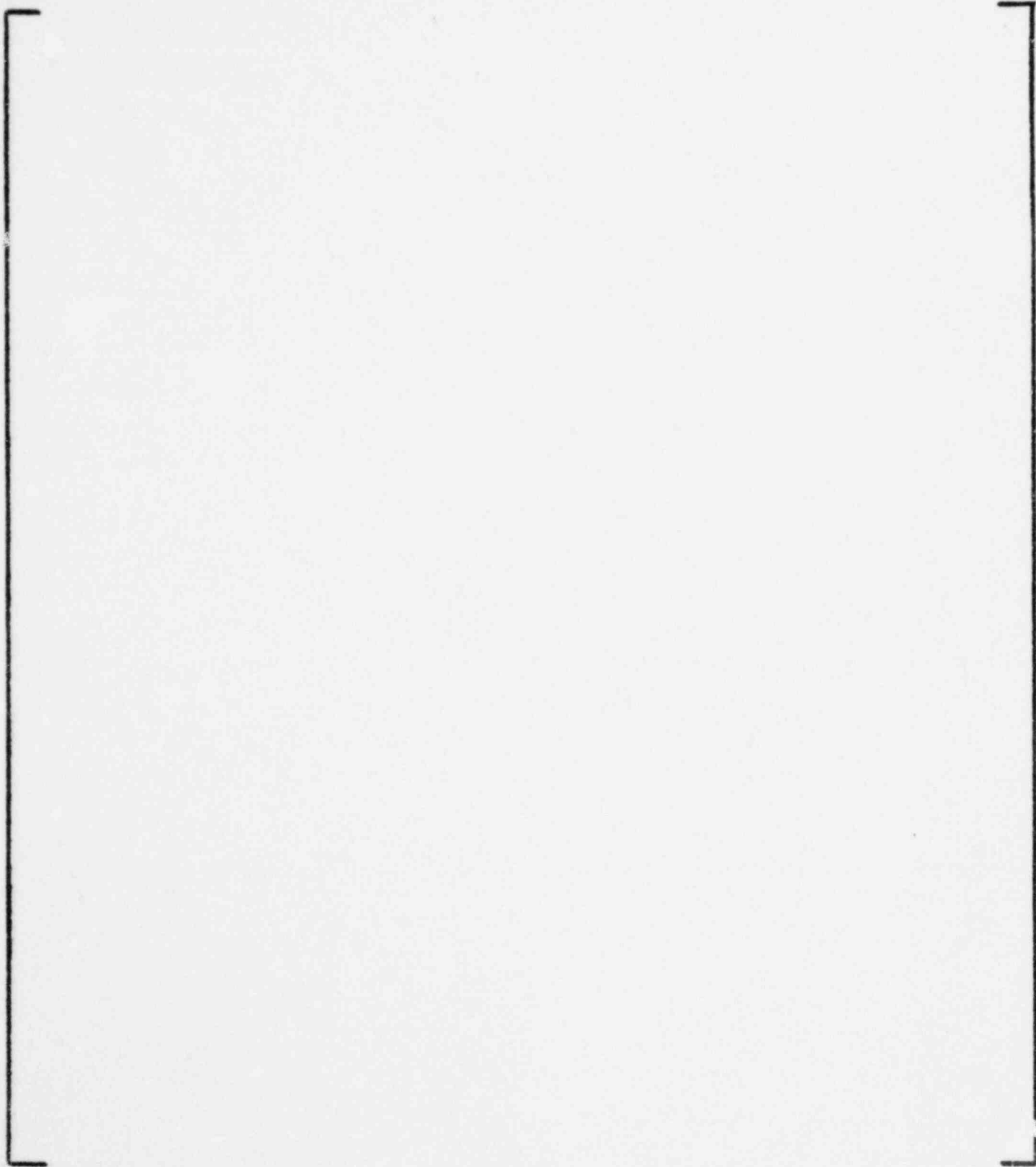
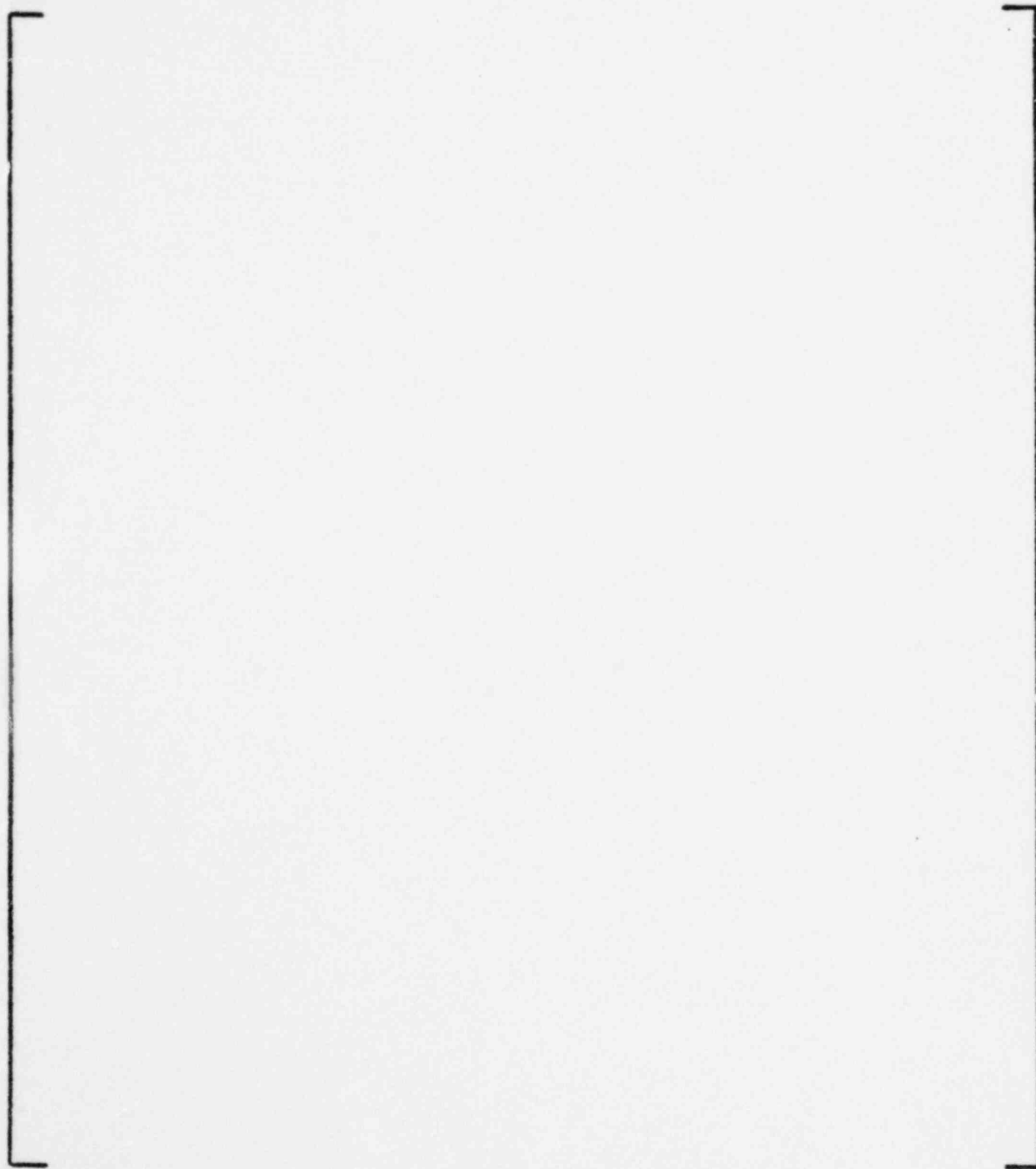


Figure 3-26

DISTRIBUTION OF DEVIATIONS IN F,  
CALVERT CLIFFS UNIT 1 CYCLE 3



EVALUATION OF UNCERTAINTY  
IN THE NUCLEAR POWER PEAKING  
MEASURED BY THE SELF-POWERED, FIXED IN-CORE  
DETECTOR SYSTEM

PART II

SOFTWARE SYNTHESIS UNCERTAINTIES

## II.0 INTRODUCTION

The INCA system provides a method of synthesizing signals from self-powered, fixed in-core detectors into detailed three-dimensional assembly and peak pin power distributions. The actual synthesis is done in the CECOR program using libraries of precalculated coefficients generated by standard diffusion and transport theory methods, and processed by codes in the INCA system. In this part of the report the basic CECOR methods and theory are described as well as the generation of the INCA libraries. Further, an evaluation is made of the uncertainties associated with the CECOR synthesis by carrying out a computer simulation of the process. These uncertainties are combined in Part III with the basic measurement uncertainties evaluated in Part I to provide the overall uncertainties.

The synthesis of the signals into three-dimensional power distributions is carried out in the CECOR program. This is done by using precalculated power-to-signal ratios to obtain the powers in instrumented assemblies at each detector level. The powers in uninstrumented assemblies are then obtained through the use of precalculated coupling coefficients which relate the power in an assembly to the average power in its neighbors. The axial power distribution in each assembly is then obtained using a few mode Fourier expansion. The peak pin powers are constructed using precalculated pin/box factors. The CECOR methods are described in Chapter 1.

Chapter 2 describes the generation of the various INCA coefficients used in the CECOR process. The coefficients are obtained from detailed multi-group diffusion theory calculations and are processed by codes in the INCA system to provide the INCA libraries.

The uncertainties associated with the CECOR synthesis process are evaluated in Chapter 3. This is done by using a computer simulation over three cycles in which signals are taken from three-dimensional calculations. These are processed through CECOR using INCA libraries generated according to the procedures in Chapter 2. The resulting CECOR power distributions are then compared to the calculated power distributions to evaluate the synthesis uncertainties.



## II.1 INCA ANALYTICAL METHODS

### 1.0 GENERAL

The C-E in-core detector signal analysis system, INCA, was originally developed and described in 1969<sup>(1.1)</sup>. Since then, many improvements have been made and the code has evolved to the present INCA/CECOR system<sup>(1.2-1.5)</sup> which is in use for all C-E reactors. It provides a method to synthesize a limited number of fixed, self-powered in-core detector readings into detailed full-core radial and axial distributions for assembly and peak pin powers.

Basically, the system uses prefit data from detailed, two-dimensional, multi-group diffusion theory calculations to convert detector readings to local box power values through the use of power/signal ( $W$ ) factors. These are provided for instrumented assemblies at each axial detector level in the core. The planar power distributions at each detector level are obtained through the use of pre-calculated average coupling coefficients  $\langle CC \rangle$ , which relate the power in an uninstrumented assembly to the average power in its neighboring assemblies. The axial power distributions are obtained by a few mode Fourier expansion which matches the box powers at each detector level. Subsequently, the peak pin powers in each assembly are obtained by the application of pin/box ( $F_p$ ) factors which are pre-calculated using fine mesh, two-dimensional transport theory corrected diffusion theory.

This chapter describes the analytical methods in detail, starting with the conversion of signal to power. This is followed by a discussion of the radial expansion, axial synthesis, the determination of pin peaking, and the types of edited output quantities.

## 1.1 DESCRIPTION OF CECOR METHODS

### 1.1.1 Definitions and System Description

In the following list of symbols, the integer  $i$  designates a fuel assembly or cell and the control rod it contains in the plan view, while  $n$  (1,2,3,4 or 5) indicates the axial detector level or position. The axial coordinate ( $z$ ) is measured from the bottom of the core.

- $\alpha_n$  = distance from the top of the  $n$ th detector to the core bottom.
- $\beta_n$  = distance from the bottom of the  $n$ th detector to the core bottom.
- $H_i$  = distance from the bottom of control rod  $i$  to the core bottom.
- $S_k$  = distance from the bottom of the  $k$ th rod bank region to the core bottom ("rod bank region" is defined below).
- $\delta_{rod}$  = dead band or uncertainty in rod location; [            ]
- $L_i$  = length of a part-length rod in assembly  $i$ .
- $I_{in}^{Rh}$  = rhodium detector background corrected current or signal from the  $n$ th axial detector of fuel assembly  $i$ .
- $P_{in}$  = power in assembly  $i$  integrated only over the length of axial detector  $n$ .
- $P_i(z)$  = power in assembly  $i$  per unit axial length at height  $z$ .
- $P_i$  = total power generated in fuel assembly  $i$ .
- $P_B$  = total power generated in a given batch of fuel assemblies.
- $P_C$  = total core power, normalized to calorimetric power.
- $W_{in}$  = power-to-signal coefficient which relates the integrated power in assembly  $i$  over the length of detector  $n$  to the signal from detector  $n$ .
- $CALIB_{in}$  = calibration factor in terms of rhodium activation per Rh atom per unit Maxwellian flux,  $\phi_0^{MAX}$ , impinging on the detector sheath.
- $V_{in}^{Rh}$  = volume of the  $n$ th rhodium detector located in assembly  $i$ .
- $\sigma_a^{Rh}(N^{Rh})$  = microscopic neutron absorption cross section of a rhodium detector as a function of Rh concentration,  $N^{Rh}$ .
- $S_{in}^{Rh}$  = sensitivity of rhodium detector  $n$  located at assembly  $i$ , relating detector current produced per unit Maxwellian flux at the detector sheath.

- $W_{in}^i$  = ratio of the power in assembly  $i$  integrated over the length of the  $n$ th detector to the rhodium detector activation per Rh atom.
- $\langle CC \rangle_{in}$  = average coupling coefficient for assembly  $i$  at the  $n$ th detector level.
- $P_{jn}^i$  = power in assembly  $j$  (neighboring assembly  $i$ ) integrated over the length of the axial detector  $n$ .
- $N_i$  = number of neighboring assemblies to assembly  $i$ .
- $h$  = assembly pitch.
- $M_{in}^2$  = neutron migration area at assembly  $i$ , level  $n$ .
- $k_{\infty in}$  = infinite multiplication factor at assembly  $i$ , level  $n$ .
- $I_{\ell n}$  = the set of instrumented boxes neighboring an uninstrumented box  $\ell$  at level  $n$ .
- $U_{\ell n}$  = the set of uninstrumented boxes neighboring an uninstrumented box  $\ell$  at level  $n$ .
- $U_n$  = the total number of uninstrumented boxes at level  $n$ .
- $B_i$  = axial fitting parameter for assembly  $i$ , as a function of core height,  $H$ , and extrapolation distance,  $\delta_i$ .

The axial configuration for a typical 4 detector level system is shown in Figure 1-1. The various axial portions of the core with different control rod bank configurations or patterns are defined as control rod bank regions. The coefficients used in each axial zone or control rod bank region are taken from the library for the corresponding rod configuration pattern. By finding these sets, the entire control bank configuration can be specified in terms of the population of each set and its withdrawal,  $S_k$ , as indicated in Figure 1-1.

To find the various rod bank sets, one scans all values of  $H_i$  to see which rods have their  $H_i$  within a specified dead band,  $\delta_{rod}$ , about the first one examined. The dead band represents the uncertainty in measuring rod positions and in keeping the rods aligned in a bank, and is generally taken as [     ] The process is then repeated for the remaining rods. The members of a set, distinguished by their  $i$  indices, are then compared with the membership of certain banks known in the library and distinguished by indices  $j$ . From

this procedure, the core configuration can be described completely as follows: the lowest axial rod bank region from 0 to  $S_1$  is bank  $j^0$  pattern, the next region from  $S_1$  to  $S_2$  is bank  $j^1$  pattern, etc., until the height of the upper bank limit is equal to the full core height. Normally, it is expected that only two to four rod banks will be present and thus the total number of possible bank configurations in the library will be less than fifteen, so the sorting among various alternative configurations is rapid.

Part-length control rods require special treatment since both the top and bottom of the poisoned section define bank region limits. This can be done by adding to the array of rod withdrawal values the additional values  $H_i + L_i$ , where  $L_i$  is the length of the part-length rod in assembly  $i$ .

### 1.1.2 Signal-to-Box Power Conversion

The power integral over a detector level in an instrumented assembly is obtained by multiplying the background corrected integrated detector signal by constants measured and supplied by the manufacturer, and constants calculated from fine-mesh, two-dimensional, multi-group diffusion theory calculations. The signal-to-box power conversion for an instrumented assembly  $i$  at detector level  $n$  is expressed by:

$$P_{in} = I_{in}^{Rh} W_{in} \quad (1.1)$$

where

$$W_{in} = \frac{CALIB_{in} W'_{in}}{S_{in}^{Rh}} \quad (1.2)$$

$$CALIB_{in} = \frac{\int_E \int_{V_{in}^{Rh}} \sigma_a^{Rh} (N^{Rh}) \phi(r, E) dr dE}{\phi_o^{MAX}} \quad (1.3)$$

$$W'_{in} = \frac{P_{in}}{\int_{E_{in}}^{E_{Rh}} \int_{V_{in}}^{V_{Rh}} \sigma_a (N^{Rh}) \phi \, dV \, dE} \quad (1.4)$$

consistent with the definitions in 1.1.1.

The detector sensitivity,  $S$ , relates the current,  $I$ , produced by the detector to the incident neutron flux at the surface of the detector. The initial sensitivity and relative calibration of the sensitivity are supplied by the vendor. As described in Chapter I.2, the sensitivity as a function of depletion for a given detector is determined by

$$S^{Rh}(t) = S_0 \left(1 - \frac{Q(t)}{Q_\infty}\right)^n \quad (1.5)$$

where

$S_0$  = the initial sensitivity for the detector, supplied by the vendor.

$\frac{Q(t)}{Q_\infty}$  = the fraction of the total available charge for the detector at time  $t$ , where  $Q_\infty$  is supplied by the vendor.

$n$  = the experimentally determined fitting parameter.

The  $W'$  are calculated for each assembly with a detector as a function of life from fine-mesh, 2-D planar depletion calculations using multi-group diffusion theory. The  $W'$  are then fit as a function of assembly burnup for each detector location. In current C-E cores, control rods do not enter instrumented assemblies. As a consequence, the  $W'$  presently are only calculated for unredded configurations. Future C-E core design include control rods in instrumented assemblies. For such cores the  $W'$  will be calculated for each control rod region. If the axial length of a detector corresponds to more than one rod region, the  $W'$  will be obtained by volume weighting the values for the respective rod regions.

### 1.1.3 Planar Power Distributions

At each detector level the powers in the uninstrumented assemblies are determined from the measured powers in instrumented assemblies. This is accomplished through the use of radial coupling coefficients.

The average coupling coefficient of an assembly at detector level  $n$  is defined as the ratio of the average power in the surrounding boxes to the power in the assembly itself. For the usual case of a cell surrounded by four boxes, this is

$$\langle CC \rangle_{in} = \frac{\sum_{j=1}^4 p_{jn}^i}{4P_{in}} \quad (1.6)$$

where  $P_{jn}^i$  denotes the power in boxes neighboring cell  $i$ . More generally,

$$\langle CC \rangle_{in} = \frac{\sum_{j=1}^{N_i} p_{jn}^i}{N_i P_{in}} \quad (1.7)$$

where  $N_i$  is the number of neighbors of box  $i$ .

The average coupling coefficient given by Eq. (1.7) is insensitive to mild power tilts across the core. In addition it has been found that local perturbation effects in a cell (e.g., from rods) essentially affect the coupling coefficient for only the subject box, i.e.,

$$\delta \langle CC \rangle_{in} = \frac{-h^2}{N_i M_{in}^2} \delta k_{\infty in} \quad (1.8)$$

as can be derived from the modified one-group diffusion equation. Eq. (1.8) has, in fact, been tested and found to accurately predict such perturbations in  $\langle CC \rangle_{in}$ .

In practice, the coefficients are pre-calculated from Eq. (1.7) using box power distributions obtained from either 2-D fine-mesh or 3-D coarse-mesh depletion calculations using multi-group diffusion theory, and are then fit as a function of burnup for each assembly. Explicit sets of burnup fitted coefficients are prepared for each control rod configuration or rod bank region. The actual values of  $\langle CC \rangle_{in}$  used in CECOR are obtained from these sets of fitted coefficients using average assembly burnup values obtained by integration over detector level  $n$ . When a detector level is penetrated by more than one rod bank region, the coefficients are obtained by volume weighting respective values for each rod bank region.

Knowing the average coupling coefficient values at a given detector level, the power in any uninstrumented box  $\ell$  may be obtained from:

$$P_{\ell n} = \frac{\sum_{j=1}^{N_{\ell}} P_{jn}^{\ell}}{N_{\ell} \langle CC \rangle_{\ell n}} \quad (1.9)$$

Originally<sup>(1.1)</sup>, INCA worked on the octant or quarter core basis, where symmetry was assumed and all instrument readings were reflected into the octant of interest. As a consequence, each uninstrumented box was surrounded by four instrumented boxes and Eq. (1.9) itself could be solved directly for each uninstrumented box. In the actual CECOR full core calculation, each uninstrumented box is not surrounded by four instrumented neighbors. In fact, many boxes have only one or two instrumented neighbors; and some have none. As a result, Eq. (1.9) cannot be solved directly for each uninstrumented box alone, since some of the neighboring powers are also unknown. However, at each level  $n$ , the equation may be written for every uninstrumented box,  $\ell=1, \dots, U_n$ , and then rearranged with the unknown powers

on one side of the equation and the known powers on the other. Thus, if  $I_{\ell n}$  and  $U_{\ell n}$  are the sets of instrumented and uninstrumented boxes neighboring  $\ell$ , respectively, then

$$N_{\ell} \langle CC \rangle_{\ell n} P_{\ell n} - \sum_{j \in U_{\ell n}} P_{jn}^{\ell} = \sum_{j \in I_{\ell n}} P_{jn}^{\ell}, \quad \ell = 1, \dots, U_n \quad (1.10)$$

where the summation on the left hand side is over uninstrumented neighbors, and the summation on the right hand side is over instrumented neighbors. When all the equations for each uninstrumented box are written and grouped, a  $U_n \times U_n$  matrix equation results:

$$A \underline{P} = \underline{S} \quad (1.11)$$

where for the unknown power  $P_{\ell n}$ , the  $\ell$ -th row of the matrix  $A$  has  $N_{\ell} \langle CC \rangle_{\ell n}$  on the diagonal and  $-1$  on the off-diagonals for those uninstrumented boxes which neighbor box  $\ell$ . The matrix  $A$  is symmetric when each assembly is coupled to all its neighbors. In addition,  $A$  is very sparse, with elements on the diagonal and  $N_{\ell}$  (usually 3 or 4) other elements in any row  $\ell$ . If uninstrumented assemblies are surrounded by four instrumented assemblies this new CECOR formulation reverts back to the original INCA scheme.

The solution for the unknown powers is obtained by solving Eq. (1.11). Symbolically:

$$\underline{P} = A^{-1} \underline{S} \quad (1.12)$$

This system is solved at each detector level.

Since the matrix can be large (on the order of 200x200), efficient solution routines are needed. From the standpoint of speed and memory requirements, a modification of the conjugate gradient method<sup>(1.6)</sup> which takes advantage of the unique nature of the  $A$  matrix is used.

A feature of this formulation is that if an instrument fails, the box is simply treated as uninstrumented and the resulting larger set of equations



is solved. For this to work, average coupling coefficients are precalculated and provided for all boxes, uninstrumented or instrumented. This concept also provides a way of checking detectors, since the actual detector power may be compared to the deduced power obtained by treating the box as uninstrumented. If the difference exceeds a predetermined criterion, it is an indication that either the detector has failed or a local perturbation may have occurred.

#### 1.1.4 Axial Power Distribution

Using the power in the assembly at each detector level, the detailed axial shape can be synthesized by using a Fourier expansion. This axial fitting technique is described in detail in Reference 1.4. Basically, the axial power distribution in an assembly is represented as the sum of the first  $N$  Fourier modes

$$P_i(z) = \sum_{n=1}^N a_n \sin n \pi B_i z \quad (1.13)$$

where  $P_i(z)$  is the power per unit length for assembly  $i$ ,  $a_n$  are the unknown combining coefficients,  $z$  is the axial elevation in fraction of the core height,  $H$ , and  $B_i$  is the fitting parameter given by

$$B_i = \frac{H}{H+2\delta_i} \quad (1.14)$$

Note that  $\delta_i$  is essentially an extrapolation distance. The  $N$  combining coefficients, and thus the axial power distributions are obtained by matching the box power at each level to the integral of Eq. (1.13) over the axial extent of each of the  $N$  detectors. Thus,

$$P_{in} = \int_{\beta_n}^{\alpha_n} dz \left( \sum_{n=1}^N a_n \sin n \pi B_i z \right), n=1, \dots, N \quad (1.15)$$

is used to solve for the  $a_n$  values for assembly  $i$ , where  $\beta_n$  and  $\alpha_n$  are the elevations for the bottom and top of detector level  $n$ , respectively. For instrumented assemblies, the  $P_{in}$  values are obtained directly from detector measurements. For uninstrumented assemblies, the values are obtained from planar power distribution solutions at each level, using the coupling coefficient formulation described in 1.1.3.

For four-detector systems, the fit is performed with three modes matching the bottom three detectors and three modes for the top three detectors. The distribution in the top or bottom half of the core is the appropriate fit. Four modes could also be used to match all 4 levels simultaneously. The accuracy in the axial synthesis and the magnitude of the axial peak-to-average power is essentially the same, although slightly better using 4 modes at once. For five axial detectors, one fit used over the whole range and five Fourier modes is used. This results in a significant improvement in the fitted results, especially for the more extreme shapes. This means that the accuracy of the axial synthesis is higher for a five detector system.

This is illustrated by a comparison of the two axial synthesis schemes using 4 or 5 detectors in the analysis of a variety of one-dimensional shapes<sup>(1.4)</sup>. The analysis is based on 17 axial shapes, ranging from typical to highly skewed in nature. A small representative sample of the shapes analyzed is shown in Figure 1-2. The statistical results are given in Table 1.I. These show that the single and overlapping expansions have essentially equivalent errors for the four level system, and that the five level system is clearly superior overall.

A larger base of 846 typical axial shapes from one- and three-dimensional calculations for both first and later cycle cores was similarly analyzed

with 4 and 5 level synthesis schemes. A sample of representative shapes is shown in Figure 1-3. The superiority of the five level system is again evident from this analysis, as indicated by the results in Table 1.II.

An important parameter in the Fourier expansion is the extrapolation distance ( $\delta$ ) or fitting parameter B. For 4 detector systems, B is a function of core life and is radial core zone dependent. B is obtained from nominal 3-D design depletion studies. It is chosen for each zone so as to drive the error in fitting the axial peak to average power ratio in each assembly towards zero. Figure 1-4 shows the characteristic behavior of B for a reload core in which the peripheral outer new fuel has a different shape than the inner old fuel. When five or more detector segments are available, a single depletion independent value of B can be used throughout the core.

#### 1.1.5 Total Power

Determination of radial and axial power distributions for the assemblies is completed using the methodology described in the previous sections. The total powers generated in each assembly,  $P_i$ , are obtained by integration over the axial shapes. Summation over the assemblies in a batch gives batch power,  $P_B$ , and summation over the batches gives the reactor power,  $P_C$ . The batch, assembly, axial assembly nodal, and core power are all normalized to the calorimetric power. The nodal burnups are updated by integrating the energy production over the elapsed time since the previous time point. This information is used to update the assembly, batch and core exposure counters. These, in turn, provide information advantageous to fuel management, and are used to evaluate the fits for INCA coefficients. Detailed edits of the assembly data are described in 1.2.

#### 1.1.6 Peak Pin Power Distributions

Detailed three-dimensional peak pin power distributions are obtained axially at each node for each assembly through the use of precalculated pin/box ( $F_p$ ) factors, which are fit to the assembly burnup. The pin/box factor is

defined as the ratio of the maximum 1-pin power in the box to the average pin power in the box. The precalculated values are obtained from detailed two-dimensional depletion calculations, using multi-group, transport theory corrected diffusion theory, for each rod bank configuration or region. The peak pin power at any axial location is then obtained using

$$P_{pi}(z) = F_{pi}(z) P_i(z) \quad (1.16)$$

where  $F_{pi}(z)$  is taken from the appropriate coefficient set and evaluated with the local assembly burnup at that elevation.

The 3-D pin power distributions can then be examined to find the peak pin power ( $F_{qi}$ ) for each assembly and for the core ( $F_q$ ). Axial integrals can be formed to find the peak pin channel power ( $F_{ri}$ ) for each assembly and for the core ( $F_r$ ). Further, the peak pin power to the average pin power can be obtained for each axial elevation,  $F_{xy}(z)$ , and for the core as a whole, ( $F_{xy}$ ). Conversions are also made to give peak linear rates in terms of actual powers rather than as ratios. The code also provides most of the parameters required to estimate DNB ratios. The DNBR calculation is not performed in INCA/CECOR, but in external programs, so it is not treated in this topical report. An overview of the edits is given in 1.2.

#### 1.1.7 Detection of Azimuthal Flux Tilt

An algorithm is present in the CECOR code which provides guidance regarding the presence and magnitude of an azimuthal power tilt in the reactor. It uses symmetric groups of instruments to detect and compute the magnitude of the ratio of the first harmonic to the fundamental mode. Precalculated fundamental and first harmonic form functions are used in the process. If the flux in a three-dimensional system is expanded in a harmonic series, i.e.,

$$\phi(r, \theta) = \phi_0(r, \theta) + \sum_{i=1}^{\infty} a_i \phi_i(r, \theta) \quad (1.17)$$

and is truncated after two terms, the following basic equation results:

$$\varnothing(r, \theta) \cong \varnothing_0(r, \theta) \left\{ 1 + a_1 \frac{\varnothing_1(r, \theta)}{\varnothing_0(r, \theta)} \right\} \quad (1.18)$$

Thus, the ratio of total flux to the first harmonic flux is

$$\frac{\varnothing(r, \theta)}{\varnothing_0(r, \theta)} = \{ 1 + a_1 f(r, \theta) \} \quad (1.19)$$

Analogously, from bare cylinder theory,

$$f_B(r, \theta) = g(r)f(\theta) = \frac{J_1(r)}{J_0(r)} \cos\theta \quad (1.20)$$

This suggests the following functional form for use in reflected heterogeneous systems:

$$f(r, \theta) = g(r) f(\theta) = \left\{ \frac{\varnothing_1(r, \theta)}{\varnothing_0(r, \theta) \cos\theta} \right\} \cos\theta \quad (1.21)$$

In CECOR, indications of any azimuthal flux tilting are obtained by comparing the signals from symmetrically located detectors at each level, and fitting them to the functional form:

$$\varnothing(r, \theta) = \varnothing_0(r, \theta) \left\{ 1 + sg(r) \cos(\theta - \theta_0) \right\} \quad (1.22)$$

where the fundamental flux pattern is  $\varnothing_0$ , the first harmonic tilt amplitude,  $s$ , and the orientation of the tilt,  $\theta_0$ . The functional  $g(r)$  is used to relate the tilt signals from different radial groups, and is obtained from 2-D diffusion theory calculations, where little sensitivity to fuel depletion is noted.

Estimates of  $s$  and  $\theta_0$  are obtained for each symmetric group for each axial level of detectors. The amplitudes and angles are then vectorially combined to obtain the best statistical estimate for  $s$ . Additionally, the components are weighted by the square of  $g(r)$ , since symmetric groups farthest from the core center provide the best estimates of tilt.

Several comments can be made concerning use of this algorithm to perceive power tilts:

- (1) The method formally considers first harmonic flux tilts, such as those caused by mild xenon oscillations and not higher mode tilts, i.e., those caused by sudden local perturbations such as dropped control elements.
- (2) A "noise" level exists where tilts indicated from individual groups are not well orientated with those from other groups. The deviations in tilt magnitude between the groups are generally less than 1%, however, and cause no operational concern.
- (3) Tilts larger than 2-5% indicate a higher possibility of a power tilt of some kind, and usually require close surveillance to continue operation.
- (4) Tilts higher than 10% indicate a high probability of either a flux tilt or an instrument problem. Simulated ejected control rod tests have shown that this type of tilt is large and leads to an indicated amplitude as large as 25%.

The tilt monitoring system is used to detect small tilts from the nominal symmetric design. Allowable tilts are currently limited to the range of 2 to 5% before the operator must intervene to reduce the tilt. The actual limits on the tilt are imposed through the Technical Specifications for each plant. For these small tilts, the system works adequately. Tilts due to unanticipated events would generally be larger than this and will be

detected, although the accuracy of the determination will decrease with the increasing tilting. However, such cases will be disallowed by the monitoring system, and corrective action will be taken.

## 1.2 DESCRIPTION OF INCA/CECOR EDITS

The INCA/CECOR programs calculate the assembly power in every bundle at all axial heights (usually every 2% in core height). They then use a local peaking factor at each of these axial nodes to determine the hottest pin. The assembly power at each node is used to increment the burnup history at each node in proportion to the energy extracted from the core in the period covered by the CECOR case.

These three quantities: box power, pin power, and box burnup at every node in the core, are available for editing in various ways for the convenience of the user. They are searched to find the core maximum value of each, integrated radially for axial (1-D) averages, and integrated axially for radial (2-D) averages. Other axial integrations cover just the instrumented regions. Powers are edited both in absolute (MW or kw/ft) values for determining limits, and are normalized to core average power for comparison with design models.

Normal editing in CECOR includes the following:

	<u>CECOR Edits</u>	<u>Number of Values</u>
Each instrument:	signal at each level	(4-5)
	burnup at each level	(4-5)
	power at each level	(4-5)
	alarm limit at each level	(4-5)
Each assembly:	burnup at instrument levels	(4-5)
	average burnup	(1)
	maximum burnup	(1)
	power at instrument levels -MW	(4-5)
	integrated power	(1)
	average relative power density	(1)
	maximum power	(1)
	maximum 1-pin linear heat rate - kw/ft	(1)
	max. relative pin power (3-D peak)	(1)
	integrated radial peaking factor ( $F_r$ )	(1)
	planar radial peaking factor ( $F_{xy}$ )	(1)
	axial shape index (ASI)	(1)
	peak of axial distribution ( $F_z$ )	(1)

Other than instrument level and axially integrated data, the following assembly quantities may be in a table or displayed graphically:

Each assembly:	box axial power distribution - normalized to core	(50)
	box axial power distribution - normalized to assembly	(50)
	peak pin axial power distribution - normalized to core	(50)
	axial burnup distribution	(50)



Also several overall core quantities can be edited:

Core:	core burnup	(1)
	core power - MW	(1)
	average axial power distribution	(50)
	average axial burnup distribution	(50)
	peak of axial power	(1)
	peak of axial burnup	(1)
	axial shape index	
	maximum of all the "each box" quantities	(~10)
	batchwise burnups	(~4-6)

- 1.1 R. L. Hellens, T. G. Ober, R. D. Ober, "Method of Analyzing In-Core Detector Data in Power Reactors," Trans. Am. Nucl. Soc., 12 (820), 1969.
- 1.2 T. G. Ober, P. H. Gavin, "Use of In-core Instrumentation in Combustion Engineering Power Reactors," Trans. Am. Nucl. Soc., 19 (218), 1974.
- 1.3 W. B. Terney, T. G. Ober, E. A. Williamson, Jr., "Three-Dimensional Calculational Verification of C-E's In-core Instrumentation System with Lifetime," Trans. Am. Nucl. Soc., 22 (681), 1975.
- 1.4 W. B. Terney, G. H. Marks, E. A. Williamson, Jr., and T. G. Ober, "Axial Power Distributions from Fourier Fitting of Fixed In-Core Detector Powers," Trans. Am. Nucl. Soc., 22 (682), 1975.
- 1.5 W. B. Terney, E. A. Williamson, Jr., T. G. Ober, "Calculational Verification of the Combustion Engineering Full Core Instrumentation Analysis System - CECOR," Trans. Am. Nucl. Soc., 24 (429), 1976.
- 1.6 A. Ralston, "A First Course in Numerical Analysis," McGraw Hill Book Co., 1967.

TABLE 1.1

Error\* Analysis of the Axial Peak to Average  
Power Ratio for 1-D Axial Shapes

<u>Case</u>	<u>Mean Error</u>	<u>Standard Deviation</u>	<u>Maximum Error</u>
4 detectors centered at 20, 40, 60, 80% of core height			
2 sets of 3 modes	0.1%	3.5%	9.3%
1 set of 4 modes	0.5%	3.1%	8.4%
5 detectors centered at 10, 30, 50, 70, 90% of core height			
2 sets of 3 modes	0.0%	1.2%	2.7%
1 set of 5 modes	0.2%	0.7%	1.5%

$$* \% \text{ error} = \frac{\text{real-fit}}{\text{real}} \times 100$$

TABLE 1. II

Error\* Analysis of the Axial Peak to Average  
Power Rates for All Shapes

<u>Case</u>	<u>Mean Error</u>	<u>Standard Deviation</u>	<u>Maximum Error</u>
4 detectors	0.1%	1.4%	+12%
5 detectors	0.1%	0.8%	- 6%

$$* \% \text{ error} = \frac{\text{real-fit}}{\text{real}} \times 100$$

Figure 1-1  
 AXIAL CONTROL ROD AND DETECTOR ARRANGEMENT  
 FOR FOUR DETECTOR SYSTEM

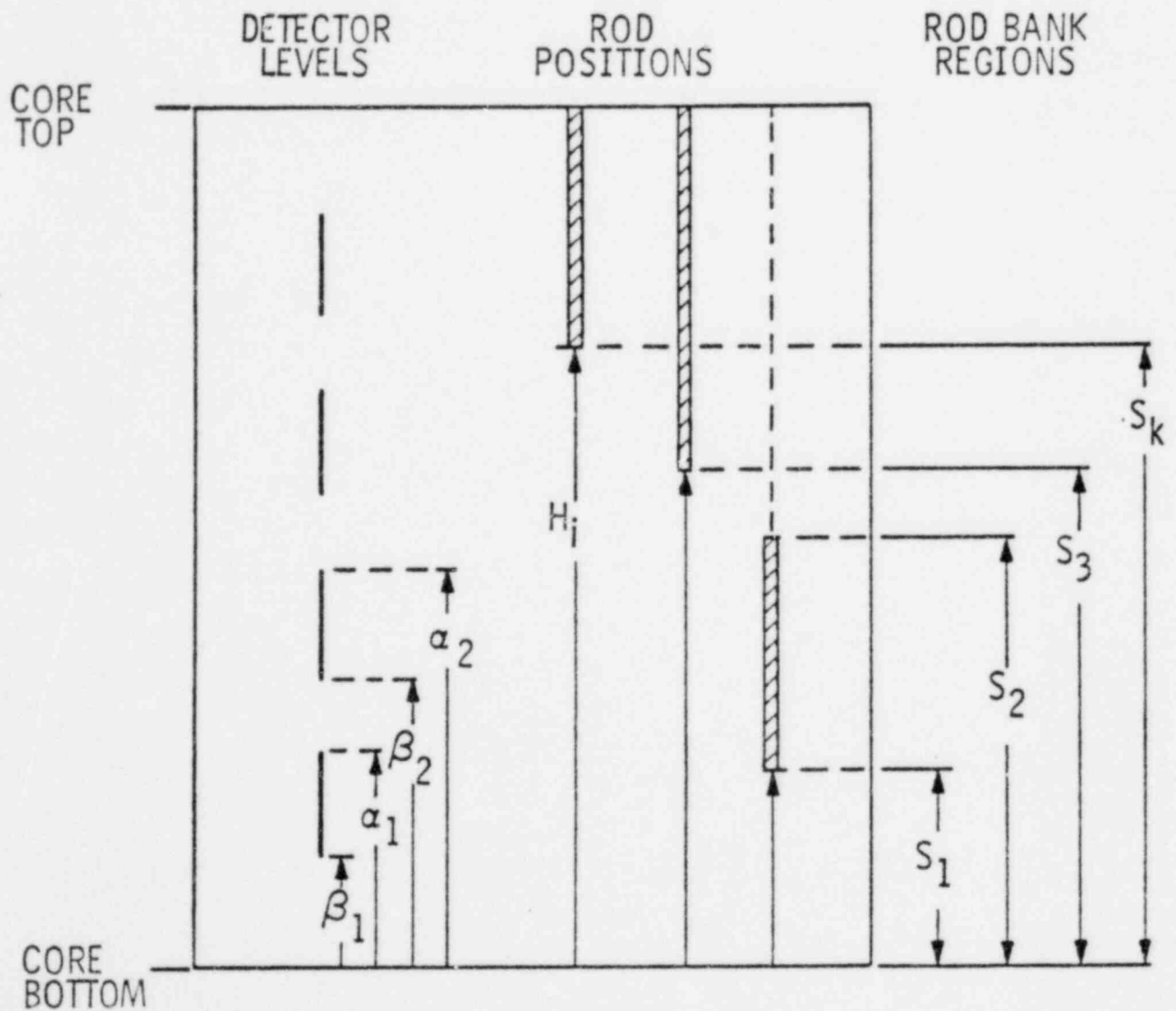


Figure 1-2  
REPRESENTATIVE AXIAL SHAPES FROM ONE-DIMENSIONAL ANALYSES

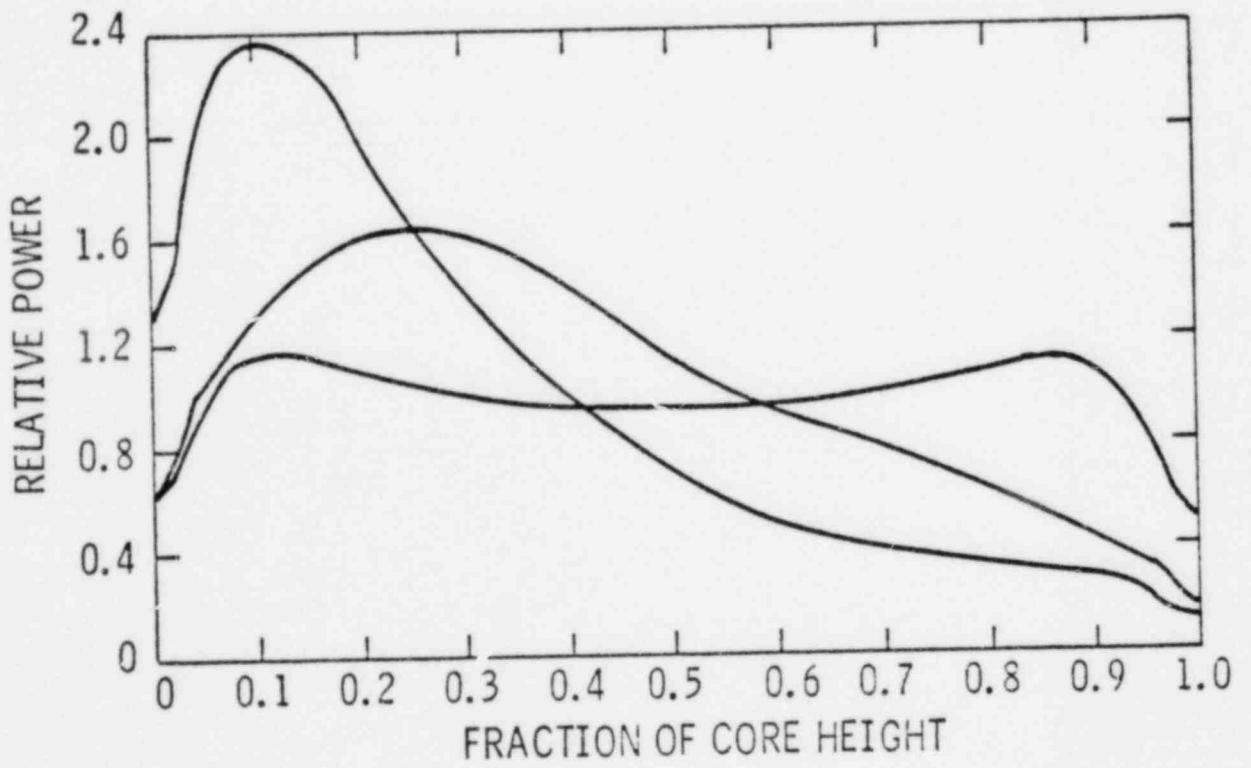


Figure 1-3  
TYPICAL AXIAL SHAPES  
ONE- AND THREE-DIMENSIONAL ANALYSIS

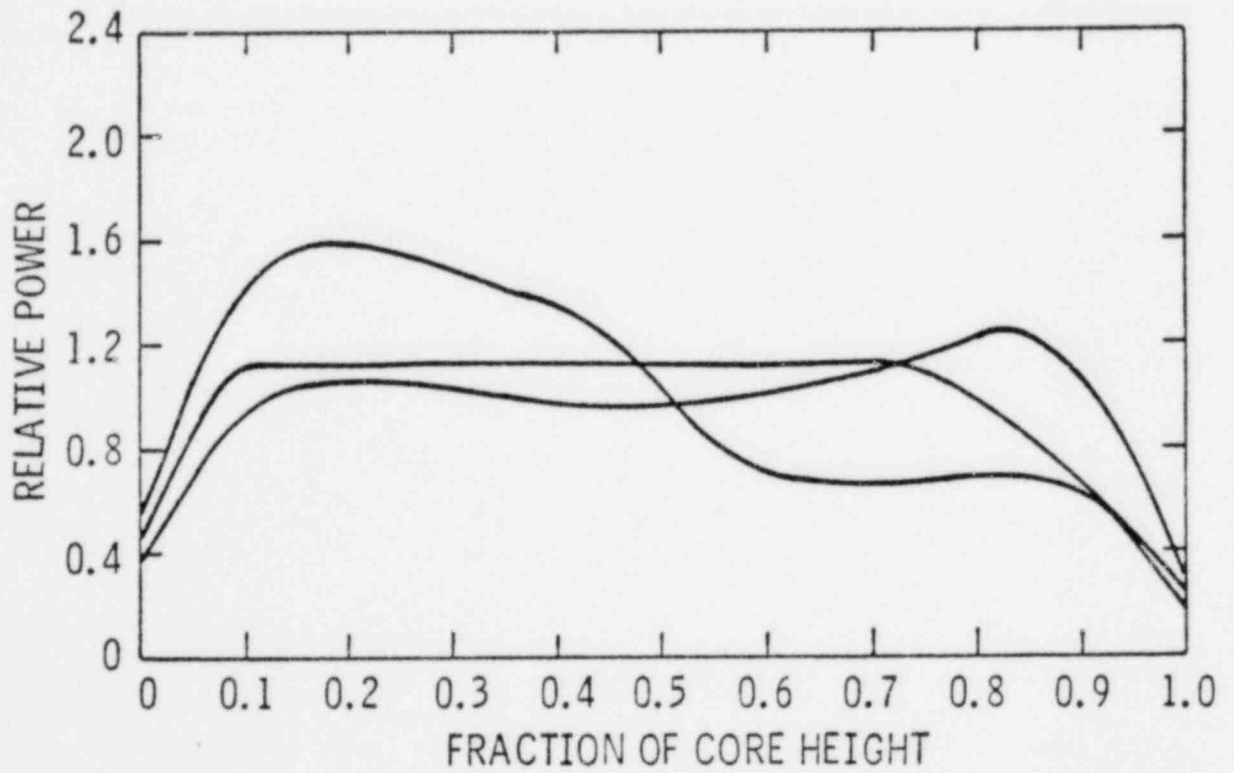
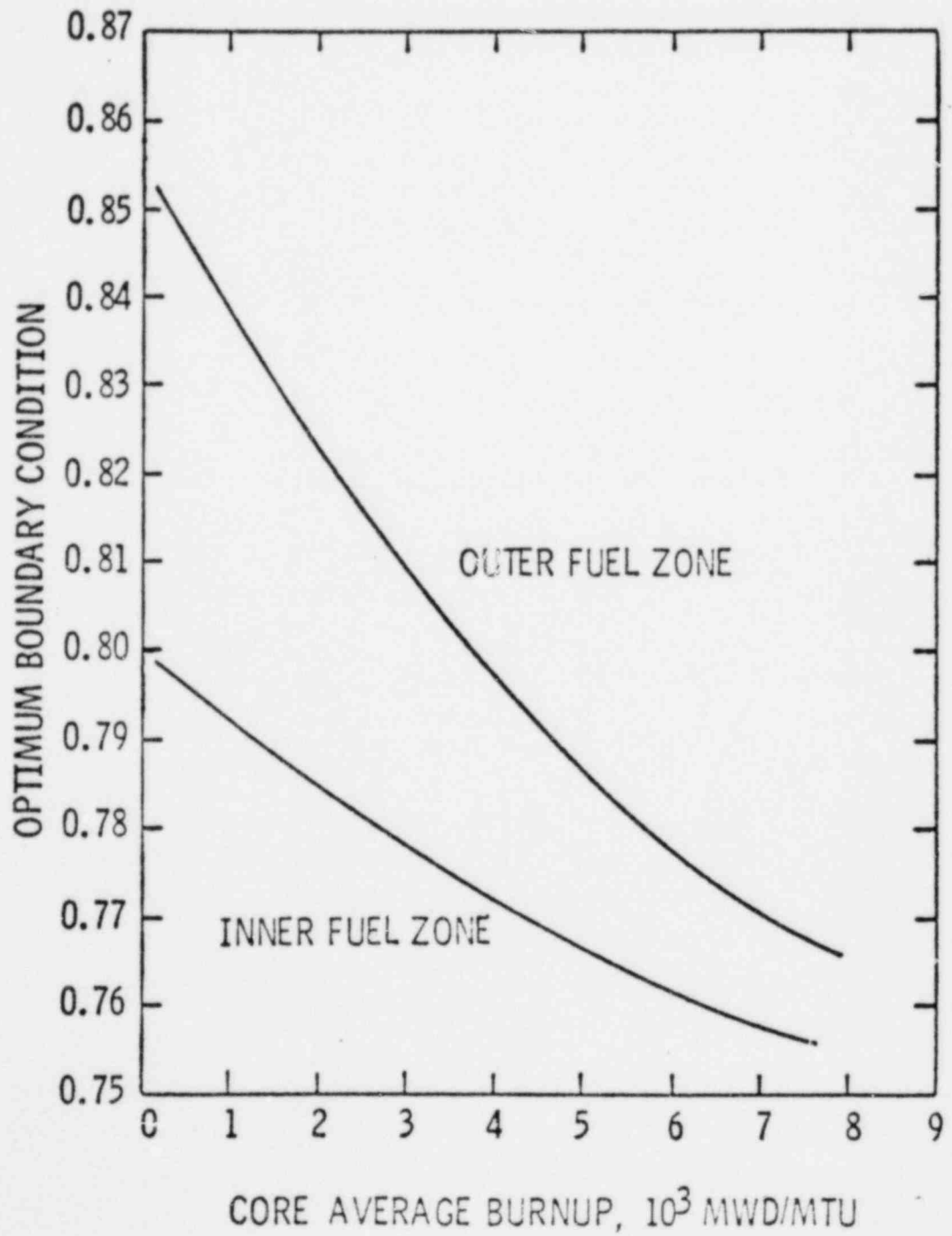


Figure 1-4  
TYPICAL CYCLE 2  
CECOR AXIAL BOUNDARY CONDITIONS





## II.2 INCA LIBRARIES

### 2.0 INTRODUCTION

The INCA/CECOR system relies on the use of a large library of predetermined coefficients which are used to convert the measured signals into detailed, three-dimensional assembly and peak pin power distributions. The values of these coefficients depend on the assembly and axial location, core configuration, control rod configuration, and the local assembly or nodal burnup.

The library coefficients  $\langle CC \rangle$ ,  $W'$ , and  $F_p$  defined in Chapter 1 are based on detailed, two-dimensional depletion calculations<sup>(2.1)</sup> using multi-group diffusion theory. Each assembly, instrument, and pin cell is explicitly represented in these calculations for each normal control rod configuration. The coefficient values are calculated for each assembly and instrument, and are fit as functions of the local burnup for each assembly. The two-dimensional calculations are taken to represent explicit axial regions or planes in the core.

For first cycles, which have separable power distributions, a core average plane is used with the various control rod configurations for cores with either four or five detector levels. For later cycles, which generally do not have separable power distributions, a plane representing the axial mid-region of the core is currently used. This leads to acceptable uncertainties, as shown in Part II. The use of several different planes to represent the different axial regions of the core would lead to lower uncertainties, since the axial variation of the coefficients would be included. The  $\langle CC \rangle$  could also be obtained directly from the normal, reload 3-D calculations. Multi-level coefficients may be used in the future for reload cores with either four or five detector levels. This will lead to lower synthesis uncertainties than those quoted in Part II.

The following sections describe the actual form of the coefficient library and the processes used in its generation.

## 2.1 FORMALISM

### 2.1.1 Signal-to-Box Power Conversion Factors

The coefficient  $W'_{in}$  has been defined in Section 1.1.2 as the conversion factor which relates the integrated power in assembly  $i$  over the length of detector  $n$  to the rhodium activation. These values are based on 2-D line-mesh calculations which explicitly represent the rhodium detector for every instrumented assembly. For new core designs where rods are present in instrumented assemblies, the values of  $W'_{in}$  are calculated for every rod bank configuration.

The behavior of  $W'$  with burnup is illustrated in Figure 2-1 for typical assemblies in each batch of a first cycle core. The burnup dependence is represented using cubic polynomial fits as a function of assembly burnup. Thus,  $W'(i,n)$  is computed in CECOR using

$$W'(i,n) = W^0(i,n) \cdot \sum_{j=0}^3 A_j(i,n) \cdot BU^j(i,n) \quad (2.1)$$

where

$W^0(i,n)$  = initial value of  $W'(i,n)$ .

$BU(i,n)$  = the average exposure in assembly  $i$  over the axial extent of detector  $n$ .

$A_j(i,n)$  = fitted polynomial coefficient in INCA library.

The  $A_j(i,n)$  coefficients are normally updated once per cycle, while the burnup values  $BU(i,n)$  are updated for each time step in CECOR.

### 2.1.2 Single Pin Power Peaking Factors

The one pin peaking factor,  $F_p$ , is defined as the ratio of the maximum pin power in an assembly to the average pin power in that assembly. In general,  $F_p$  depends on the assembly type, fuel burnup, core location, and control rod configuration. Therefore, it is calculated for every assembly in the plane for each rod bank configuration. The relative range of values for  $F_p$  is quite large, varying from 1.1 to greater than 2.0 in some peripheral or rodded fuel assemblies. Additionally, the shape of  $F_p$  with burnup differs among assemblies, as is illustrated in Figure 2-2. The burnup dependence is represented by fits of up to the third order for each assembly of each control rod configuration. Thus, the local pin peaking factor for axial node k of assembly i is obtained in CECOR using

$$F_p(i,k) = F_p^o(i,m) \cdot \sum_{j=0}^3 R_j(i,m) \cdot BU^j(i,k) \quad (2.2)$$

where

$F_p^o(i,m)$  = initial value of  $F_p$  for assembly i, control rod configuration m.

$BU(i,k)$  = exposure at axial node k of assembly i.

$R_j(i,m)$  = fitted library coefficient for assembly i, control rod configuration m.

### 2.1.3 Coupling Coefficients

The average coupling coefficient,  $\langle CC \rangle_{in}$ , has been defined in Section 1.1.3 as the ratio of the average power of neighboring boxes to the average power of assembly i at detector level n. Its value depends on the assembly type, location, burnup, neighboring assemblies, and control rod configuration.

A comparison of typical shapes of  $\langle CC \rangle$  with burnup for rodded and unrodded assemblies is shown in Figure 2-3. The calculated values of  $\langle CC \rangle$  are fit as a

function of assembly burnup over the detector length. By having values for every assembly, an instrumented location can simply be treated as uninstrumented for the purpose of eliminating failed detector signals, or as a diagnostic method of testing for failing detectors.

The INCA library representation for  $\langle CC \rangle_{in}$  uses a cubic polynomial fit with burnup, i.e.,

$$\langle CC \rangle(i,n) = \langle CC \rangle^o(i,m) \cdot \sum_{j=0}^3 G_j(i,m) \cdot BU^j(i,n) \quad (2.3)$$

where

- $\langle CC \rangle^o(i,m)$  = initial value of  $\langle CC \rangle$  for assembly  $i$ , configuration  $m$ .
- $BU(i,n)$  = average exposure in assembly  $i$  over detector level  $n$ .
- $G_j(i,m)$  = fitted library coefficient for assembly  $i$ , control rod configuration  $m$ .

#### 2.1.4 Azimuthal Tilt Functions

As described in Section 1.1.7, use is made of radial functions,  $g(r)$ , derived from two-dimensional diffusion theory solutions to detect small flux tilts. These tilt functions closely approximate the  $J_1/J_0$  ratio predicted from bare cylinder theory. A typical  $g(r)$  is shown in Figure 2-4 along with the analogous cylinder functions. The smoothness of the function is readily seen. The burnup dependence of these functions has been found to be insignificant over the length of the cycle.

#### 2.1.5 Axial Fitting Parameters

The axial fitting parameter,  $B$ , is precalculated by radial fuel zone as a function of core-average burnup based on normal, 3-D depletion studies with the ROCS code. (2.2, 2.3) The method of calculating  $B$  is described in Section 1.1.4. In CECOR, the individual assembly values of  $B$  are obtained from the corresponding zonal fits as a function of core-average burnup.

It is apparent from the previous sections that the INCA libraries are both large and complex. In a typical application, approximately 5000 coefficients must be stored and retrieved upon demand. An automated computer code system has been developed to facilitate both the generation and quality assurance of these libraries. The sequence of steps required to produce a typical library is shown schematically in Figure 2-5.

The generation of the basic data required for INCA, i.e., the pointwise powers, fluxes, and concentrations, is currently performed through standard fine mesh diffusion theory calculations using the PDQ-7 computer code<sup>(2.1)</sup>. Approximately 15 such calculations are required. Primary editing of the PDQ-7 files is performed by the CERISE code, a proprietary code of C-E. This operation transforms the pointwise PDQ-7 data into assembly-wise data required by INCA. Summary files are written for use in Paths B-D in Figure 2-5. Detector signals consistent with the library are also generated for testing the completed library.

The generation of the INCA library is indicated in Path B of Figure 2-5 and is the work of the INCLIB code, a C-E proprietary code. At this stage, libraries are available for quality assurance testing and then actual use at the reactor site.

All the codes<sup>(2.1-6)</sup> used in generating the libraries and their functions are given in Table 2.I. These codes are quality assured and maintained in accordance with internal quality assurance procedures for computer codes. To adequately test the library, the INCA code is executed using the file created in Step B and the signals in Step A in a fashion identical to the manner in which the PDQ-7 cases were executed. The results are stored and compared to the original CERISE data (Step D).

Final testing of the INCA program and libraries must be performed at the reactor site. Sample test cases from the above effort serve to verify the coding and the data. Test results and procedures are properly recorded and documented for future reference.

2.3 REFERENCES

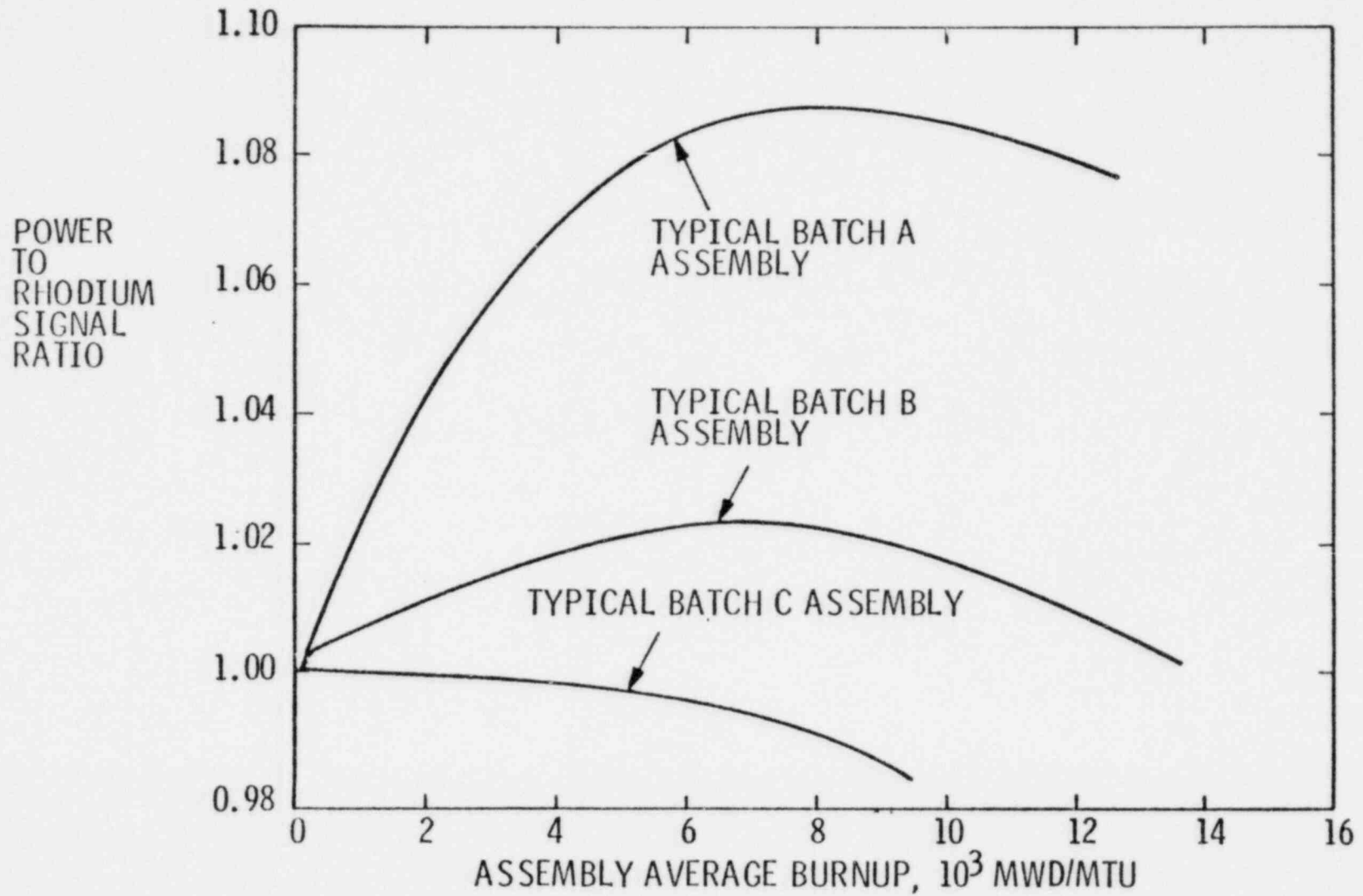
- 2.1 W. R. Caldwell, "PDQ-7 Reference Manual," WAPD-TM-678, January, 1969.
- 2.2 T. G. Ober, J. C. Stork, I. C. Rickard, J. K. Gasper, "Theory Capabilities and Use of the Three-Dimensional Reactor Operation and Control Simulator (ROCS)," Nucl. Sci. and Eng., 64 (605), 1977.
- 2.3 T. G. Ober, J. C. Stork, R. P. Bandera, W. B. Terney, "Extension of the ROCS Coarse Mesh Physics Simulator to Two Energy Groups," Trans. Am. Nucl. Soc., 28 (763), 1978.
- 2.4 A. Jonsson, et.al, "Discrete Integral Transport Theory Extended to the Case with Surface Sources," Atomkernenergie, Bd. 24, 1974.
- 2.5 A. Jonsson, et.al., "Verification of a Fuel Assembly Spectrum Code Based on Integral Transport Theory," Trans. Am. Nucl. Soc., 28 (778), 1978.
- 2.6 Combustion Engineering Standard Safety Analysis Report (CESSAR), Chapter 4.3.

TABLE 2.1

Summary of Computer Codes Used  
in Generation of INCA Libraries

CODE	TYPE	DESCRIPTION	TYPICAL NUMBER OF CASES
DIT/CEPAK (2.4,2.5, 2.6)	Cross section generation	standard design depletion calculations	5 depletions (of ~10 time steps each)
PDQ-7 (2.1)	2-D fine mesh 2 or 4 group diffusion theory calculations	standard unrodded design 2-D depletion plus several rodded cases	15 cases
ROCS (2.2,2.3)	3-D coarse mesh 2-group diffusion theory calculations	standard unrodded design 3-D depletion	10 cases
CERISE	PDQ-editor	provides edited information (i.e., detector signals, assembly power, etc.)	one for each PDQ- case
INCLIB	INCA library generator	fits all INCA coefficients to burnup and provides properly formatted library	one per core

Figure 2-1  
POWER TO RHODIUM SIGNAL CONVERSION FACTORS  
vs ASSEMBLY AVERAGE BURNUP



11.2.8



Figure 2-2  
SINGLE PIN PEAKING FACTOR VARIATION WITH BURNUP

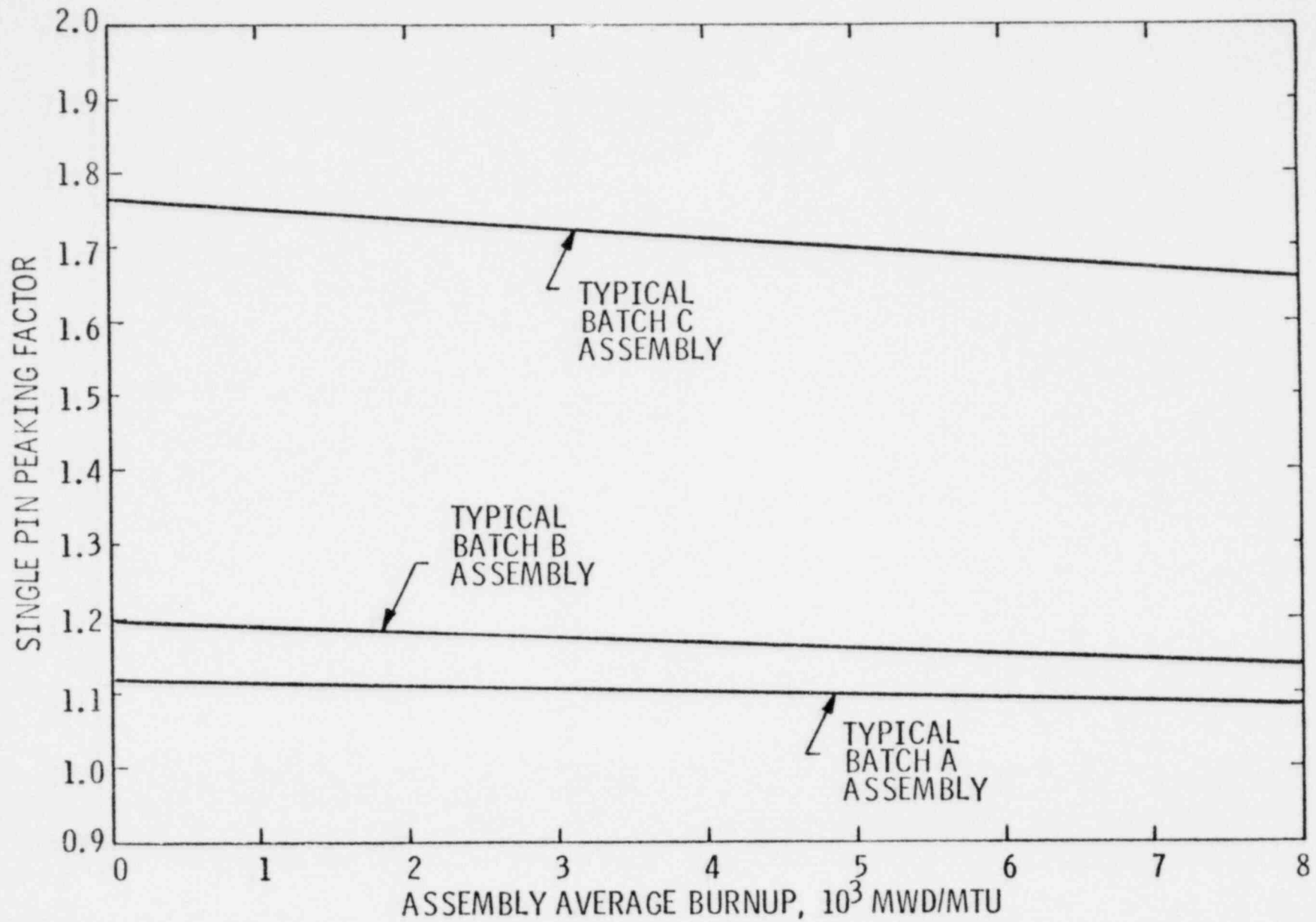


Figure 2-3  
TYPICAL AVERAGE COUPLING COEFFICIENT BEHAVIOR

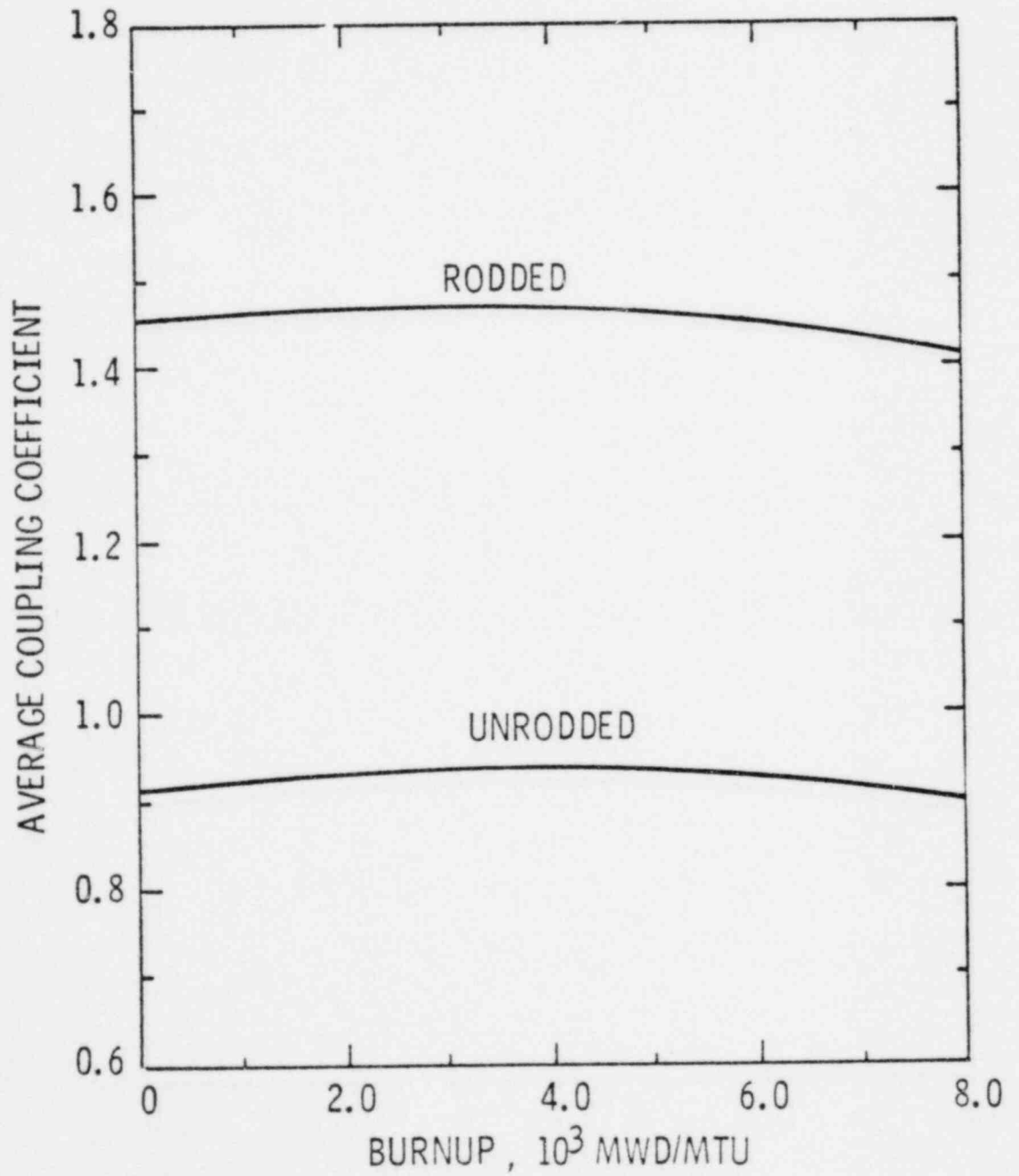


Figure 2-4  
RADIAL TILT FUNCTION  $g(r)$

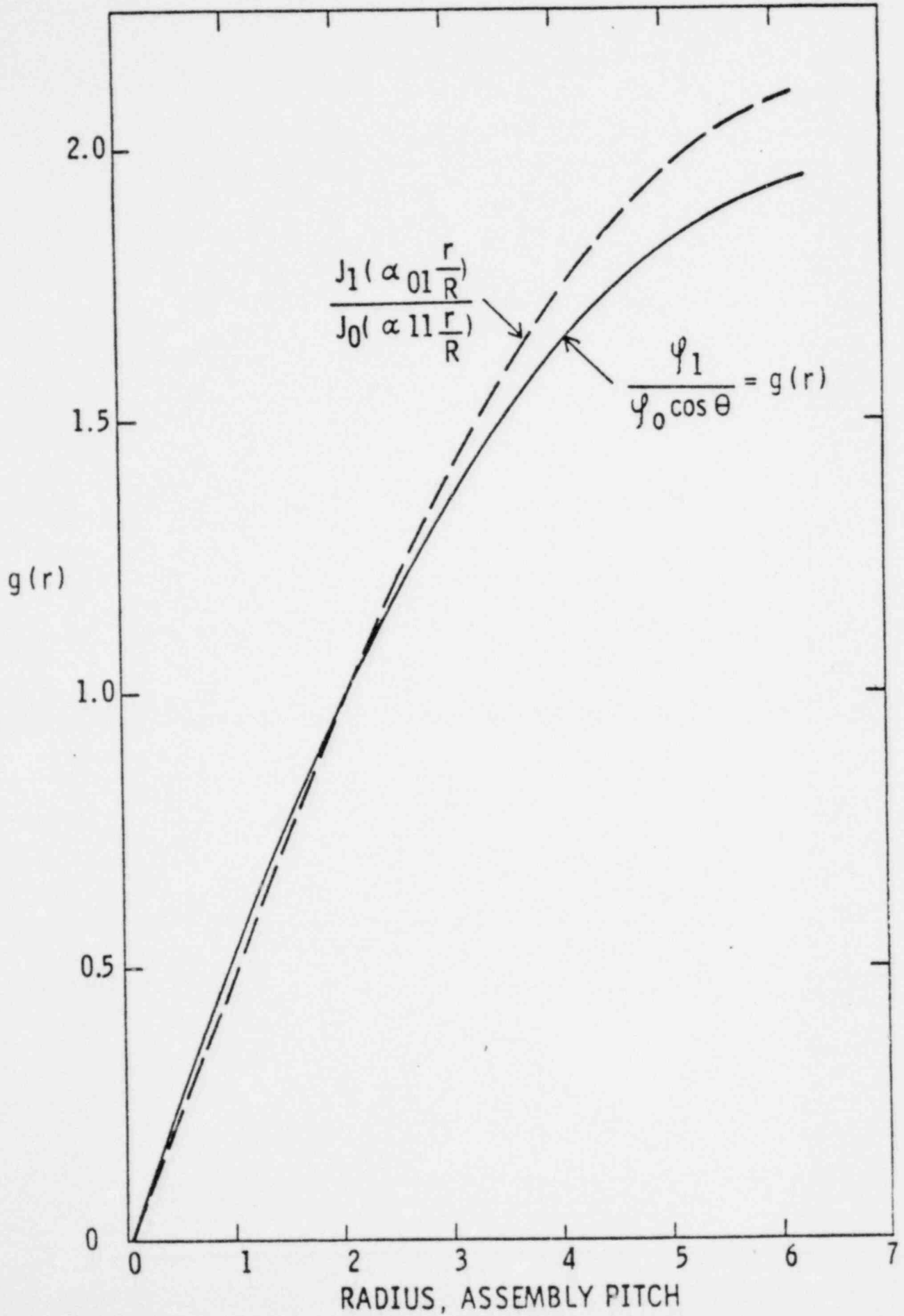
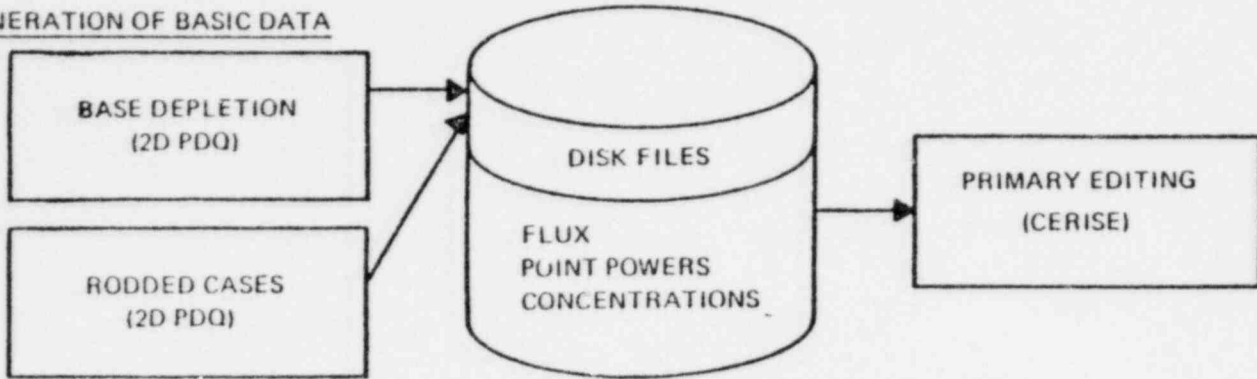


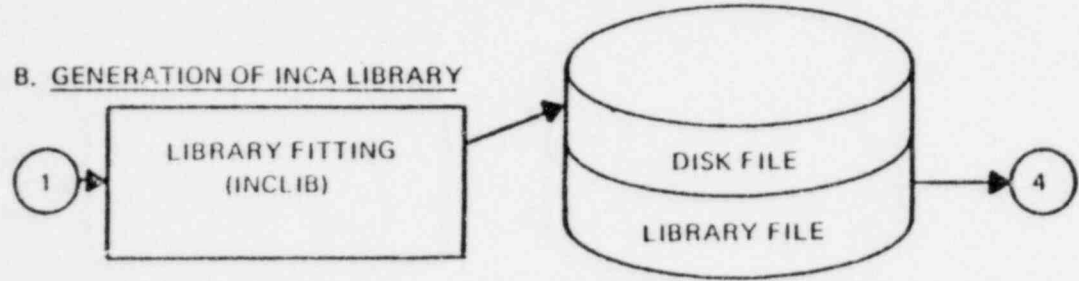
Figure 2-5

### GENERATION AND QUALITY ASSURANCE OF INCA LIBRARIES

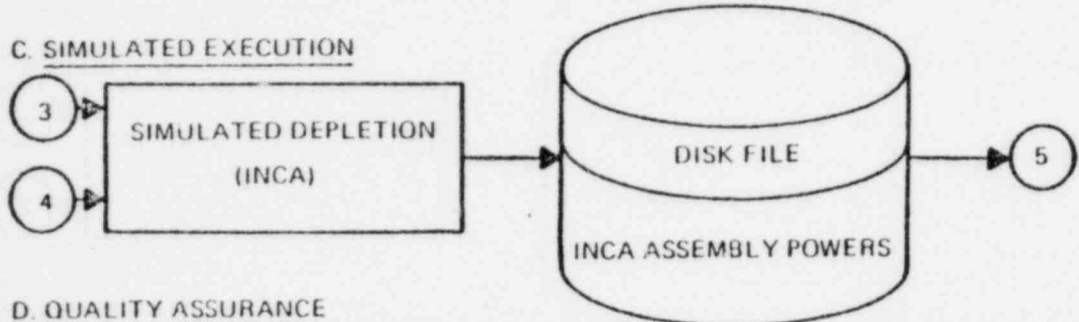
A. GENERATION OF BASIC DATA



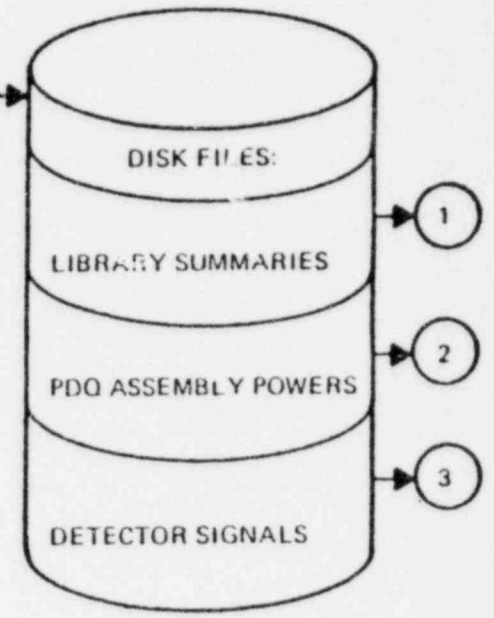
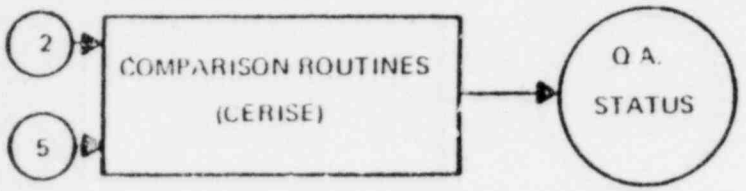
B. GENERATION OF INCA LIBRARY



C. SIMULATED EXECUTION



D. QUALITY ASSURANCE



II.2.12

## II.3 SYNTHESIS UNCERTAINTIES

### 3.0 INTRODUCTION

#### 3.0.1 Description of Methods

The uncertainties to be attributed to the INCA software system are evaluated by separate analyses of (1) assembly or box power synthesis errors and (2) pin peaking synthesis errors consisting of INCA system synthesis errors and basic pin/box calculational errors.

Box power synthesis errors arise in the process of extrapolating to uninstrumented locations axially and radially.

Pin power synthesis errors arise because the pin power is not measured directly but is inferred from the use of calculated pin/box factors (cf. II.2). Uncertainties in the pin/box factors are due to:

- a) The calculative process itself.
- b) The reconstruction of the calculated pin/box factors by INCA/CECOR.

In this chapter, the terminology used refers to these two sources of uncertainty as the pin peaking calculational uncertainty and the pin peaking synthesis error, respectively.

##### 3.0.1.1 Box Power Uncertainty Analysis

The analysis of box power synthesis uncertainties is based upon comparisons of reference three-dimensional diffusion theory calculations against INCA system synthesis calculations, [

]

The analysis has been done for the first three cycles of Calvert Cliffs (CC) Unit 1, using three-dimensional core-follow calculations performed with the two-group ROCS code (References 3.1 and 3.2) as a source for the true power distribution [

] The box power distribution synthesis errors were thus determined by comparison of the ROCS reference calculations and the CECOR synthesis calculations for the three reactor cycles. [

] The core layout and maneuver structure in the ROCS reference calculation and the CECOR synthesis models are described in Section 3.1.1.

Estimates have been made at each timepoint for (1) box power synthesis uncertainty in power sharing ( $\sigma_{SF_r}$ ) by comparing ROCS and CECOR values of [

(2) the overall box power synthesis uncertainty ( $\mu_{SF_q}$ ,  $\sigma_{SF_q}$ ) by comparing ROCS and CECOR values of [

] (3) the planar peak box power synthesis uncertainty ( $\mu_{SF_{xy}}$ ,  $\sigma_{SF_{xy}}$ ) by comparing ROCS and CECOR values of [

] The calculational and statistical models used in the box power uncertainty analysis are described in Section 3.1.2.

### 3.0.1.2 Pin Peaking Uncertainty Analysis

The component of pin peaking uncertainty attributed to synthesis error ( $\mu_{SF_p}$ ,  $\sigma_{SF_p}$ ) is estimated using [

] for existing reload core models. [

] These differences form a conservative basis for estimating the pin peaking synthesis error, [

]

The analysis of the pin peaking synthesis uncertainty has been made using [ ] calculations performed with the PDQ code (Reference 3.3) for several C-E reload cores, including Calvert Cliffs Unit 2 Cycle 2, St. Lucie Unit 1 Cycle 2, Millstone Unit 2 Cycle 2, and Calvert Cliffs Unit 1 Cycle 4. Descriptions of the reactor configurations and PDQ models used for the pin peaking synthesis analysis are given in Section 3.2.1. The calculational and statistical models are described in Section 3.2.2.

The basic pin peak calculation uncertainty ( $\mu_{CFP}$ ,  $\sigma_{CFP}$ ) has been determined with the use of data from two series of critical experiments which simulate typical C-E MARK V fuel assembly designs:

- (1) Combustion Engineering Sponsored Critical Experiments (C-E Criticals) performed at the Westinghouse Reactor Evaluation Center (WREC);
- (2) KRITZ Experiments, sponsored jointly by C-E and NWU and performed at the KRITZ critical facility of AB Atomenergi, Sweden.

The experiments are described in detail in Section 3.3.1. The calculational method and statistical model used in evaluating the pin-peaking calculational uncertainty are described in Sections 3.3.2 and 3.3.3.

### 3.0.2 Summary of Results

The estimates of box power synthesis uncertainty for the parameters  $F_r$ ,  $F_q$  and  $F_{xy}$ , as well as the number of degrees of freedom in the sample estimates, are summarized in Table 3.I. The results are described in Section 3.1.3.

The estimate of pin peaking or  $F_p$  synthesis error is included in Table 3.I, and results are described in Section 3.2.3. Similarly, the estimate of basic  $F_p$  calculational uncertainty is included in Table 3.I, and results are described in Section 3.3.4.



## 3.1 BOX POWER SYNTHESIS UNCERTAINTIES

### 3.1.1 Description of Calculation Models

#### 3.1.1.1 ROCS Reference Models

The three-dimensional ROCS models and calculations used in the box power distribution synthesis analysis were based on the core layouts and operating histories for the first three cycles of Calvert Cliffs (CC) Unit 1, as described in Chapter 3 of Part I. The operating histories for these three cycles are typical of other 217 assembly C-E reactors, and include operations with reduced power and partial insertion of the lead rod bank (Rod Bank 5). The ROCS calculations were performed using quarter-core geometry with 24 axial planes. The quarter-core models used are consistent with the full-core layout and loading patterns for Cycles 1 through 3 as shown in Figures 3-1 through 3-3, respectively. These figures also show the box locations for Rod Bank 5 and the 45 in-core detector strings. The ROCS maneuver structures for the three cycles, including rod insertions, are given in Tables 3.II through 3.IV. The 3-D ROCS calculation results are identical to those described in Chapter 3 of Part I.

#### 3.1.1.2 CECOR Synthesis Models

The CECOR models used for the box power synthesis calculations use full-core geometry corresponding to the layouts in Figures 3-1 through 3-3 for Cycles 1 through 3 of Calvert Cliffs Unit 1. The axial geometries of the ROCS and CECOR models, including the four detector levels, are shown in Figure 3-4.

The maneuver structures used in the CECOR models are identical to the ROCS maneuver structures in Tables 3.II through 3.IV. [

]

[ ] Test signals were not used in the CECOR calculations for instruments which were failed according to the operating history. Thus the error analysis includes the effect of failed detectors on the full-core solution. The failed instruments for each CECOR model timepoint are given in Tables 3.V through 3.VII for Cycles 1 through 3 of Calvert Cliffs Unit 1.

[

] INCA library polynomial fits of coefficient values as a function of local burnup were then produced for each cycle according to the formalism described in Section 2.1.

Axial synthesis boundary conditions used in the CECOR calculations were obtained by using the results of design three-dimensional ROCS depletion calculations [ ] for Cycles 1 through 3 of Calvert Cliffs Unit 1.

#### 3.1.1.3 Summary of Calculation Models

The CECOR calculations used in the box power synthesis uncertainty analysis were modeled consistently from the reference three-dimensional ROCS core-follow calculations for Cycles 1 through 3 of Calvert Cliffs Unit 1, using the geometries, maneuver structures, INCA coefficient libraries, failed instruments, and axial boundary conditions described above. The BOC exposure distributions used for the CECOR depletion calculations for Cycles 2 and 3 were obtained by shuffling EOC exposures from the previous cycles, according to INCA system procedures.

### 3.1.2 Statistical Model for Calculation of Box Power Synthesis Uncertainties

#### 3.1.2.1 Definitions

$N_F$  Number of boxes or assemblies in full core; =217

$K$  Number of Axial planes in ROCS core model; =24

$K_L$   
 $K_U$   
 $N_{LU}$

$J$  Number of axial nodes in CECOR core model; =51

$h_k$  Thickness of plane  $k$  of ROCS core model

$h_c$  Uniform mesh thickness between CECOR axial nodes

$H$  Total core height;

$$= \sum_{k=1}^K h_k = (J-1)h_c$$

$P_{ik}^R$  Calculated value of power for box  $i$  of ROCS plane  $k$  from the ROCS reference calculation

$P_{ij}^C$  Calculated value of power per axial mesh thickness  $h_c$  for box  $i$  at axial node  $j$  from the CECOR synthesis calculation

$P_{ik}^C$  Calculated value of summed axial power for box  $i$  corresponding to ROCS plane  $k$  from the CECOR synthesis calculation;

$$= \sum_{j \in k} P_{ij}^C$$

$P_i^R$  Calculated value of axially integrated power for box  $i$  from the ROCS reference calculation, obtained by summing;

$$= \sum_{k=1}^K P_{ik}^R$$

$P_i^C$  Calculated value of axially integrated power for box i from the CECOR reference calculation, obtained by the trapezoidal rule;

$$= \sum_{i=1}^J P_{ij}^C - 1/2 (P_{i1}^C + P_{iJ}^C)$$

$P_k^R$  Calculated value of power for ROCS plane k from the ROCS reference calculation;

$$= \sum_{i=1}^{N_F} P_{ik}^R$$

$P_k^C$  Calculated value of power corresponding to ROCS plane k from the CECOR synthesis calculation;

$$= \sum_{i=1}^{N_F} P_{ik}^C$$



$\sigma_S$  The standard deviation of box power differences between truth and synthesis calculation.

$\mu_S$  The bias of box power differences between truth and synthesis calculation

$S_S$  Sample standard deviation of box power differences between truth and synthesis calculation.

$\bar{D}_S$  Sample bias of box power differences between truth and synthesis calculation.

$M_2$  Number of data points for a sample 2.

$N_{TOT}$  Total sample size.

$N_{DEG}$  Total number of degrees of freedom.

Estimates of the one-sided upper tolerance limit are given by  $\bar{D}_S + kS_S$ , where  $\bar{D}_S$  and  $S_S$  are the sample bias and standard deviation, respectively, and  $k$  is the probability/confidence factor for the sample.

### 3.1.2.2 $F_r$ Uncertainty: $S_{Fr}$

For the  $F_r$  box power synthesis uncertainty the box to core-average values of axially integrated assembly powers from the CECOR and ROCS calculations are compared for all 217 full core boxes. The normalization is:

$$\sum_{i=1}^{N_F} p_i^C = \sum_{i=1}^{N_F} p_i^R = P \quad (3.1)$$

where  $P$  is the total core power.

3.1.2.3  $F_q$  Uncertainty:  $S_{S_{Fq}}, \bar{D}_{S_{Fq}}$

3.1.2.4  $F_{xy}$  Uncertainty:  $S_{S_{Fxy}}$ ,  $\bar{D}_{S_{Fxy}}$

3.1.2.5 Summary of Sample Variances and Biases

The sample variances and biases given by Equations 3.4, 3.6, 3.7, 3.9 and 3.10 are estimates of the variances and biases attributed to the synthesis errors for box power  $F_r$ ,  $F_q$  and  $F_{xy}$ .

### 3.1.2.6 Procedure for Pooling Estimates for the Variance and Bias

The estimates for the variances and biases discussed above are applicable for comparisons at each timepoint. Pooling over the timepoints is accomplished by calculating the bias  $\bar{D}$  and variance  $S^2$  for the entire set of sample comparison cases,  $\ell = 1, \dots, L$ , using the definitions:

$$\begin{aligned} \bar{D} &= \frac{\sum_{\ell=1}^L \sum_{i=1}^{M_{\ell}} D_{\ell i}}{\sum_{\ell=1}^L M_{\ell}} \\ &= \frac{\sum_{\ell=1}^L M_{\ell} \bar{D}_{\ell}}{\sum_{\ell=1}^L M_{\ell}} \end{aligned} \quad (3.11)$$

$$S^2 = \frac{\sum_{\ell=1}^L \sum_{i=1}^{M_{\ell}} (D_{\ell i} - \bar{D})^2}{\sum_{\ell=1}^L (M_{\ell} - 1)} \quad (3.12)$$

where  $D_{\ell i}$  is the difference for data point  $i$  of sample  $\ell$ ,  $\bar{D}_{\ell}$  is the bias for sample  $\ell$ , and  $M_{\ell}$  is the number of data points for sample  $\ell$ .

In cases where the sample bias values are identically zero for the whole data set, then  $\bar{D}$  is zero and the expression for the pooled variance reduces to:

$$S^2 = \frac{\sum_{\ell=1}^L \sum_{i=1}^{M_{\ell}} D_{\ell i}^2}{\sum_{\ell=1}^L (M_{\ell} - 1)} \quad (3.13)$$



or equivalently, using the sample variances  $S_{\ell}^2$ :

$$S^2 = \frac{\sum_{\ell=1}^L (M_{\ell} - 1) S_{\ell}^2}{\sum_{\ell=1}^L (M_{\ell} - 1)} \quad (3.14)$$

### 3.1.2.7 Procedure for Computing One-Sided Tolerance Limits

For a normal distribution, the one-sided tolerance limit, when needed, is obtained from the total sample size and number of degrees of freedom using Reference 3.11. For pooled data sets the total sample size is defined by

$$N_{TOT} = \sum_{\ell=1}^L M_{\ell} \quad (3.15)$$

where  $M_{\ell}$  is the number of data points in sample  $\ell$ , and the total number of degrees of freedom is defined by

$$N_{DEG} = \sum_{\ell=1}^L (M_{\ell} - 1) \quad (3.16)$$

For worst-case data sets, the sample numbers for size and degrees of freedom are used, i.e.,

$$N_{TOT} = M_{\ell} \quad (3.17)$$

$$N_{DEG} = M_{\ell} - 1 \quad (3.18)$$

for data set  $\ell$ .

GENERAL PROCEDURE FOR JUSTIFYING AND CONFIRMING POOLABILITY

[

]

### 3.1.3 Evaluation of Box Power Synthesis Uncertainties

The method of estimating the variance  $\sigma_S^2$  and bias  $\mu_S$  to be attributed to box power distribution synthesis uncertainties has been described in detail in Section 3.1.2. The data for the quantities of interest are summarized below for each reactor.

#### 3.1.3.1 Calvert Cliffs Unit 1 Cycle 1

Table 3.VIIIa gives the ROCS-CECOR timepoint comparison results for the quantities  $F_r$ ,  $F_q$  and  $F_{xy}$ . Typical maps showing  $F_r$  and  $F_q$  comparison data are shown for the timepoints:

- (1) 500 Mw /T near BOC in Figures 3-5a and 3-5b;
- (2) 10,000 MWD/T near MOC in Figures 3-5c and 3-5d;
- (3) 16,000 MWD/T near EOC in Figures 3-5e and 3-5f.

For these respective timepoints, comparison plots of the  $F_{xy}$  data are shown in Figures 3-5g through 3-5i, and core-average axial power shape comparisons are shown in Figures 3-5j through 3-5l. The comparisons at 16,000 MWD/T reflect the 18% insertion of Rod Bank 5 as indicated by the maneuver structure in Table 3.II. A comparison of assembly burnup values for 16,000 MWD/T near EOC is shown in Figure 3-5m. The results of time pooling for the three quantities are given in Table 3.VIIIb.

### 3.1.3.2 Calvert Cliffs Unit 1 Cycle 2

Table 3.IXa gives the ROCS-CECOR timepoint comparison results for the quantities  $F_r$ ,  $F_q$  and  $F_{xy}$ . Typical maps showing  $F_r$  and  $F_q$  comparison data are shown for the timepoints:

- (1) 325 MWD/T near BOC in Figures 3-6a and 3-6b;
- (2) 4192 MWD/T near MOC in Figures 3-6c and 3-6d;
- (3) 8330 MWD/T near EOC in Figures 3-6e and 3-6f.

For these respective timepoints, comparison plots of the  $F_{xy}$  data are shown in Figures 3-6g through 3-6i, and core average axial power shape comparisons are shown in Figures 3-6j through 3-6l. A comparison of assembly burnup values for 8330 MWD/T near EOC is shown in Figure 3-6m. The results of time pooling for the three quantities are given in Table 3.IXb.

[ ] The results of normality testing for the  $F_q$ ,  $F_r$  and  $F_{xy}$  data from Cycle 2 are summarized in Table 3.IXd. These results show that the  $F_q$  data pass the D-prime test at the 5% significance level, while both the  $F_r$  and  $F_{xy}$  data fail the D-prime test at the 5% significance level.

### 3.1.3.3 Calvert Cliffs Unit 1 Cycle 3

Table 3.Xa gives the ROCS-CECOR timepoint comparison results for the quantities  $F_r$ ,  $F_q$  and  $F_{xy}$ . Typical maps showing  $F_r$  and  $F_q$  comparison data are shown for the timepoints:

- (1) 495 MWD/T near BOC in Figures 3-7a and 3-7b;
- (2) 801 MWD/T in Figures 3-7c and 3-7d;
- (3) 5994 MWD/T near MOC in Figures 3-7e and 3-7f;
- (4) 8578 MWD/T near EOC in Figures 3-7g and 3-7h.

For these respective timepoints, comparison plots of the  $F_{xy}$  data are shown in Figures 3-7i through 3-7l, and core average axial power shape comparisons are shown in Figures 3-7m through 3-7p. The comparisons at 801 MWD/T reflect the 50% insertion of Rod Bank 5 as indicated by the maneuver structure in Table 3.IV. A comparison of assembly burnup values for 8578 MWD/T near EOC is shown in Figure 3-7q. The results of timepoint pooling for the three quantities are given in Table 3.Xb.

#### 3.1.3.4 Summary of Core Box Power Synthesis Errors

The standard deviation and bias of the uncertainty in  $F_r$ ,  $F_q$  and  $F_{xy}$  assigned for each reactor cycle are summarized in Table 3.XI. [

The results of pooling the data in Table 3.XI for Cycles 1,2, and 3 are given in Table 3.XII along with results of the Bartlett and Normal Deviate Tests. [



[

The  $F_r$  distribution fails the normality test at 5% significance, although the data points are contained within a normal distribution shape, as shown by Figure 3-9. [

]

The  $F_{xy}$  distribution shown in Figure 3-10 also fails the normality test at 5% significance. [

]

The overall box power distribution synthesis uncertainties to be applied for all cycles and reactors are taken from the [ ] values in Table 3.XI

as discussed above. Since this table gives the sample biases and standard deviations [

] for  $F_r$ ,  $F_q$  and  $F_{xy}$ .

[

] In addition, the 95%/95% probability/confidence limits on the basic assembly power distribution synthesis uncertainties are given in Table 3.I.

## 3.2 PIN PEAKING SYNTHESIS UNCERTAINTY

### 3.2.1 Description of Pin Peaking Models

The estimate of pin peaking synthesis uncertainty is based upon two-dimensional quarter-core PDQ calculations for the following reactors:

- (1) Calvert Cliffs (CC) Unit 2 Cycle 2
- (2) St. Lucie (SL) Unit 1 Cycle 2
- (3) Millstone (ML) Unit 1 Cycle 2
- (4) Calvert Cliffs (CC) Unit 1 Cycle 4

The full-core layouts and loading patterns for these reactors are shown in Figures 3-11 through 3-14, respectively. The calculations were based on consistent design PDQ models [

coefficient libraries are generated [ ] Since INCA

]

### 3.2.2 Statistical Model for Calculation of Pin Peaking Synthesis Uncertainty

#### 3.2.2.1 Definitions

$N_Q$	Number of boxes or assemblies in quarter-core; =62
$F_{pi}^T$	Calculated value of pin/box factor [ ] in the PDQ model
$F_{pi}^M$	Calculated value of pin/box factor [ ] in the PDQ model
$D_{pi}$	Difference [ ]
$\sigma_{S_{Fp}}$	The standard deviation of pin peaking differences between truth and synthesis calculation
$\mu_{S_{Fp}}$	The bias of pin peaking differences corresponding to truth minus synthesis calculation
$S_{S_{Fp}}$	Sample standard deviation of pin peaking differences [ ]
$\bar{D}_{S_{Fp}}$	Sample bias of pin peaking differences [ ]

Estimates of the one-sided tolerance limit are given by  $\bar{D}_{S_{Fp}} + kS_{S_{Fp}}$ , where  $S_{S_{Fp}}$  and  $\bar{D}_{S_{Fp}}$  are the sample standard deviation and bias, respectively, and  $k$  is the sample probability/confidence factor.

#### 3.2.2.2 F<sub>p</sub> Synthesis Uncertainty: $S_{S_{Fp}}, \bar{D}_{S_{Fp}}$

For the pin peaking synthesis uncertainty [ ] PDQ calculations are compared for all quarter core boxes with no normalization. The differences which correspond to truth minus synthesis are given as:

$$D_{pi} = F_{pi}^T - F_{pi}^M \quad i=1, \dots, N_Q \quad (3.19)$$

$$\bar{D}_{S_{Fp}} = \frac{1}{N_Q} \sum_{i=1}^{N_Q} D_{pi} \quad (3.20)$$

The bias is in general non-zero. The sample variance of the difference is then:

$$S_{S_{Fp}}^2 = \frac{1}{N_Q - 1} \sum_{i=1}^{N_Q} (D_{pi} - \bar{D}_{S_{Fp}})^2 \quad (3.21)$$

The sample variance and bias given by Equations 3.20 and 3.21 are estimates of the variance and bias attributed to synthesis errors for  $F_p$  in the INCA/CECOR system.

#### 3.2.2.3 Procedure for Pooling Estimates for the Variance and Bias

The procedures and criteria for pooling the data are as described in Section 3.1.2.6.

#### 3.2.2.4 Procedure for Computing One-Sided Tolerance Limit

The methods of obtaining the probability/confidence factor, one-sided tolerance limit and degrees of freedom are as described in Section 3.1.2.7.

### 3.2.3 Evaluation of Pin Peaking Synthesis Uncertainty

The method of estimating the variance  $\sigma_{SFP}^2$  and bias  $\mu_{SFP}$  to be attributed to pin peaking synthesis uncertainty has been described in detail in Section 3.2.2. The data for pin peaking synthesis errors are summarized below for each reload cycle.

#### 3.2.3.1 Calvert Cliffs Unit 2 Cycle 2

Figure 3-15 shows a map comparing the PDQ [ ] calculation values of assembly pin peaking [ ]. The sample bias and standard deviation are given in Table 3.XIII.

#### 3.2.3.2 St. Lucie Unit 1 Cycle 2

Figure 3-16 shows a map comparing the PDQ [ ] calculation values of assembly pin peaking [ ]. The sample bias and standard deviation are given in Table 3.XIII.

#### 3.2.3.3 Millstone Unit 2 Cycle 2

Figure 3-17 shows a map comparing the PDQ [ ] calculation values of assembly pin peaking [ ]. The sample bias and standard deviation are given in Table 3.XIII.

#### 3.2.3.4 Calvert Cliffs Unit 1 Cycle 4

Figure 3-18 shows a map comparing the PDQ [ ] calculation values of assembly pin peaking [ ]. The sample bias and standard deviation are given in Table 3.XIII.

### 3.2.3.5 Summary of Pin Peaking Synthesis Errors

The results of pooling the data for the four reactor reload cycles are included in Table 3.XIII along with the results of the Bartlett and Normal Deviate Tests. Both tests are satisfied, and so pooling of the data is not rejected on this basis.

Table 3.XIV summarizes the results of tests for normality for the individual reactor and pooled data sets. The results show that the data for each reactor passes the D-prime test at the 5% significance level or better. The pooled data set fails the D-prime test at the 5% significance level, but passes at the 4.5% significance level, and so is considered marginal.

[

]

The overall INCA system pin peaking synthesis uncertainty to be applied for all reload cycles is taken from the pooled values in Table 3.XIII as discussed above. [

] Table 3.I quotes the pin peaking synthesis uncertainty in units of percent of average pin/box value. In addition, Table 3.I gives the associated number of degrees of freedom and the 95%/95% probability/confidence limit on the basic pin peaking synthesis uncertainty.

### 3.3 PIN PEAKING CALCULATIVE UNCERTAINTY

The INCA system determines the maximum pin power in a given fuel assembly by employing the pin/box power factor as described in II.2. The pin/box factor, also called  $F_p$ , is defined for a given axial elevation as the ratio between peak and average power within a given assembly.

Since neither  $F_p$  nor local pin power can be measured directly, the synthesis process must rely on calculated values for  $F_p$ . This section describes the calculative method and the uncertainty that pertains to it.

#### 3.3.1 Description of Critical Experiments

To provide data applicable to the evaluation of the uncertainty in the calculated pin/box factor,  $F_p$ , three series of critical experiments have been performed which simulate typical C-E fuel assembly designs. Each of these is described briefly below.

##### 3.3.1.1 Combustion Engineering Sponsored Critical Experiments (C-E Criticals)

A series of critical experiments were performed for Combustion Engineering by Westinghouse Corporation at the Westinghouse Reactor Evaluation Center (WREC) employing the CRX reactor. The experimental program consisted of approximately 70 critical configurations of fuel rods. The basic core configuration was a 30x30 square, fuel rod array of Zr-4 clad  $UO_2$  fuel having an enrichment of 2.72 w/o U-235. Fuel rods were removed to create internal water holes or channels to accommodate control rods or to simulate control rod channels and water gaps representative of C-E assembly designs (primarily the MARK V 14x14 design).

The majority of the experiments employed a lattice pitch of [ ] inches with several experiments repeated with a lattice pitch of [ ] inches. These values of [ ] and [ ] inches, together with the fuel pellet



dimensions and enrichment and the rod diameter, resulted in hydrogen to fuel ratios representative of the MARK V design at room and at operating temperatures, respectively.

The fuel rod assemblies were fully reflected with  $H_2O$  on the four sides. The experiments were conducted at room temperature. Both borated and unborated cores were employed. A given configuration was made critical by adjusting the water height. The reactivity worths of incremental water height changes were made to provide a means of interpolating to exact criticality. Axial bucklings were obtained by fitting measured activities along a rod to a cosine function.

Power distribution measurements were made by measuring the gross fission product gamma activities of selected irradiated fuel rods and relating these values to the relative power in the rods. Low background or pre-scanned fuel rods were used in the experiments to minimize corrections to the data after irradiation.

The fission rate measurement system employed two separate scintillation counters. Each consisted of a NaI (1-3/4 x 2 inch) crystal optically coupled to a photomultiplier tube with its associated counting electronics (amplifiers, discriminators, scalers). One detector unit, termed the monitor channel, was used to measure the gross  $\gamma$ -activity of a single monitor rod which had been irradiated in the experiment. The information from this measurement was used to account for the decrease of the fission product activity with time, since the rods selected for measurement were analyzed sequentially. The monitor channel was used to set the count time interval for each rod measurement by counting to a preset number of counts (usually 20,000). The other detector system, termed the data channel, was used to measure the gross  $\gamma$ -activity of the rods selected for measurement. The data channel was housed in a lead container with 6 to 12 inch walls. A 1/2 inch high slot in the lead permitted a half-inch length of fuel rod to be scanned. The fuel rod being analyzed was placed in a mechanism which allowed it to be moved axially. The rod was stopped at each axial position

to be scanned. The housing for the monitor channel was similar except that the monitor rod position was fixed. Both scalers in the counting channels were started simultaneously and the data channel stopped when the preset count in the monitor rod had been reached. See Figure 3-20 for a block schematic of the system.

The detectors were set to measure the  $\gamma$ -activity above 0.5 MeV. The discriminator settings were calibrated daily with a  $^{22}\text{Na}$   $\gamma$ -source. The  $^{22}\text{Na}$  source emits two photons, a 0.510 MeV and a 1.28 MeV  $\gamma$ -ray. The discriminator voltage was set to detect gross  $\gamma$ -activity with energies above 0.5 MeV. Since both detectors were calibrated with the same source and only the relative count rates from the two detectors were used, the difference between the source spectrum and the fission product gamma spectrum is not a pertinent factor.

In order to minimize the effect of instrument drift, one of the irradiated rods from the experiment was chosen as a "reference". The reference rod was counted at the start of a measurement set, after every five or six rods during the measurement period and again at the end of the period. The data from the reference rod measurements were plotted as a function of time and then fitted by a least square method to a straight line. The data from the measurements of the other fuel rods were normalized (as required) to this reference line to correct for instrument drift.

Each experiment in which fission rate measurements were made was performed only once and in each experiment each selected rod was measured only once (except for the reference rod). Overall uncertainties in the measured values were determined by comparing values from symmetric rod locations. These uncertainties would include both small contributions due to discriminator settings, instrumentation drift and counting statistics (<0.3% based on accumulated counts >100,000) and contributions due to rod misalignments during the irradiation and during the subsequent measurements.

## Experiments Analyzed

For this analysis, the experimental configurations which contained large water holes (unrodded) and for which power distributions were measured were selected for inclusion. These are designated C-E #12, C-E #32, C-E #43, C-E #53, and C-E #56. Pertinent core parameters are contained in Table 3.XV. Core layouts with the fuel rods selected for power measurements designated by numbers are shown in Figs. 3-21 through 3-23. The gamma activity for each of the numbered rods was measured at selected points along the rod (representing the axial power distribution). The activities for each rod were summed to provide a total activity which is proportional to the total power in the rod.

TABLE 3.XV  
C-E CRITICALS

<u>Lattice</u>	<u>Core Configuration</u>		<u>No. of Fuel Rods</u>	<u>Temp. of Core</u>	<u>Soluble Boron</u>	<u>No. of Control Rod Channels</u>
	<u>Fuel Rod Array</u>	<u>Fuel Cell Pitch (Inch)</u>			<u>Conc. PPM</u>	

### 3.3.1.2 KRITZ Experiments

A program of critical experiments, sponsored jointly by Combustion Engineering and KWU, was performed at the KRITZ critical facility of AB Atomenergi, Studsvik, Sweden. The program consisted of analyzing a number of core configurations of interest to C-E and KWU. Both UO<sub>2</sub> and mixed-oxide cores

were included. The C-E configurations were representative of the MARK V assembly (14x14 with 5 large control rod channels). A basic cell pitch of [      ] inches was used for all lattices.

A description of the fuel rods, both  $UO_2$  and mixed-oxide, is given in Table 3.XVI. The cores are relatively large both in cross sectional area and height. Each core contained about 1450 rods (265 cm in length). The core was reflected with water on the four sides and the bottom. Soluble boron was employed for gross reactivity control.

Core criticality was obtained by adjusting the water height. The water temperature was raised by passing the moderator through a 500 kw electric heater outside the core and circulating the water until the desired equilibrium temperature was reached. Once the experiment is started, the water is not circulated. Temperature measurements were made at 3 axial positions to insure equilibrium conditions were reached. In the higher temperature experiments, some cooldown occurred during the experiment. Its effect on reactivity was accounted for by adjusting the reported soluble boron concentration. The small amount of cooldown did not affect the power distribution.

The axial buckling was inferred by fitting data from axial gamma scans of the irradiated rods to a cosine function. Copper wire activation measurements were also employed to determine axial bucklings.

Fission rate measurements were made in selected fuel rods by a gamma scan technique. The fuel rod to be measured was placed vertically between two NaI scintillation detectors (See Figure 3-24). The rod was scanned downward and upward over a distance of 11 cm around the center. The scan speed was about 0.9 mm/sec. The rod was also rotated slowly during the scan at about 3 rpm.

The gross fission product  $\gamma$ -activity above 0.6 MeV was measured. The 0.6 MeV threshold corresponds to a minimum in the fission gamma spectrum as

well as to an energy region where the natural background activity of the rods is relatively flat. Calibrations were performed to establish the discriminator settings. Since the same detectors were used to measure all rods, intercalibration between the detectors was not a pertinent factor.

In each measurement set, a reference rod was measured at regular intervals (about every 40 minutes) during the period. As appropriate for the type of rod being measured, a  $UO_2$ , a 2.0% Pu or a 3.2% Pu rod was selected. The measurement data from the reference rods were corrected for background (both room and rod) and for instrument dead time and the results fitted to equations of the form  $At^{-\alpha}$  (one for each type rod). The count data for the rods measured to determine power distribution were then referenced to the values from the fitted equations. In this way, the values for each rod were corrected for fission product decay and any instrument drift that might have occurred.

The rod background was minimized by using either fresh rods, or, in two instances, several previously irradiated rods with well characterized backgrounds. The activities of the latter were below 10% of the activities after re-irradiation. The measured backgrounds of the fresh and irradiated rods were  $\sim 40$  cps and  $< 130$  cps, respectively with a room background of  $\sim 8$  cps included.

Instrument dead time corrections were less than 0.6%. Any error in this correction was further compensated because the fission rate distributions were expressed as a ratio to a selected rod.

Each experiment was performed once. Each rod in a particular experiment was measured once (except for the reference rods).

Measurement uncertainties are derived from comparisons of fission rate values in symmetric locations in the core. The C-E experiments in KRITZ contained relatively few symmetric location points. However, in the KWU sponsored KRITZ experiments, a number of symmetric measurements were made.

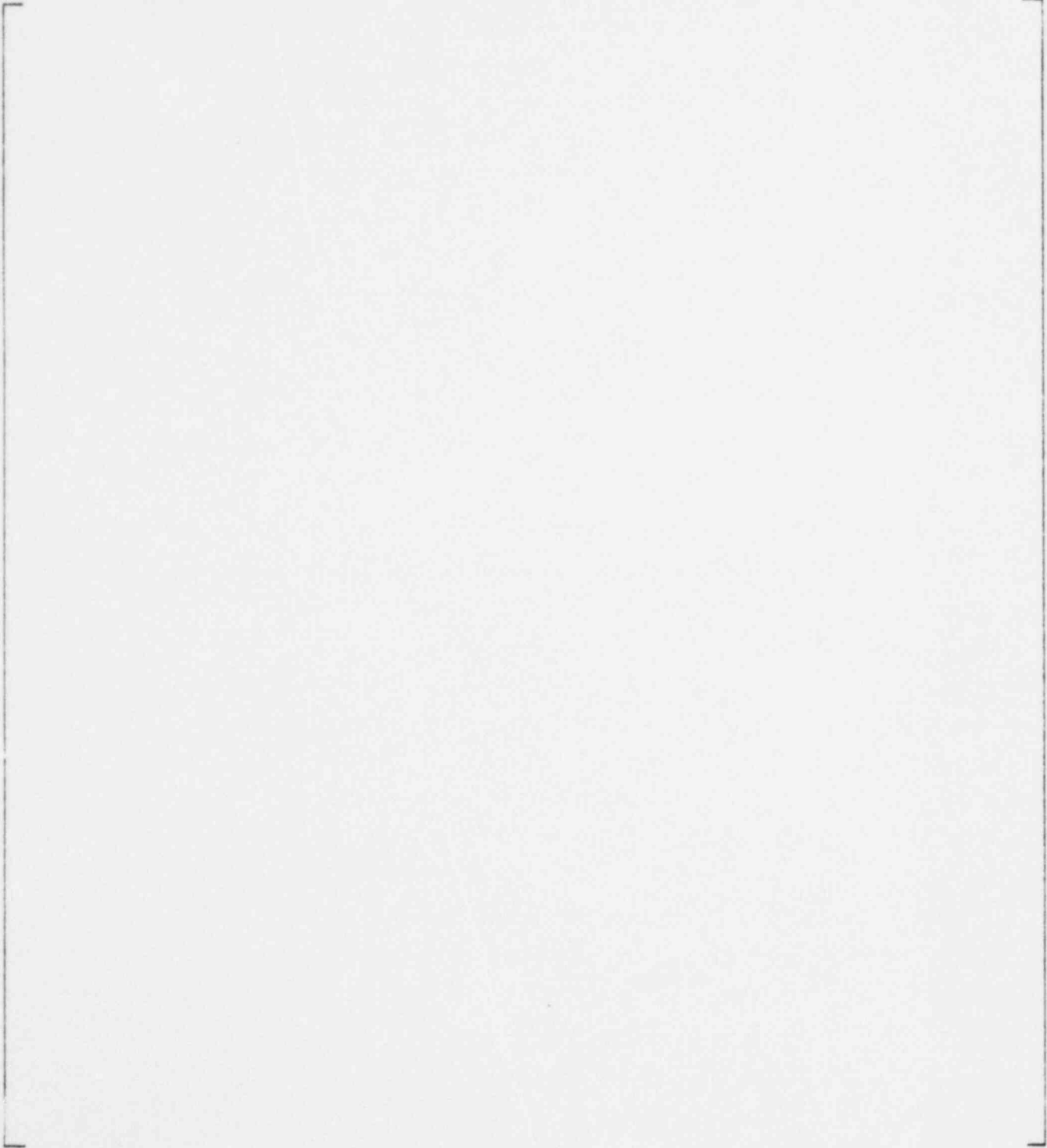
These have been used together with the C-E KRITZ data to establish an overall measurement uncertainty. This approach is justified since the fuel and the experimental arrangements are identical except for the size and locations of the water holes. The fission rate measurement technique is identical and the procedure of rotating the rods during measurements essentially eliminates uncertainties due to water hole induced flux gradient differences for the two types of arrangements.

#### Experiments Analyzed

U-WH2 Experiment - The experiment was performed at 229°C (445°F). The core configuration is shown in Figure 3-25.

Pu-WH2 Experiment - Experiments were performed at 24.6°C (76°F) and 231°C (448°F). The core configurations are shown in Figure 3-26.

TABLE 3.XVI  
FUEL SPECIFICATION (KRITZ EXPERIMENTS)

A large, empty rectangular frame with a thin black border, centered on the page. It appears to be a placeholder for a table that is not present in this document.

### 3.3.1.3 BNWL Critical Experiments

Combustion Engineering, Inc. sponsored a series of critical experiments performed by the Battelle Northwest Laboratory at the Plutonium Recycle Criticality Facility (PRCF). The experimental program included a number of  $UO_2$  and mixed-oxide fueled configurations of interest to C-E. Unshimmed, shimmed and control rodded configurations were included in the program. The basic lattice consisted of a central 14x14 fuel pin arrangement, which simulated the C-E MARK V assembly design, surrounded by a driver region of  $UO_2$  fuel rods. The configuration of the central region (in one lattice the driver region was also modified) was varied to investigate mixed-oxide assembly designs. Power distributions were measured in all cores. The fuel rod specifications are given in Figure 3-27.

The fuel rods were arranged in a spacer grid with a basic cell pitch of [ ] inches. All experiments were conducted at about 20°C (68°F).

The basic procedure for a given configuration was to assemble the array and adjust the concentration of boron in the moderator to achieve criticality with a very small excess reactivity when fully reflected and with the control rods fully withdrawn. The majority of the irradiations were performed while on a very slowly rising reactor period with control rods withdrawn and an effectively infinite reflector at all boundaries. In all cases, the excess reactivity of the fully reflected array was determined.

The relative power distribution was determined from measurements of the gross fission product gamma activity in each of the selected fuel rods in the array. Each fuel rod selected for measurement was counted on a dual channel counting system as illustrated in Figure 3-28. This system automatically corrected for fission product decay during the measurement period.

The fission rate measurement technique was very similar to the one employed for the C-E Critical experiments. The system employed two matching counting systems--one measured the rods of interest (called the traverse system), and another provided a means of correcting the measurements for radioactive



decay during counting (called the decay system). A fuel rod of similar exposure history to those being measured was placed in the decay system at the start of the measurement and left there for the duration of the measurements. The decay system was electronically arranged to stop the traverse system after a preset number of counts has been obtained from the decay rods, thereby correcting for decay. Both systems were matched according to gain and energy discrimination. An integral counting method was used; only gammas with energies greater than 0.470 MeV were counted.

The fuel rods were rotated at about 20 RPM about their longitudinal axis in the traverse system during the counting periods in order to average the circumferential fuel rod activity. The decay rod was not rotated.

The collimator aperture of the traverse system was rectangular, 0.375 inches x 0.75 inches, such that a 0.375 inch long axial segment of the fuel rod was scanned at each point.

Each rod was counted at its axial mid-plane to obtain the rod-to-rod power distribution within the array. Two rods in each array were traversed in two-inch intervals to obtain the axial power shapes.

A reference rod was selected from each experiment and counted at selected intervals throughout each measurement period. The data from these measurements were used to correct for the decrease in fission product  $\gamma$ -activity with time and any drift in the electronics of the counting systems.

The background  $\gamma$ -activity for each fuel rod was determined prior to re-irradiation during an experiment. The background levels of the fuel rods were considerably higher than those for the rods in the C-E Criticals and the KRITZ experiments, since the rods were used in several experiments.

The count data from the measurements on the reference rods were corrected for background and instrument dead time and fitted to a linear function with time. The count data from each fuel rod measurement was also corrected for background and dead time and was normalized to the count rate from the

reference rod at the appropriate time interval. This procedure essentially eliminated the effects of any instrument drift and also corrected for gross fission product decay with time.

#### Experiments Analyzed

- GPL-88 - This is a  $UO_2$  core with a central 14x14 fuel rod region with 5 large (C-E) water holes. The outer region is composed of  $UO_2$  fuel rods with no water holes. See Figure 3-29 for a schematic of the core layout.
- GPL-92 - The core layout is identical to GPL-88 except that borated glass absorbers (shims) occupy the positions shown in Figure 3-30.

### 3.3.2 Statistical Model for Calculation of $F_p$ Uncertainty

#### 3.3.2.1 Definitions

$C_j^{\ell}$  = calculated value at position  $j$  of experiment no.  $\ell$ ,  $j=1, \dots, M_{\ell}$ ,  $\ell=1, \dots, L$ .

$M_{ij}^{\ell}$  = measured value at symmetric positions  $i$  of rod  $j$ , measurement no.  $\ell$ ,  $i=1, \dots, N$ .

$M_j^{\ell}$  = averaged measured value at position  $j$  of experiment no.  $\ell$ ,  $j=1, \dots, M_{\ell}$ .

$T_j^{\ell}$  = true value of power at position  $j$  of experiment no.  $\ell$ ,  $j=1, \dots, M_{\ell}$ .

$\xi_j^{\ell}$  = random error of the calculation for position  $j$ .

$CB_j^{\ell}$  = systematic error (bias) of the calculation for position  $j$ .

$\delta_{ij}^{\ell}$  = random error of measurement  $M_{ij}^{\ell}$

$\delta_j^{\ell}$  = random error of  $M_j^{\ell}$ .

$MB_j^{\ell}$  = systematic error (bias) of the measurement for position  $j$ .

It is assumed that the random errors are normally distributed, and independent, i.e.,

$$\xi_j^{\ell} \sim N(0, \sigma_{C_{\ell}}^2); \quad \delta_j^{\ell} \sim N(0, \sigma_{M_{\ell}}^2); \quad \delta_{ij}^{\ell} \sim N(0, \tau_{\ell}^2); \quad (3.22)$$

where,

$$\sigma_{M_{\ell}}^2 = \frac{\tau_{\ell}^2}{N}, \quad (3.23)$$

is the measurement variance associated with  $M_j^l$  which is obtained by folding  $N$  measurements of symmetrically located pins.

The following relations between calculation, truth and measurement hold:

$$C_j^l = T_j^l + CB_j^l + \xi_j^l \quad (3.24)$$

$$M_{ij}^l = T_j^l + MB_j^l + \delta_{ij}^l \quad (3.25)$$

$$M_j^l = T_j^l + MB_j^l + \delta_j^l \quad (3.26)$$

The difference between calculation and measurement is:

$$D_j^l = C_j^l - M_j^l = DB_j^l + \xi_j^l - \delta_j^l \quad (3.27)$$

$$DB_j^l = CB_j^l - MB_j^l \quad (3.28)$$

$$D_j^l = \text{observed difference.}$$

$$DB_j^l = \text{true difference.}$$

One also has the relations,

$$\bar{D}_l = \frac{1}{M_l} \sum_{j=1}^{M_l} D_j^l = \bar{DB}_l + \bar{\xi}_l - \bar{\delta}_l \quad (3.29)$$

$$\bar{\xi}_l = \frac{1}{M_l} \sum_{j=1}^{M_l} \xi_j^l \sim N(0, \frac{\sigma_{C_l}^2}{M_l}) \quad (3.30)$$

$$\bar{\delta}_l = \frac{1}{M_l} \sum_{j=1}^{M_l} \delta_j^l \sim N(0, \frac{\sigma_{M_l}^2}{M_l}) \quad (3.31)$$

Consider the relationship between  $\sigma_{C\ell}^2$ ,  $\sigma_{M\ell}^2$  and  $\sigma_{D\ell}^2$ . Let  $E(x)$  be the expected value and  $D^2(x)$  the variance of any random variable  $x$ .

From Eqns. (3.22), (3.27) we have

$$E(D_j^\ell) = E(DB_j^\ell) = DB_j^\ell \quad (3.32)$$

$$D^2(D_j^\ell) = D^2(\xi_j^\ell) + D^2(\delta_j^\ell) = \sigma_{C\ell}^2 + \sigma_{M\ell}^2 = \sigma_{D\ell}^2 \quad (3.33)$$

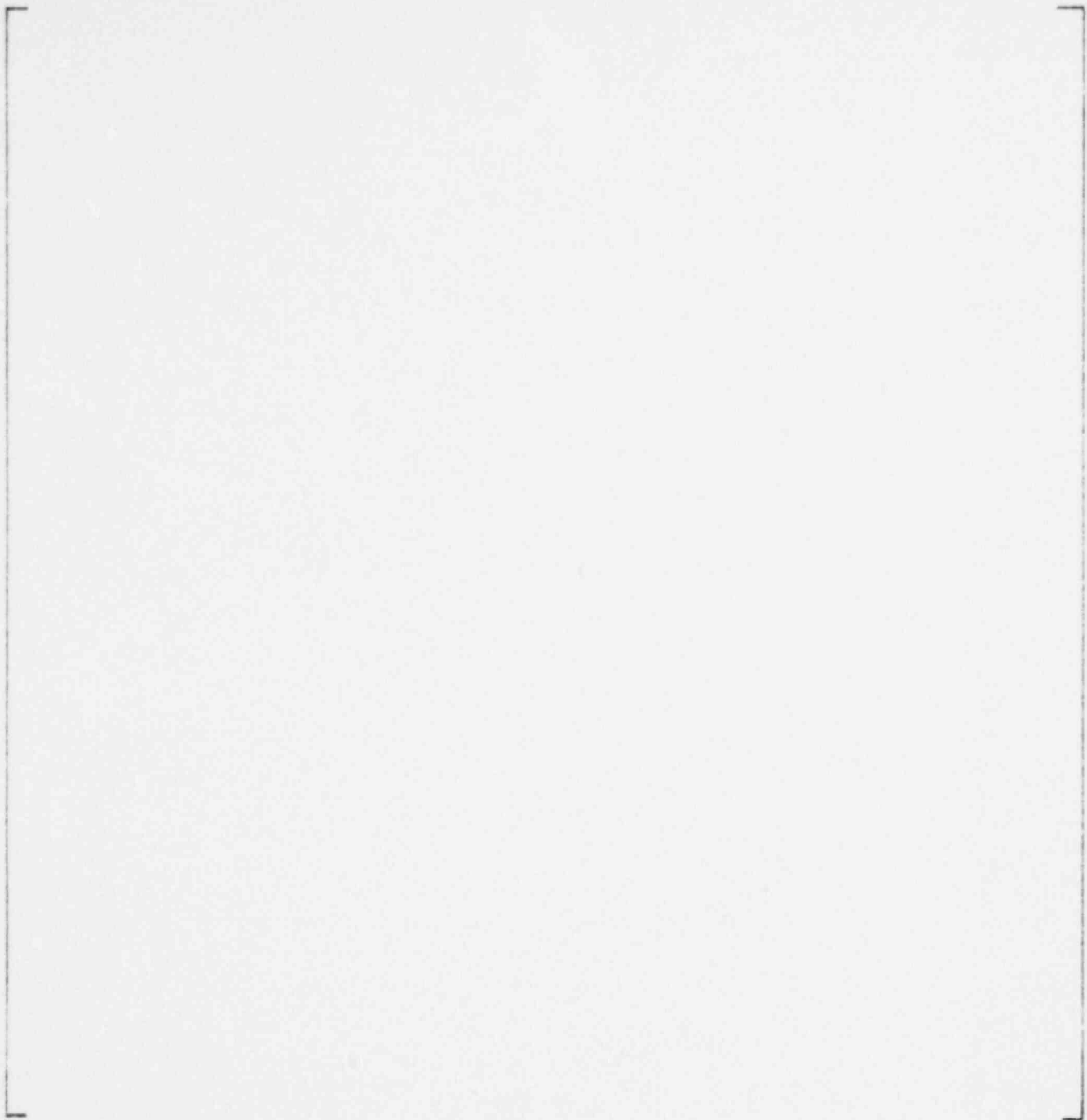
This follows because  $\xi$  and  $\delta$  are independent variables. Eq. (3.33) defines  $\sigma_{D\ell}$ . By rearranging (3.33) we have the basic relation for  $\sigma_{C\ell}$ , namely

$$\boxed{\sigma_{C\ell}^2 = \sigma_{D\ell}^2 - \sigma_{M\ell}^2} \quad (3.34)$$

### 3.3.2.2 The Sample Variance for the Difference Between Calculation and Measurement

The sample variance for the difference between calculation and measurement is,



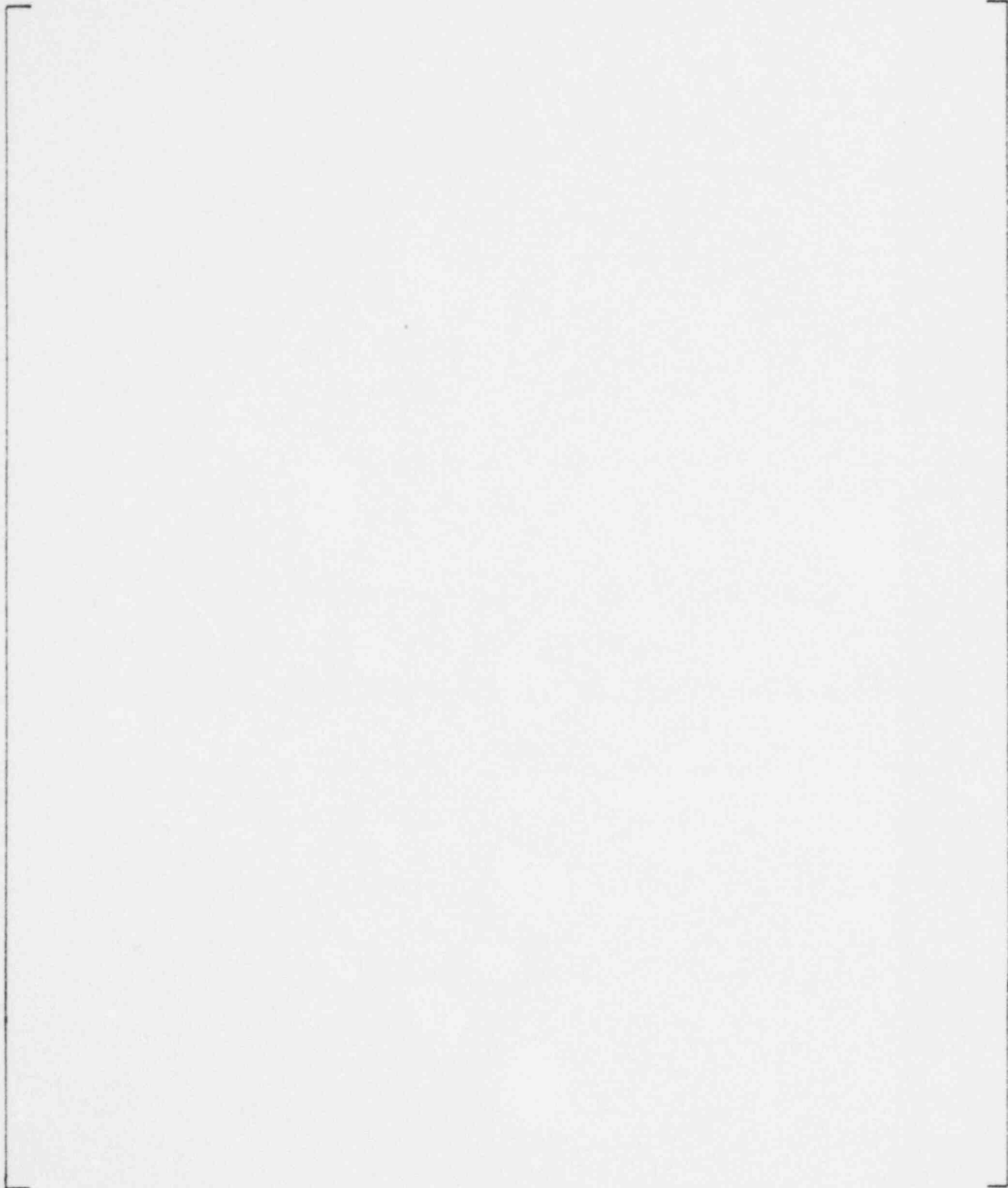


3.3.2.3 The Measurement Uncertainty

3.3.2.4 An Estimate of  $\sigma_{Cl}^2$



3.3.2.5 The Variance of  $S_C^2$



### 3.3.2.6 The Number of Degrees of Freedom

To obtain a tolerance limit, one treats  $S_C^2$  as though it was proportional to a chi-square distributed random variable with  $f$  degrees of freedom and finds the constant of proportionality, and  $f$ , by equating the means and variances. One gets:

$$f_C = \frac{2E^2(S_C^2)}{D^2(S_C^2)} \quad (3.59)$$

### 3.3.2.7 Procedure for Pooling Estimates



### 3.3.3 Calculational Method

#### 3.3.3.1 Design Method

The design method for generating in-core instrument system data employs the PDQ code in either four or two neutron energy groups and the assignment of one mesh volume per fuel rod with its associated water.

#### 3.3.3.2 Method of Incorporating Transport Results Into the Design Method

The design procedure is extended by integral transport theory in a multigroup formulation modeling the details of the assembly geometry without homogenization and accounting for all relevant spectrum interaction effects between fuel and other components of the assembly such as burnable absorbers, control rods or water holes. The following is a summary of the method.

The transport calculations are done with the DIT code (Refs. 3.4, 3.5) and adjustments are made in such a way that the entire PDQ calculation, including edits, provides pin/box factors no smaller than those from direct DIT calculations when applied to an individual assembly. This is achieved by applying a combination of multipliers to the PDQ edited fine mesh power distribution and fitting of PDQ diffusion parameters. The combination is determined by DIT and PDQ assembly calculations covering each type of fuel and the entire lifetime of the fuel in the core. It can be shown, Appendix 3.1, that this approach leads to an uncertainty,  $\sigma_C$ , that is identical to that of DIT.

#### 3.3.3.3 Pin/Box Factor and Pin Power Distribution Calculations for Comparison with Measurement

To make direct comparisons between calculated results using DIT and the Critical Experiments described above, the latter are taken for the centrally located assembly in the core where effects of the global distribution are a minimum. The experimental results are then reduced to remove the global

component using PDQ calculations for the core and for the central assembly. The experimental results thus obtained are compared directly to DIT calculations. The method for removing the global distribution introduces an additional uncertainty in the experimental values. The size of this uncertainty is negligible and has been investigated in detail. This small uncertainty component is automatically retained in the final estimate of the uncertainty for the calculational method since it will be part of  $S_{D\ell}$ .

### 3.3.4 Statistical Error and Bias Evaluation

The evaluation of the calculational uncertainty for local pin peaking must be based upon comparisons with experiments for those pins that may have the peak value. Estimates based on the entire set of measured pins within an assembly are not sufficient since they do not provide the bias for peak pins. Furthermore, the statistical error (estimate of standard deviation) observed in comparing measurement and calculation is not necessarily the same for peak pins as for the entire population of fuel pins.

This evaluation is, therefore, based upon comparisons of peak location only. In the C-E design these locations are always next to CEA water holes or other positions where fuel has been replaced by mainly moderating material. When performing the comparisons, both measurements and calculations are normalized to unit average power (fission rate) for the assembly (the majority of cases) or for those pins that were measured when the measurements were done for less than all pins (KRITZ). Biases and standard deviations are expressed in percent of peak power.

#### 3.3.4.1 Geometry

The calculation of local pin peak by transport theory methods is undertaken in assembly geometry with all symmetries in the design and in the boundary conditions accounted for. Thus, the 1/8 assembly geometry is the unit of interest.

In all the experiments, multiple measurements were done for pins located symmetrically in the core. The purpose of doing duplicate measurements is to provide estimates of the effect of any asymmetries in the experimental situation. Prior to comparison with calculated results, this information is utilized to reduce the experimental uncertainty by folding the measurements into 1/8 core as reflected by Equation (3.23). Figures 3-31 to 3-38 show the comparisons between measurements and calculation.

#### 3.3.4.2 The Bias, $\bar{D}$

The primary information from the comparison of measurements and calculations consists of the bias,  $\bar{D}_\ell$  and the sample standard deviation  $S_{D_\ell}$  with notation as explained in 3.3.2.1.

For the entire set of experiments, Table 3.XVII and Figure 3-39 show the observed values of  $\bar{D}_\ell$ .

TABLE 3.XVII  
The Bias: Calculation - Measurement



Table 3.XVII shows that the bias is of the order of 1% with the calculation overestimating peak power. Although small, this calculational error is expected on theoretical grounds and it is appropriate therefore that it appears in the bias instead of being a contribution to the variance. Figure 3-39 shows that the bias has a definite trend with the wetness of these lattices. Indicated on the Figure is the location of C-E 14x14 and 16x16 fuel assembly designs. The majority of the experiments cluster around this location while the two BNWL experiments have very high wetnesses

atypical of the designs. These two lattices have, therefore, been removed from the analysis. There is an indication that the two Pu lattices depart slightly from the trend and the cold lattice (with essentially zero bias) is atypical of operating conditions. The hot lattice is also atypical of the U fuel cycles without Pu recycle since the enrichment is as high as 3%. These two lattices have nonetheless been retained in the analysis. Excluding them would only change the average bias from [ ] an entirely insignificant amount. Credit has not been taken for the best fit through all points of Figure 3-39 showing a bias of approximately [ ] at C-E fuel design operating conditions. Using the higher bias would be a credit since transport effects are incorporated in PDQ as described by 3.3.3.2. The credit would be small: about 0.3% of peak power. In conclusion, therefore, the DIT calculational bias is taken as:

[ ]

#### 3.3.4.3 The Random Component of Observed Differences Between Calculation and Measurement, $\sigma_D$

The method of estimating  $\sigma_D$  was described in 3.3.2.2. Table 3.XVIII shows the results for all lattices except the BNWL lattices which were excluded as described in 3.3.4.2.



TABLE 3.XVIII  
The Standard Deviation From Comparisons  
of Calculations and Measurement

The last line in the table shows the pooled estimate calculated as described in 3.3.2.7. The justification for pooling the individual sample variances is as follows.

- (1) The physical situation encountered by the calculational method is very similar for all these experiments. This is particularly true for the C-E criticals which have wetness ratios identical to conditions for C-E operating cores. Figures 3-31 to 3-35 show that the magnitude of the peaking at the water holes is very nearly the same for all these cases. Hence it is physically unrealistic to expect different calculational errors for these cases which constitute the major part of the data base. Since the calculational error is dominant in  $\sigma_D$  it is therefore physically unrealistic to expect the sample values to reflect an inhomogeneous data base. Statistical testing confirms this expectation.

- (2) The distribution of observed differences was subjected to a normality test (Reference 3.9) which shows that it is not unreasonable to assume that the differences are normally distributed. The hypothesis that individual  $S_{D\ell}$  are based on samples from one parent population with the single standard deviation  $\sigma_D$ , was subjected to the Bartlett tests (References 3.6 and 3.7). The calculated test statistic is

In conclusion the pooled estimate of the standard deviation of the difference between calculation and measurement is

$$\sigma_D \cong S_D = [ \quad ]$$

#### 3.3.4.4 The Measurement Uncertainty, $\sigma_M$

As described in 3.3.2.3, the measurement uncertainty, including effects due to counting statistics, counting geometry, fuel inhomogeneity and asymmetries in the core configuration, is obtained by comparing symmetrically located measurements. The resulting measurement uncertainty is shown in Table 3.XX along with the appropriate number of points measured using the notation of 3.3.2.3.

The distributions of measurement errors for individual experiments have been subjected to tests for normality according to ANSI N15.5-1974 (Reference 3.9). The tests show that it is not unreasonable to assume that the measurement

errors are normally distributed. Figure 3-40 shows a typical distribution for the C-E criticals. The  $\epsilon_{ij}$  used in the figure is consistent with the definition in Eq. (3.43).

TABLE 3.XX  
The Measurement Uncertainty in  
Critical Experiments

--

The justifications for pooling the individual measurement uncertainties are as follows:

--

In conclusion, the pooled estimate of the measurement uncertainty is

$$\sigma_M \cong S_M = [ \quad ]$$

#### 3.3.4.5 The Computational Uncertainty, $\sigma_C$

The computational uncertainty,  $\sigma_C$  is related to the measurement and difference uncertainty by Eq. (3.34):

$$\sigma_C^2 = \sigma_D^2 - \sigma_M^2$$

Since it has been shown that the individual case estimates of  $\sigma_D$  and  $\sigma_M$  (i.e.,  $S_{D\ell}$  and  $S_{M\ell}$ ) can be pooled, Eq. (3.64) can be used to form the pooled estimate of  $\sigma_C$ :

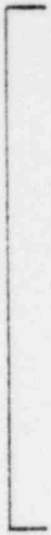
$$\sigma_C^2 \cong S_C^2 = S_D^2 - S_M^2 \quad (3.64)$$

This results in



3.3.4.6 Summary





3.4 REFERENCES

- 3.1 T. G. Ober, J. C. Stork, I. C. Rickard, J. K. Gasper, "Theory, Capabilities and Use of the Three-Dimensional Reactor Operation and Control Simulator (ROCS)," Nucl. Sci. and Eng., 64 (605), 1977.
- 3.2 T. G. Ober, J. C. Stork, R. P. Bandera, W. B. Terney, "Extension of the ROCS Coarse Mesh Physics Simulator to Two Energy Groups," Trans. Am. Nucl. Soc., 28 (763), 1978.
- 3.3 W. R. Caldwell, "PDQ-7 Reference Manual," WAPD-TM-678, January, 1967.
- 3.4 A. Jonsson, et al., "Discrete Integral Transport Theory Extended to the Case with Surface Sources," Atomkernenergie, Bd. 24, 1974.
- 3.5 A. Jonsson, et al., "Verification of a Fuel Assembly Spectrum Code Based on Integral Transport Theory," Trans. Am. Nucl. Soc., 28 (778), 1978.
- 3.6 A. Hald, "Statistical Theory with Engineering Applications," J. Wiley & Sons, Inc., 1955.
- 3.7 W. J. Dixon, F. J. Massey, Jr., "Introduction to Statistical Analysis," McGraw Hill Book Co., 1969.
- 3.8 S. L. Meyer, "Data Analysis for Scientists and Engineers," J. Wiley & Sons, Inc., 1975.
- 3.9 "Assessment of the Assumption of Normality (Employing Individual Observed Values)." ANSI N15.15-1974.
- 3.10 W. J. Conover, "Practical Nonparametric Statistics," J. Wiley & Sons, Inc., 1971.



- 3.11 "Factors for One-Sided Tolerance Limits and for Variables Sampling Plans," Sandia Corporation Monograph, SCR-607, 1963.
- 3.12 H. Cramer, "Mathematical Methods of Statistics," Princeton University Press, 1946.

## APPENDIX 3.1

### TRANSPORT THEORY ADJUSTMENTS IN THE DESIGN PDQ MODEL

Transport theory adjustments are made by a combination of fitted diffusion constants in PDQ and correction factors on the PDQ edited power distributions. This combination is determined by doing comparable DIT and PDQ assembly calculations covering the life of the fuel. The transport theory adjusted PDQ is such that it gives pin/box factors no smaller than DIT (adjusted for its bias as determined in 3.3.4.2) throughout the cycle. Therefore, the resulting bias in PDQ is always zero.



TABLE 3.I  
Summary of Synthesis Uncertainties

<u>Box Power</u> <sup>+</sup>	<u><math>\bar{D}</math></u>	<u>S</u>	<u>Number of Degrees of Freedom</u>	<u>k95/95</u>	<u><math>\bar{D} + kS</math></u>
$F_r$	[	]	216	[	]
$F_{xy}$			260		
$F_q$			216		
<u>Pin Peaking</u> <sup>++</sup>					
$F_p (S)$			244		
$F_p (C)$			27		

+ Quoted in percent of peak box value.

++ Quoted in percent of average pin to box value.

TABLE 3.II  
Calvert Cliffs Unit 1 Cycle 1

ROCS Maneuver Structure

Man #	Bu	Power	Rods <sup>†</sup>	Comparisons
00	0	20%	0%	
01	100	50%	0%	
02	500	80%	0%	*
03	850	100%	0%	*
04	1000	100%	0%	*
05	2000	100%	0%	*
06	3000	100%	0%	*
07	4000	100%	0%	*
08	5000	100%	0%	*
09	6000	100%	0%	*
10	7000	100%	0%	*
11	8000	100%	0%	*
12	9000	100%	0%	*
13	10000	100%	0%	*
14	11000	100%	0%	*
15	12000	100%	0%	*
16	13000	100%	0%	*
17	14000	100%	0%	*
18	15000	100%	0%	*
19	15500	100%	0%	*
20	16000	95%	18%	*
21	16500	68%	18%	*
22	16670	57%	18%	*

<sup>†</sup> Lead Bank

TABLE 3.III  
Calvert Cliffs Unit 1 Cycle 2

RDCS Maneuver Structure

Man #	Bu	Power	Rods <sup>†</sup>	Comparisons
00	0	49%	0%	
01	75	70%	0%	*
02	150	80%	0%	*
03	200	90%	0%	*
04	325	100%	0%	*
05	990	100%	0%	*
06	1436	100%	0%	*
07	1746	100%	0%	*
08	2087	100%	0%	*
09	2722	100%	0%	*
10	3341	100%	0%	*
11	3970	100%	0%	*
12	4192	100%	0%	*
13	5056	102%	0%	*
14	6000	101%	0%	*
15	6446	103%	0%	*
16	7000	103%	0%	*
17	7360	103%	0%	*
18	7600	90%	0%	*
19	8280	90%	3.2%	*
20	8330	90%	3.2%	*

<sup>†</sup> Lead Bank

TABLE 3.IV  
Calvert Cliffs Unit 1 Cycle 3

ROCS Maneuver Structure

Man #	Bu	Power	Rods <sup>†</sup>	Comparisons
00	0	27%	50%	
01	177	84%	0%	*
02	495	82%	0%	*
03	801	57%	50%	*
04	1202	91%	0%	*
05	1611	93%	0%	*
06	2021	99%	0%	*
07	2238	99%	15.8%	*
08	2582	93%	0%	*
09	3011	94%	0%	*
10	3811	95%	0%	*
11	4626	95%	0%	*
12	5434	94%	0%	*
13	5849	97%	7.2%	*
14	5994	96%	0%	*
15	6442	94%	0%	*
16	6547	94%	0%	*
17	6658	94%	0%	*
18	6869	0%	0%	
19	6869	95%	0%	*
20	7147	95%	0%	*
21	7327	87%	6.7%	*
22	7554	96%	6.7%	*
23	7738	96%	6.7%	*
24	7964	100%	6.7%	*
25	8149	95%	6.7%	*
26	8578	100%	8.2%	*
27	8969	100%	0%	*
28	9440	100%	0%	*

<sup>†</sup> Lead Bank

TABLE 3.V

Calvert Cliffs Unit 1 Cycle 1  
 CECOR MANEUVER STRUCTURE AND FAILED DETECTORS

Burnup	Power Level	Rod+ Insertion	Failed Detectors			
			Level 1	Level 2	Level 3	Level 4
0	20%	0%	None	None	None	None
100	50%	0%	None	None	None	None
500	80%	0%	None	None	None	None
850	100%	0%	None	None	23	None
1000	100%	0%	None	None	23	None
2000	100%	0%	None	None	23	None
3000	100%	0%	20	None	23	None
4000	100%	0%	20	None	23	None
5000	100%	0%	20	None	23	None
6000	100%	0%	20	None	23	None
7000	100%	0%	20	None	23	None
8000	100%	0%	20	None	23	None
9000	100%	0%	20	None	23	35
10000	100%	0%	20	None	23	35
11000	100%	0%	20	None	23	35
12000	100%	0%	20	None	23	35
13000	100%	0%	20	None	23	35
14000	100%	0%	20, 26	None	23	35, 8
15000	100%	0%	20, 26	None	23	35, 8
15500	100%	0%	20, 26	None	23	35, 8
16000	95%	18%	20, 26	35	23	35, 8
16500	68%	18%	20, 26	35	23	35, 8
16700	57%	18%	20, 26	35	23	35, 8

+ Lead Bank



TABLE 3.VI

Calvert Cliffs Unit 1 Cycle 2  
 CECOR MANEUVER STRUCTURE AND FAILED DETECTORS

Burnup	Power Level	Rod+ Insertion	Failed Detectors			
			Level 1	Level 2	Level 3	Level 4
0	49%	0%	3,14,15,25,44,1,7	3,14,15,18,25,31,1,7,44	3,14,15,25,44,1,7	3,14,15,25,44,1,7
75	70%	0%	"	"	"	"
150	80%	0%	"	"	"	"
200	90%	0%	"	"	"	"
325	100%	0%	"	"	"	"
990	100%	0%	"	"	"	"
1436	100%	0%	"	"	"	"
1746	100%	0%	"	"	"	"
2087	100%	0%	"	"	"	"
2722	100%	0%	"	"	"	3,14,15,25,30,44,1,7
3341	100%	0%	"	3,14,15,18,25,31,43, 44,1,7	"	3,14,15,25,30,33, 44,1,7
3970	100%	0%	"	3,14,15,18,24,25,31, 43,44,1,7	"	"
4192	100%	0%	"	"	"	"
5056	102%	0%	"	"	"	"
6000	101%	0%	"	"	"	2,3,14,15,25,30, 33,44,1,7
6446	103%	0%	"	"	"	"
7000	103%	0%	"	"	"	"
7360	103%	0%	"	3,14,15,18,24,25,31, 42,43,1,7,44	3,14,15,25,29,44, 1,7	"
7600	90%	0%	"	"	"	"
8280	90%	3.2%	"	"	"	"
8330	90%	3.2%	"	"	"	"

+Lead Bank

TABLE 3.VII

Calvert Cliffs Unit 1 Cycle 3  
 CECOR MANEUVER STRUCTURE AND FAILED DETECTORS

Burnup	Power Level	Rod+ Insertion	Failed Detectors			
			Level 1	Level 2	Level 3	Level 4
0	27%	0%	4,5,6,16,19,22,23,33	4,6,23,33,35,42	3,4,5,6,16,19,23,33	4,5,6,23,33
177	84%	0%	"	"	"	"
495	82%	0%	"	"	"	"
801	57%	50%	"	"	"	"
1202	91%	0%	"	"	"	"
1611	93%	0%	"	"	"	"
2021	99%	0%	"	4,6,23,33,34,35,42	"	4,5,6,23,33,34
2238	99%	15.8%	"	"	"	"
2582	93%	0%	"	"	"	"
3011	94%	0%	"	"	"	"
3811	95%	0%	4,5,6,16,19,21,22,23,33	"	3,4,5,6,16,19,23,33,34	"
4626	95%	0%	"	"	"	"
5434	94%	0%	"	"	"	4,5,6,23,33,34,35
5849	97%	7.2%	"	"	"	"
5994	96%	0%	"	"	"	"
6442	94%	0%	4,5,6,16,19,21,22,23,33,34	"	"	"
6547	94%	0%	"	"	"	4,5,6,20,23,33,34,45
6658	94%	0%	"	"	"	"
6869	95%	0%	"	"	3,4,5,6,8,16,19,23,33,34	"
7174	95%	0%	"	"	"	"
7327	87%	6.7%	"	"	"	"
7554	96%	6.7%	"	"	3,4,5,6,8,16,19,21,23,33,34	"
7738	96%	6.7%	"	"	"	"
7964	100%	6.7%	"	"	"	"
8149	95%	6.7%	"	"	"	"
8578	100%	8.2%	"	"	"	"
8969	100%	0%	"	"	"	"
9440	100%	0%	"	"	"	"

+ Lead Bank

TABLE 3.VIIIa  
Calvert Cliffs Unit 1 Cycle 1

BIAS AND STANDARD DEVIATION OF DIFFERENCE BETWEEN ROCS AND CECOR CALCULATIONS

Burnup (MWD/T)	$F_q$			$F_r$			$F_{xy}$		
	$\bar{D}_S$	$S_S$	$N_F$	$\bar{D}_S$	$S_S$	$N_F$	$\bar{D}_S$	$S_S$	$N_{LU}$
500			217			217			14
850			217			217			14
1000			217			217			14
2000			217			217			14
3000			217			217			14
4000			217			217			14
5000			217			217			14
6000			217			217			14
7000			217			217			14
8000			217			217			14
9000			217			217			14
10000			217			217			14
11000			217			217			14
12000			217			217			14
13000			217			217			14
14000			217			217			14
15000			217			217			14
15500			217			217			14
16000			217			217			14
16500			217			217			14
16700			217			217			14

+Worst-case Value

TABLE 3.VIIIb  
 Calvert Cliffs Unit 1 Cycle 1  
RESULTS OF BOX POWER DATA POOLING AND  
BARTLETT AND NORMAL DEVIATE TESTS

Pooled Time Point and Test Results\*

	$\bar{D}_S$	$S_S$	$N_{DEG}$	Bartlett $F_{cal}(20, \infty)$	Normal Deviate $P_{cal}(D\ell_1, D\ell_2)$
$F_q$					
$F_r$					
$F_{xy}$					

Power Synthesis Results

	$\bar{D}_S$	$S_S$	$N_{DEG}$
$F_q^+$			
$F_r^+$			
$F_{xy}^+$			

--

TABLE 3. IXa  
Calvert Cliffs Unit 1 Cycle 2

BIAS AND STANDARD DEVIATION OF DIFFERENCE BETWEEN ROCS AND CECOR CALCULATIONS

Burnup (MWD/T)	$F_q$			$F_r$			$F_{xy}$		
	$\bar{D}_S$	$S_S$	$N_F$	$\bar{D}_S$	$S_S$	$N_F$	$\bar{D}_S$	$S_S$	$N_{LU}$
75			217			217			14
150			217			217			14
200			217			217			14
325			217			217			14
990			217			217			14
1436			217			217			14
1746			217			217			14
2087			217			217			14
2722			217			217			14
3341			217			217			14
3970			217			217			14
4192			217			217			14
5056			217			217			14
6000			217			217			14
6446			217			217			14
7000			217			217			14
7360			217			217			14
7600			217			217			14
8280			217			217			14
8330			217			217			14

+ Worst-case Value

TABLE 3. IXb  
 Calvert Cliffs Unit 1 Cycle 2  
RESULTS OF BOX POWER DATA POOLING AND  
BARTLETT AND NORMAL DEVIATE TESTS

Pooled Time Point and Test Results\*

	$\bar{D}_S$	$S_S$	$N_{DEG}$	Bartlett $F_{cal}(19, \infty)$	Normal Deviate $P_{cal}(\bar{D}l_1, \bar{D}l_2)$
$F_q$	[				]
$F_r$					
$F_{xy}$					

Box Power Synthesis Results

	$\bar{D}_S$	$S_S$	$N_{DEG}$
$F_q^+$	[		
$F_r^+$			
$F_{xy}^{++}$			

--	--	--	--	--	--

TABLE 3.IXc  
Calvert Cliffs Unit 1 Cycle 2

NORMALITY TEST RESULTS [ ]

Burnup (MWD/T)	$N_{TOT}$	$S_S$	[ ]

[ ]

TABLE 3.IXd  
 Calvert Cliffs Unit 1 Cycle 2

NORMALITY TEST RESULTS [ ]

	<u>N<sub>TOT</sub></u>	<u><math>\bar{D}_S</math></u>	<u>S<sub>S</sub></u>	D-Prime Test	
				<u>D'</u>	<u>α(%)</u>
F <sub>q</sub>					
F <sub>r</sub> <sup>+</sup>					
F <sub>xy</sub> <sup>+</sup>					

[ ]



TABLE 3.Xa  
Calvert Cliffs Unit 1 Cycle 3

BIAS AND STANDARD DEVIATION OF DIFFERENCE BETWEEN ROCS AND CECOR CALCULATIONS

Burnup (MWD/T)	$F_q$			$F_r$			$F_{xy}$		
	$\bar{D}_S$	$S_S$	$N_F$	$\bar{D}_S$	$S_S$	$N_F$	$\bar{D}_S$	$S_S$	$N_{LU}$
495			217			217			14
801			217			217			14
1202			217			217			14
1611			217			217			14
2021			217			217			14
2238			217			217			14
2582			217			217			14
3011			217			217			14
3811			217			217			14
4626			217			217			14
5435			217			217			14
5849			217			217			14
5994			217			217			14
6442			217			217			14
6547			217			217			14
6658			217			217			14
6869			217			217			14
7147			217			217			14
7327			217			217			14
7554			217			217			14
7738			217			217			14
7964			217			217			14
8149			217			217			14
8578			217			217			14
8969			217			217			14
9440			217			217			14

+ Worst-case Value

TABLE 3.Xb  
 Calvert Cliffs Unit 1 Cycle 3  
RESULTS OF BOX POWER DATA POOLING AND  
BARTLETT AND NORMAL DEVIATE TESTS

Pooled Time Point and Test Results\*

	<u><math>\bar{D}_S</math></u>	<u><math>S_S</math></u>	<u><math>N_{DEG}</math></u>	<u>Bartlett</u> <u><math>F_{cal}(26, \infty)</math></u>	<u>Normal Deviate</u> <u><math>P_{cal}(\bar{D}\ell_1, \bar{D}\ell_2)</math></u>
$F_q$	$\left[ \begin{array}{c} \\ \\ \\ \end{array} \right]$				
$F_r$					
$F_{xy}$					

Box Power Synthesis Results

	<u><math>\bar{D}_S</math></u>	<u><math>S_S</math></u>	<u><math>N_{DEG}</math></u>
$F_q^+$	$\left[ \begin{array}{c} \\ \\ \\ \end{array} \right]$		
$F_r^+$			
$F_{xy}^{++}$			

--	--	--	--	--	--

TABLE 3.XI  
Calvert Cliffs Unit 1

SUMMARY OF BOX POWER SYNTHESIS ERROR BIAS AND  
STANDARD DEVIATION RESULTS FOR CYCLES 1, 2 AND 3

<u>Quantity</u>	<u>Cycle</u>	$\bar{D}_S$	$S_S$	$N_{DEG}$
$F_q$	1	[		]
	2+			
	3			
$F_r$	1			
	2+			
	3			
$F_{xy}$	1			
	2+			
	3			

[

]

TABLE 3.XII  
 Calvert Cliffs Unit 1  
RESULTS OF POOLING SYNTHESIS ERRORS FOR CYCLES 1, 2, 3

	$\bar{D}_S$	$S_S$	$N_{DEG}$	
$F_q^+$	[			[
$F_r^+$				]
$F_{xy}^+$				]
	[			
	]			

TABLE 3.XIII

Bias and Standard Deviation of Difference for [ ] PDQ Calculations for Pin Peaking, And Results of Data Pooling

Reactor	Cycle	Burnup (MWD/T)	$\bar{D}_{S_{FP}}$	$S_{S_{FP}}$	$N_{DEG}$
Calvert Cliffs Unit 2	2	[ ]	[ ]	[ ]	61
St. Lucie Unit 1	2				61
Millstone Unit 2	2				61
Calvert Cliffs Unit 1	4				61
Pooled Result**					244

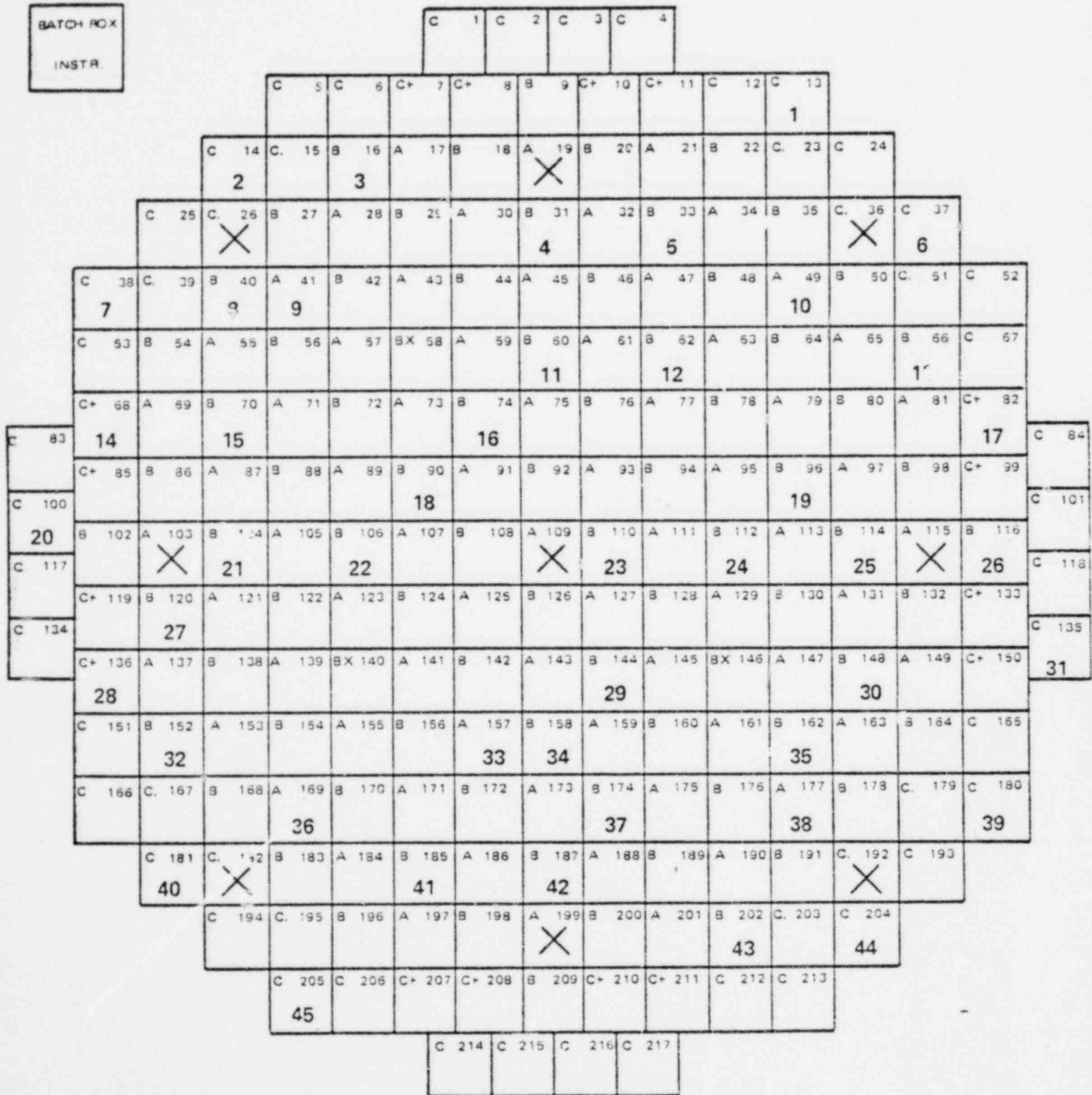
[ ]

[ ]

TABLE 3.XIV  
 Normality Test Results for Pin-Peaking Synthesis Error Data

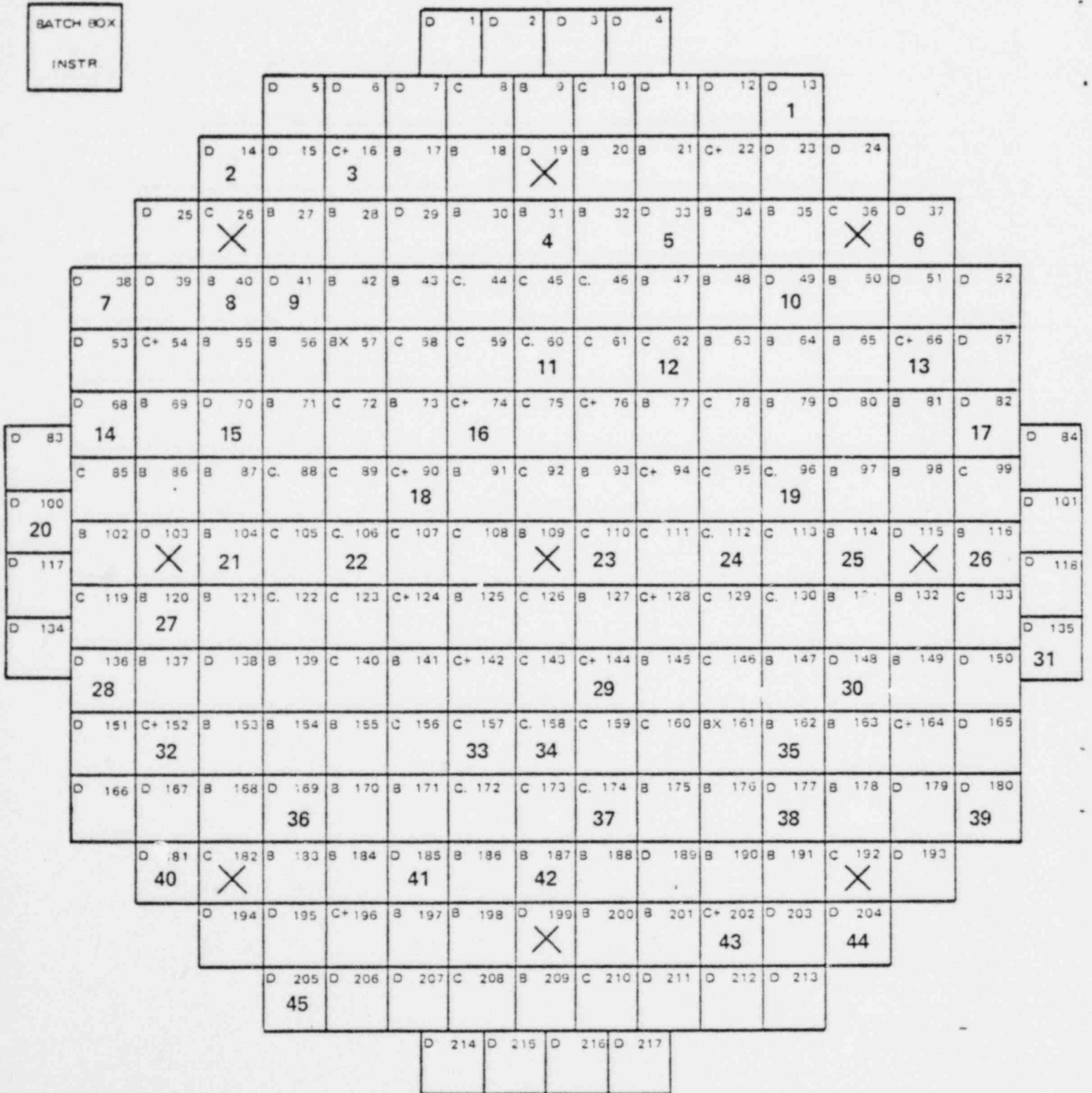
<u>Reactor</u>	<u>Cycle</u>	<u>N<sub>TOT</sub></u>	<u>S<sub>SFP</sub></u>
Calvert Cliffs Unit 2	2	62	[ ]
St. Lucie Unit 1	2	62	
Millstone Unit 2	2	62	
Calvert Cliffs Unit 1	4	62	
Pooled Data		248	

**Figure 3-1**  
**LOADING & INSTRUMENT PATTERN**  
**CALVERT CLIFFS UNIT 1 CYCLE 1**



\* BX INDICATES TEST ASSEMBLY  
 X INDICATES ROD BANK 5 LOCATIONS

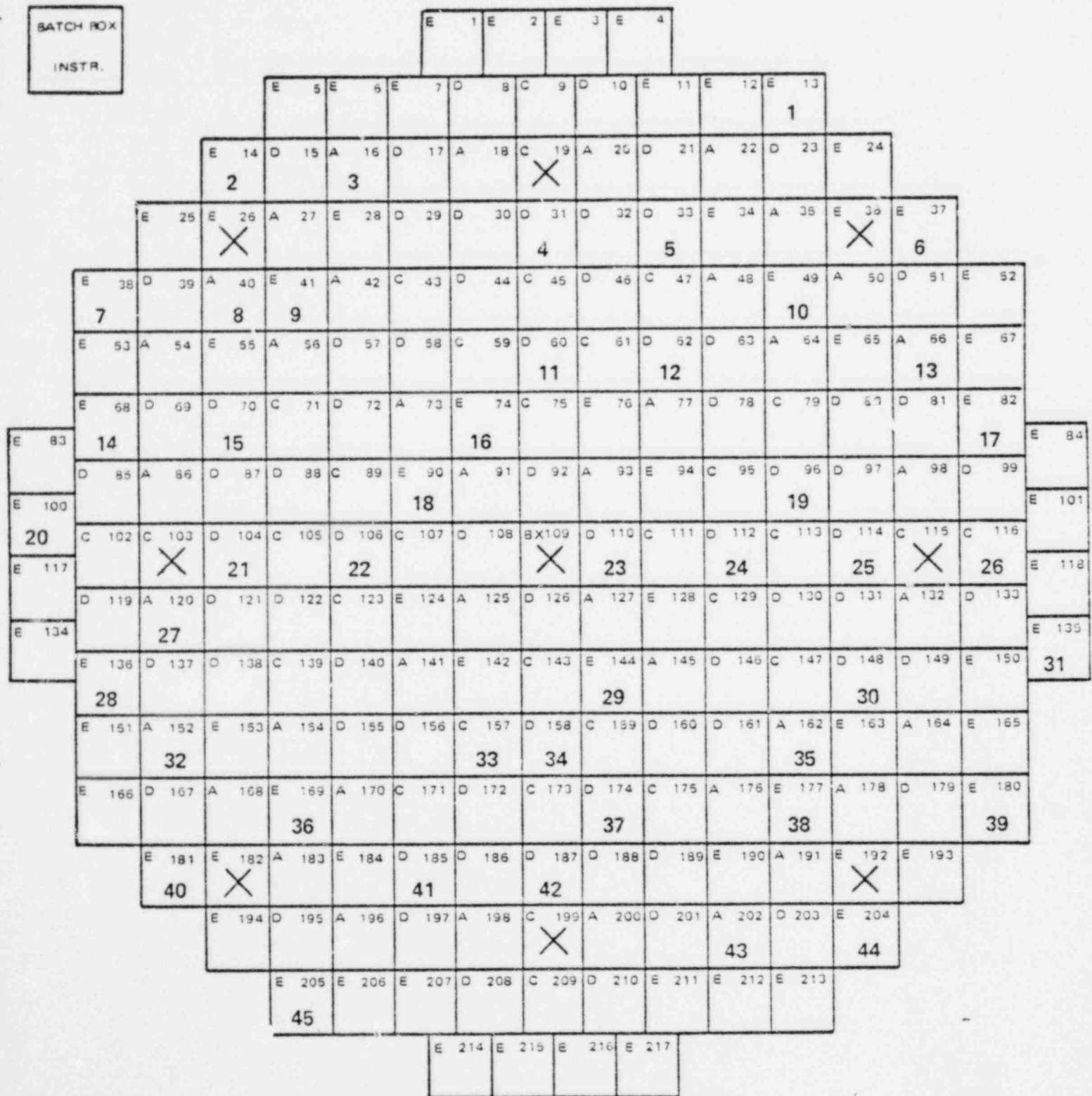
**Figure 3-2**  
**LOADING & INSTRUMENT PATTERN**  
**CALVERT CLIFFS UNIT 1 CYCLE 2**



\* BX INDICATES TEST ASSEMBLY  
 X INDICATES ROD BANK 5 LOCATIONS



**Figure 3-3**  
**LOADING & INSTRUMENT PATTERN**  
**CALVERT CLIFFS UNIT 1 CYCLE 3**



\* BX INDICATES TEST ASSEMBLY  
 X INDICATES ROD BANK 5 LOCATIONS

Figure 3-4  
CALVERT CLIFFS UNIT 1  
AXIAL GEOMETRIES FOR ROCS AND CECOR MODELS

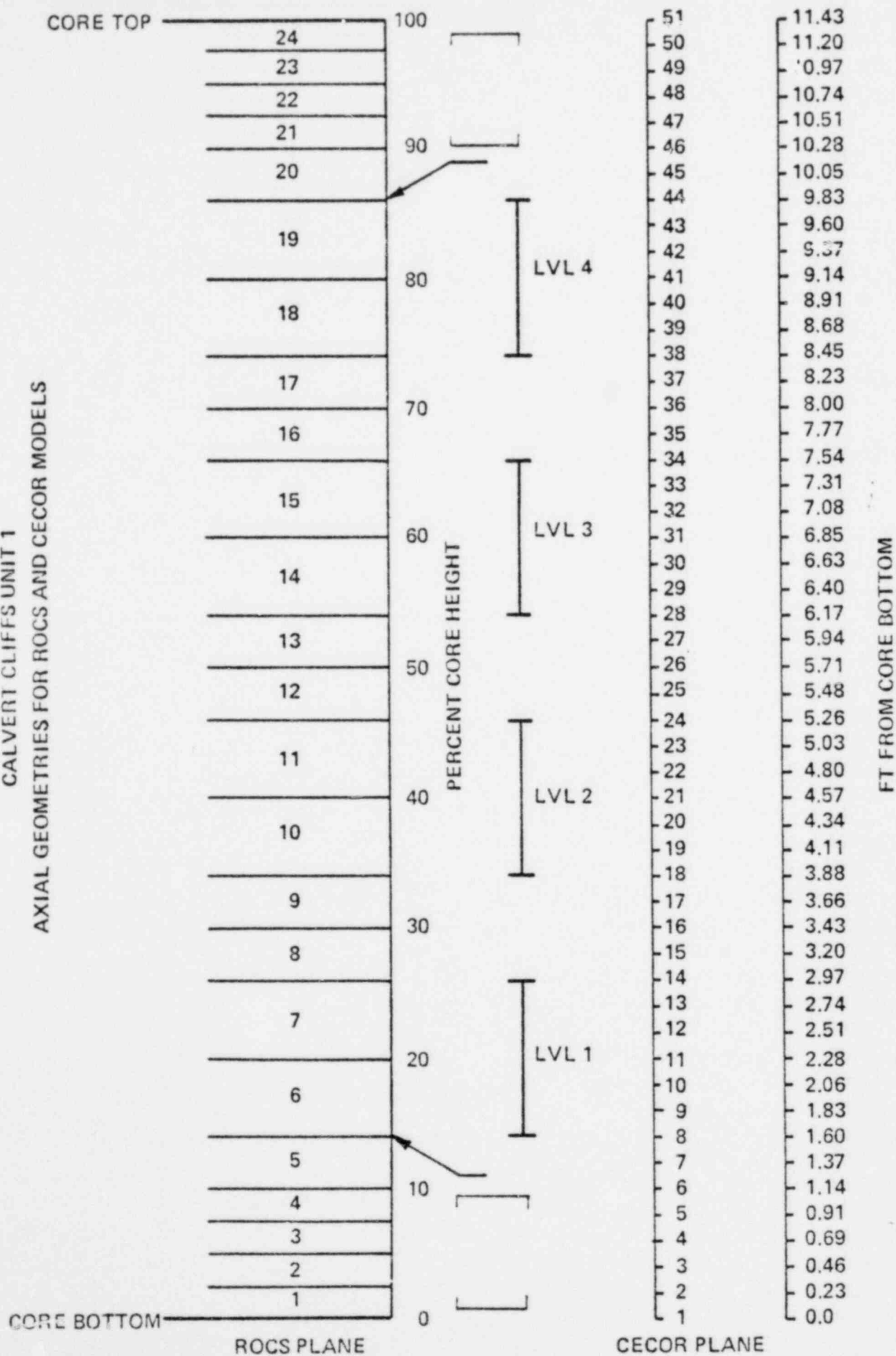


Figure 3.5a  
CALVERT CLIFFS UNIT 1 CYCLE 1  
COMPARISON OF ROCS (R) AND CECOR (C) BOX POWER FRACTIONS  
500 MWD/T

Figure 3-5b  
CALVERT CLIFFS UNIT 1 CYCLE 1  
COMPARISON OF ROCS (R) AND CECOR (C) BOX PEAK TO CORE AVERAGE POWER  
500 MWD/T

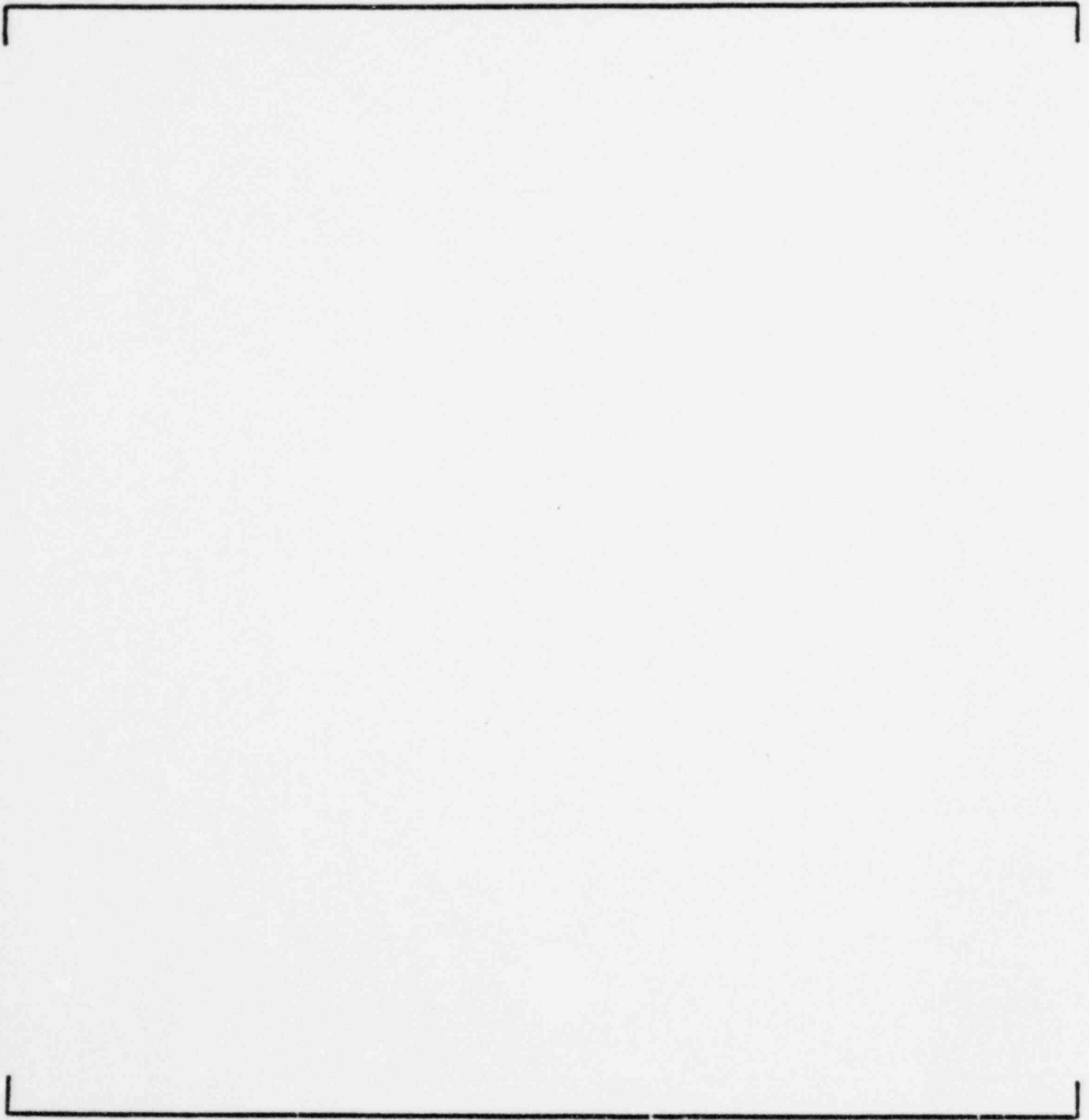


Figure 3-5c  
CALVERT CLIFFS UNIT 1 CYCLE 1  
COMPARISON OF ROCS (R) AND CECOR (C) BOX POWER FRACTIONS  
10,000 MWD/T

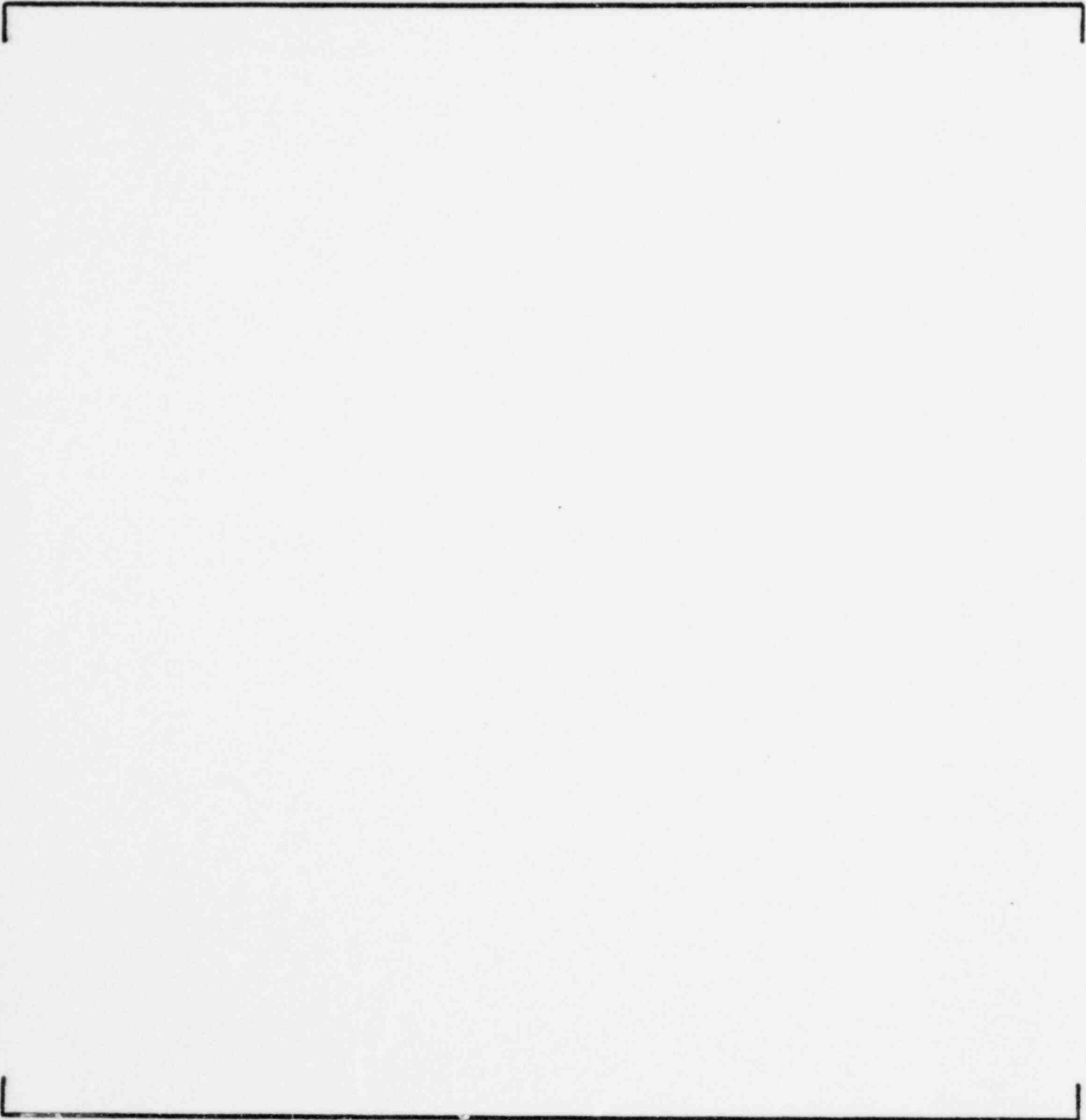


Figure 3-5d  
CALVERT CLIFFS UNIT 1 CYCLE 1  
COMPARISON OF ROCS(R) AND CECOR (C) BOX PEAK TO CORE AVERAGE POWER  
10,000 MWD/T

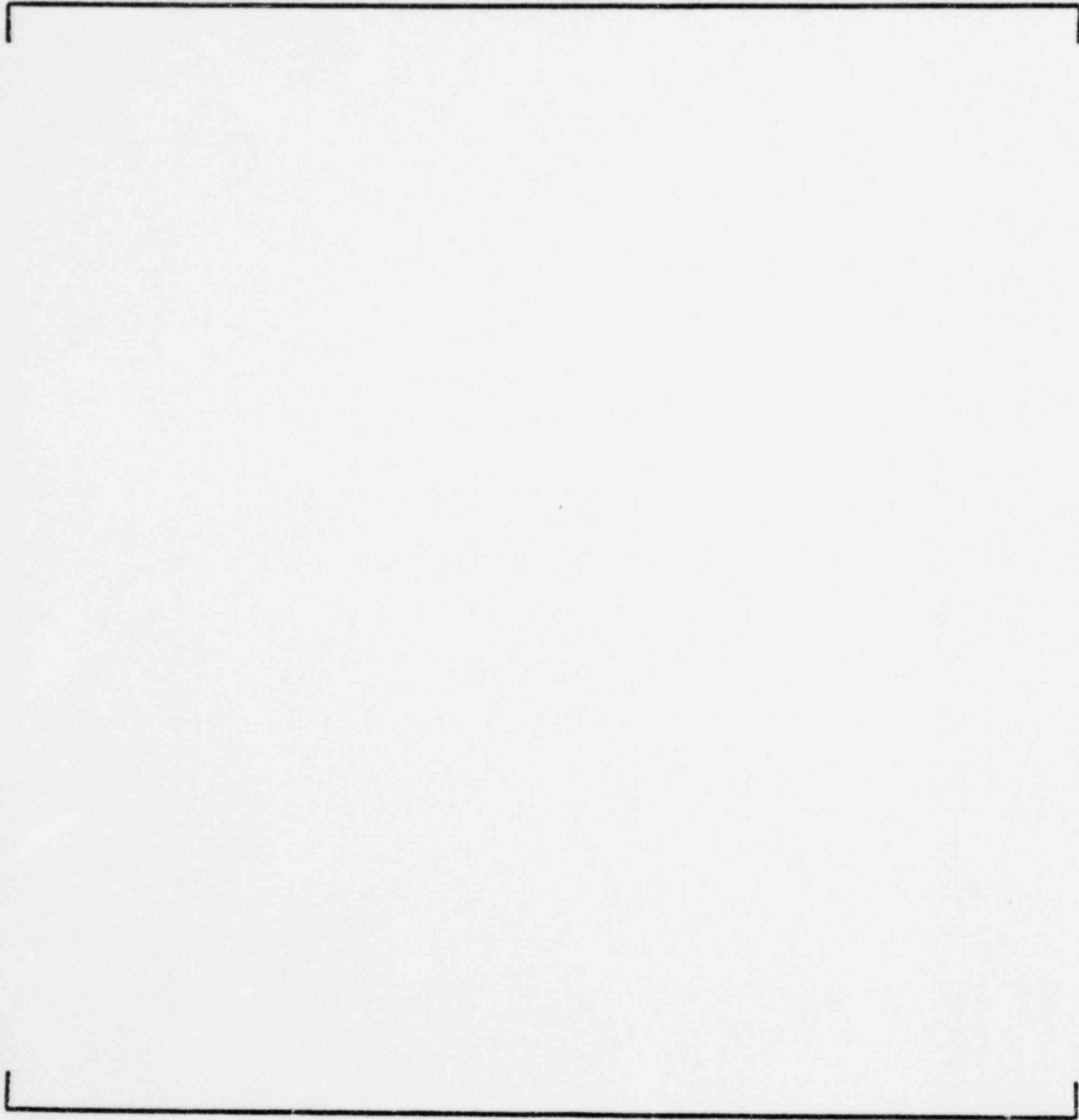


Figure 3-5a  
CALVERT CLIFFS UNIT 1 CYCLE 1  
COMPARISON OF ROCS (R) AND CECOR (C) BOX POWER FRACTIONS  
16,000 MWD/T (18% ROD BANK 5 INSERTION)

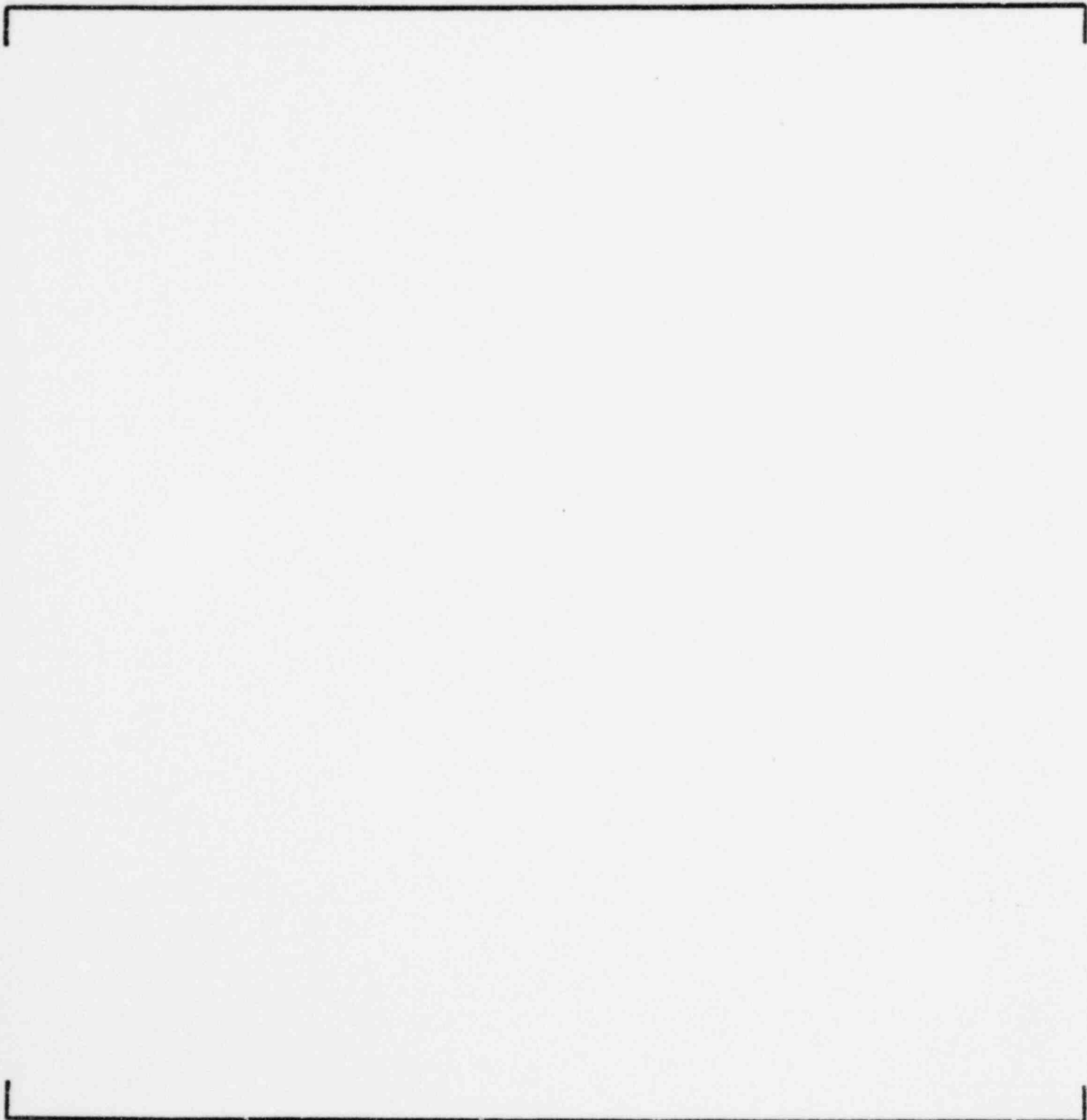


Figure 3-5f  
CALVERT CLIFFS UNIT 1 CYCLE 1  
COMPARISON OF ROCS (R) AND CECOR (C) BOX PEAK TO CORE AVERAGE POWER  
16,000 MWD/T (18% ROD BANK 5 INSERTION)



Figure 3-5g  
CALVERT CLIFFS UNIT 1 CYCLE 1  
COMPARISON OF ROCS AND CECOR PLANAR PEAK TO PLANE AVERAGE BOX POWERS  
500 MWD/T

11.3.93

Figure 3-5h  
CALVERT CLIFFS UNIT 1 CYCLE 1  
COMPARISON OF ROCS AND CECOR PLANAR PEAK TO PLANE AVERAGE BOX POWERS  
10,000 MWD/T



Figure 3-5i  
CALVERT CLIFFS UNIT 1 CYCLE 1  
COMPARISON OF ROCS AND CECOR PLANAR PEAK TO PLANE AVERAGE BOX POWERS  
16,000 MWD/T (18% ROD BANK 5 INSERTION)

Figure 3-5j  
CALVERT CLIFFS UNIT 1 CYCLE 1  
COMPARISON OF ROCS AND CECOR CORE AVERAGE AXIAL SHAPES  
500 MWD/T

11.3.96



Figure 3-5k  
CALVERT CLIFFS UNIT 1 CYCLE 1  
COMPARISON OF ROCS AND CECOR CORE AVERAGE AXIAL SHAPES  
10,000 MWD/T



II.3.97

Figure 3-51  
CALVERT CLIFFS UNIT 1 CYCLE 1  
COMPARISON OF ROCS AND CECOR CORE AVERAGE AXIAL SHAPES  
16,000 MWD/T (18% ROD BANK 5 INSERTION)

11.3.98

Figure 3-5 m  
CALVERT CLIFFS UNIT 1 CYCLE 1  
COMPARISON OF ROCS (R) AND CECOR (C) ASSEMBLY BURNUP  
16000 MWD/T

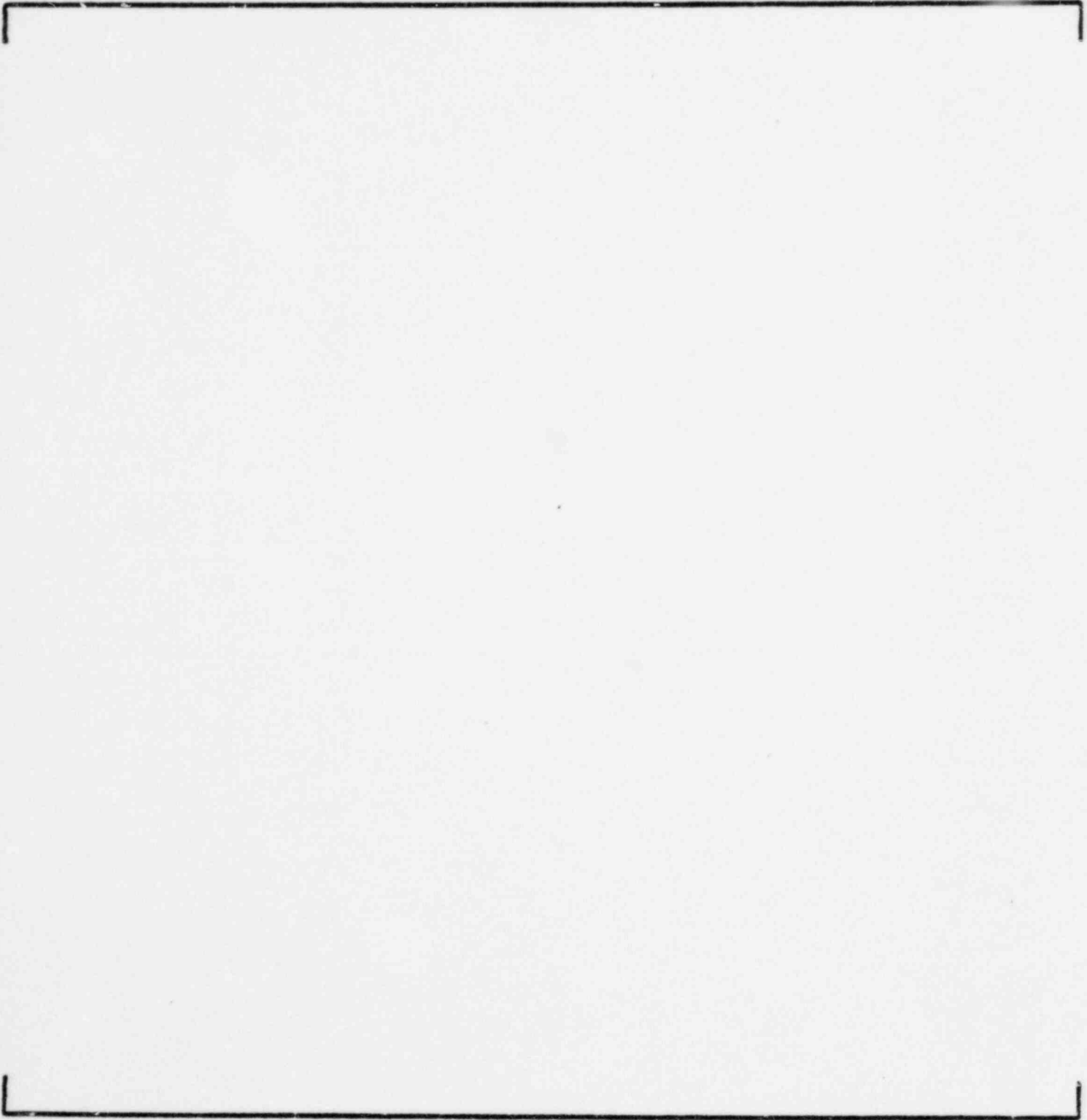


Figure 3-6a  
CALVERT CLIFFS UNIT 1 CYCLE 2  
COMPARISON OF ROCS (R) AND CECOR (C) BOX POWER FRACTIONS  
325 MWD/T



Figure 3-6b  
CALVERT CLIFFS UNIT 1 CYCLE 2  
COMPARISON OF ROCS (R) AND CECOR (C) BOX PEAK TO CORE AVERAGE POWER  
325 MWD/T

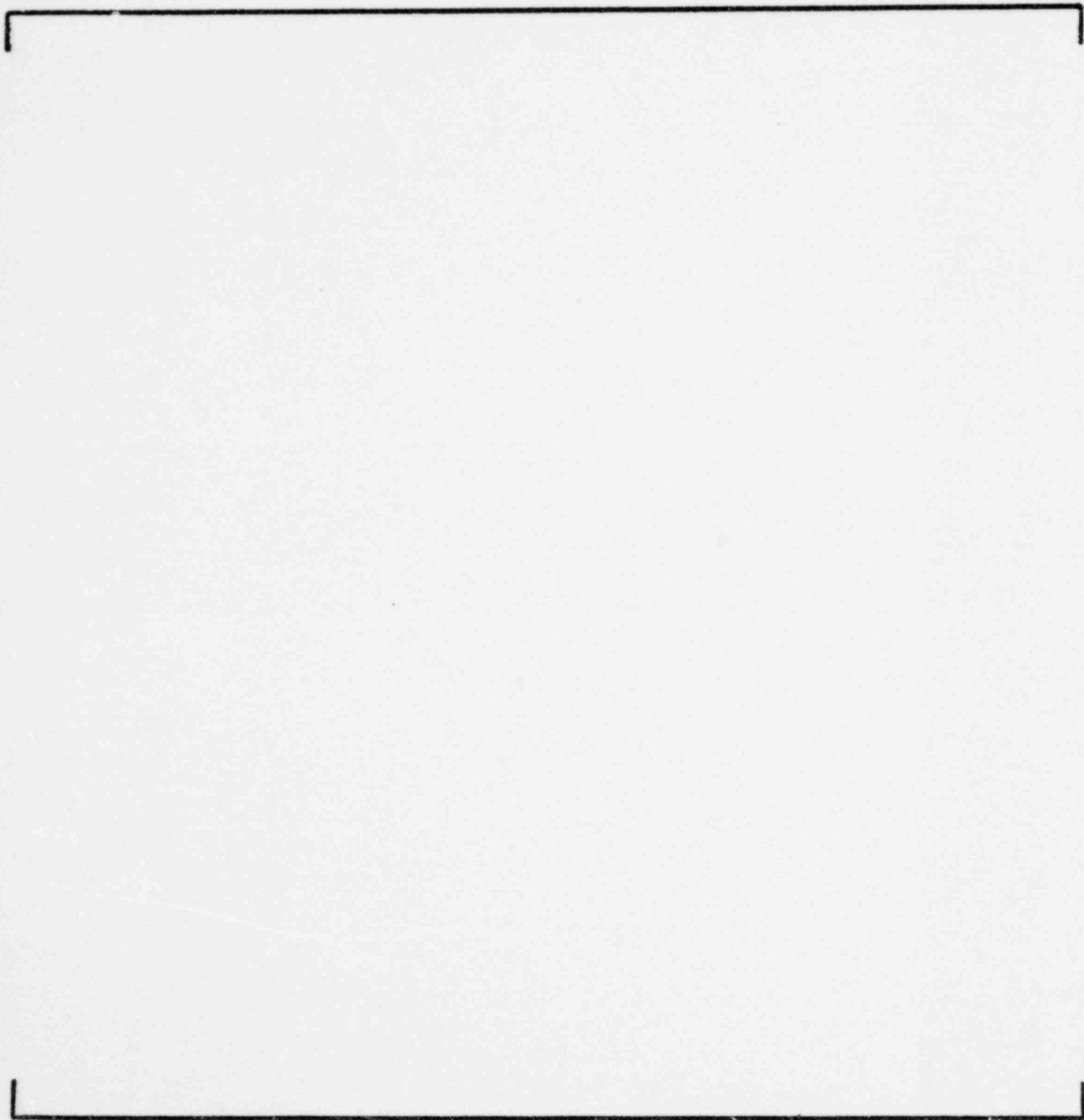


Figure 3-6c  
CALVERT CLIFFS UNIT 1 CYCLE 2  
COMPARISON OF ROCS (R) AND CECOR (C) BOX POWER FRACTIONS  
4192 MWD/T

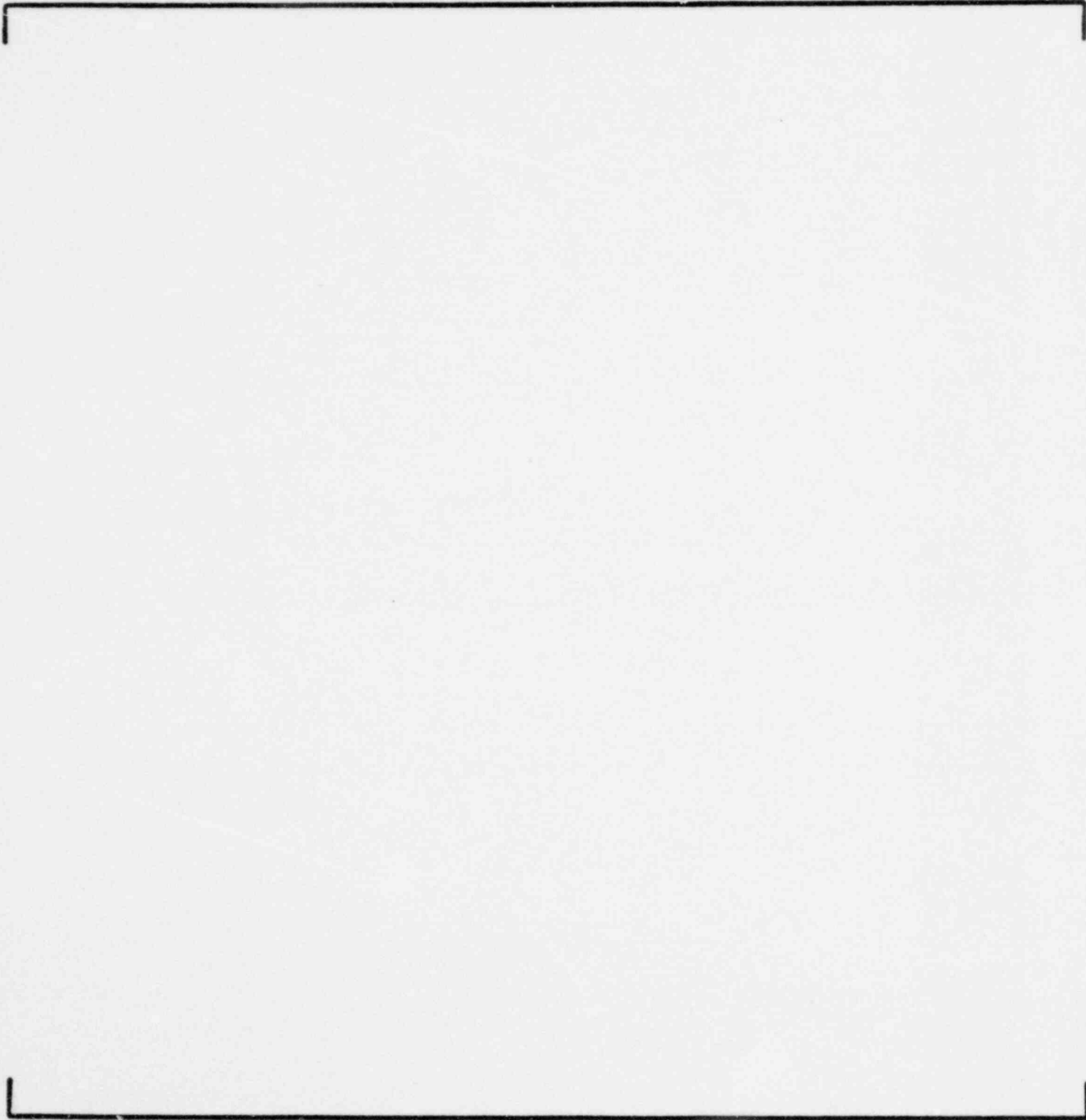


Figure 3-6d  
CALVERT CLIFFS UNIT 1 CYCLE 2  
COMPARISON OF ROCS (R) AND CECOR (C) BOX PEAK TO CORE AVERAGE POWER  
4192 MWD/T

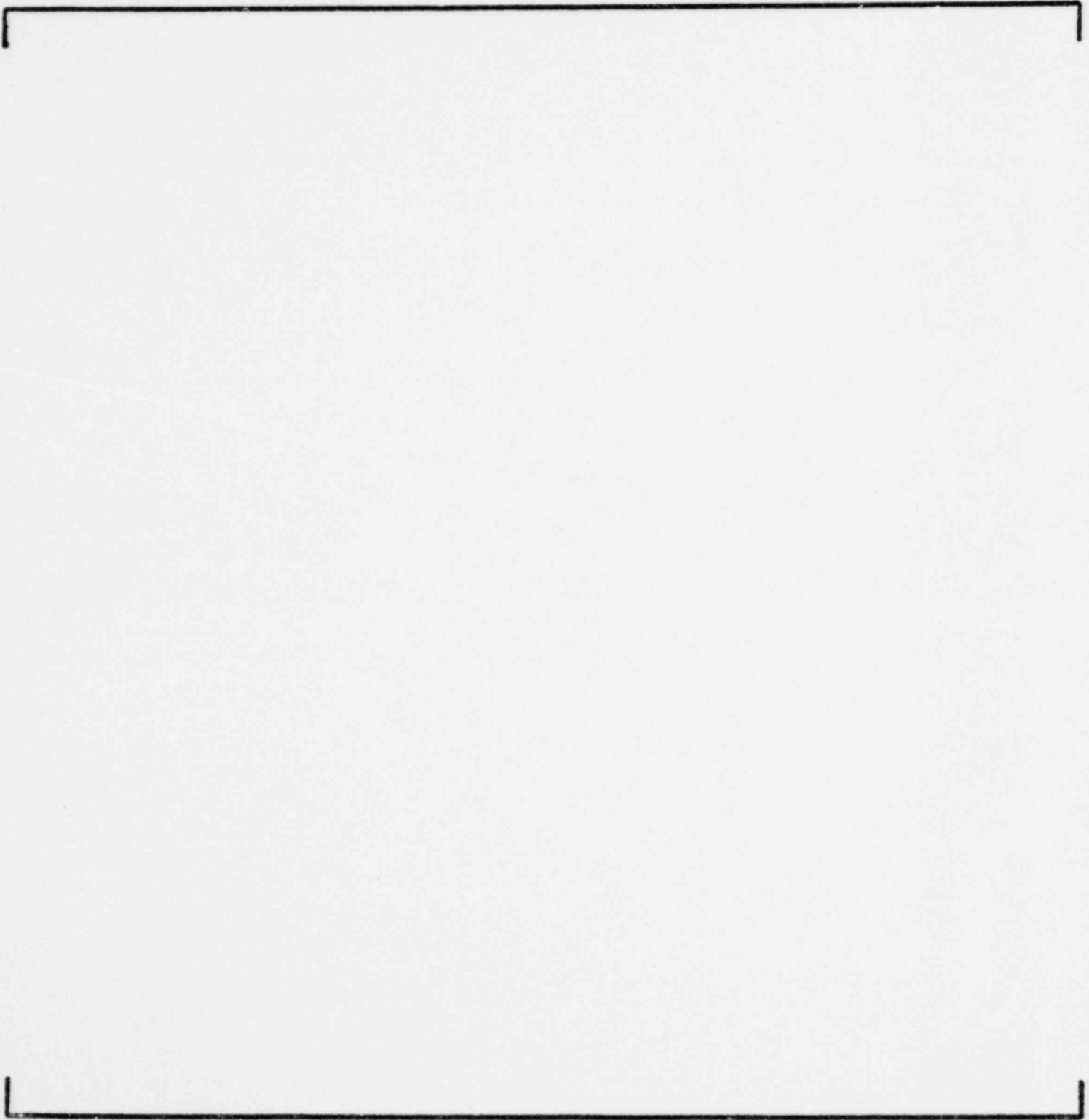


Figure 3-6e  
CALVERT CLIFFS UNIT 1 CYCLE 2  
COMPARISON OF ROCS (R) AND CECOR (C) BOX POWER FRACTIONS  
8330 MWD/T

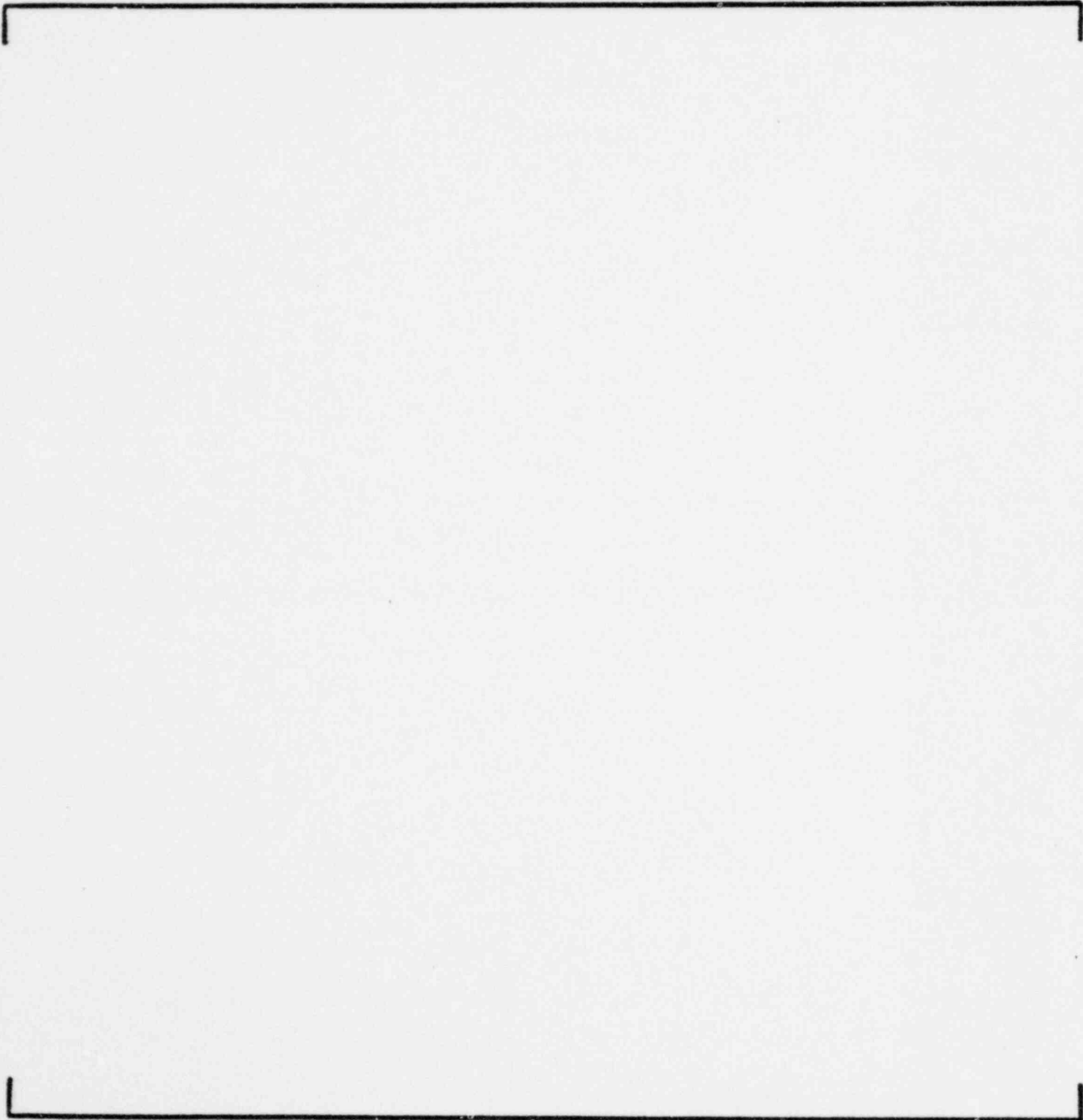


Figure 3-6f  
CALVERT CLIFFS UNIT 1 CYCLE 2  
COMPARISON OF ROCS (R) AND CECOR (C) BOX PEAK TO CORE AVERAGE POWER  
8330 MWD/T

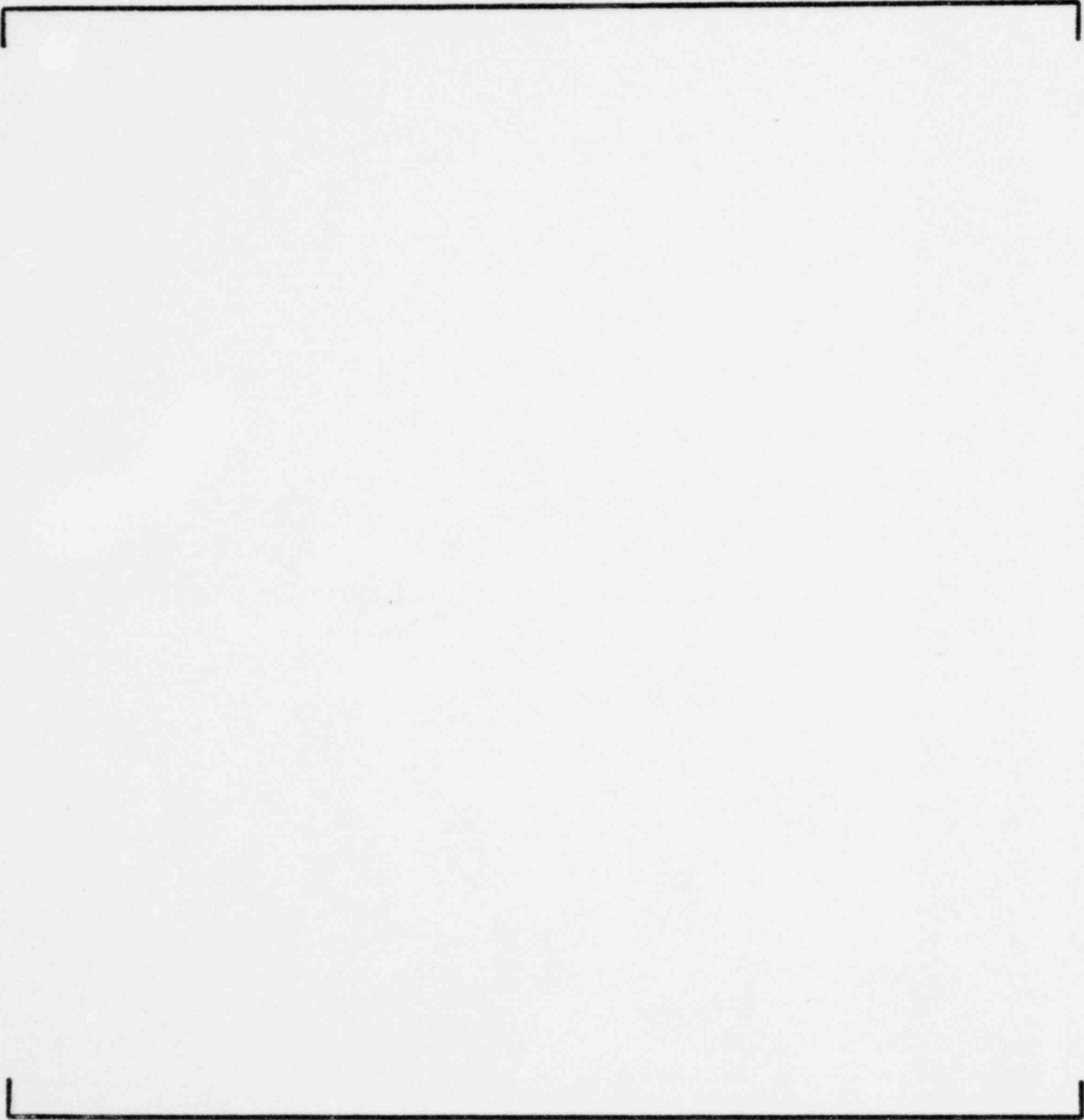


Figure 3-6g  
CALVERT CLIFFS UNIT 1 CYCLE 2  
COMPARISON OF ROCS AND CECOR PLANAR PEAK TO PLANE AVERAGE BOX POWERS  
325 MWD/T

II.3.106

Figure 3-6h  
CALVERT CLIFFS UNIT 1 CYCLE 2  
COMPARISON OF ROCS AND CECOR PLANAR PEAK TO PLANE AVERAGE BOX POWERS  
4192 MWD/T



II.3.107

Figure 3-6i  
CALVERT CLIFFS UNIT 1 CYCLE 2  
COMPARISON OF ROCS AND CECOR PLANAR PEAK TO PLANE AVERAGE BOX POWERS  
8330 MWD/T

II.3.108



Figure 3-6j  
CALVERT CLIFFS UNIT 1 CYCLE 2  
COMPARISON OF ROCS AND CECOR CORE AVERAGE AXIAL SHAPES  
325 MWD/T



11.3.109

Figure 3-6k  
CALVERT CLIFFS UNIT 1 CYCLE 2  
COMPARISON OF ROCS AND CECOR CORE AVERAGE AXIAL SHAPES  
4192 MWD/T

II.3.110

Figure 3-6I  
CALVERT CLIFFS UNIT 1 CYCLE 2  
COMPARISON OF ROCS AND CECOR CORE AVERAGE AXIAL SHAPES  
8330 MWD/T

II.3.111

Figure 3-6 m  
CALVERT CLIFFS UNIT 1 CYCLE 2  
COMPARISON OF ROCS (R) AND CECOR (C) ASSEMBLY BURNUP  
8330 MWD/T

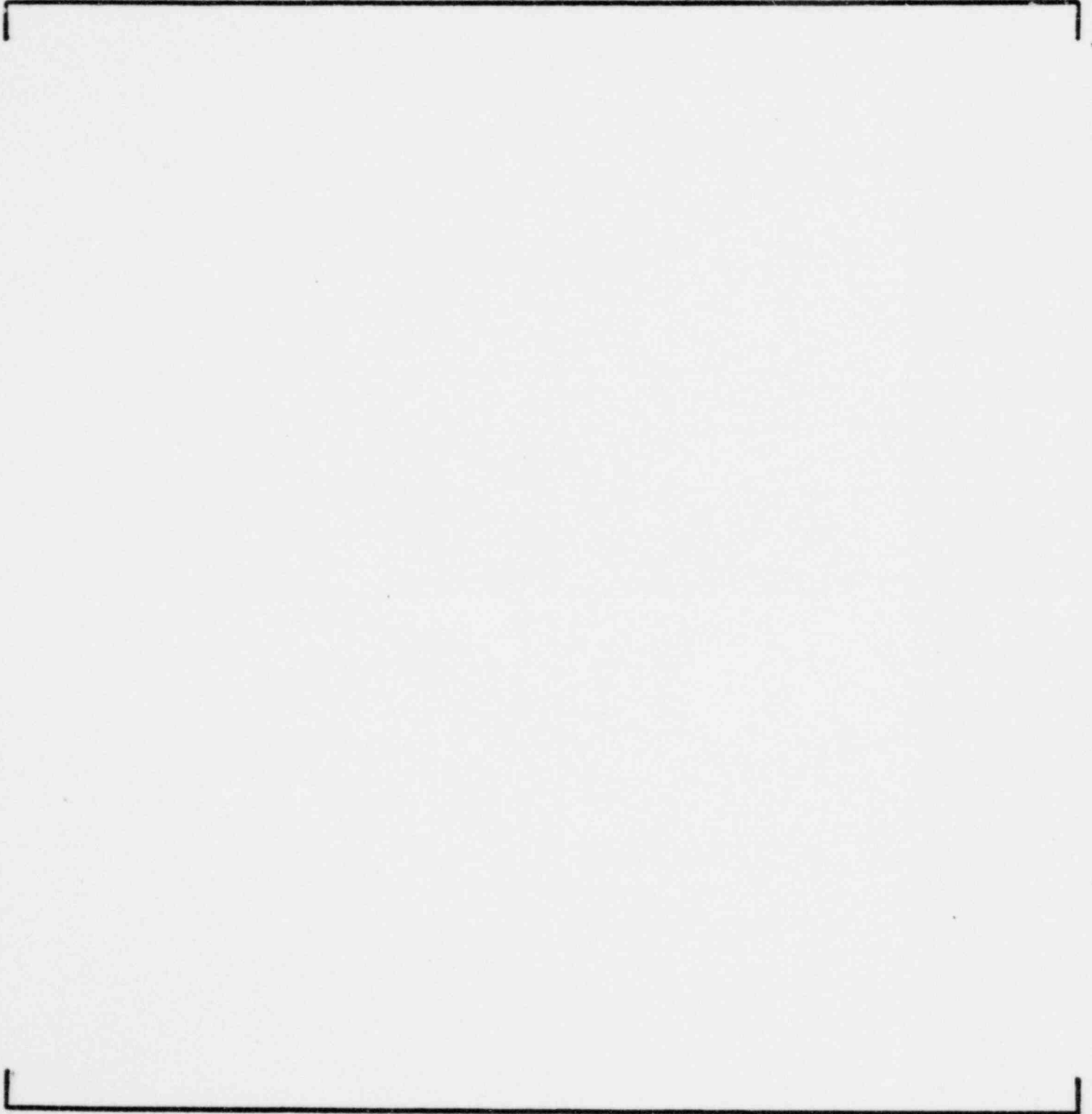


Figure 3-7a  
CALVERT CLIFFS UNIT 1 CYCLE 3  
COMPARISON OF ROCS (R) AND CECOR (C) BOX POWER FRACTIONS  
495 MWD/T

Figure 3-7b  
CALVERT CLIFFS UNIT 1 CYCLE 3  
COMPARISON OF ROCS (R) AND CECOR (C) BOX PEAK TO CORE AVERAGE POWER  
495 MWD/T

Figure 3-7c  
CALVERT CLIFFS UNIT 1 CYCLE 3  
COMPARISON OF ROCS (R) AND CECOR (C) BOX POWER FRACTIONS  
801 MWD/T (50% ROD BANK 5 INSERTION)

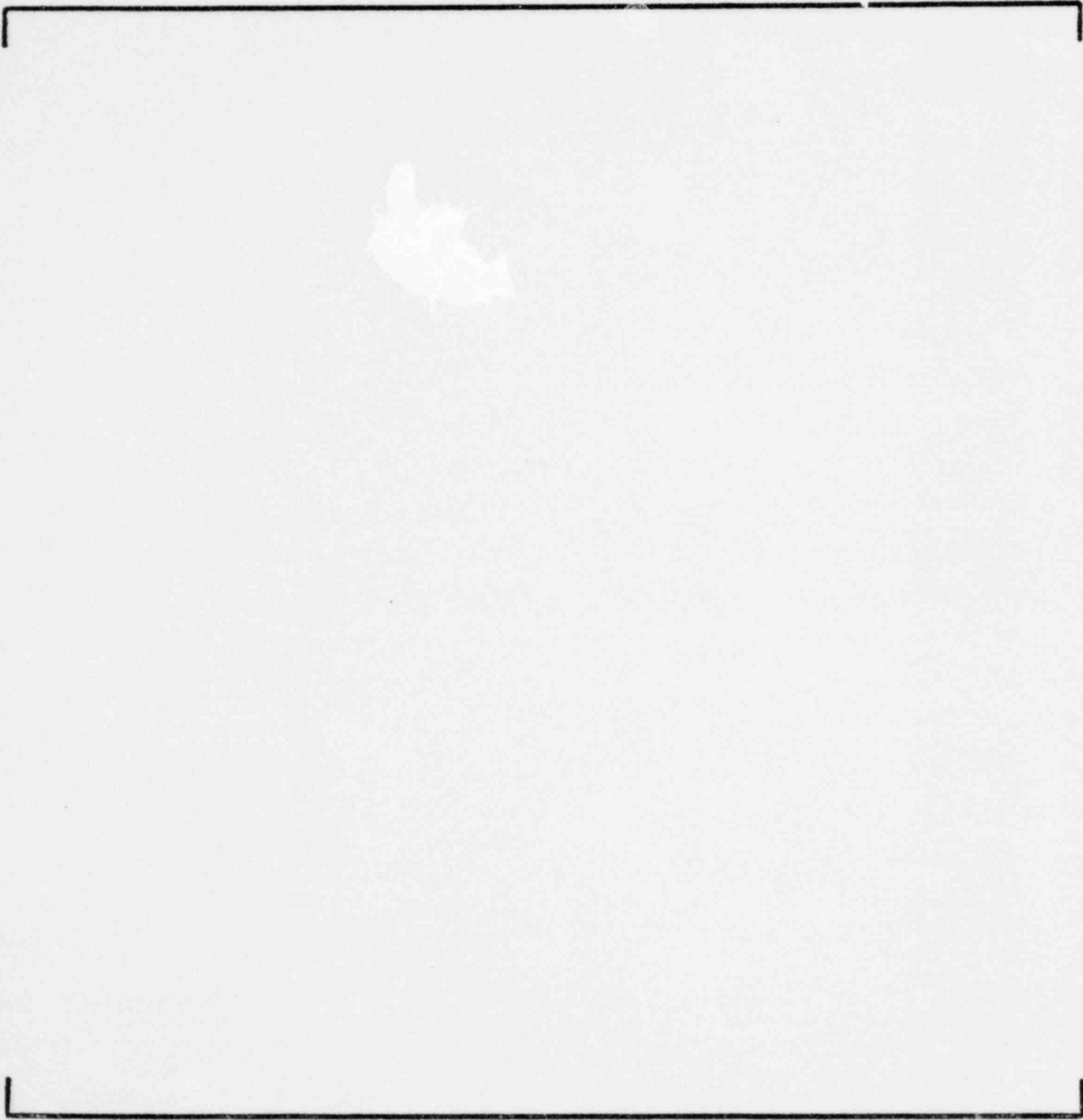


Figure 3-7d  
CALVERT CLIFFS UNIT 1 CYCLE 3  
COMPARISON OF ROCS (R) AND CECOR (C) BOX PEAK TO CORE AVERAGE POWER  
801 MWD/T (50% ROD BANK 5 INSERTION)

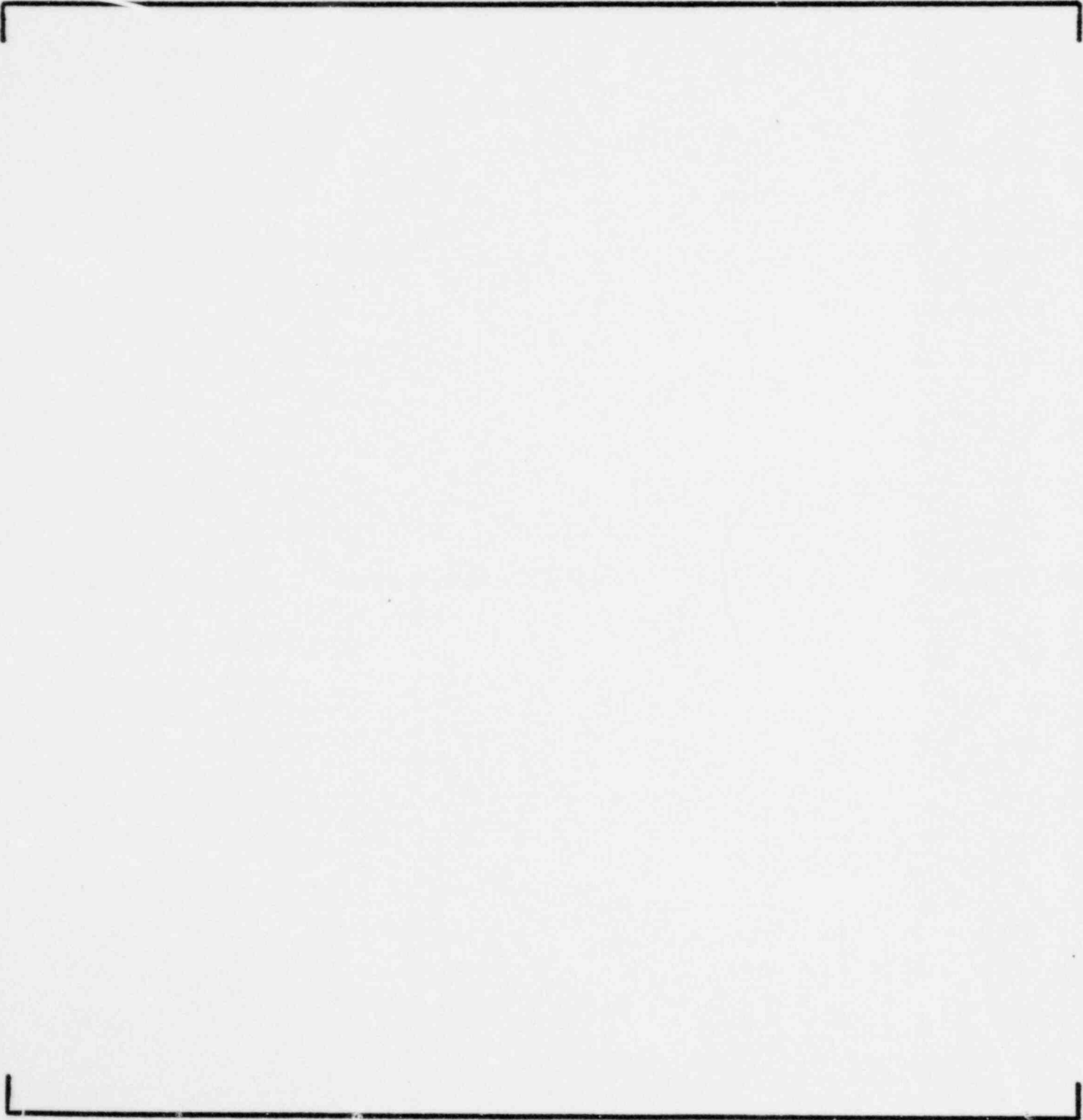




Figure 3-7e  
CALVERT CLIFFS UNIT 1 CYCLE 3  
COMPARISON OF ROCS (R) AND CECOR (C) BOX POWER FRACTIONS  
5994 MWD/T

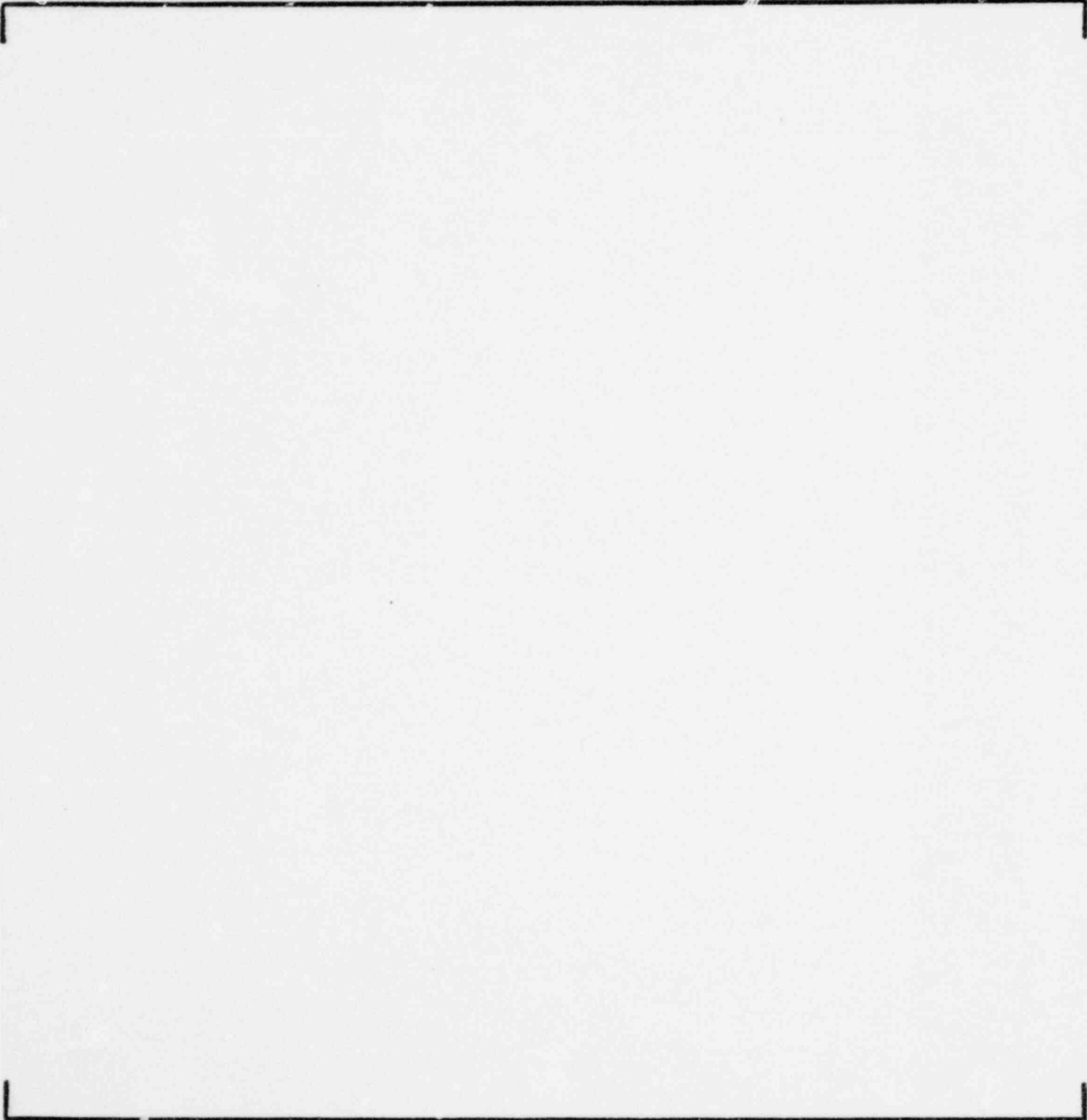


Figure 3-7f  
CALVERT CLIFFS UNIT 1 CYCLE 3  
COMPARISON OF ROCS (R) AND CECOR (C) BOX PEAK TO CORE AVERAGE POWER  
5994 MWD/T

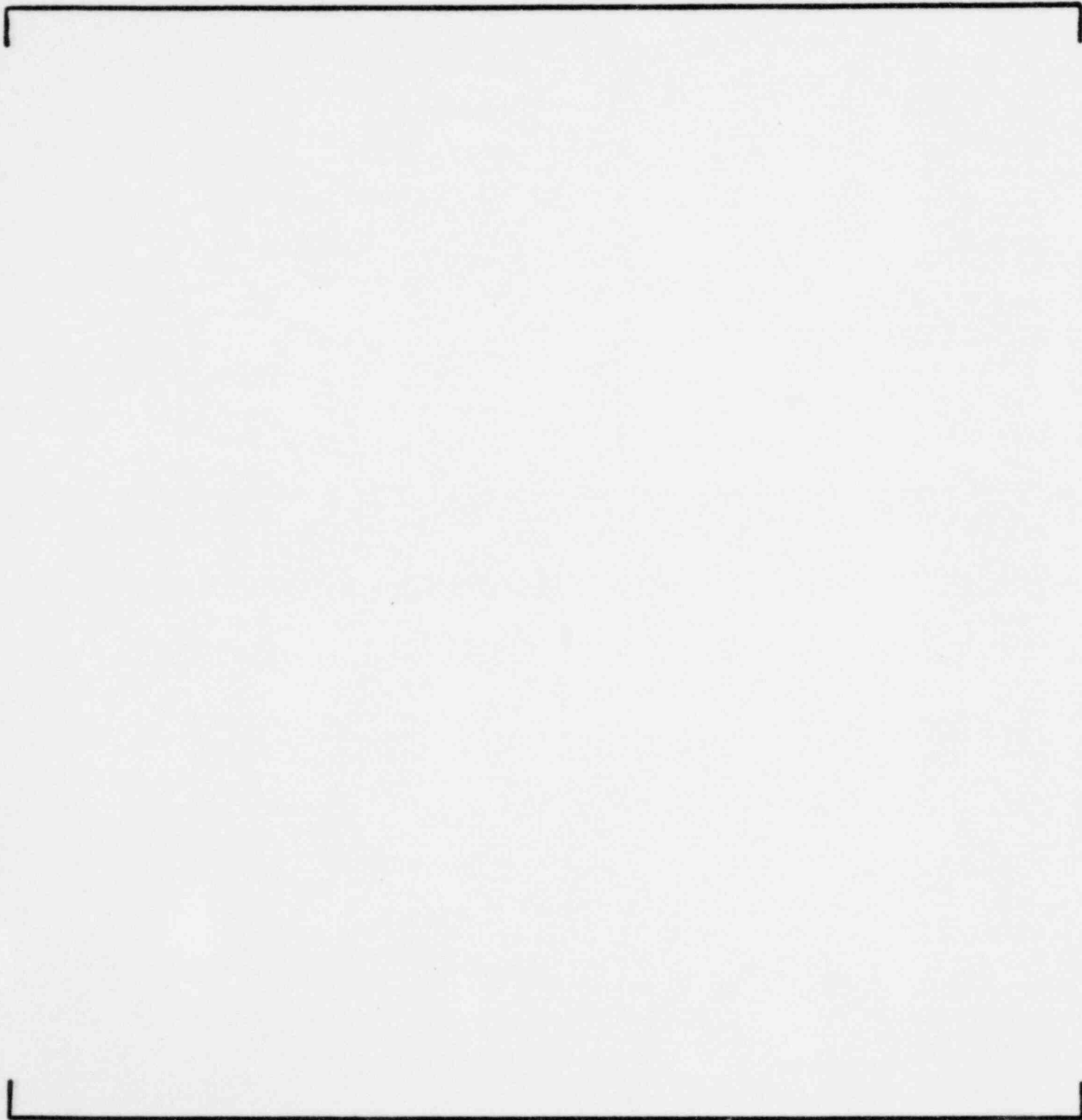


Figure 3-7g  
CALVERT CLIFFS UNIT 1 CYCLE 3  
COMPARISON OF ROCS (R) AND CECOR (C) BOX POWER FRACTIONS  
8578 MWD/T

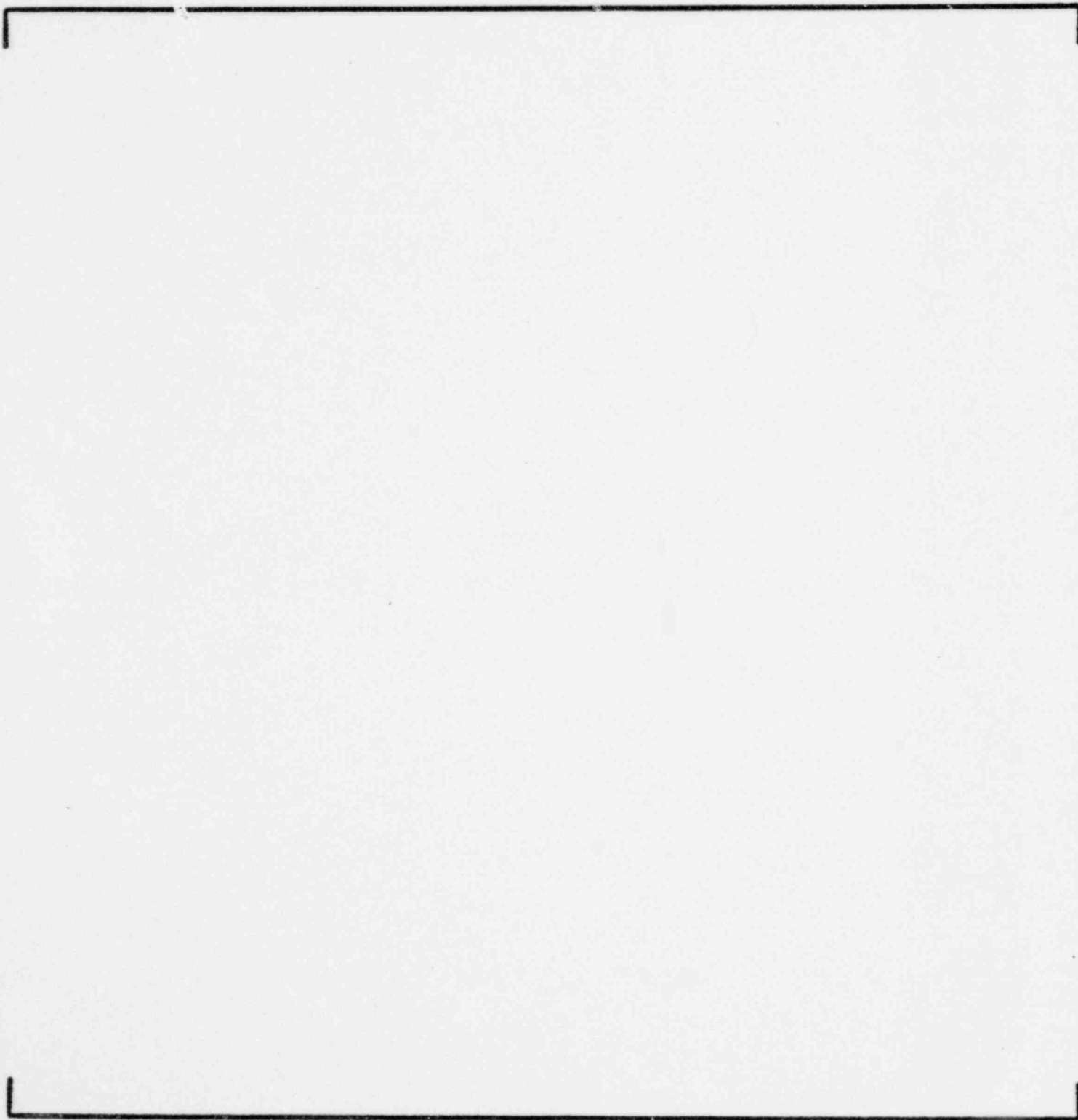


Figure 3-7h  
CALVERT CLIFFS UNIT 1 CYCLE 3  
COMPARISON OF ROCS (R) AND CECOR (C) BOX PEAK TO CORE AVERAGE POWER  
8578 MWD/T

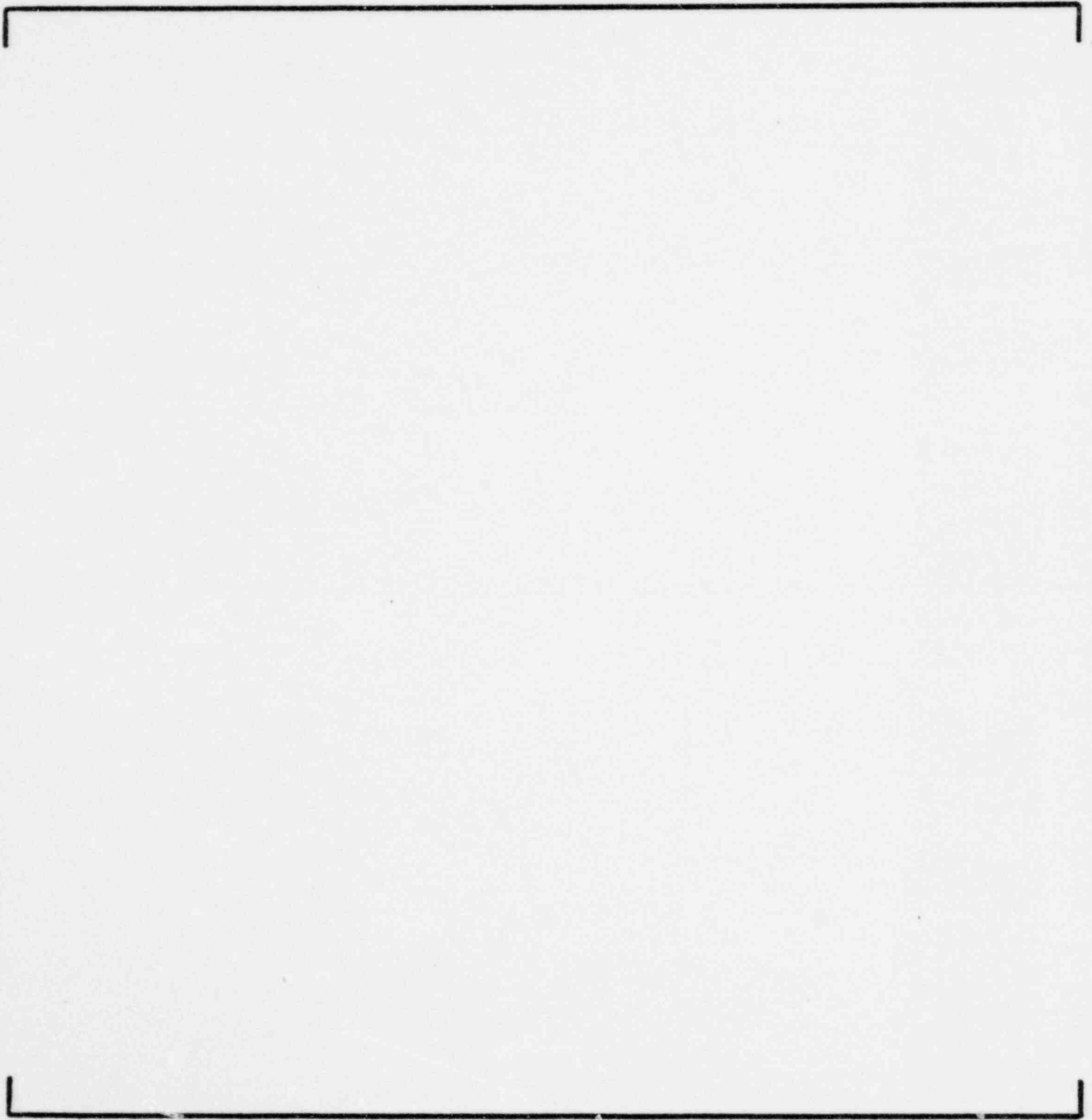


Figure 3-7i  
CALVERT CLIFFS UNIT 1 CYCLE 3  
COMPARISON OF ROCS AND CECOR PLANAR PEAK TO PLANE AVERAGE BOX POWERS  
495 MWD/T

11.3.121

Figure 3-7j  
CALVERT CLIFFS UNIT 1 CYCLE 3  
COMPARISON OF ROCS AND CECOR PLANAR PEAK TO PLANE AVERAGE BOX POWERS  
801 MWD/T (50% ROD BANK 5 INSERTION)

11.3.122

Figure 3-7k  
CALVERT CLIFFS UNIT 1 CYCLE 3  
COMPARISON OF ROCS AND CECOR PLANAR PEAK TO PLANE AVERAGE BOX POWERS  
5994 MWD/T

11.3.123

Figure 3-71  
CALVERT CLIFFS UNIT 1 CYCLE 3  
COMPARISON OF ROCS AND CECOR PLANAR PEAK TO PLANE AVERAGE BOX POWERS  
8578 MWD/T

11.3.124

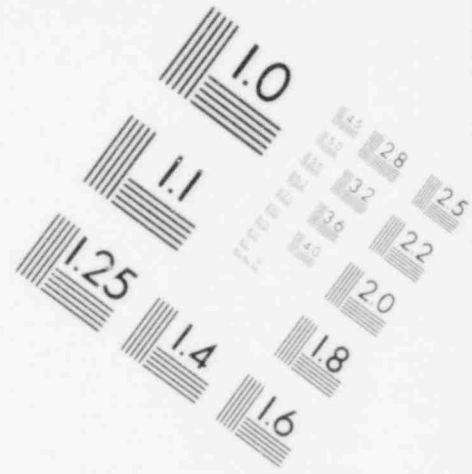
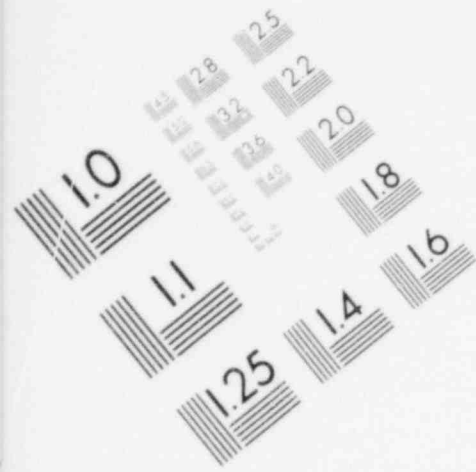


Figure 3-7m  
CALVERT CLIFFS UNIT 1 CYCLE 3  
COMPARISON OF ROCS AND CECOR CORE AVERAGE AXIAL SHAPES  
495 MWD/T

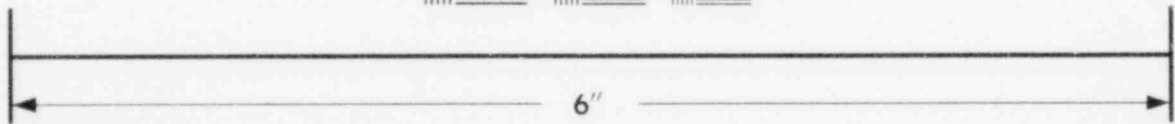
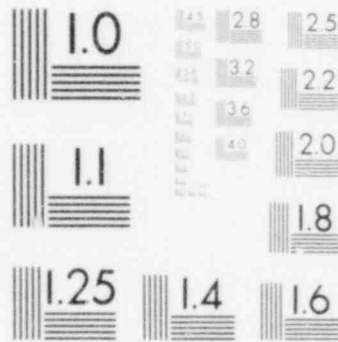
11.3.125

Figure 3-7n  
CALVERT CLIFFS UNIT 1 CYCLE 3  
COMPARISON OF ROCS AND CECOR CORE AVERAGE AXIAL SHAPES  
801 MWD/T (50% ROD BANK 5 INSERTION)

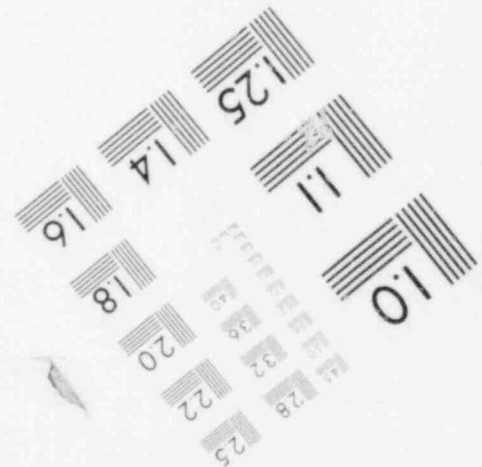
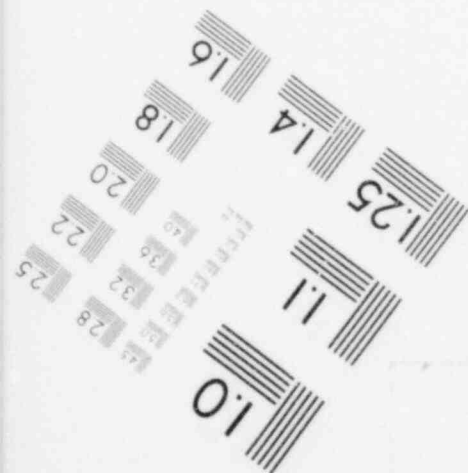
11.3.126



**IMAGE EVALUATION  
TEST TARGET (MT-3)**



**MICROCOPY RESOLUTION TEST CHART**



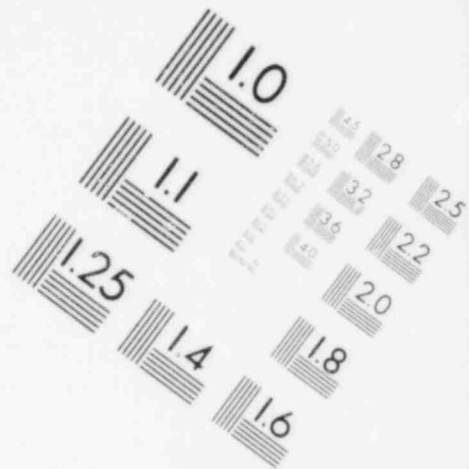
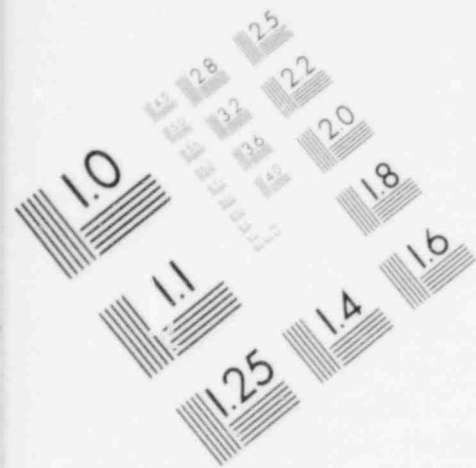
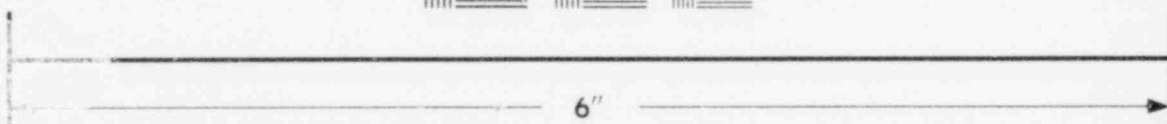


**IMAGE EVALUATION  
TEST TARGET (MT-3)**



**MICROCOPY RESOLUTION TEST CHART**

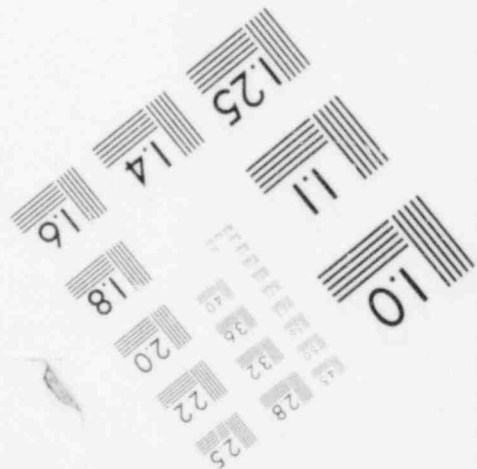
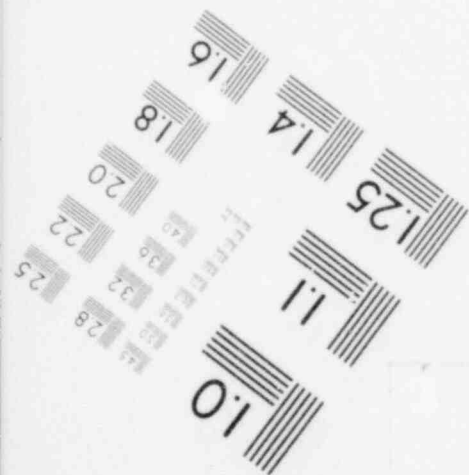
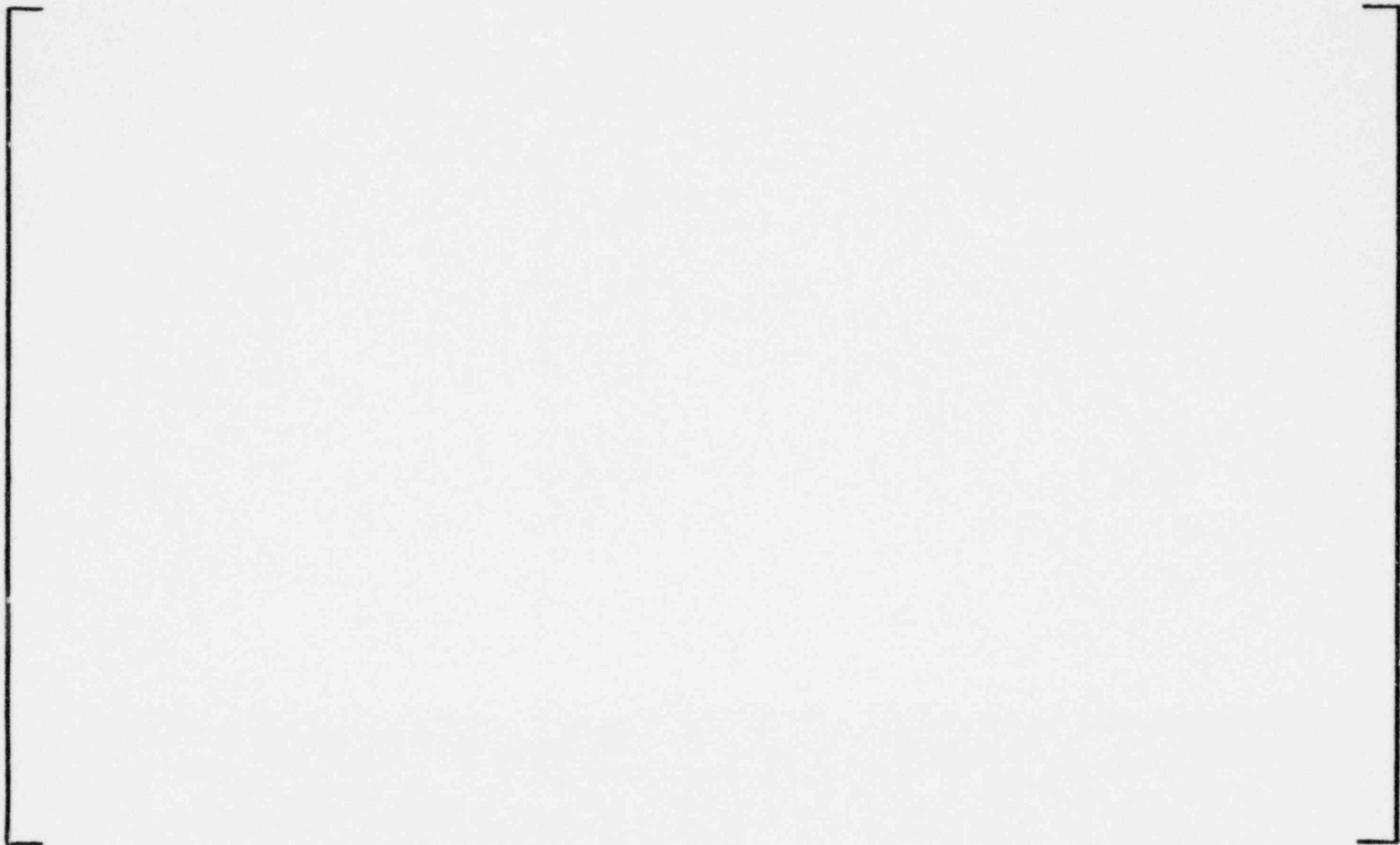


Figure 3-7o  
CALVERT CLIFFS UNIT 1 CYCLE 3  
COMPARISON OF ROCS AND CECOR CORE AVERAGE AXIAL SHAPES  
5994 MWD/T

11.3.127

Figure 3-7p  
CALVERT CLIFFS UNIT 1 CYCLE 3  
COMPARISON OF ROCS AND CECOR CORE AVERAGE AXIAL SHAPES  
8578 MWD/T



11.3.128

Figure 3-7 q  
CALVERT CLIFFS UNIT 1 CYCLE 3  
COMPARISON OF ROCS (R) AND CECOR (C) ASSEMBLY BURNUP  
8578 MWD/T

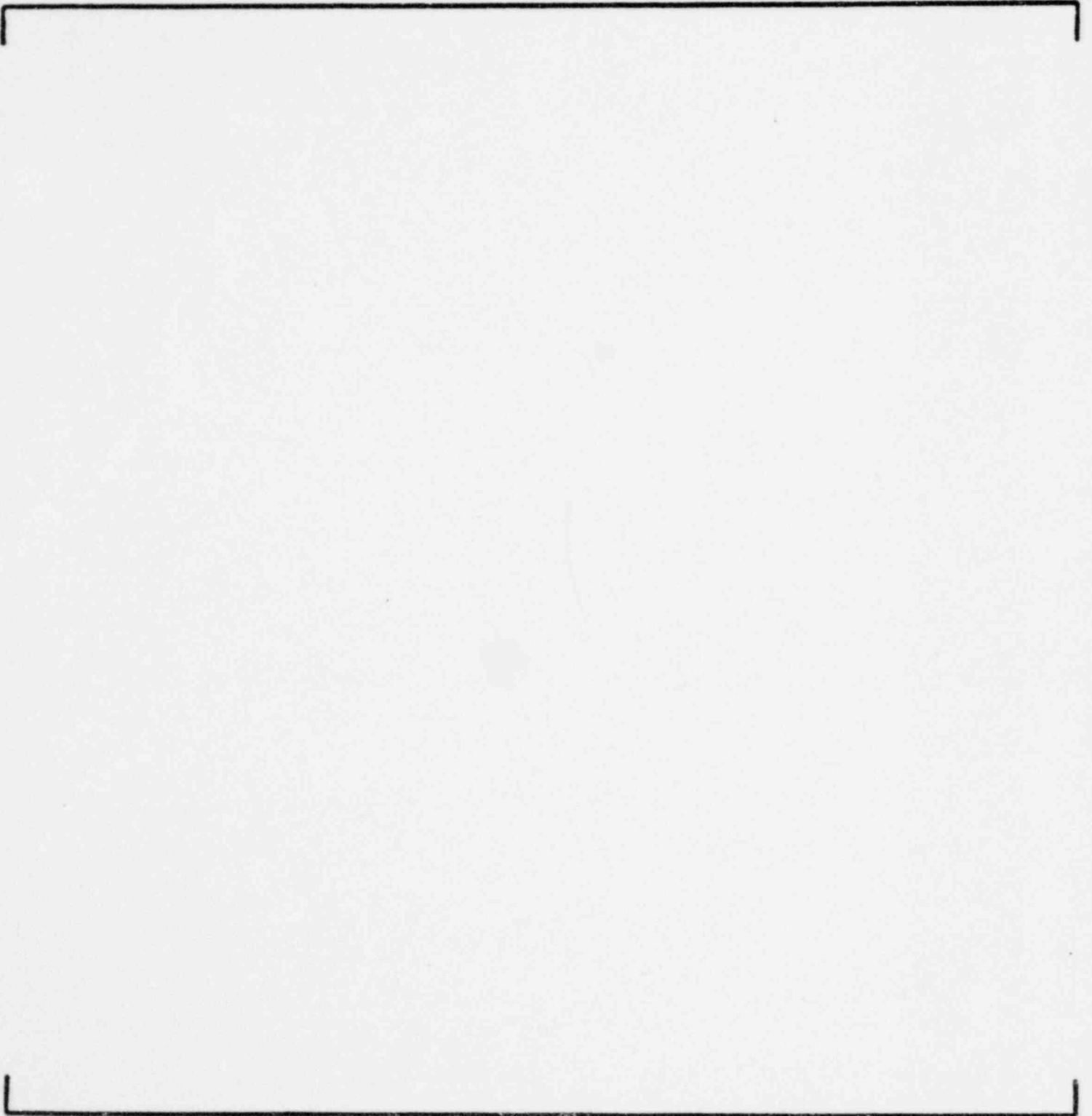


Figure 38  
DISTRIBUTION OF DEVIATIONS IN F<sub>q</sub> BOX SYNTHESIS  
CALVERT CLIFFS UNIT 1 CYCLE 2

II.3.130



Figure 3-9  
DISTRIBUTION OF DEVIATIONS IN Fr BOX SYNTHESIS  
CALVERT CLIFFS UNIT 1 CYCLE 2

II.3.131

Figure 3-10  
DISTRIBUTION OF DEVIATIONS IN  $F_{xy}$  BOX SYNTHESIS  
CALVERT CLIFFS UNIT 1 CYCLE 2

II.3.132

Figure 3-11  
LOADING & INSTRUMENT PATTERN  
CALVERT CLIFFS UNIT 2 CYCLE 2

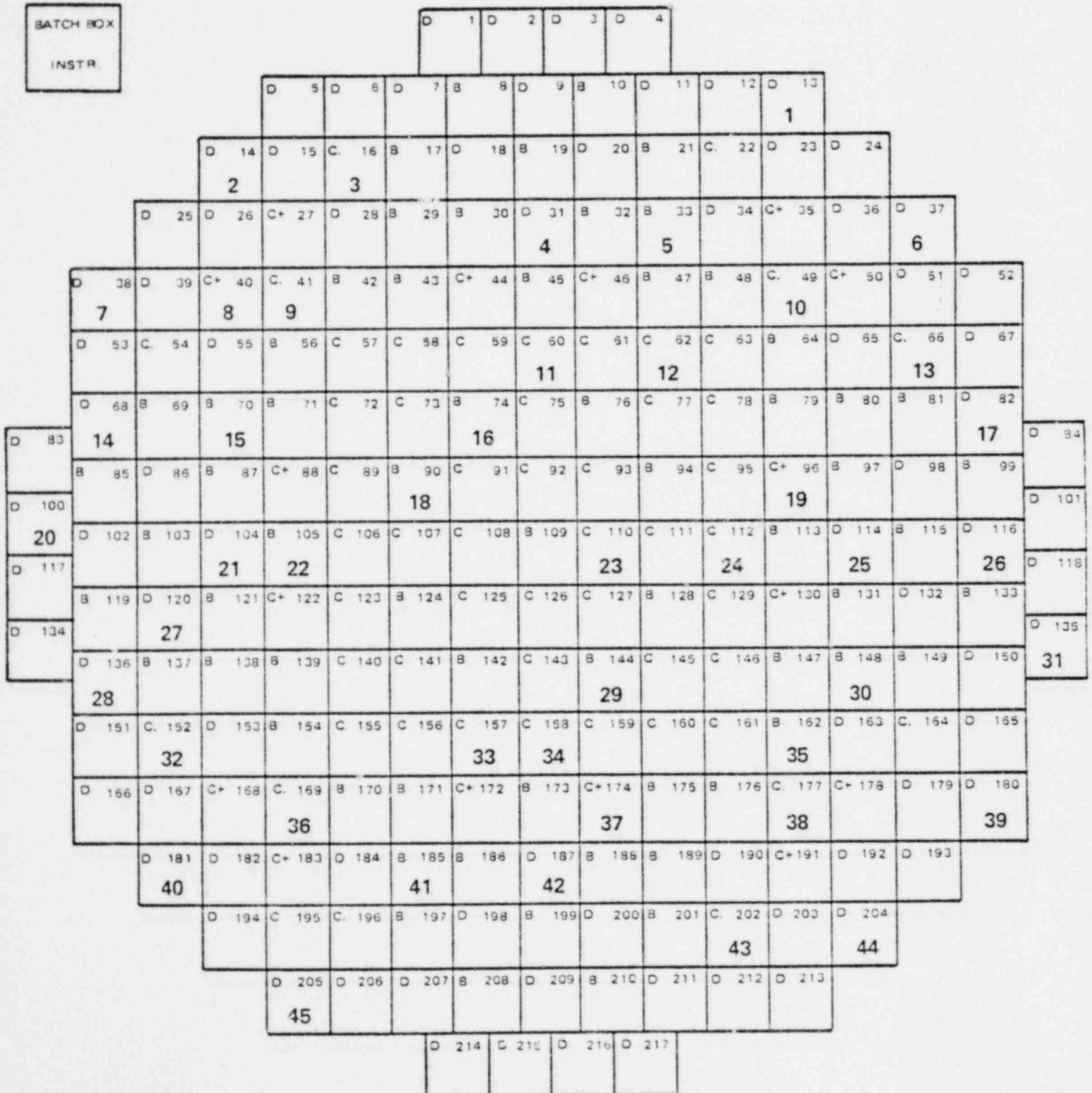


**Figure 3-12**  
**LOADING & INSTRUMENT PATTERN**  
**ST. LUCIE CYCLE 2**

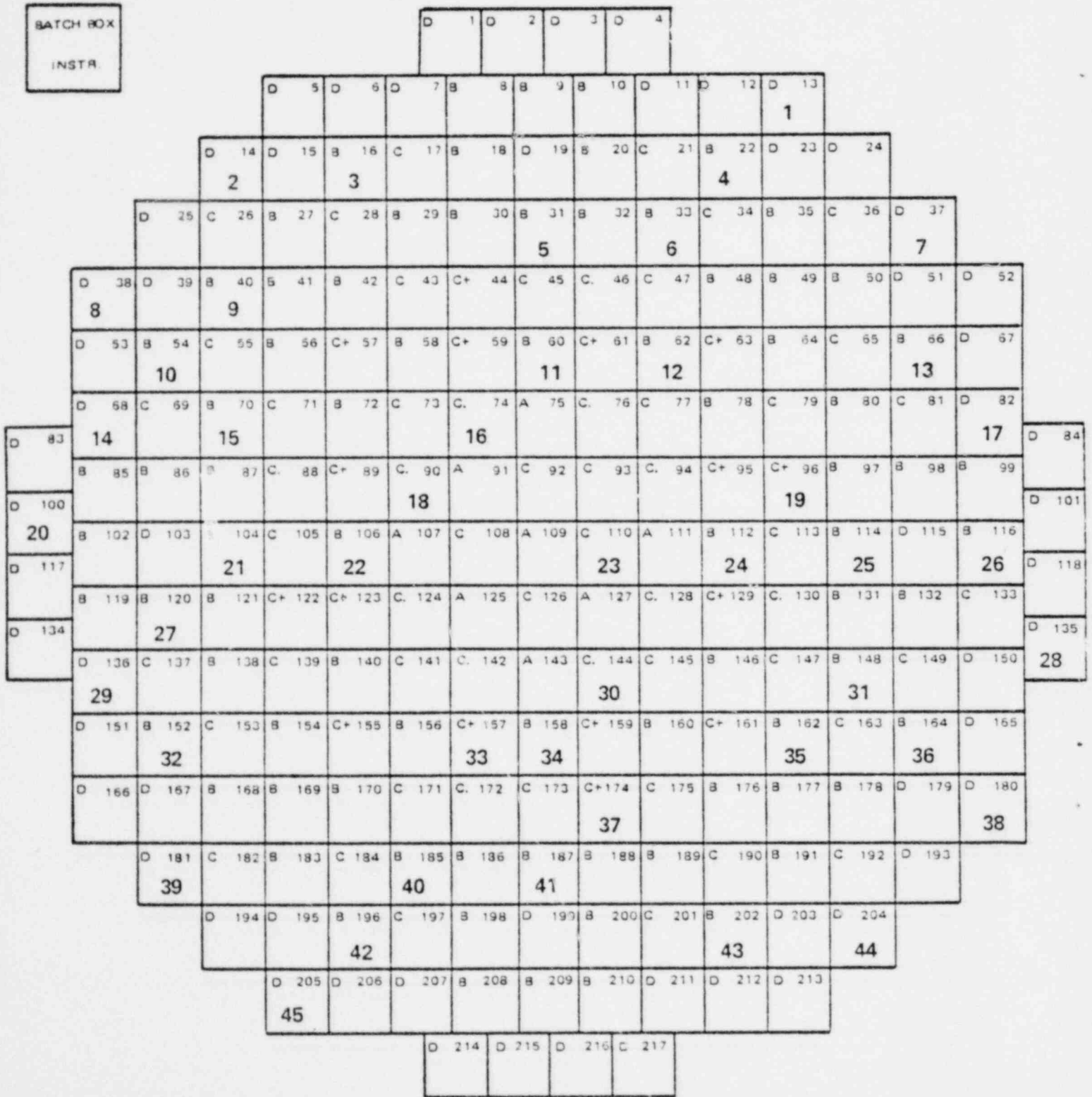


**Figure 3-13**  
**LOADING & INSTRUMENT PATTERN**  
**MILLSTONE II CYCLE 2**

BATCH BOX  INSTR.		D 1 D 2 D 3 D 4															
		D 5	D 6	D 7	C 8	B 9	C 10	D 11	D 12	D 13							
												44					
		D 14	D 15	C+ 16	B 17	B 18	D 19	B 20	B 21	C+ 22	D 23	D 24					
		42	43						29								
		D 25	C 26	B 27	B 28	D 29	B 30	B 31	B 32	D 33	B 34	B 35	C 36	D 37			
								27	28								
D 38	D 39	B 40	D 41	B 42	B 43	C 44	C 45	C 46	B 47	B 48	D 49	B 50	D 51	D 52			
41	25																
D 53	C+ 54	B 55	B 56	B 57	C 58	C 59	C 60	C 61	C 62	B 63	B 64	B 65	C+ 66	D 67			
26								8	9	30							
D 68	B 69	D 70	B 71	C 72	B 73	C+ 74	B 75	C+ 76	B 77	C 78	B 79	D 80	B 81	D 82			
D 83	40	24		7										31			
		C 85	B 86	B 87	C 88	C 89	C+ 90	C 91	C 92	C 93	C+ 94	C 95	C 96	B 97	B 98	C 99	
D 100	39	6										11					
D 101			B 102	D 103	B 104	C 105	C 106	B 107	C 108	B 109	C 110	B 111	C 112	C 113	B 114	D 115	B 116
D 117	23		5							1	10	12	32				
D 118			C 119	B 120	B 121	C 122	C 123	C+ 124	C 125	C 126	C 127	C+ 128	C 129	C 130	B 131	B 132	C 133
D 134	22											13					
D 135	33	D 136	B 137	D 138	B 139	C 140	B 141	C+ 142	B 143	C+ 144	B 145	C 146	B 147	D 148	B 149	D 150	
21								2									
D 151	C+ 152	B 153	B 154	B 155	C 156	C 157	C 158	C 159	C 160	B 161	B 162	B 163	C+ 164	D 165			
20						4	3						14	15			
D 166	D 167	B 168	D 169	B 170	B 171	C 172	C 173	C 174	B 175	B 176	D 177	B 178	D 179	D 180			
								16							34		
D 181	C 182	B 183	B 184	D 185	B 186	B 187	B 188	D 189	B 190	B 191	C 192	D 193					
38					18	17											
D 194	D 195	C+ 196	B 197	B 198	D 199	B 200	B 201	C+ 202	D 203	D 204							
		19							35								
D 205	D 206	D 207	C 208	B 209	C 210	D 211	D 212	D 213									
37							36										
		D 214	D 215	D 216	D 217												

**Figure 3-14**  
**LOADING & INSTRUMENT PATTERN**  
**CALVERT CLIFFS UNIT 1 CYCLE 4**

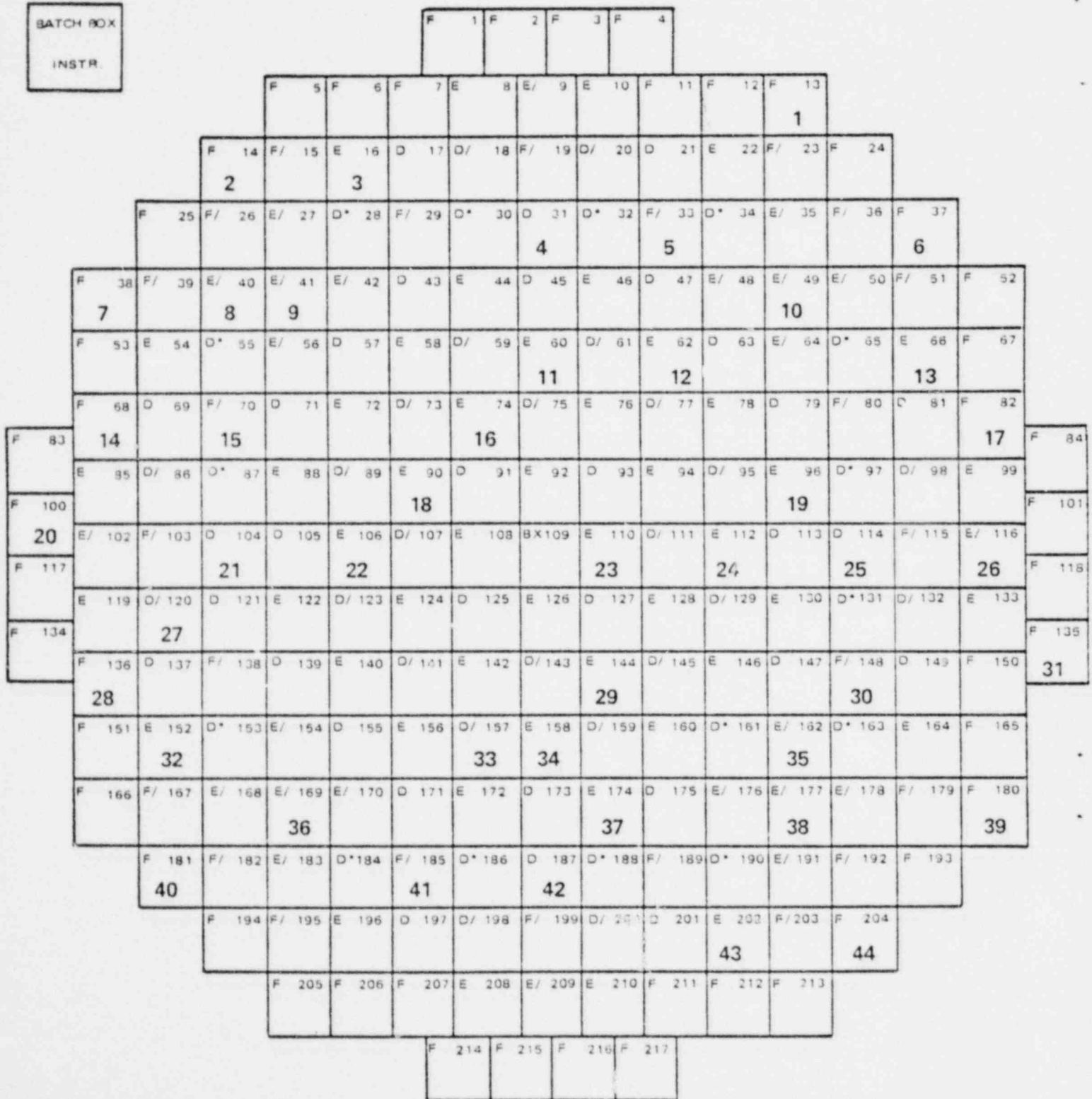


Figure 3-15

CALVERT CLIFFS UNIT 2 CYCLE :

COMPARISON OF [

] PDC PEAK PIN TO BOX AVERAGE PIN POWER

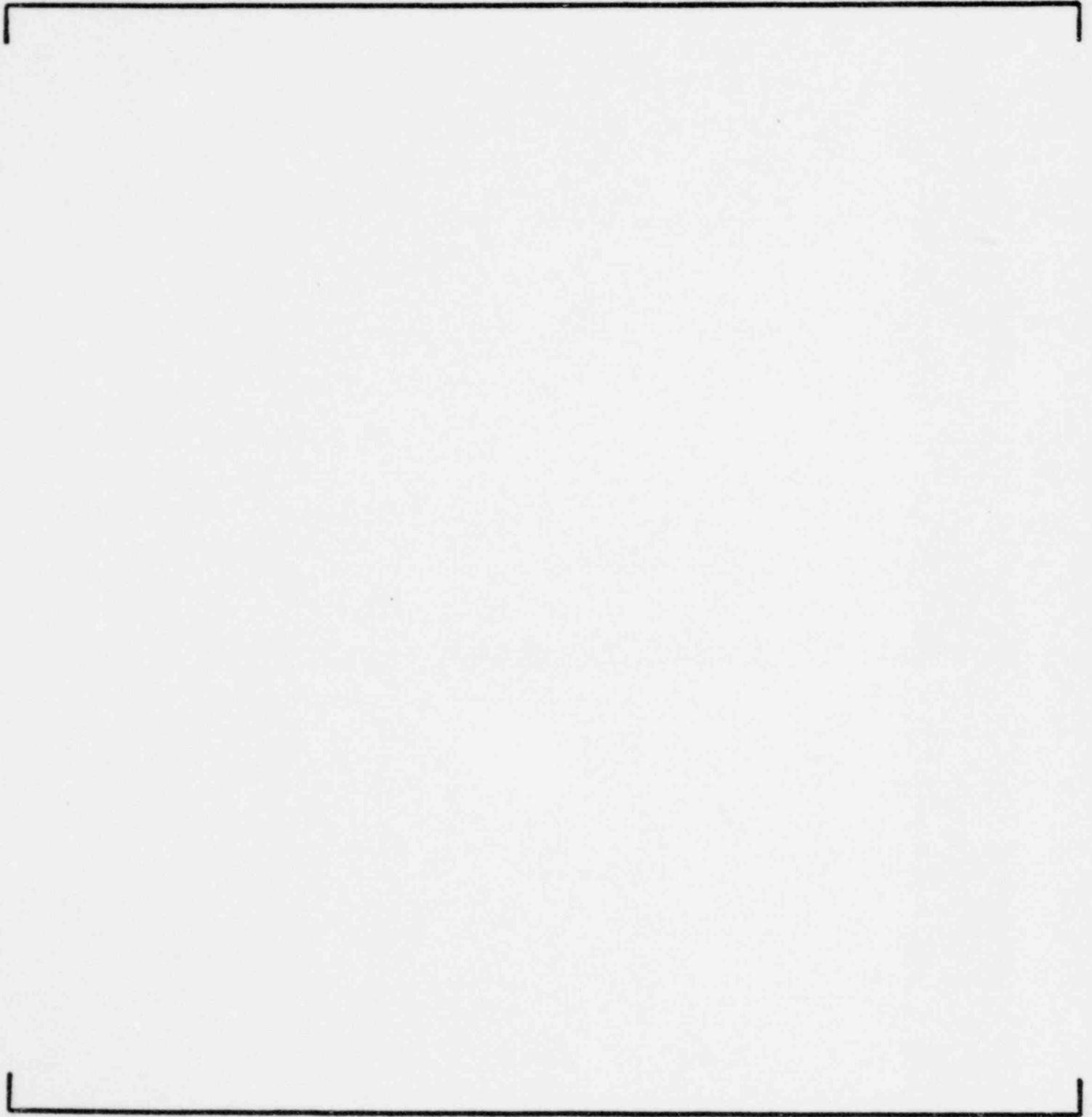


Figure 3-16

ST. LUCIE UNIT 1 CYCLE 2

COMPARISON OF [

] PDQ PEAK PIN TO BOX AVERAGE PIN POWER

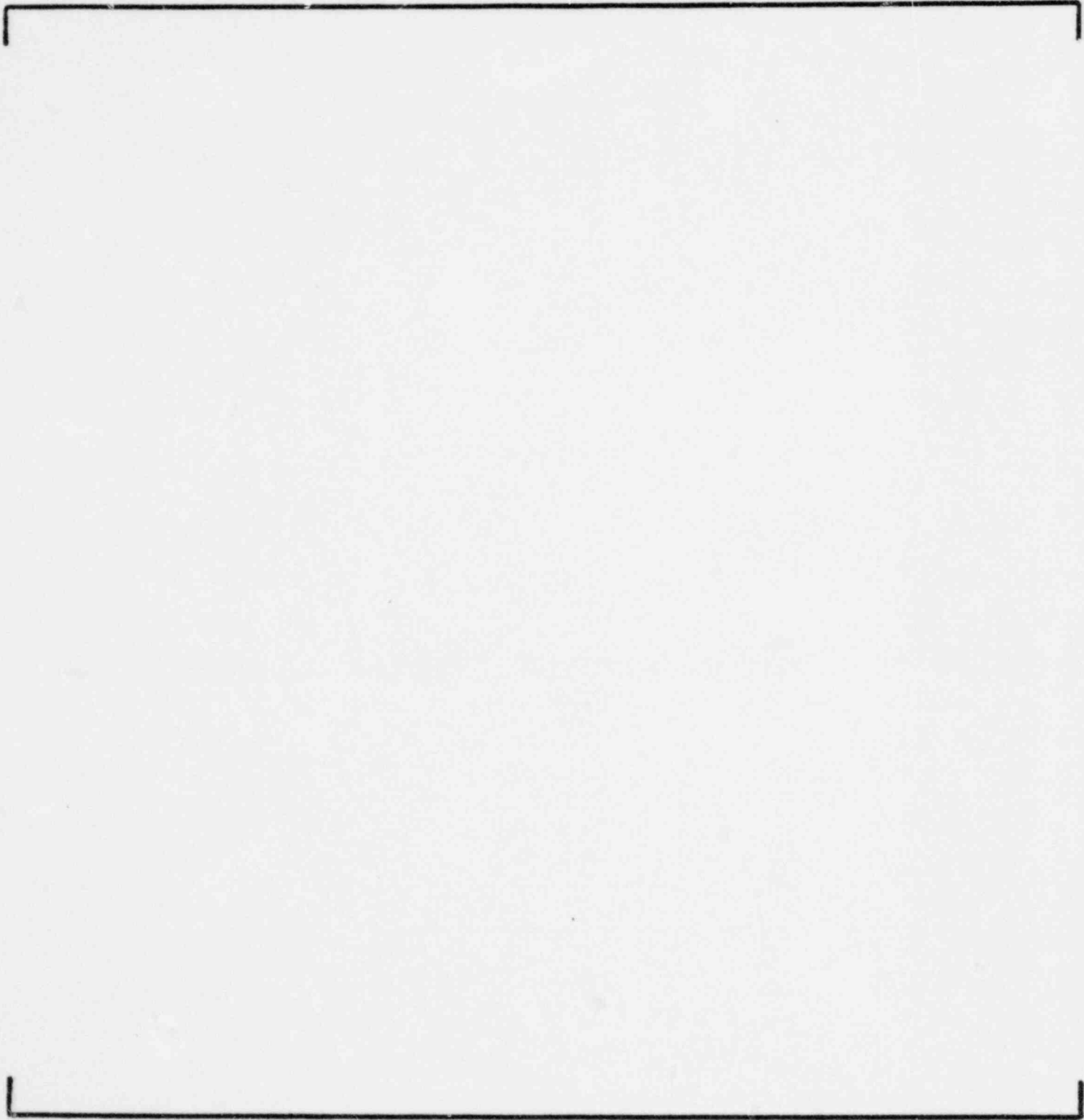




Figure 3-17

MILLSTONE UNIT 2 CYCLE 2

COMPARISON OF [

] PDQ PIN PEAK TO BOX AVERAGE PIN POWER

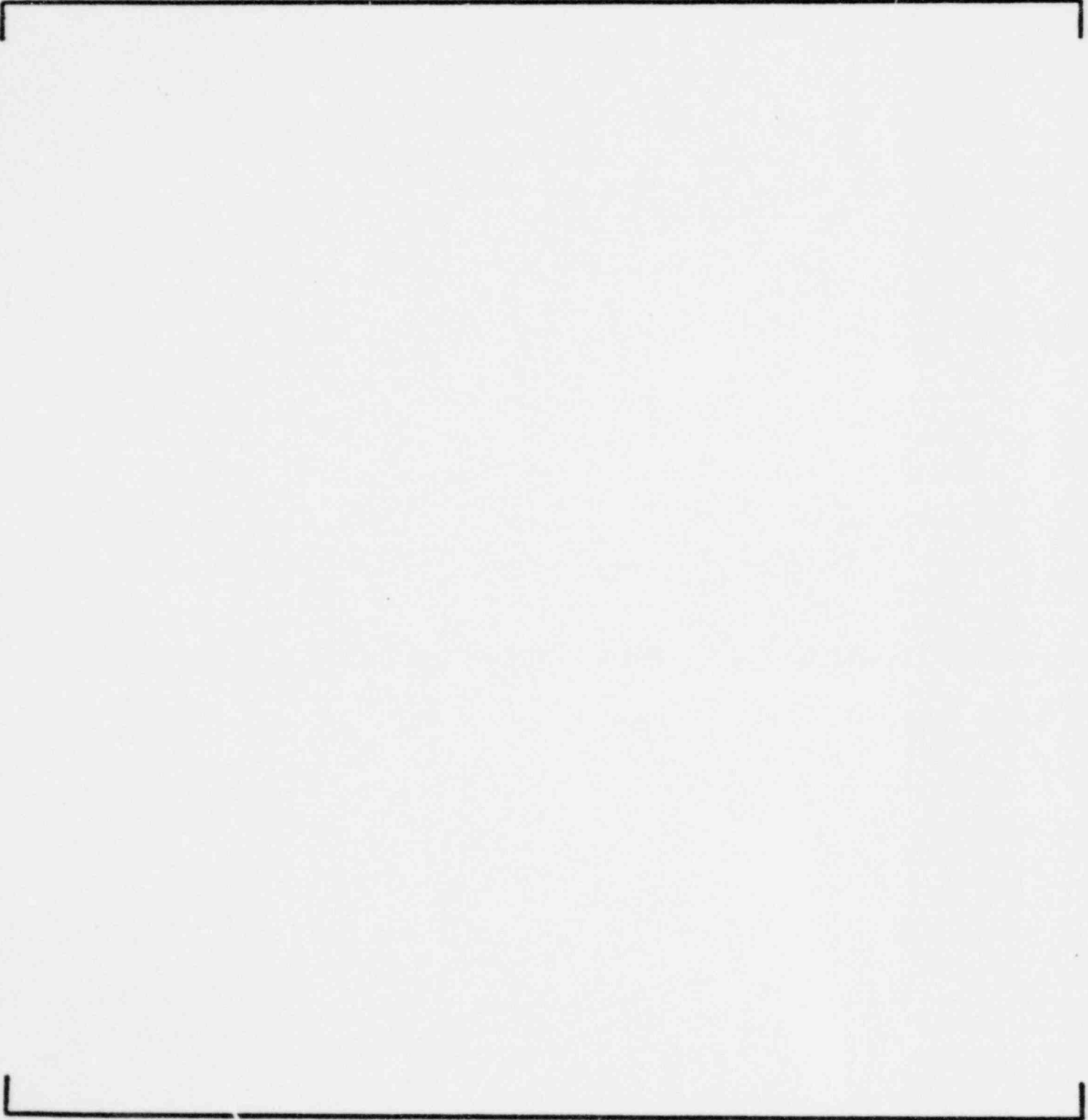


Figure 3-18

CALVERT CLIFFS UNIT 1 CYCLE 4

COMPARISON OF [

] PDQ PIN PEAK TO BOX AVERAGE PIN POWER

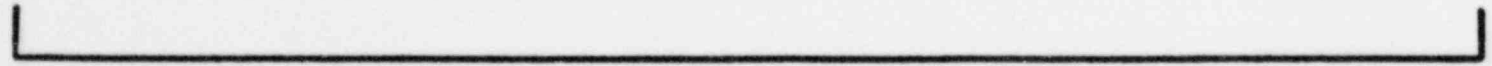
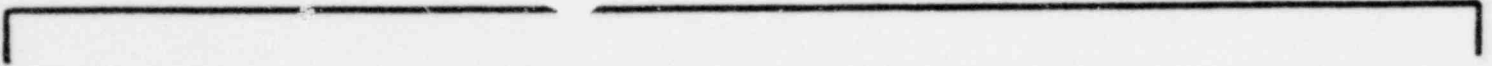
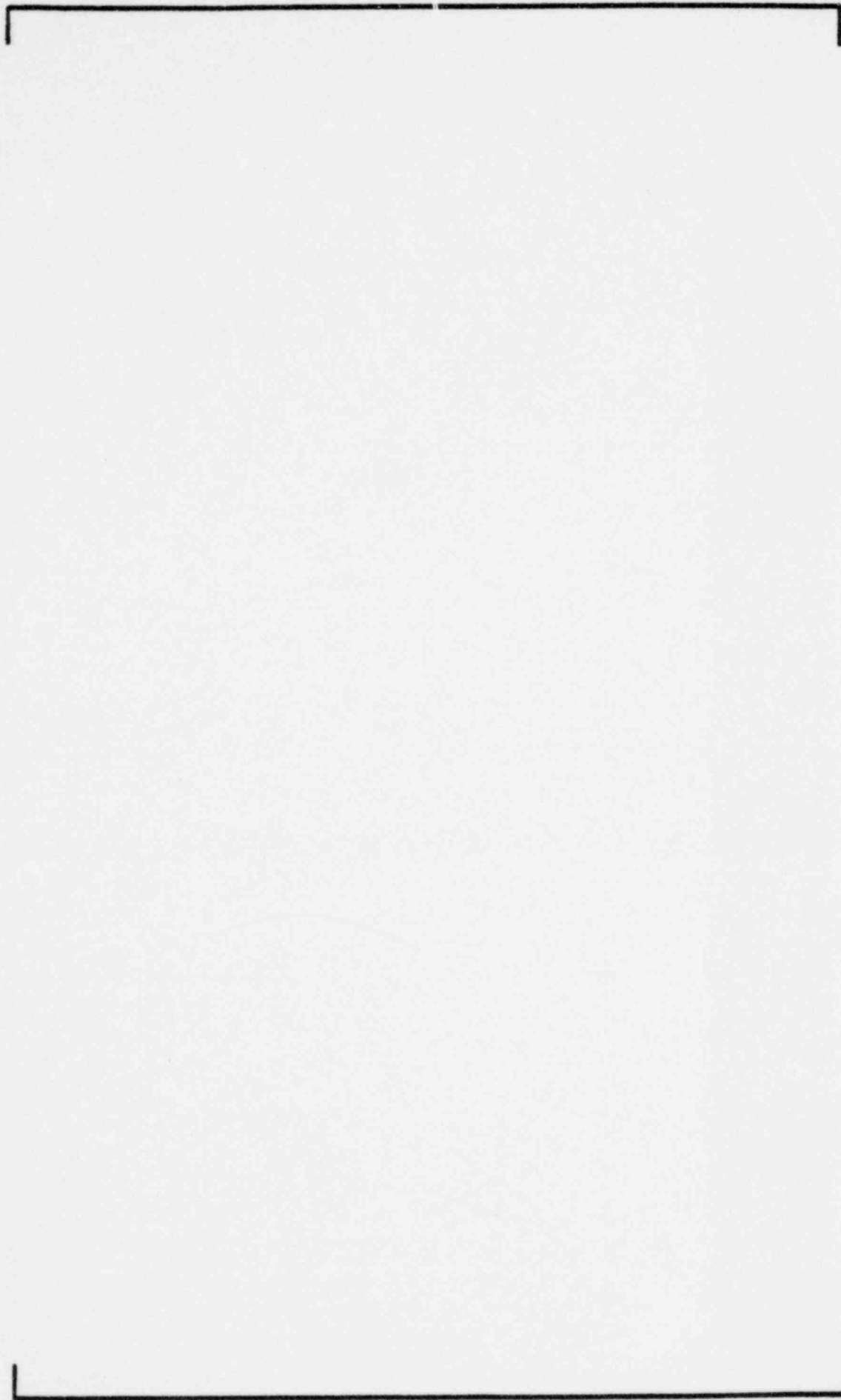


Figure 3-19  
DISTRIBUTION OF DEVIATIONS IN F<sub>p</sub> SYNTHESIS



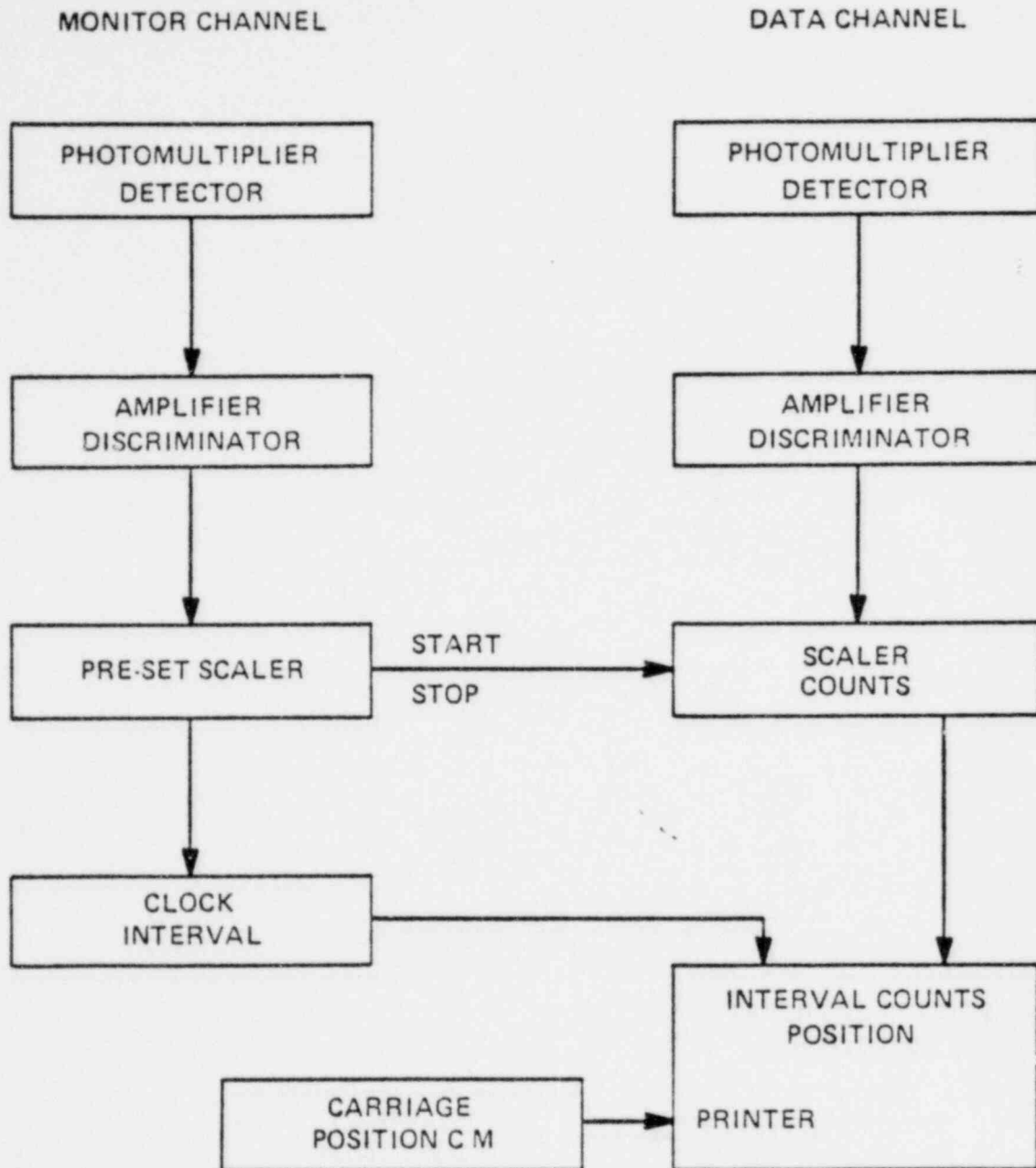


Figure 3-20  
 BLOCK DIAGRAM OF  
 SEMI-AUTOMATIC FUEL ROD SCANNER  
 FOR C-E CRITICALS

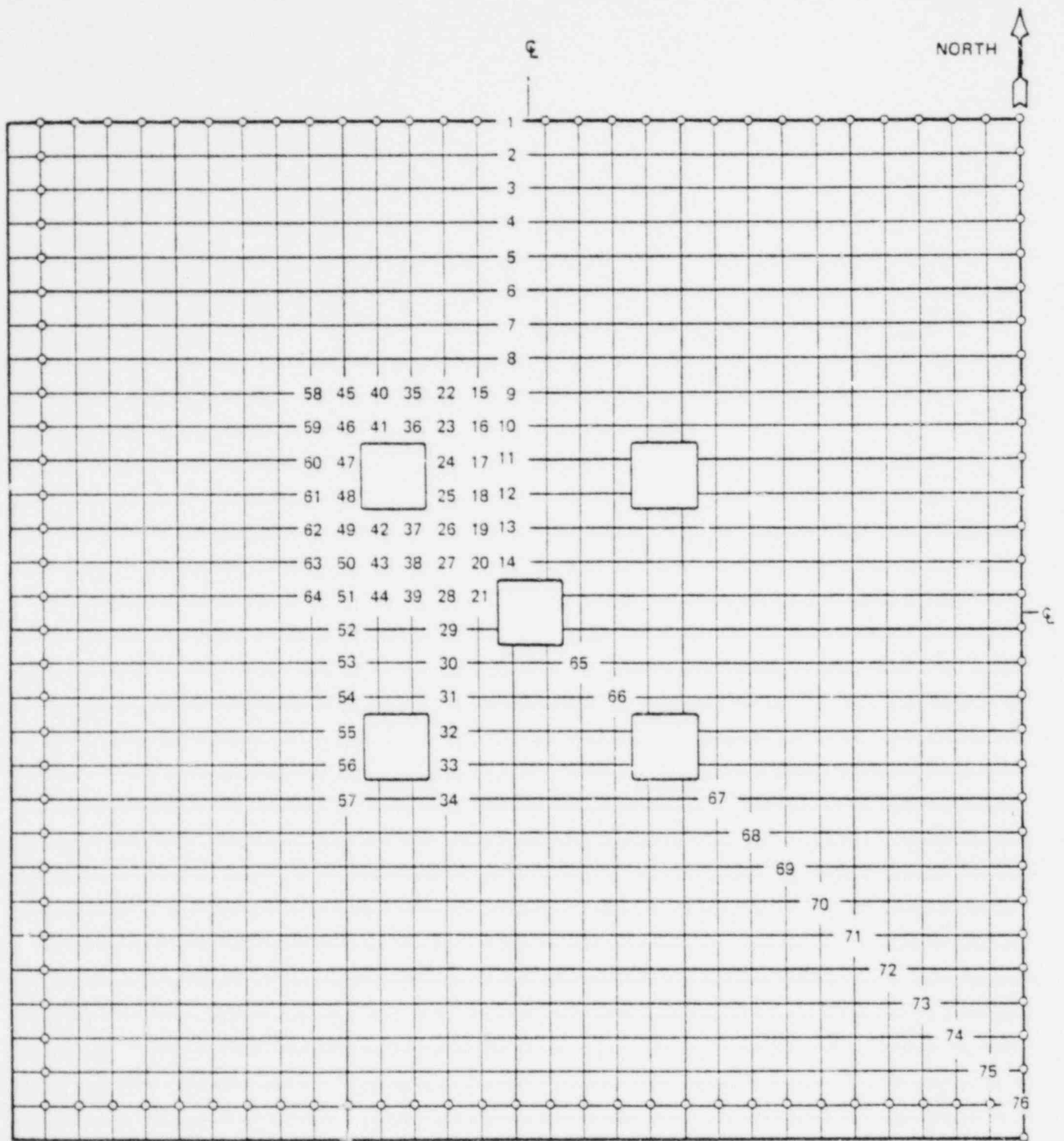


Figure 3-21  
 NUMBERING SYSTEM FOR POWER SCAN AND BUCKLING MEASUREMENTS  
 CE No. 12

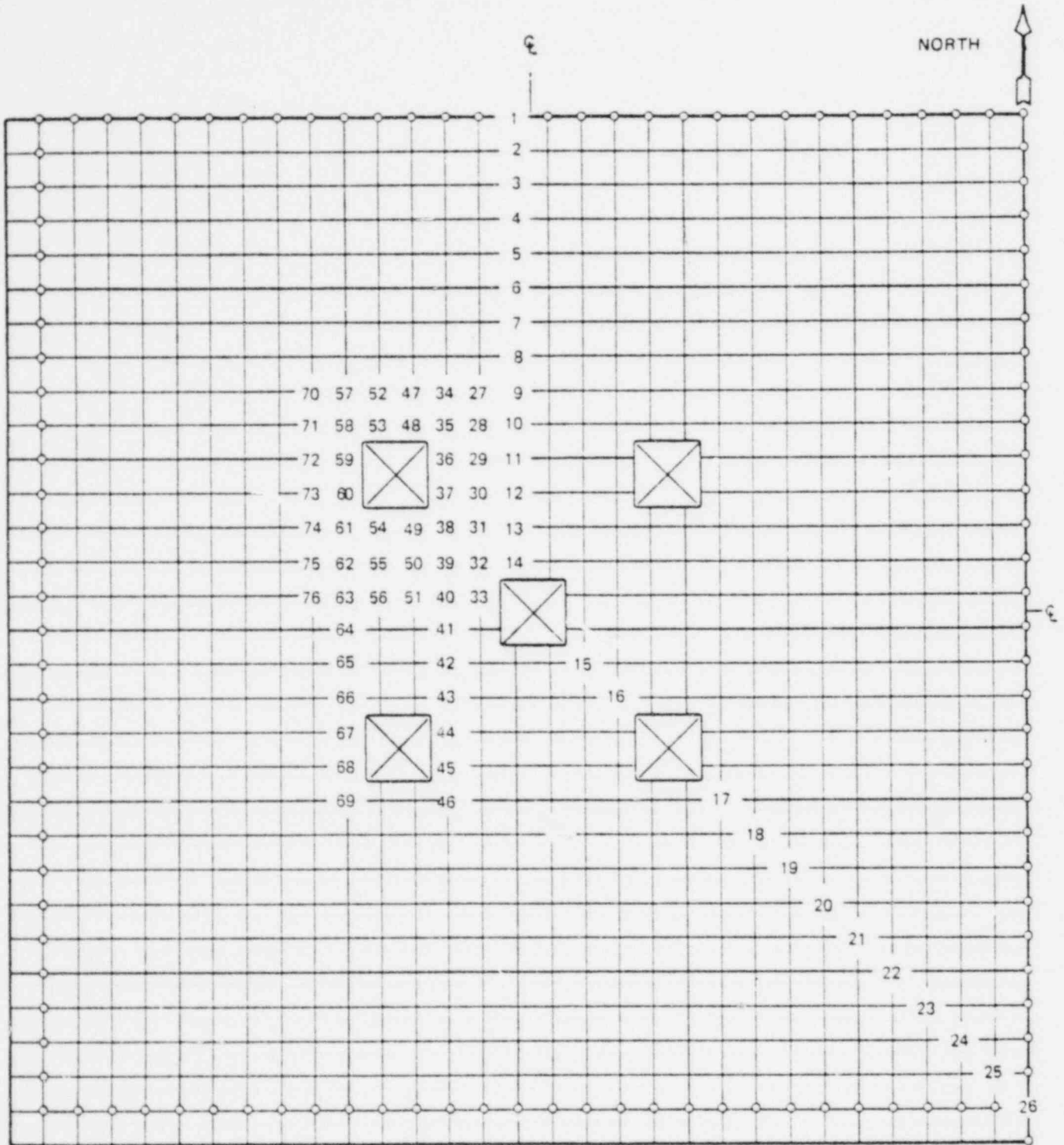


Figure 3-22

NUMBERING SYSTEM FOR POWER SCAN AND BUCKLING MEASUREMENTS  
CE No. 43

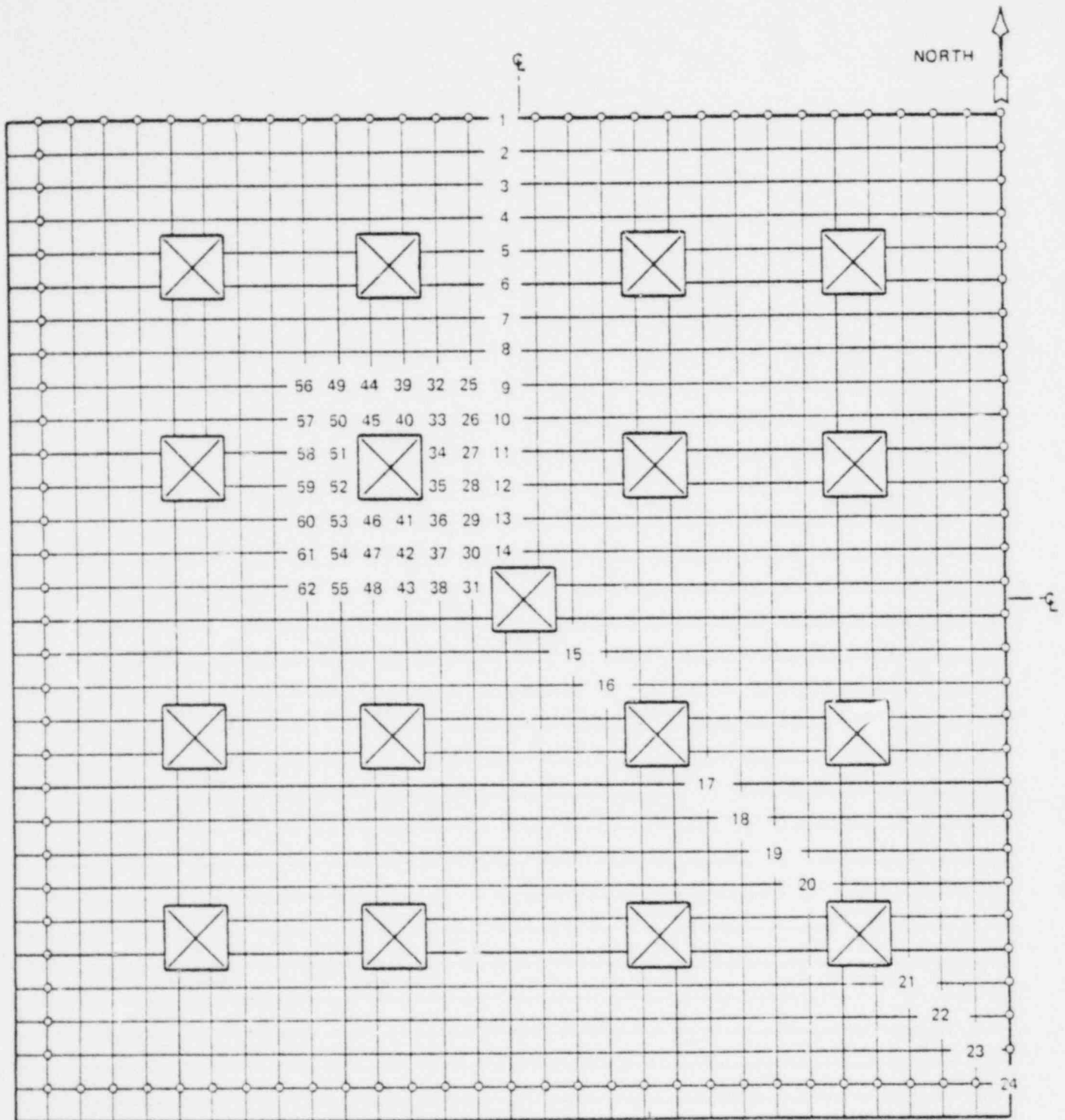


Figure 3-23

NUMBERING SYSTEM FOR POWER SCAN AND BUCKLING MEASUREMENTS  
 CE No. 32, 53, 56

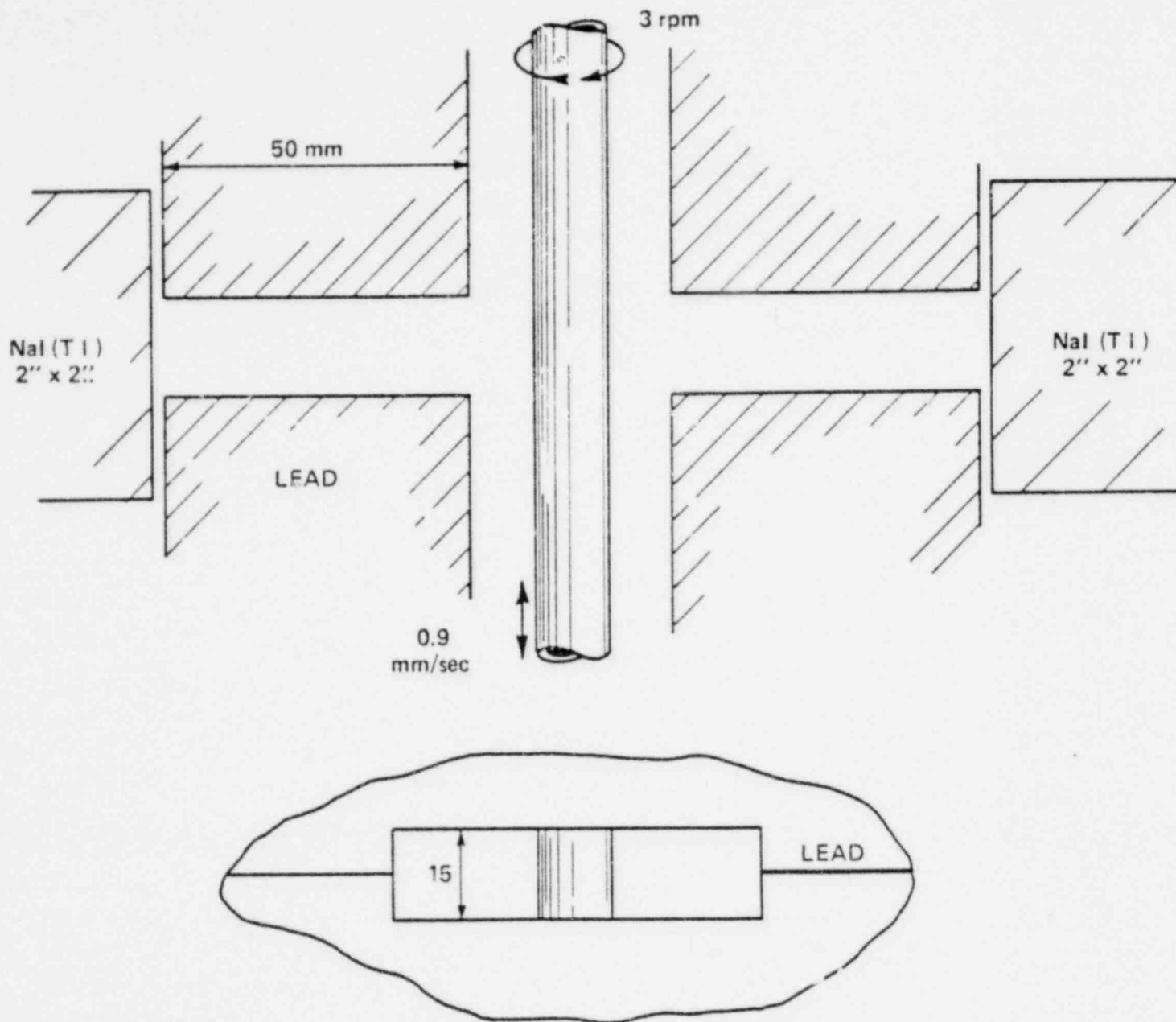


Figure 3-24  
 ARRANGEMENT FOR THE GAMMA SCANNING  
 KRITZ EXPERIMENTS



□ UO<sub>2</sub> - ROD

■ ROD FOR FISSION RATE MEASUREMENT

□ WATER HOLE

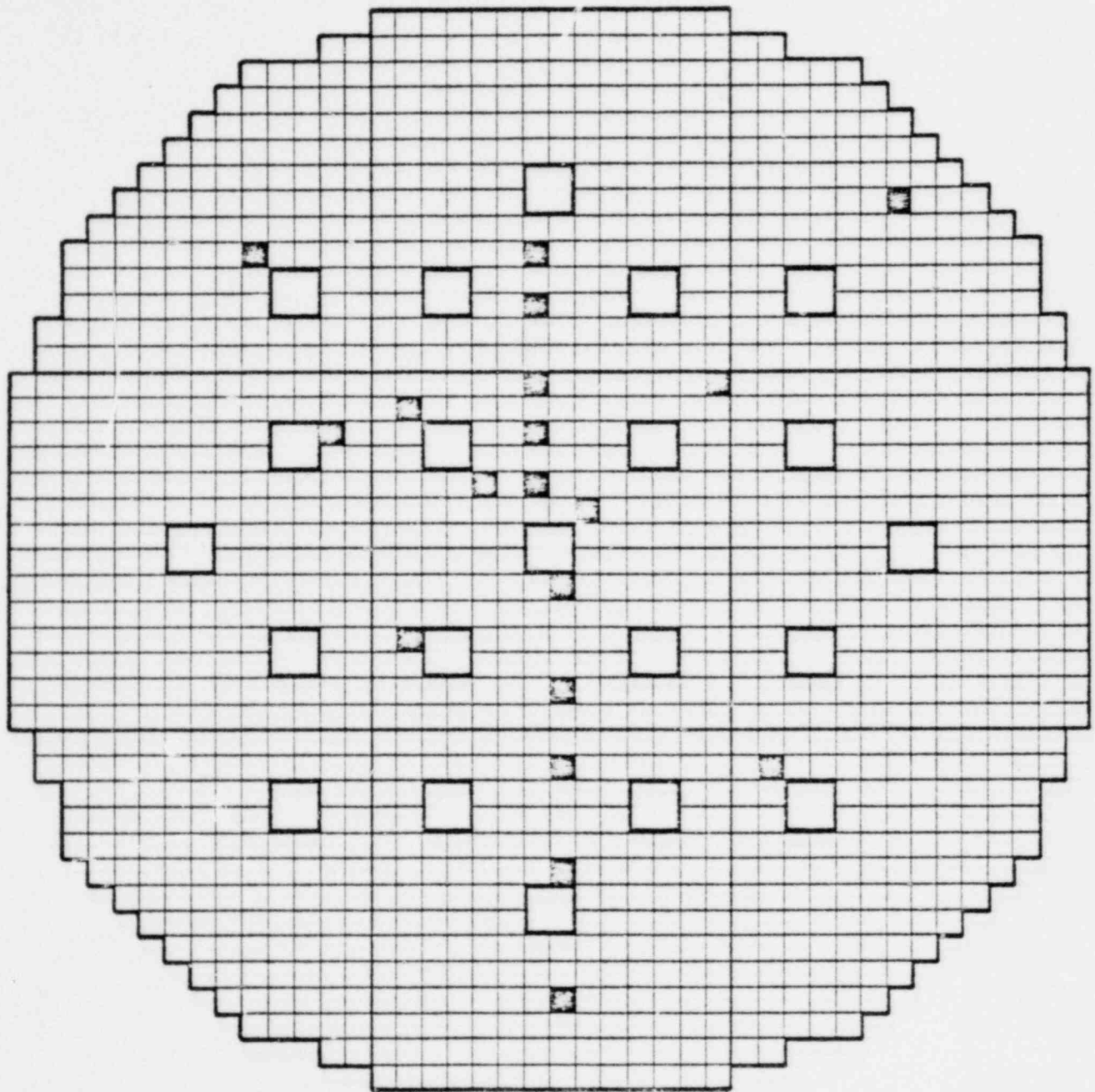


Figure 3-25  
KRITZ U-WH2 CORE LAYOUT

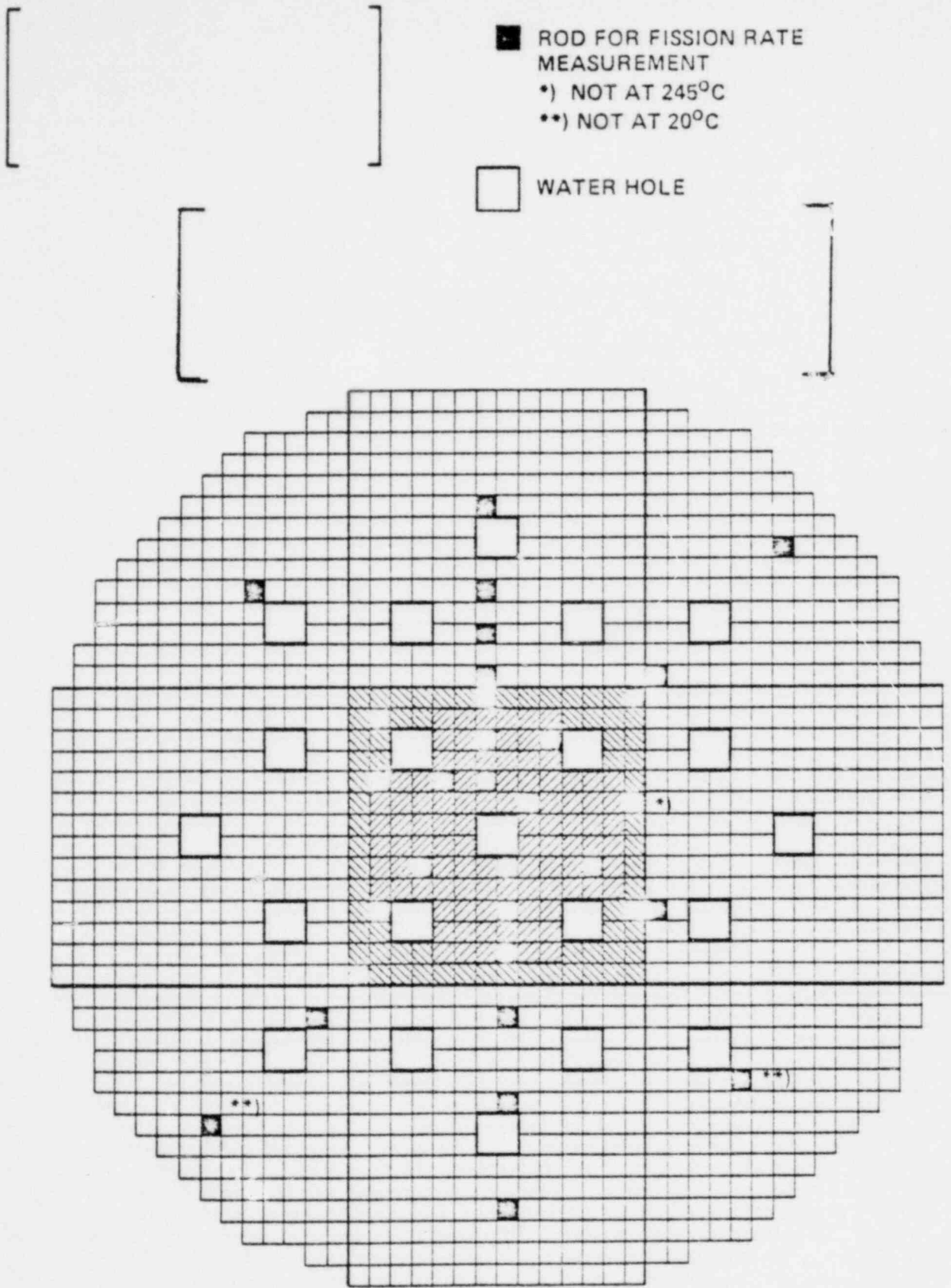
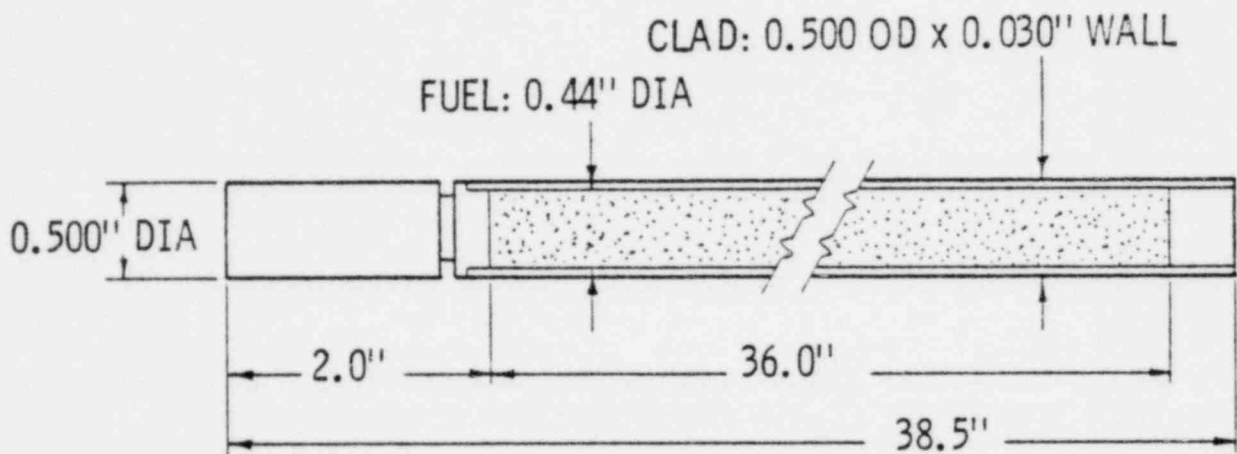


Figure 3-26  
 KRITZ  
 LATTICE Pu - WH2

FUEL SPECIFICATIONS: 2.35% ENRICHED  $UO_2$

FUEL RODS

1. ROD DIMENSIONS



2. CLADDING: 6061 ALUMINUM TUBING

3. TOTAL WEIGHT OF LOADED FUEL RODS: 917 gm (AVERAGE)

FUEL LOADING

1. FUEL MIXTURE VIBRATIONALLY COMPACTED
2. 825 gm OF  $UO_2$  POWDER/ROD, 726 gm OF U/ROD, 17.08 gm OF U-235/ROD
3. ENRICHMENT -  $2.35 \pm 0.05$  w/o U-235
4. FUEL DENSITY -  $9.20 \text{ gm/cm}^3$  (84% THEORETICAL DENSITY)

Figure 3-27  
BNWL FUEL DESCRIPTION

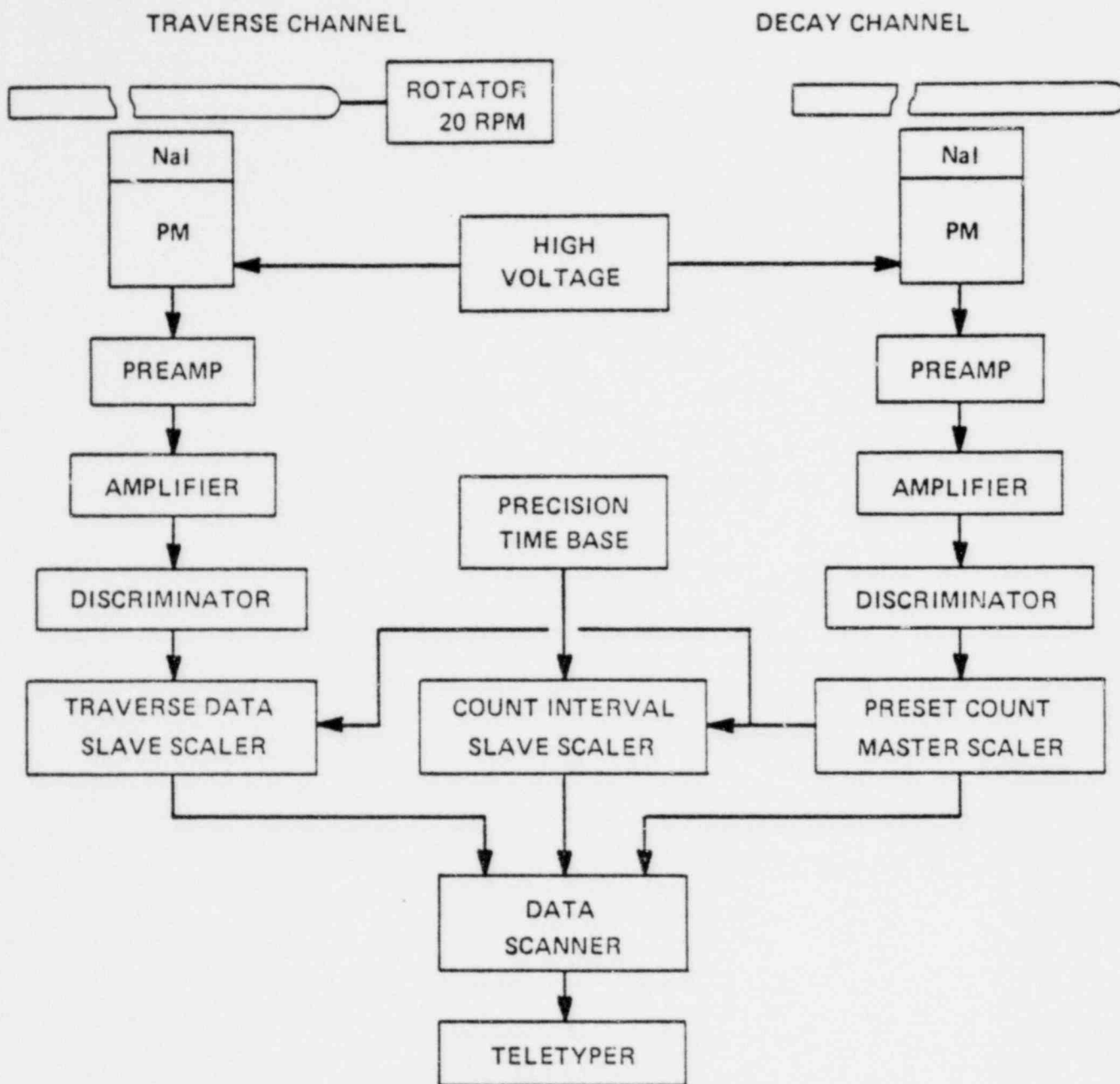
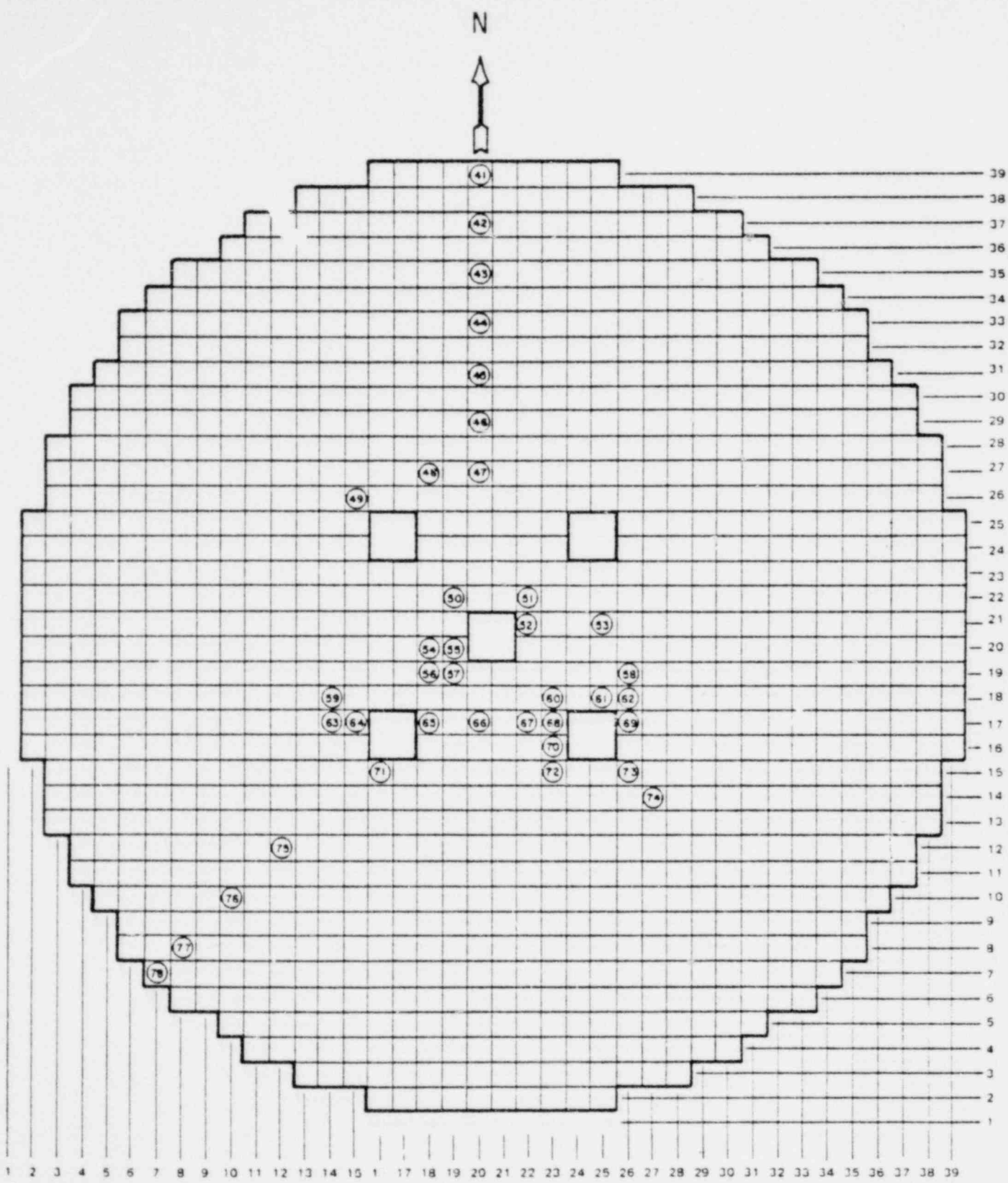


Figure 3-28

DUAL CHANNEL GAMMA SCANNING SYSTEM

BNWL EXPERIMENTS



[  
 $UO_2$  - 2.35%  $^{235}U$  CORE W/WATER HOLES. BNWL GPL-88  
 ]

Figure 3-29

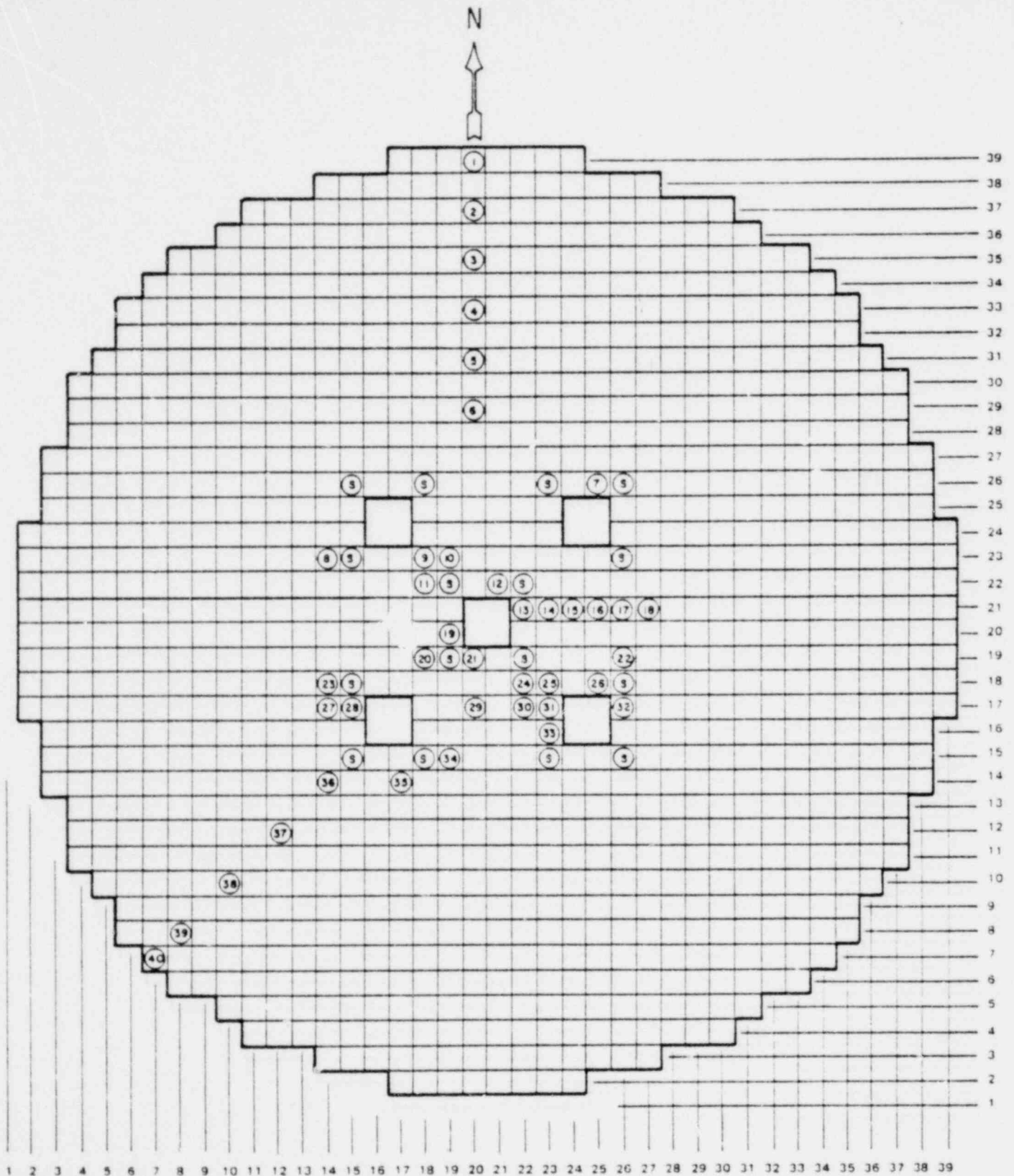


Figure 3-30  
 $UO_2$  2.35%  $^{235}U$  CORE W/WATER HOLES AND KG-33 GLASS SHIMS.  
 BNWL GPL-92

$$\% \text{ DIFF} = \frac{\text{DIT} - \text{MEAS}}{\text{DIT}} \times 100$$

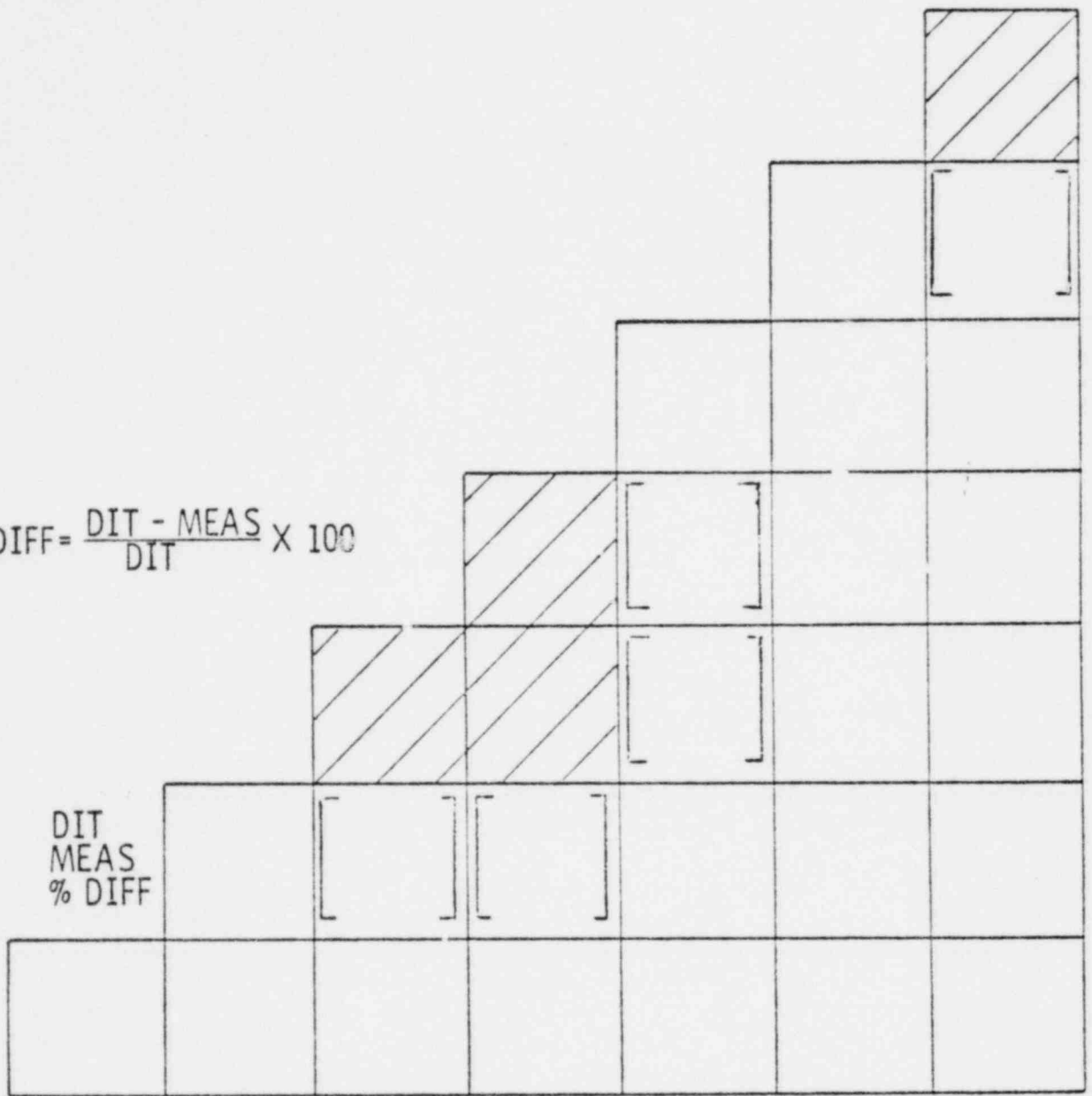


Figure 3-31  
 DIT (K=1) vs MEASURED PIN POWERS  
 CE No. 12



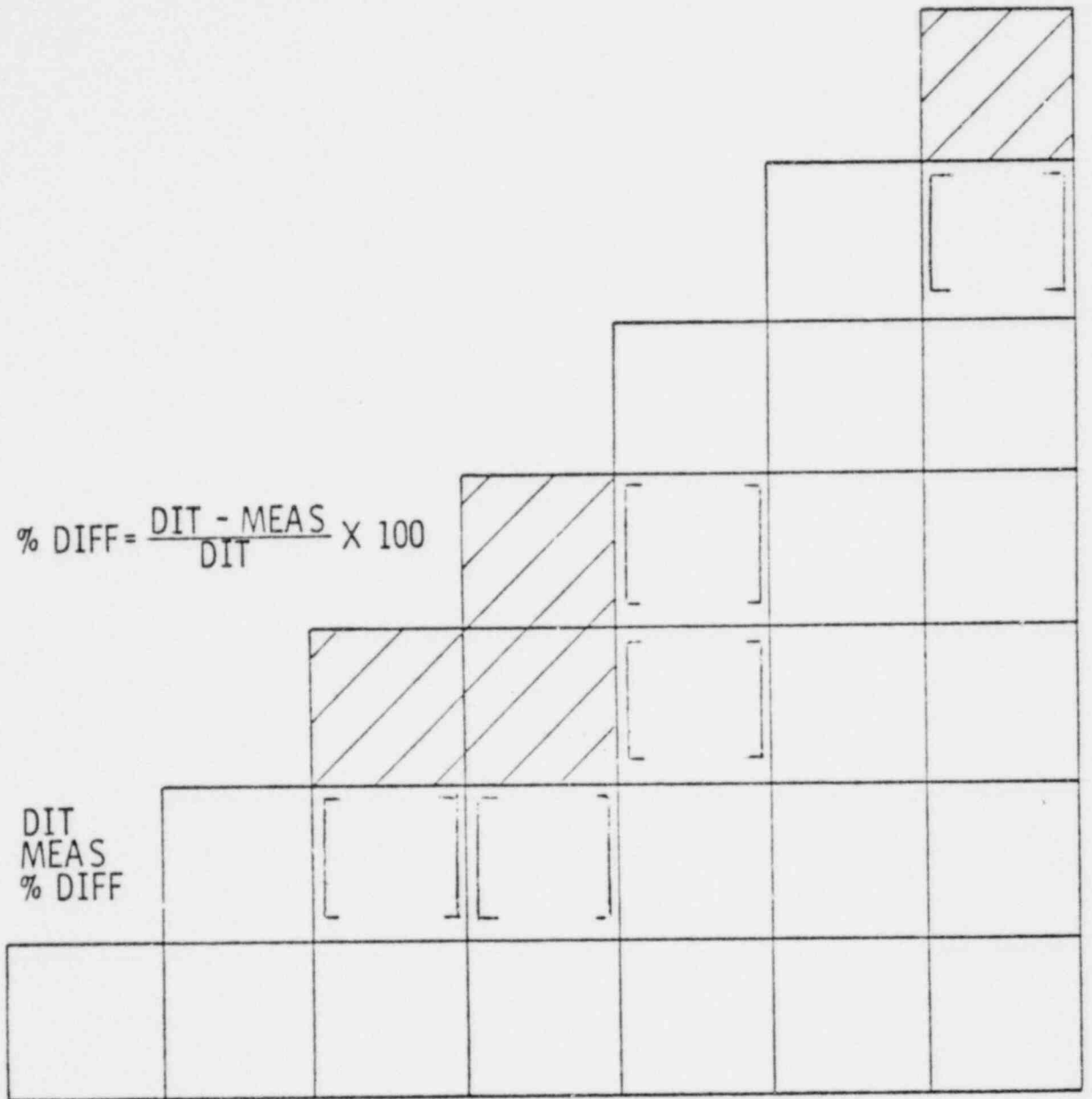


Figure 3-32  
 DIT (K=1) vs MEASURED PIN POWERS  
 CE No. 32



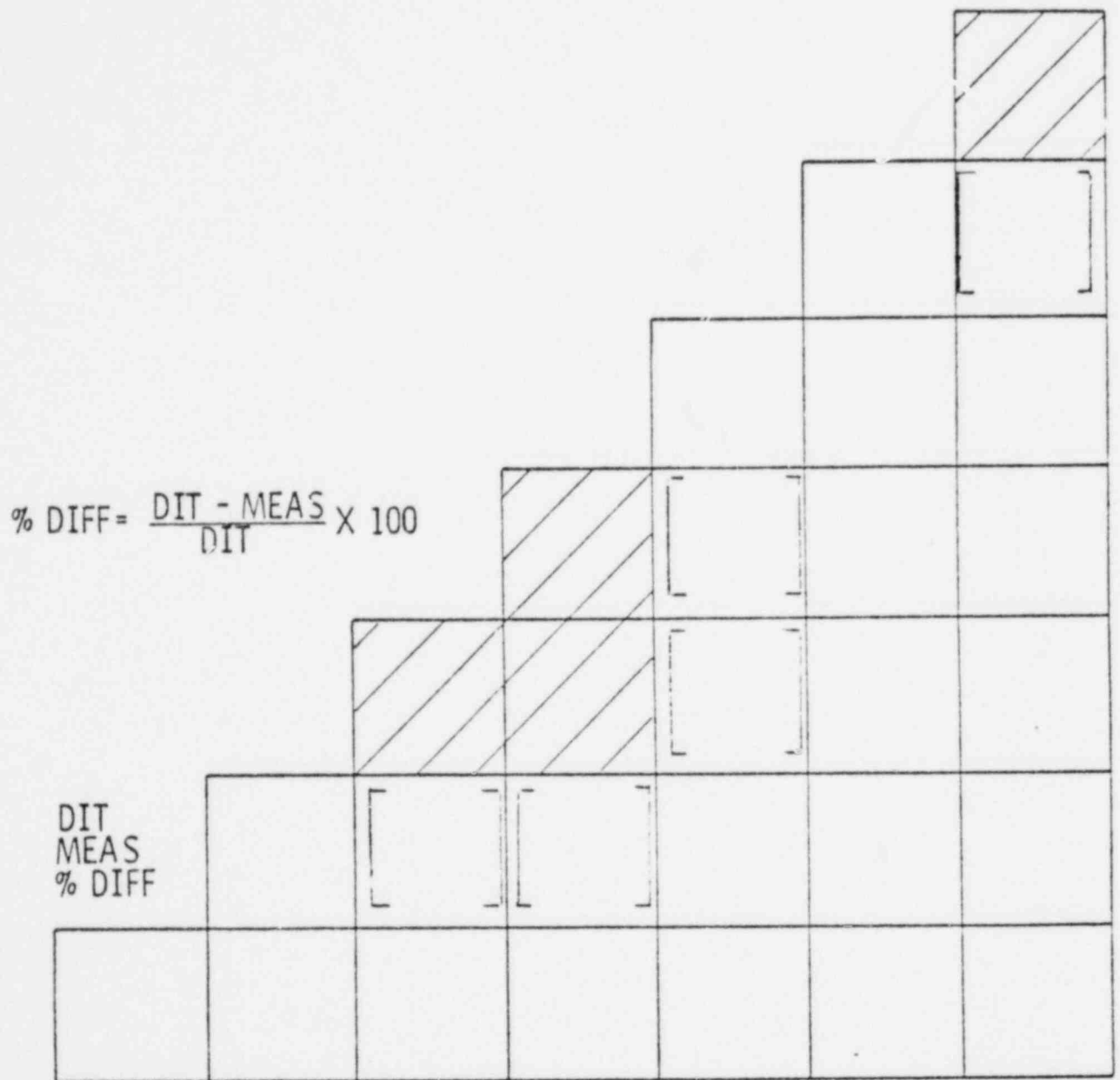


Figure 3-33  
 DIT (K=1) vs MEASURED PIN POWERS  
 CE No. 43

$$\% \text{ DIFF} = \frac{\text{DIT} - \text{MEAS}}{\text{DIT}} \times 100$$

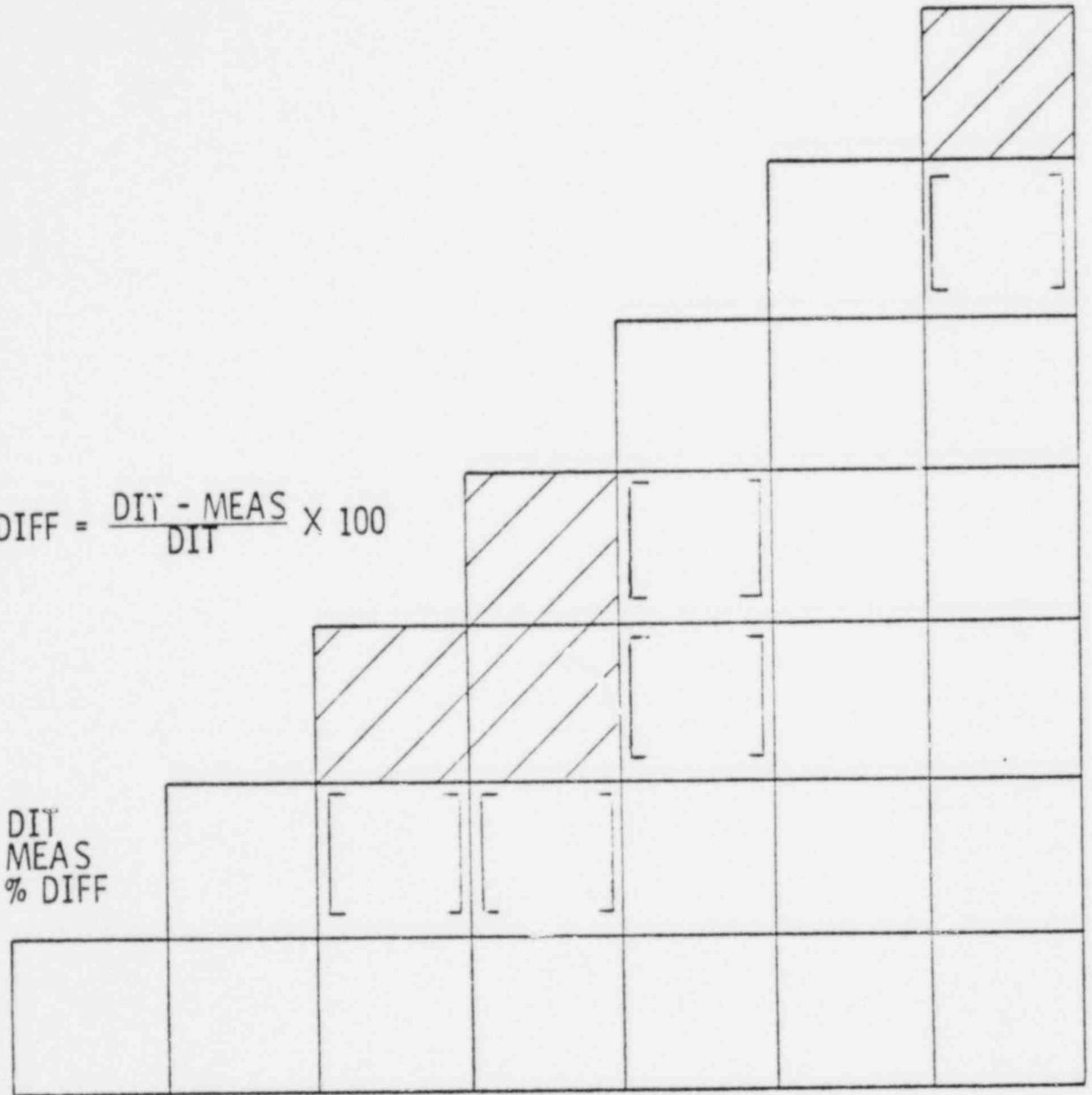


Figure 3-34  
 DIT (K=1) vs MEASURED PIN POWERS  
 CE No. 53 CORE

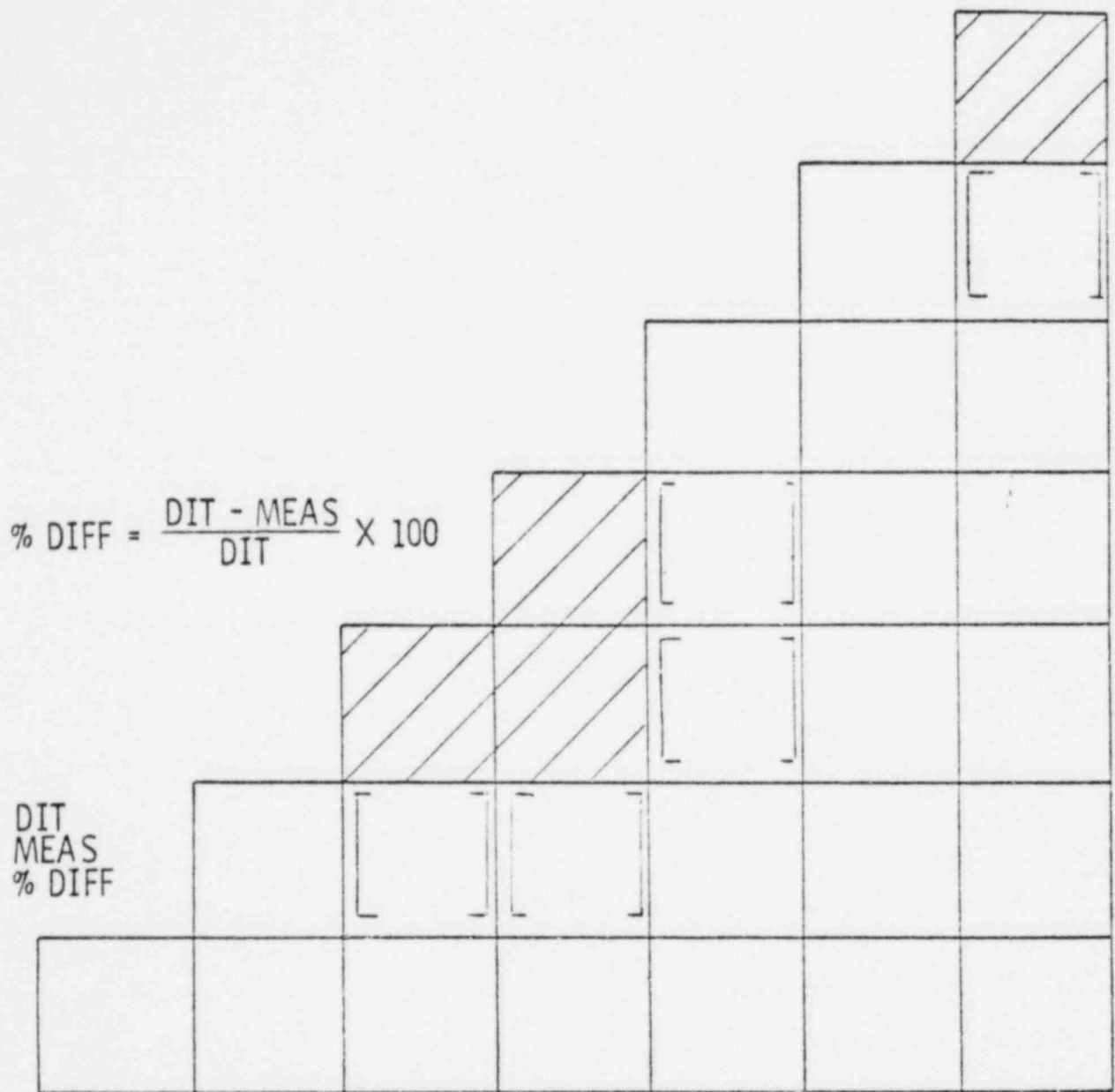


Figure 3-35  
 DIT (K=1) vs MEASURED PIN POWERS  
 CE No. 56 CORE

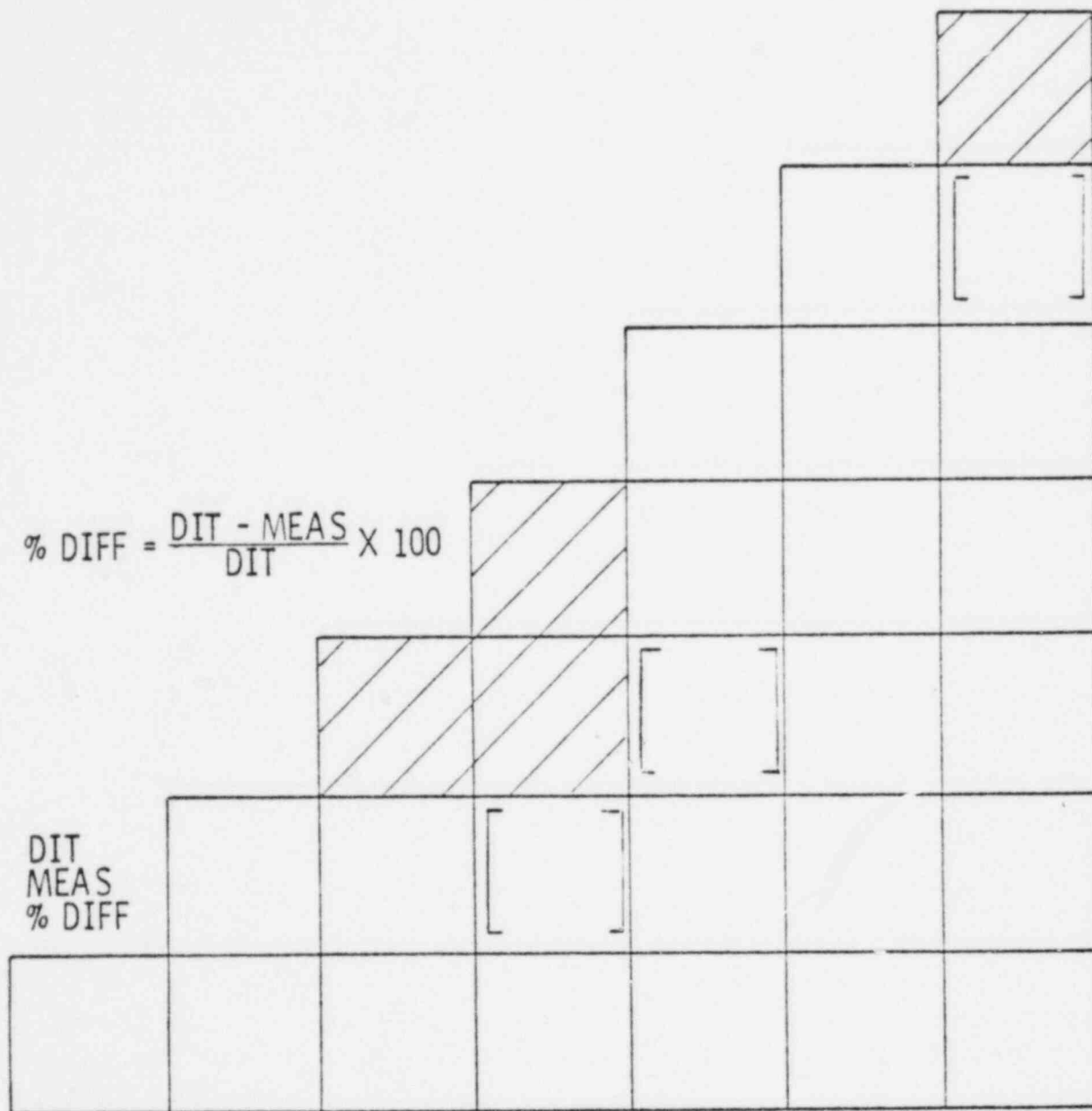


Figure 3-36  
DIT (K=1) vs MEASURED PIN POWERS  
KRITZ U-WH2 CORE

$$\% \text{ DIFF} = \frac{\text{DIT} - \text{MEAS}}{\text{DIT}} \times 100$$

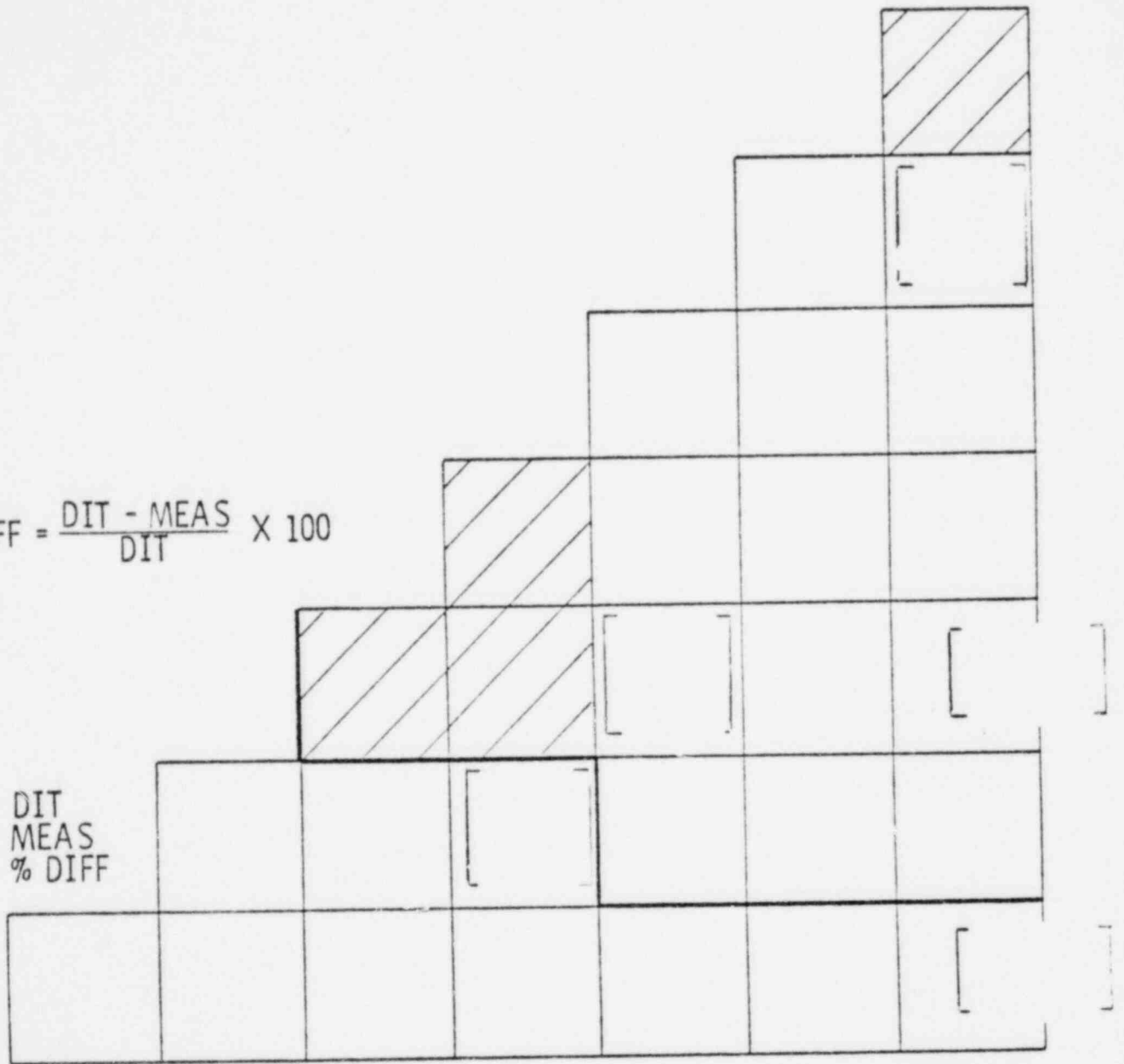


Figure 3-37  
 DIT (K=1) vs MEASURED PIN POWERS  
 KRITZ Pu-WH2 CORE (COLD)

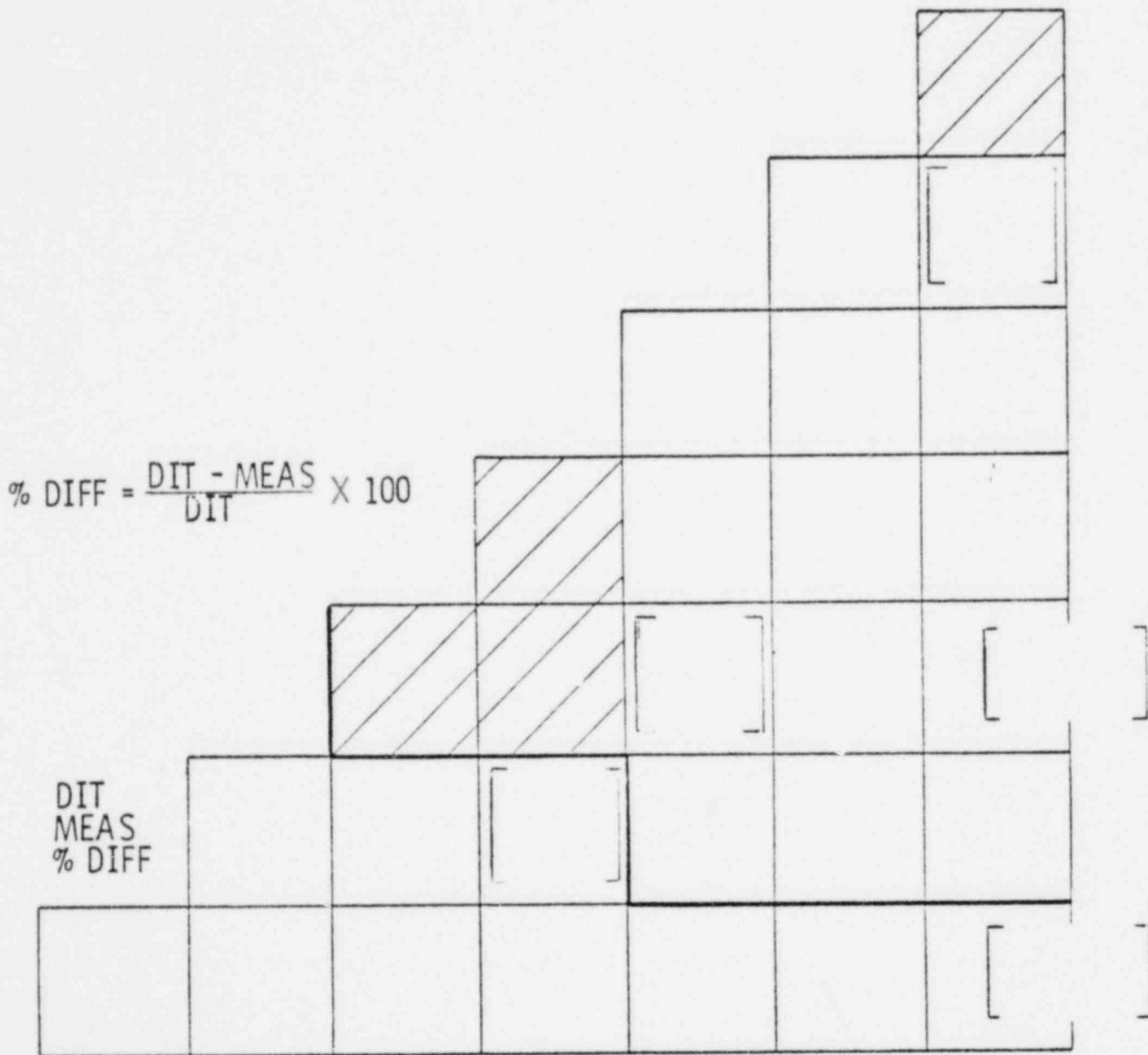


Figure 3-38  
 DIT (K=1) vs MEASURED PIN POWERS  
 KRITZ Pu-WH2 (HOT)

11.3.161

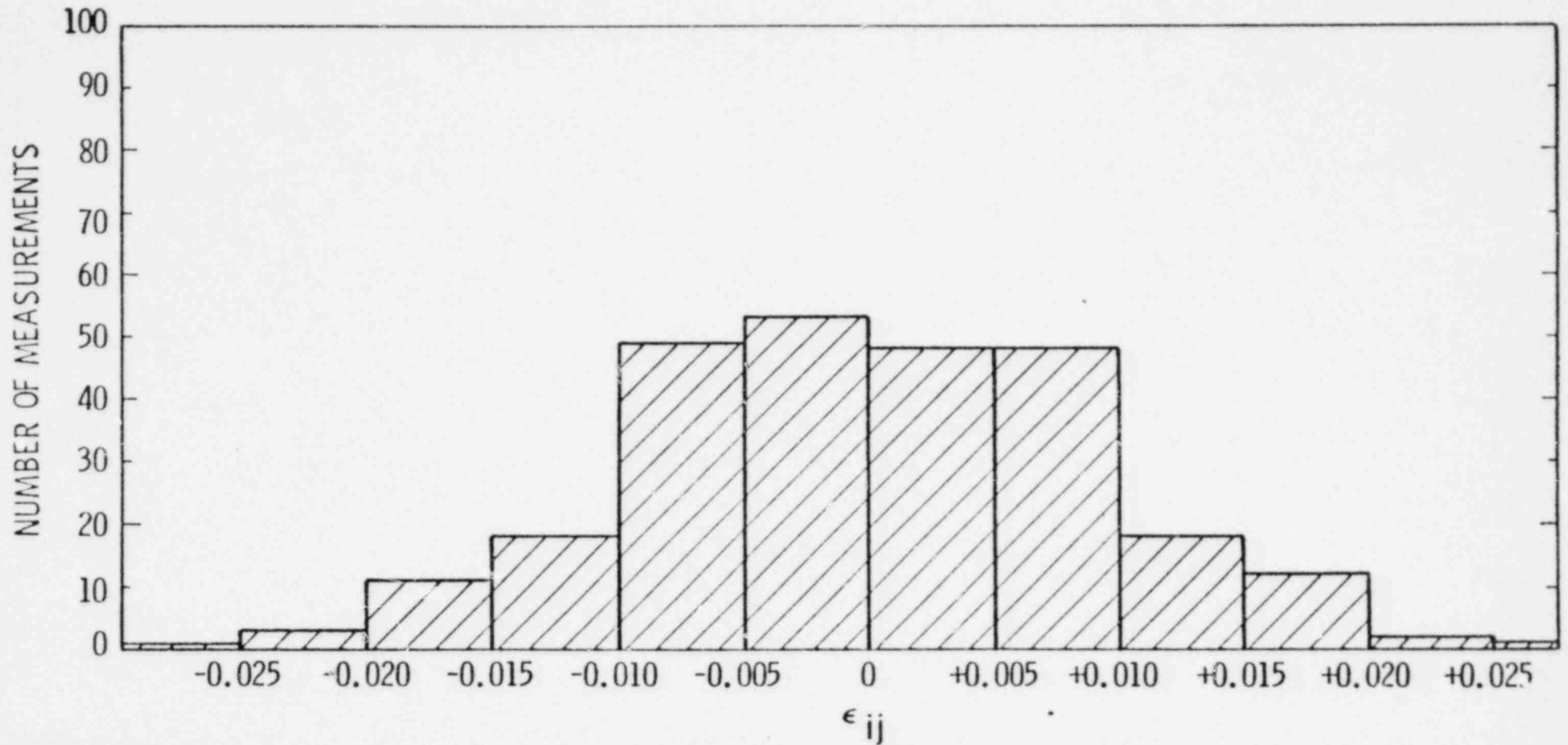
Figure 3-39

COMPARISON OF MEASURED/DIT BIAS AS A FUNCTION OF  
HYDROGEN/URANIUM ATOM RATIO

Figure 3-40

SUMMARY OF RUNS 12, 32, 43, 53, 56

DISTRIBUTION OF  $\epsilon_{ij}$





EVALUATION OF UNCERTAINTY  
IN THE NUCLEAR POWER PEAKING  
MEASURED BY THE SELF-POWERED, FIXED IN-CORE  
DETECTOR SYSTEM

PART III  
COMBINED UNCERTAINTIES

### III.1 COMBINED MEASUREMENT AND SYNTHESIS UNCERTAINTIES

#### 1.0 INTRODUCTION

The individual contributors of measurement and synthesis uncertainties to the overall uncertainty are:

- The box power measurement uncertainty, (Chapter I.3)
- The box power synthesis uncertainty, (Chapter II.3.1)
- The pin/box synthesis uncertainty, (Chapter II.3.2)
- The pin/box calculational uncertainty. (Chapter II.3.3)

Numerical estimates for the respective component variances, tolerance limits and the corresponding number of degrees of freedom,  $f$ , were derived in the individual chapters referenced. Table 1.I lists these quantities for each of the three peaking factors  $F_q$ ,  $F_r$ , and  $F_{xy}$ . The units used in the table are relative units, (%).

#### 1.1 STATISTICAL MODEL

A one-sided lower tolerance limit for the random error in pin peaking measured by INCA/CECOR is to be established for each of the three peaking factors,  $F_q$ ,  $F_r$  and  $F_{xy}$ . Table 1.I contains separate estimates of the mean error and variance for box peaking ( $F_{qBOX}$ ,  $F_{rBOX}$ ,  $F_{xyBOX}$ ) and for pin/box factors ( $F_p$ ). The pin peaking factors are related to  $F_{BOX}$  and  $F_p$  by:

$$F_q = F_{qBOX} \cdot F_p \quad (1.1)$$

$$F_r = F_{rBOX} \cdot F_p \quad (1.2)$$

$$F_{xy} = F_{xyBOX} \cdot F_p \quad (1.3)$$

One task of the statistical model is therefore to combine the uncertainties of box peaking and pin/box factors in order to obtain the overall uncertainty. This will be described in 1.1.3.

Each of the two factors on the right hand side of Eqs. (1.1 - 1.3) are associated with two independent components of the random error. The uncertainty in the pin/box factors has two components designated "calculation" and "synthesis" in Table 1.I. The model for combining these two components is described in 1.1.1. Each box peaking factor,  $F_{qBOX}$ ,  $F_{rBOX}$  and  $F_{xyBOX}$  is associated with two independent components of the random error, viz., the measurement error and the synthesis error. The statistical model for combining these two is described in 1.1.2.

### 1.1.1 Combination of the Pin/Box Synthesis and Calculative Uncertainty

Since local pin peaking cannot be measured directly, box power is converted to peak pin power through the use of calculated pin/box factors,  $F_p$ , as reflected by Equations 1.1 - 1.3 and described in detail in II.1. The calculation is associated with a random error,  $\delta F_p(C)$ . The mean and variance of this error were established in II.3.3. The calculations on which  $F_p$  are based are incorporated in the CECOR and INCA libraries as described in II.2. This process gives rise to a synthesis error,  $\delta F_p(S)$ , which is in addition to the calculational error. The total error in the INCA/CECOR pin/box factor is therefore:



[ ]

] Since the sample means and variances of Table 1.I are either unbiased or conservatively biased estimates, Eqs. (1.5) and (1.6) may be used also for sample means and variances, i.e.:

[ ] (1.7)  
[ ] (1.8)

These relations are used in 1.1.3 to obtain the overall uncertainty.

1.1.2 Combination of Box Synthesis and Measurement Uncertainties

For each one of the box power peaking factors, Table 1.I contains an estimate of the mean and the variance of the associated random error. This error originates from the synthesis process and from the measurement itself. In order to obtain the overall box power peaking uncertainty these two components must be combined. The nature of the combination depends on the analytical relationship between measurement and synthesis errors. This relationship is implicit in the analytical methods for performing the radial coupling and the axial expansion as described in II.1. It can be shown that the combined error is of the form

[ ]

$$\left[ \right] \quad (1.10)$$

$$\left[ \right] \quad (1.11)$$

where  $(\mu_{BOX}, \sigma_{BOX})$  characterizes the uncertainty in INCA box power and  $(\mu_{BS}, \sigma_{BS})$ ,  $(\mu_{BM}, \sigma_{BM})$  are the box synthesis and measurement uncertainties, respectively.

Since  $\mu_{BM}$  is identical to zero Eq. (1.10) reduces to

$$\mu_{BOX} = \mu_{BS} \quad (1.12)$$

[ ] Eq. (1.11)

can conservatively be replaced by:

$$\sigma_{BOX}^2 \leq \sigma_{BS}^2 + \sigma_{BM}^2 \quad (1.13)$$

Eqs. (1.12) and (1.13) show that the component means and variances combine additively. [ ]

### 1.1.3 Combination of Box Peaking and Pin/Box Factor Uncertainties

The box peaking factor uncertainty is characterized by  $(\mu_{BOX}, s_{BOX})$  and estimated by the method described in 1.1.2. The pin/box factor uncertainty

is characterized by  $(\mu_p, \sigma_p)$  estimated by the method described in 1.1.1. The overall uncertainty for pin peaking will be characterized by  $(\mu, \sigma)$  and the method for estimating it is described in this section.

Eqs. (1.1 - 1.3) show the single analytical relationship between the box peaking and the pin/box factors. It follows from these relationships that the random errors are related by:



If the relative units of Table 1.I are used, Eqs. (1.17) and (1.18) are therefore equivalent to

$$\mu = \mu_{\text{BOX}} + \mu_p \quad (1.19)$$

$$\sigma^2 = \sigma_{\text{BOX}}^2 + \sigma_p^2 \quad (1.20)$$

Rewriting Eqs. (1.19) and (1.20) in terms of individual components and using sample means and variances from (1.7), (1.8), (1.14) and (1.15) yields the final form for the overall, combined uncertainty:

$$\mu \cong \bar{D} = \bar{D}_{BS} + \bar{D}_{PC} + \bar{D}_{PS} \quad (1.21)$$

$$\sigma^2 \leq S^2 = S_{BS}^2 + S_{BM}^2 + S_{PC}^2 + S_{PS}^2 \quad (1.22)$$

#### 1.1.4 Determination of a Tolerance Limit for the Combined Uncertainty

$\bar{D}$  and  $S$  from Eqs. (1.21) and (1.22) are estimates of the true distribution characteristics  $\mu$  and  $\sigma$  and are therefore themselves subject to random errors. A one-sided, lower tolerance limit is constructed such that the INCA power distribution measurement uncertainty can be estimated on a 95%/95% probability/confidence level.

Table 1.I lists, for each individual component, the individual 95%/95% probability/confidence limits and the associated number of degrees of freedom (d.f.) as determined in the appropriate section of this report. The component d.f.'s will be used to construct the overall tolerance limit. Accordingly, each sample variance is assumed to be proportional to a chi-square distributed variable with the number of d.f. given in Table 1.I. Justification for these assumptions are given in the appropriate section of this report. [

] Finally, for all other cases normality tests did not refute assumptions of normal distributions. Hence in all cases the assumption of chi-square distributed sample variances is justified.

Expressing each sample variance in Eq. (1.22) as proportional to a  $\chi^2$ -distribution gives:

$$\frac{\sigma^2 \chi_f^2}{f} = \frac{\sigma_{BS}^2 \chi_{fBS}^2}{f_{BS}} + \frac{\sigma_{BM}^2 \chi_{fBM}^2}{f_{BM}} + \frac{\sigma_{pC}^2 \chi_{fpC}^2}{f_{pC}} + \frac{\sigma_{pS}^2 \chi_{fpS}^2}{f_{pS}} \quad (1.23)$$

Taking the variance of both sides in (1.23) yields the following relationship

$$\frac{\sigma^4}{f} = \frac{\sigma_{BS}^4}{f_{BS}} + \frac{\sigma_{BM}^4}{f_{BM}} + \frac{\sigma_{pC}^4}{f_{pC}} + \frac{\sigma_{pS}^4}{f_{pS}} \quad (1.24)$$

Finally, estimating the population variances by the sample variances yields the following relationship:

$$\frac{S^4}{f} = \frac{S_{BS}^4}{f_{BS}} + \frac{S_{BM}^4}{f_{BM}} + \frac{S_{pC}^4}{f_{pC}} + \frac{S_{pS}^4}{f_{pS}} \quad (1.25)$$

The overall number of d.f. is determined from (1.25) and the 95%/95% probability/confidence multiplier,  $k_{95/95}$ , is determined by Reference 1.1. The lower one-sided tolerance limit for the deviation between INCA/CECOR and the true power is then determined by:

$$\bar{D} - k_{95/95} S \quad (1.26)$$



## 1.2

NUMERICAL RESULTS FOR THE OVERALL INCA/CECOR MEASUREMENT UNCERTAINTY

Following the method described in 1.1 using the data from Table 1.I, the following numerical estimates result for each one of the uncertainties associated with  $F_q$ ,  $F_r$  and  $F_{xy}$ .

The lower, one-sided tolerance limits of the overall uncertainty for core peaking factors measured by INCA/CECOR:

	$\bar{D}(\%)$	S(%)	f	k	$\bar{D} - kS(\%)$
$F_q$	[				-6.24
$F_r$					-6.04
$F_{xy}$					-5.29

Thus the overall measurement uncertainty is such that there is a 95% probability that at least 95% of the true  $F_q$ ,  $F_{xy}$ , and  $F_r$  values will be less than the values inferred from INCA/CECOR measurement plus 6.2, 5.3 and 6.0% respectively.

These uncertainties are to be used in conjunction with Technical Specification limits on  $F_q$ ,  $F_{xy}$  and  $F_r$  to establish appropriate LCO and LSSS limits for plant operation and safety analysis.

1.3 REFERENCES

- 1.1 "Factors for One-Sided Tolerance Limits and for Variables Sampling Plans," Sandia Corporation Monograph, SCR-607, 1963, Table 2.4.

Table 1.I  
 Summary of Measurement and Synthesis  
 Uncertainty Components+  
 For INCA/CECOR Core Peaking Factors

Parameter	Uncertainty Component	$\bar{D}$ (%)	S (%)	f	$\bar{D} - kS$ (%)
$F_q$	Box (meas)				
	(synth)				
	Pin (calc)				
	(synth)				
$F_r$	Box (meas)				
	(synth)				
	Pin (calc)				
	(synth)				
$F_{xy}$	Box (meas)				
	(synth)				
	Pin (calc)				
	(synth)				

+Note that the statistics in this table use the convention that deviations correspond to INCA/CECOR measurement minus truth. In Chapters I.3 and II.3 the reverse sign convention is used.